Northumbria University
NEWCASTLE

MEAN FIELD THEORIES AND DIFFERENTIAL IDENTITIES FOR MULTISPECIES ISING MODELS AND EXPONENTIAL RANDOM GRAPH MODELS

OLEG SENKEVICH

PhD

2022

MEAN FIELD THEORIES AND DIFFERENTIAL IDENTITIES FOR MULTISPECIES ISING MODELS AND EXPONENTIAL RANDOM GRAPH MODELS

OLEG SENKEVICH

A thesis submitted in partial fulfilment of the requirements of the University of Northumbria at Newcastle for the degree of Doctor of Philosophy

Faculty of Engineering and Environment

January 2022

Abstract

This work is concerned with the mean field theories (MFTs) of multispecies Ising models and various probabilistic ensembles of graphs known as exponential random graph models (ERGMs). The MFT is a universal approximation, in which the true Hamiltonian of the model is linearised by introducing self-consistent mean fields, and it turns out that the mean field self-consistency equations can be obtained as low viscosity solutions of certain viscous partial differential equations (PDEs) that arise from differential identities obeyed by the Helmholtz free energies of the so-called mean field models, whose exact thermodynamic solutions coincide with the mean field self-consistency equations.

Thermodynamic equations of state are obtained for the multi-component analogue of the Curie-Weiss (CW) model and analysed in detail for the 2-component case. This analysis largely extends the preceding works by providing a good orientation in the parameter space of the 2-component CW model, which reveals that, unlike the original CW model, the 2-component model admits critical points in nonzero fields and can exhibit any number from one to four of (meta)stable macrostates. The results are confirmed by Monte-Carlo (MC) simulations, and some applications of the model are discussed.

The above discussion is followed by the mean field analysis of a particular class of ERGMs, known as homogeneous Markov random graphs. Such models are precisely described by the MFT at large sizes due to their infinite-dimensional nature, and this work provides a simple unified approach to study such models at the macroscopic level, reveals a possibility of (meta)stable macrostates of moderate connectance at arbitrarily low temperatures, and gives a general result relating the order of the interactions with the maximum number of (meta)stable macrostates. MC simulations show that, as expected, the theory seems to be exact for macroscopic observables of large homogeneous ERGMs, but often fails at the microscopic level or for the models of small size. The results suggest that the long-tailed distributions, common in real-world networks, cannot be fully explained by the spontaneous symmetry breaking in homogeneous ERGMs, and for this reason, the heterogeneous ERGM, based on the multicomponent CW model, is introduced and discussed.

Contents

Acknowledgements

I am grateful to Dr Antonio Moro for his supervision, Dr Gino Biondini and Dr Adriano Barra for useful discussions, Leverhulme Trust and Northumbria University for funding this research.

Declaration

I declare that the work contained in this thesis has not been submitted for any other award and that it is all my own work. I also confirm that this work fully acknowledges opinions, ideas and contributions from the work of others. The work was done in collaboration with Dr Antonio Moro.

Any ethical clearance for the research presented in this thesis has been approved. Approval has been sought and granted through the *ethics online system* on *28/01/2019*.

I declare that the Word Count of this thesis is 40000 ± 5000 **words**.

Name: Oleg Senkevich

Date: 24 January 2022

Chapter 1

Introduction

1.1 Multi-species Ising models

Ising models are discrete statistical models with pairwise dependencies (interactions) between their binary degrees of freedom ("spins"). Such models first appeared in physics as qualitative models of magnetism and are famous for explaining the emergence of spontaneous magnetisation in ferromagnetic materials along with a number of other effects. Despite the conceptual simplicity of such models, their exact solution is found only for the cases of 1-dimensional lattice, 2-dimensional lattice in zero field [Onsager (1944)] and the Ising model on a fully connected graph known as the Curie-Weiss model. For this reason, numerous approximations have been used to gain valuable insights about the behaviour of such models, the simplest and one of the earliest of which is the mean field theory (MFT) [Weiss (1907)]. The main assumption of the MFT is that every spin experiences an average field created by all the other spins in the model, which, essentially, turns a many-body problem into a single-body problem. This assumption greatly simplifies the analysis, however, it is invalid when the number of direct interactions of all or most of the spins is low, which is usually the case in physical applications, where the nearest neighbours interactions on low dimensional lattices are commonplace.

As will be discussed in Section 2.1.2, Ising models can be regarded as maximum-entropy statistical ensembles with prescribed expected values and pairwise correlators of spins. This interpretation resulted in numerous recent applications of such models in computational biology [Schneidman et al. (2006); Lezon et al. (2006); Stein et al. (2015); Agliari et al. (2016)], sociology [Contucci

et al. (2008)], finance [Bury (2013)] and other fields. Ising models in such applications are often defined on complex networks whose average degrees may be relatively high, which makes the MFT more successful quantitatively, and in most of these new applications the parameters of the Ising models are treated as unknowns which should be estimated from data [Nguyen et al. (2017)].

Sometimes the number of the parameters can be greatly reduced by separating the spins into several classes[1] (species) with distinctive interaction strengths within and between the classes [Agliari et al. (2016); Contucci et al. (2008)]. In such cases the Ising models are said to be *multi-species* [Fedele et al. (2013)], and the MFT for such models is considered in this work.

Unfortunately, statistical learning of the parameters is often impossible even for the simplest Ising models due to the degeneracy of the probability distributions arising in certain regions of their parameter spaces. This work provides a detailed analysis of the MFT for the general two-species Ising models (through the study of the two-component Curie-Weiss model) and gives a good orientation in its parameter space.

1.2 Exponential random graph models

Exponential random graph models (ERGMs) are statistical ensembles of graphs naturally arising as maximum-entropy statistical models of real-world networks. It is hard to say where ERGMs were first introduced, given the broadness of this class of network models and the lack of a generally accepted definition. The early models of [Erdős and Rényi (1959)] and [Holland and Leinhardt (1981)] which assumed statistical independence of links (edges) belong to ERGMs and are famously too simple to mimic most of the real-world networks. Markov graphs introduced in [Frank and Strauss (1986); Strauss (1986)] are more sophisticated examples of ERGMs in which the edges sharing a common node can be statistically dependent. A more general class of models was introduced in [Wasserman and Pattison (1996)] under the name "$p*$" which is supposed to be understood as a generalisation of the "p_1" model from [Holland and Leinhardt (1981)], and since such models are defined by exponential families of probability distributions over graphs, they became known as ERGMs. In later works [Snijders et al. (2006); Robins, Snijders, Wang, Handcock and Pattison (2007)] the concept of ERGMs was pushed further, and the terms ERGMs and $p*$

[1] The number of classes is assumed to be much smaller than the number of spins.

were used interchangeably as referring to the families of probability distributions that are not log-linear in the parameters, hence, strictly speaking, not exponential. Since this work is concerned with all kinds of models mentioned above, we vaguely define ERGMs as families of probability distributions over graphs that can be naturally expressed in some exponential form[2].

Not surprisingly, comparison between the real-world networks and the simplest nontrivial ERGM, known as Erdős-Rényi model [Erdős and Rényi (1959)], with the same (on average) number of links revealed their vast differences implying high amounts of information encoded in the empirical networks' features other than the total number of edges. For example, the real-world networks may exhibit levels of clustering that are extremely unlikely in the Erdős-Rényi model with the same (on average) number of links. Such features, clearly, cannot be captured by a model with uncorrelated edges, but the main virtue of ERGMs is that the required edge correlations can be introduced in an easily interpretable way. This fact has been giving some hope that valuable insights about real-world networks can be obtained by embedding some of their information into ERGMs, which after the correct parameter estimation should resemble the features of such networks at the level of individual samples. However, it soon became clear that there are serious problems that prevent ERGMs with a relatively small number of parameters from mimicking sufficiently large real-world networks [Park and Newman (2005); Newman (2010); Annibale and Courtney (2015)], and in this work we show that these problems are quite general. It turns out that all infinite-dimensional homogeneous ERGMs are very similar in the thermodynamic limit where their behaviour is precisely described by the mean field theory, and this lack of variability largely limits their potential in the real-world data analysis.

Note that, unlike Ising models, the statistical dependencies of edges in ERGMs are not assumed to be pairwise, and the presence or absence of an edge is given by the corresponding entry of the adjacency matrix, which can be either 0 or 1 (as opposed to (-1,1)-spins of Ising models). In what follows all models with binary degrees of freedom are referred to as *Ising-like* to unify the discussion of the methods that are equally applicable to all such models; and the maximum order of statistical dependencies is called the order of the model, e.g. pairwise interactions correspond to the order two, triple-wise to the order three, etc. This terminology transfers to the MFTs, i.e. the MFT of a model of order n is called the MFT of order n.

[2]Which does not have to be log-linear in all of the free parameters, as will be discussed in Section 4.6.4.

1.3 Outline of the work

Essentially, this work is mainly concerned with two conceptually different mean field theories: one of the order two with an arbitrary number of independent observables; and another of an arbitrary order but with only one independent observable. We show how both MFTs are related to the solutions of certain integrable partial differential equations (PDEs) and how they can be applied in various contexts.

The rest of the text is structured as follows. Chapter 2 introduces basic concepts, facts and methods from statistical mechanics needed to proceed and exemplifies them on a Curie-Weiss (CW) model, which is the simplest nontrivial instance of the kind of models we consider. Chapter 3 is concerned with a multicomponent Curie-Weiss (MCW) model, which is a particular multidimensional generalisation of the CW model. This is followed by the analysis of various ERGMs in Chapter 4. Note that Chapter 3 and Chapter 4, which contain most of the original results, can be read independently after the background information from Chapter 2 is familiar. Finally, Chapter 5 draws general conclusions about the outcomes and the methodology of this work.

The notation used in this work is explained in Appendix A, the additional figures for the MCW model can be found in Appendix B, and the links to the code developed for this work can be found in Appendix C.

Chapter 2

Background

This chapter introduces basic concepts and facts, which are well known from probability theory and classical statistical mechanics [Jaynes (1957); Chandler (1987); MacKay (2003); Bishop (2006)], although the original re-elaborations in terms of presentation and notation are given in order to facilitate the discussion in the following chapters.

2.1 Basic concepts and facts from classical statistical mechanics

2.1.1 Gibbs-Boltzmann distribution

Throughout this work we will be dealing with log-linear models described by the Gibbs-Boltzmann (GB) distribution[1] of the form

$$P(\mathbf{s}) = \frac{1}{Z_N(\mathbf{t})}\mathrm{e}^{-\beta H(\mathbf{s};\mathbf{t})}; \qquad Z_N(\mathbf{t}) = \sum_{\mathbf{s}} \mathrm{e}^{-\beta H(\mathbf{s};\mathbf{t})}, \tag{2.1}$$

where $\beta = 1/T$ is the inverse temperature, N is the number of dynamic variables (degrees of freedom), $\mathbf{s}$ is the state[2] (microstate) of the system, and

$$H(\mathbf{s};\mathbf{t}) = -\sum_{i=1}^{q} t_i \Omega_i(\mathbf{s}), \tag{2.2}$$

[1] The term "distribution" is used loosely and often should be understood as a parametric family of probability distributions.

[2] As discussed in Appendix A, bold symbols are used to represent arrays.

where $\Omega_i(\mathbf{s})$ are the observables (sufficient statistics) with conjugated parameters $t_i \in \mathbb{R}$. For large systems it is useful to define a notion of a macrostate $\boldsymbol{\omega}$, which is a subset of the configuration space[3] $\mathcal{C}_N$ such that on every state $\mathbf{s}$ from this subset $\boldsymbol{\Omega}(\mathbf{s}) = \boldsymbol{\omega}$.

In physics $H(\mathbf{s};\mathbf{t})$ is known as *Hamiltonian*, $Z_N(\mathbf{t})$ is known as the *partition function*, and the Gibbs-Boltzmann distribution (2.1) defines the so-called *canonical ensemble* arising when the system is in thermal equilibrium with a heat bath. For this reason the distribution (2.1) is often referred to as equilibrium distribution, and the systems described by this distribution are said to be in (thermal) equilibrium.

In statistics the parametric family of distribution defined by (2.1) is known as the *exponential family*, and the partition function is normally referred to as the *normalising constant*.

Such families of distributions have a lot of useful properties, some of which are discussed below.

2.1.2 Entropy maximisation

In this work we denote expectations (or ensemble averages) by angle brackets $\langle . \rangle$, i.e.

$$\langle \Omega \rangle_N = \sum_{\mathbf{s}} P(\mathbf{s}) \Omega(\mathbf{s}), \tag{2.3}$$

where the subscript N shows that the expectation is computed for the model with N discrete degrees of freedom, and is absent in the thermodynamic limit (if it exists).

The entropy of a distribution $P(\mathbf{s})$ is given by

$$S_N[P] = -\sum_{\mathbf{s}} P(\mathbf{s}) \ln P(\mathbf{s}) = -\langle \ln P(\mathbf{s}) \rangle, \tag{2.4}$$

where the notation $S_N[P]$ with square brackets means that S_N is a function of $P(\mathbf{s})$ for all $\mathbf{s}$, which is usually a large number of variables.

Proposition 1. *If there exists a probability distribution $P(\mathbf{s})$ maximising the entropy (2.4) subject to the constraints $\langle \Omega_i(\mathbf{s}) \rangle_N = \omega_i$, then it is unique and has the form of a Gibbs-Boltzmann distribution (2.1) with $\mathbf{t} = \mathbf{t}(\boldsymbol{\omega})$.*

[3] The set of all possible microstates of the system.

Proof. (See, e.g. [Jaynes (1957)].) From the expression (2.4) it is easy to check that $S_N[P]$ is a concave function of $P(\mathbf{s})$ for all $\mathbf{s}$, which means that its stationary point should be a unique maximum. We now use the method of Lagrange multipliers to find the stationary point of $S_N[P]$ given the constraints on the expectations of the observables $\langle \Omega_i \rangle_N = \omega_i$ and the normalisation $\langle 1 \rangle_N = 1$, which results in the following Lagrangian function

$$\mathcal{L}_N[P](\boldsymbol{\lambda}) \equiv S_N[P] - \lambda_0 \left(\sum_{\mathbf{s}} P(\mathbf{s}) - 1 \right) - \sum_{i=1}^{q} \lambda_i \left(\sum_{\mathbf{s}} \Omega_i(\mathbf{s}) P(\mathbf{s}) - \omega_i \right).$$

Extremising the above Lagrangian function gives the following system of equations

$$\begin{cases} \dfrac{\partial \mathcal{L}_N[P](\boldsymbol{\lambda})}{\partial P(\mathbf{s})} = -\Big(\ln \big(P(\mathbf{s}) + 1 \big) \Big) - \lambda_0 - \displaystyle\sum_{i=0}^{q} \lambda_i \Omega_i(\mathbf{s}) = 0 \quad \text{for all } \mathbf{s}; \\ \dfrac{\partial \mathcal{L}_N[P](\boldsymbol{\lambda})}{\partial \lambda_0} = - \left(\displaystyle\sum_{\mathbf{s}} P(\mathbf{s}) - 1 \right) = 0; \\ \dfrac{\partial \mathcal{L}_N[P](\boldsymbol{\lambda})}{\partial \lambda_i} = - \left(\displaystyle\sum_{\mathbf{s}} \Omega_i(\mathbf{s}) P(\mathbf{s}) - \omega_i \right) = 0 \qquad \text{for all } i > 0. \end{cases} \tag{2.5}$$

The first set of equations from the system (2.5) gives

$$P(\mathbf{s}) = \exp \left(-(\lambda_0 + 1) + \sum_{i=1}^{q} \lambda_i \Omega_i(\mathbf{s}) \right),$$

which is the GB distribution with $Z_N = \exp\left(-(\lambda_0 + 1)\right)$ found from the second equation to be

$$Z_N = \sum_{\mathbf{s}} \exp \left(\sum_{i=1}^{q} \lambda_i \Omega_i(\mathbf{s}) \right), \tag{2.6}$$

which ensures normalisation. The third group of equations is the constraint on the expectations of the observables

$$\sum_{\mathbf{s}} \Omega_i(\mathbf{s}) \frac{\exp\left(\sum_{i=1}^{q} \lambda_i \Omega_i(\mathbf{s}) \right)}{Z_N} = \omega_i, \qquad i = 1, \ldots, q$$

from which the parameters t_i can, in principle, be found as $\beta t_i(\boldsymbol{\omega}) = \lambda_i(\boldsymbol{\omega}),\ i \in \{1, 2, \ldots, q\}$. □

Note that, of course, when the observables are not independent, the constraints $\langle \Omega_i(\mathbf{s}) \rangle_N = \omega_i$ should be consistent with their dependence. Otherwise the distribution satisfying such constraints cannot exist.

2.1.3 Partition function and the Helmholtz free energy

Unfortunately, using the system of equation (2.5) to find the parameters $\mathbf{t}$ corresponding to the GB distribution satisfying the desired set of constraints is usually unfeasible. Even finding the partition function is very hard for all but the simplest systems, although when it is known as a function of the parameters $\mathbf{t}$, the expectations and the higher moments of the observables can be obtained by subsequent differentiation as

$$\begin{aligned}
\langle \Omega_i \rangle_N(\mathbf{t}) &= \frac{T}{Z_N} \frac{\partial Z_N(\mathbf{t})}{\partial t_i}; \\
\langle \Omega_i \Omega_j \rangle_N(\mathbf{t}) &= \frac{T^2}{Z_N} \frac{\partial^2 Z_N(\mathbf{t})}{\partial t_i \partial t_j}; \\
\langle \Omega_i \Omega_j \Omega_k \rangle_N(\mathbf{t}) &= \frac{T^3}{Z_N} \frac{\partial^3 Z_N(\mathbf{t})}{\partial t_i \partial t_j \partial t_k}; \\
&\dots
\end{aligned}$$

which can be verified directly from the definitions (2.1) and (2.3).

Since the partition function grows exponentially with the size of the systems, the Helmholtz free energy

$$F_N(\mathbf{t}) = -\frac{1}{\beta} \ln Z_N(\mathbf{t}), \tag{2.7}$$

is introduced to study the systems in the thermodynamic limit. Similarly to obtaining the moments of the observables using the partition function, the direct calculation shows that subsequent derivatives of the free energy (2.7) can be used to obtain the cumulants, the first two of which are particularly important

$$\langle \Omega_i \rangle_N = -\frac{\partial F_N(\mathbf{t})}{\partial t_i}; \tag{2.8}$$

$$\langle \Omega_i \Omega_j \rangle_N - \langle \Omega_i \rangle_N \langle \Omega_j \rangle_N = -T \frac{\partial^2 F_N(\mathbf{t})}{\partial t_i \partial t_j}. \tag{2.9}$$

Note that the entropy of the GB distribution (2.1) can be written as

$$S_N = -\ln Z_N + \beta \langle H \rangle_N = \beta (E_N - F_N), \tag{2.10}$$

where

$$E_N[P] = \langle H \rangle_N = -\sum_{i=1}^{q} t_i \langle \Omega_i \rangle_N \tag{2.11}$$

is known as the *internal energy*. From (2.10) it is clear that

$$F_N = E_N - TS_N, \tag{2.12}$$

and, since for a model with fixed expectations of the observables $\langle \Omega_i \rangle_N$ the internal energy E_N is kept constant while, according to Proposition 1, the entropy is maximised, the free energy is minimised at equilibrium, which can be formulated as

Proposition 2. *If there exists a probability distribution $P(\mathbf{s})$ minimising the free energy $F_N[P] = E_N[P] - TS_N[P]$ subject to the constraints $\langle \Omega_i(\mathbf{s}) \rangle_N = \omega_i$, then it is unique and has the form of the Gibbs-Boltzmann distribution (2.1) with $\mathbf{t} = \mathbf{t}(\boldsymbol{\omega})$.*

Proof. Due to the imposed constraints $\langle \Omega_i(\mathbf{s}) \rangle_N = \omega_i$ the internal energy given by (2.11) is fixed at $E_N = -\sum_{i=1}^{q} t_i \omega_i$, which means that minimising the free energy $F_N[P]$ is equivalent to maximising the entropy $S_N[P]$, thus the proof is complete due to Proposition 1. □

2.1.4 Scaling of thermodynamic properties

In physics the internal energy E, the free energy F and the entropy S are known to be extensive, i.e. growing as $\mathcal{O}(N)$ when $N \to \infty$, which means that

$$\bar{E}_N = \frac{E_N}{N}; \quad \bar{F}_N = \frac{F_N}{N}; \quad \bar{S}_N = \frac{S_N}{N}, \tag{2.13}$$

known as *specific internal energy*, *specific free energy* and *specific entropy* respectively, are intensive, i.e. scaling as $\mathcal{O}(N^0)$ in the thermodynamic limit. These scaling properties of the realistic physical models come from the locality of the interactions, meaning that there is usually a notion of a distance between the dynamic variables, and the interactions decay sufficiently quickly with that distance. In general, the interactions do not have to be local, but in all models studied in this work, the observables are defined in a way that makes E_N, F_N and S_N extensive (thus $\bar{E}_N$, $\bar{F}_N$ and $\bar{S}_N$ intensive), and to distinguish such models from the others we introduce

Definition 1. *The model with the Hamiltonian (2.2) is scalable iff*[4] $\langle \Omega_i \rangle_N \underset{N\to\infty}{=} \mathcal{O}(N)$ *for all* $i \in \{1, \ldots, q\}$.

For scalable models it makes sense to introduce the following rescaled observables

$$\bar{\boldsymbol{\Omega}}(\mathbf{s}) = \frac{1}{N}\boldsymbol{\Omega}(\mathbf{s}), \tag{2.14}$$

whose expectations $\langle \bar{\boldsymbol{\Omega}}(\mathbf{s}) \rangle_N$ are intensive, thus taking finite values in the thermodynamic limit.

It is well known that certain properties of the models, such as, for example, the specific magnetisation of an Ising model, can be thought of as continuous in the thermodynamic limit despite the fact that they are discrete for any finite model. This can be formalised as

Definition 2. *Observable* $\Omega(\mathbf{s})$ *is called thermodynamically dense on an open set* $\mathcal{D} \subset \mathbb{R}$ *iff*[5] $\Omega(\mathcal{C}_N) \subset \operatorname{cl} \mathcal{D}$ *and* $\Omega(\mathcal{C}_N)$ *is a dense set in* $\mathcal{D}$.

2.1.5 Microcanonical ensemble

Since the Hamiltonian (2.2) depends on microstates only through the observables, the distribution of microstates from a given macrostate is uniform, i.e.

$$P(\mathbf{s}|\boldsymbol{\Omega} = \boldsymbol{\omega}) = \frac{P(\mathbf{s}, \boldsymbol{\Omega} = \boldsymbol{\omega})}{P(\boldsymbol{\Omega} = \boldsymbol{\omega})} = \frac{1}{g_N(\boldsymbol{\omega})}, \tag{2.15}$$

where $g_N(\boldsymbol{\omega})$ is the so-called *degeneracy factor*, which is the number of microstates $\mathbf{s}$ such that $\boldsymbol{\Omega}(\mathbf{s}) = \boldsymbol{\omega}$. The distribution (2.15) defines the so-called *microcanonical ensemble*, whose entropy is given by the famous Boltzmann entropy formula

$$\mathcal{S}_N(\boldsymbol{\omega}) = \ln g_N(\boldsymbol{\omega}). \tag{2.16}$$

The distribution (2.15) can be expressed in the equivalent form

$$P(\mathbf{s}|\boldsymbol{\Omega} = \boldsymbol{\omega}) = \frac{\mathrm{e}^{-\beta H(\boldsymbol{\omega};\mathbf{t})}}{g_N(\boldsymbol{\omega})\mathrm{e}^{-\beta H(\boldsymbol{\omega};\mathbf{t})}} \equiv \frac{\mathrm{e}^{-\beta H(\boldsymbol{\omega};\mathbf{t})}}{\mathcal{Z}_N(\boldsymbol{\omega};\mathbf{t},\beta)}, \tag{2.17}$$

[4] Here and further the notation "$\cdots \underset{N\to\infty}{=} \ldots$" stands for "$\cdots = \ldots$ as $N \to \infty$".

[5] The "cl" notation stands for closure of a set.

where $\mathcal{Z}_N(\boldsymbol{\omega}; \mathbf{t}, \beta)$ is referred to as the *microcanonical partition function*. Similarly to the free energy of the canonical ensemble, the free energy of the microcanonical ensemble is defined as

$$\mathcal{F}_N(\boldsymbol{\omega}; \mathbf{t}, \beta) = -\frac{1}{\beta} \ln \mathcal{Z}_N(\boldsymbol{\omega}; \mathbf{t}, \beta) = H(\omega; \mathbf{t}) - T\mathcal{S}_N(\omega), \tag{2.18}$$

and $\bar{\mathcal{F}}_N(\boldsymbol{\omega}; \mathbf{t}, \beta) = \mathcal{F}_N(\boldsymbol{\omega}; \mathbf{t}, \beta)/N$ is referred to as the *specific microcanonical free energy* (SMFE) in this work.

2.1.6 Specific free energy in the thermodynamic limit

Since the Hamiltonian (2.2) depends solely on the values of the observables $\boldsymbol{\Omega}$, the partition function can be evaluated by the summation over the macrostates $\boldsymbol{\Omega}(\mathbf{s}) = \boldsymbol{\omega}$ as

$$Z_N(\mathbf{t}, \beta) = \sum_{\mathbf{s}} \mathrm{e}^{-\beta H(\mathbf{s};\mathbf{t})} = \sum_{\boldsymbol{\omega}} g(\boldsymbol{\omega}) \mathrm{e}^{-\beta H(\boldsymbol{\omega};\mathbf{t})} = \sum_{\boldsymbol{\omega}} \mathrm{e}^{-\beta \mathcal{F}_N(\boldsymbol{\omega};\mathbf{t},\beta)} = \sum_{\boldsymbol{\omega}} \mathrm{e}^{-\beta N \bar{\mathcal{F}}_N(\boldsymbol{\omega};\mathbf{t},\beta)}.$$

Under the assumption that the SMFE is intensive[6] it is clear that in the above sum only the macrostates on which $\bar{\mathcal{F}}_N(\boldsymbol{\omega}; \mathbf{t}, \beta)$ is minimised as a function of $\boldsymbol{\omega}$ give a significant contribution to the partition function at large βN. Suppose there are m minima of the SMFE (usually $m = 1$) on all of which $\bar{\mathcal{F}}_N = \min_{\boldsymbol{\omega}} \bar{\mathcal{F}}_N(\boldsymbol{\omega}; \mathbf{t}, \beta)$, then[7]

$$Z_N \underset{\beta N \to \infty}{\sim} m \mathrm{e}^{-\beta N \min_{\boldsymbol{\omega}} \bar{\mathcal{F}}_N(\boldsymbol{\omega};\mathbf{t},\beta)}, \tag{2.19}$$

and the specific free energy is given by

$$\bar{F}_N(\mathbf{t}, \beta) \underset{\beta N \to \infty}{\sim} \min_{\boldsymbol{\omega}} \bar{\mathcal{F}}_N(\boldsymbol{\omega}; \mathbf{t}, \beta) - \frac{1}{\beta N} \ln m, \tag{2.20}$$

which in the thermodynamic limit reduces to

$$\bar{F}(\mathbf{t}, \beta) = \min_{\boldsymbol{\omega}} \bar{\mathcal{F}}_N(\boldsymbol{\omega}; \mathbf{t}, \beta). \tag{2.21}$$

The above relation between the canonical and microcanonical specific free energies are intuitively clear, since in the thermodynamic limit the fluctuations of the observables can be neglected, i.e.

[6] Which can be directly verified for all models studied in this work.

[7] Here and further the notation $\underset{N \to \infty}{\sim}$ stands for asymptotic equivalence as $N \to \infty$.

$\bar{\boldsymbol{\Omega}}(\mathbf{s}) = \langle\bar{\boldsymbol{\Omega}}(\mathbf{s})\rangle = \underset{\boldsymbol{\omega}}{\operatorname{argmin}}\, \bar{\mathcal{F}}(\boldsymbol{\omega};\mathbf{t},\beta)$, which means that the microcanonical and canonical ensembles become equivalent.

If the observables $\bar{\boldsymbol{\Omega}}$ are thermodynamically dense in the sense of Definition 2, then minimising $\bar{\mathcal{F}}(\boldsymbol{\omega};\mathbf{t},\beta)$ with respect to $\boldsymbol{\omega}$ requires stationarity

$$\frac{\partial\bar{\mathcal{F}}(\boldsymbol{\omega};\mathbf{t},\beta)}{\partial\boldsymbol{\omega}} = \mathbf{0}, \tag{2.22}$$

and the sum over the macrostates is replaced by an integral, which is then evaluated using Laplace's method around the lowest stationary point. The examples of this are given in Section 2.4.1 and Section 4.4.1. The stationarity condition (2.22), referred to as the *equation of state*, implicitly defines the dependence of the observables $\boldsymbol{\omega}$ on the model's parameters.

2.1.7 Multimodal distributions of macrostates

The probability that the system's observables $\boldsymbol{\Omega}(\mathbf{t})$ have some prescribed values $\boldsymbol{\omega}$ is given by

$$P(\boldsymbol{\Omega}(\mathbf{s}) = \boldsymbol{\omega}|\mathbf{t},\beta) = \frac{g_N(\boldsymbol{\omega})\mathrm{e}^{-\beta H(\boldsymbol{\omega};\mathbf{t})}}{Z_N(\mathbf{t},\beta)} = \frac{\mathrm{e}^{\ln g_N(\boldsymbol{\omega})-\beta H(\boldsymbol{\omega};\mathbf{t})}}{Z_N(\mathbf{t},\beta)} \equiv \frac{\mathrm{e}^{-\beta N\bar{\mathcal{F}}_N(\boldsymbol{\omega};\mathbf{t},\beta)}}{Z_N(\mathbf{t},\beta)}, \tag{2.23}$$

which takes its highest values when $\bar{\mathcal{F}}_N(\boldsymbol{\omega};\mathbf{t},\beta)$ takes its lowest. For this reason, if the SMFE has several minima as a function of $\boldsymbol{\omega}$, then for large βN the probability distribution becomes multimodal, since almost all the probability gets accumulated on the macrostates corresponding to these minima. This can be seen from considering the ratio of the probabilities

$$r_N(\boldsymbol{\omega}_1,\boldsymbol{\omega}_2) \equiv \frac{P(\boldsymbol{\Omega}(\mathbf{s}) = \boldsymbol{\omega}_1|\mathbf{t},\beta)}{P(\boldsymbol{\Omega}(\mathbf{s}) = \boldsymbol{\omega}_2|\mathbf{t},\beta)} = \mathrm{e}^{-\beta N\left(\bar{\mathcal{F}}_N(\boldsymbol{\omega}_1;\mathbf{t},\beta)-\bar{\mathcal{F}}_N(\boldsymbol{\omega}_2;\mathbf{t},\beta)\right)}, \tag{2.24}$$

in which, since $\bar{\mathcal{F}}_N(\boldsymbol{\omega}_1;\mathbf{t},\beta) - \bar{\mathcal{F}}_N(\boldsymbol{\omega}_2;\mathbf{t},\beta)$ is intensive, the dependence on N for large systems comes mainly from the factor βN, thus $r_N(\boldsymbol{\omega}_1,\boldsymbol{\omega}_2) \underset{\beta N\to\infty}{\to} 0$ whenever $\bar{\mathcal{F}}_N(\boldsymbol{\omega}_1;\mathbf{t},\beta) > \bar{\mathcal{F}}_N(\boldsymbol{\omega}_2;\mathbf{t},\beta)$. This explains why, as discussed in Section 2.1.6, only the global minima of the microcanonical free energy contribute to the partition function in the thermodynamic limit.

2.1.8 Stability and singularity of macrostates

Note that, although in the thermodynamic limit all the probability is distributed between the macrostates corresponding to the global minima[8] of the specific microcanonical free energy, the ratio of the probabilities corresponding to the local minima of $\bar{\mathcal{F}}_N(\boldsymbol{\omega}; \mathbf{t}, \beta)$ to the probabilities of their surrounding macrostates (on which $\bar{\mathcal{F}}_N(\boldsymbol{\omega}; \mathbf{t}, \beta)$ is higher) goes to infinity. For this reason, in many real-world applications[9] where the GB distribution (2.1) realises on a time series from some dynamics, the system should stay in the macrostates corresponding to the local minima of the SMFE for a time that is infinitely longer than the time spent in the surrounding macrostates, which means that when $\beta N \to \infty$ there is no way for the system to leave such macrostates in a finite time since the surrounding macrostates cannot be crossed infinitely quickly. This means that when $\bar{\mathcal{F}}_N(\boldsymbol{\omega}; \mathbf{t}, \beta)$ has several (local) minima as a function of $\boldsymbol{\omega}$, the averages over time are not equal to the ensemble averages as $\beta N \to \infty$, i.e. the dynamics loses ergodicity.

Even though, unlike physical applications, in many statistical problems the concept of time is redundant, in this work it is useful to introduce the notion of (meta)stability as

Definition 3. *The macrostate $\boldsymbol{\omega}$ is stable iff it corresponds to a global minimum of the specific microcanonical free energy $\bar{\mathcal{F}}_N(\boldsymbol{\omega}; \mathbf{t}, \beta)$ with respect to $\boldsymbol{\omega}$.*

Definition 4. *The macrostate $\boldsymbol{\omega}$ is metastable iff it is not stable but corresponds to a local minimum of the specific microcanonical free energy $\bar{\mathcal{F}}_N(\boldsymbol{\omega}; \mathbf{t}, \beta)$ with respect to $\boldsymbol{\omega}$.*

In what follows "(meta)stable" should be understood as stable or metastable, and the system is said to be p-stable if it exhibits exactly p simultaneously (meta)stable macrostates.

As discussed above, (meta)stable macrostates may have substantial probability under the GB distribution and, when the GB distribution (2.1) arises as the result of some stochastic dynamics, such macrostates are indeed stable (in the dynamical sense) for large βN.

Definition 5. *The macrostate is unstable iff it is neither stable nor metastable.*

Assuming $\boldsymbol{\omega}$ are thermodynamically dense in the sense of Definition 2 let $\boldsymbol{\mathcal{H}}_{\boldsymbol{\omega}} \left[\bar{\mathcal{F}}\right] (\boldsymbol{\omega}; \mathbf{t}, \beta)$ be the Hessian of $\bar{\mathcal{F}}$ with respect to $\boldsymbol{\omega}$.

[8] Almost everywhere in the parameter space there is usually only one global minimum, but there may be two or more of them at first-order phase transitions.

[9] Or in Monte Carlo simulations that use sampling based on Markov chains.

Definition 6. *The macrostate $\boldsymbol{\omega}_0$ is singular iff* $\det \boldsymbol{\mathcal{H}}_{\boldsymbol{\omega}} \left[\bar{\mathcal{F}}\right] (\boldsymbol{\omega}_0; \mathbf{t}, \beta) = 0$.

Definition 7. *The macrostate $\boldsymbol{\omega}_0$ is regular iff it is not singular.*

Note that the definitions of stability and (meta)stability do not require nondegeneracy of the Hessian, and there are (meta)stable singular macrostates introduced by

Definition 8. *Macrostate is said to be critical if it is singular and (meta)stable.*

Critical macrostates are interesting and well-studied due to the fact that these are the only singular macrostates that can be experimentally observed[10] and due to the famous *universality*, which makes different systems exhibit similar critical behaviour. For the models with only one independent observable (like the Curie-Weiss model discussed in Section 2.4 or the homogeneous ERGMs from Chapter 4) it also makes sense to introduce

Definition 9. *In a model with only one independent observable, a macrostate is said to be spinodal if it is singular and unstable.*

A spinodal macrostate is approached by a system locked in a metastable macrostate when due to the changes of the parameters, the corresponding local minimum of the SMFE disappears, resulting in a first-order phase transition without a nucleation barrier [Binder (1987)]. Note that spinodal phase transitions do occur in models with multiple independent observables, but not all macrostates covered by Definition 9 are associated with them in such models, because, as we will see, some of these macrostates can never be approached experimentally due to instability.

Finally, note that in any finite-size model the partition function from (2.1) is a sum of a finite number of analytic terms, meaning that it is an analytic function of the parameters $\mathbf{t}$; thus, strictly speaking, singular macrostates can only occur in the thermodynamic limit, where the infinite number of terms in the sum leads to its potential nonanaliticity.

2.1.9 Susceptibility, fluctuations and the stability criterion

To quantify a linear response of a subset of the observables $\{\Omega_i | i \in \{1, 2, \ldots, p\},\ p \leq q\}$ to the changes in the model's parameters, the susceptibility matrix $\boldsymbol{\chi}$ is introduced as

$$\chi_{ij}(\mathbf{t}) = \frac{\partial \langle \Omega_i \rangle_N (\mathbf{t})}{\partial t_j}, \qquad i, j \in \{1, 2, \ldots, p\}. \tag{2.25}$$

[10] The unstable singular macrostates can be approached, but always decay before they are reached due to instability.

Using (2.8) and (2.9) we obtain

$$\chi_{ij}(\mathbf{t}) = -\frac{\partial^2 F_N(\mathbf{t})}{\partial t_i \partial t_j} = \beta \left(\langle \Omega_i \Omega_j \rangle_N - \langle \Omega_i \rangle_N \langle \Omega_j \rangle_N \right), \tag{2.26}$$

which reveals a connection between the susceptibility matrix and the connected correlators of the observables.

Proposition 3. *Susceptibility matrix $\boldsymbol{\chi}$ for any subset of $p \leq q$ observables is positive semidefinite at equilibrium, i.e.*

$$\sum_{i,j} \chi_{ij} x_i x_j \geq 0 \textit{ for all } \mathbf{x} \in \mathbb{R}^p. \tag{2.27}$$

Proof. Due to the expression (2.26), the proposition is equivalent to

$$\sum_{i,j} \left(\langle \Omega_i \Omega_j \rangle_N - \langle \Omega_i \rangle_N \langle \Omega_j \rangle_N \right) x_i x_j \geq 0 \text{ for all } \mathbf{x} \in \mathbb{R}^p,$$

which is proven by the following sequence of identities

$$\begin{aligned} \sum_{i,j} \left(\langle \Omega_i \Omega_j \rangle_N - \langle \Omega_i \rangle_N \langle \Omega_j \rangle_N \right) x_i x_j &= \sum_{i,j} \langle (\Omega_i - \langle \Omega_i \rangle_N)(\Omega_j - \langle \Omega_j \rangle_N) \rangle_N x_i x_j \\ = \left\langle \sum_{i=1}^{p} (\Omega_i - \langle \Omega_i \rangle_N) x_i \sum_{j=1}^{p} (\Omega_j - \langle \Omega_j \rangle_N) x_j \right\rangle_N &= \left\langle \left(\sum_{i=1}^{p} (\Omega_i - \langle \Omega_i \rangle_N) x_i \right)^2 \right\rangle_N \geq 0. \end{aligned}$$

□

Proposition 3 is valid for models of all sizes, and the nonnegativity of the response has clear parallels with the Le Chatelier's famous principle. As discussed in Section 2.1.5, for the systems in which the GB distribution arises as a result of some underlying dynamics, the states corresponding to the local minima of the microcanonical free energy correspond to the attractors of the dynamics, in which the system can stay indefinitely long as $\beta N \to \infty$. This makes it interesting to consider the linear response in such states and derive similar relations for the susceptibility, which will provide a useful stability criterion.

Assuming the thermodynamic denseness of the observables, suppose $\boldsymbol{\omega}$ is a stationary point of the SMFE, i.e.

$$\mathbf{f}(\boldsymbol{\omega}; \mathbf{t}, \beta) \equiv \frac{\partial \bar{\mathcal{F}}(\boldsymbol{\omega}; \mathbf{t}, \beta)}{\partial \boldsymbol{\omega}} = \mathbf{0}, \tag{2.28}$$

which implicitly defines the dependence of the macrostate $\boldsymbol{\omega}(\mathbf{t}, \beta)$ on the parameters with susceptibility matrix evaluated using the implicit function theorem as

$$\boldsymbol{\chi}_{\omega} \equiv \frac{\partial \boldsymbol{\omega}(\mathbf{t}, \beta)}{\partial \mathbf{t}} = -\left(\frac{\partial \mathbf{f}(\boldsymbol{\omega}; \mathbf{t}, \beta)}{\partial \boldsymbol{\omega}}\right)^{-1} \left(\frac{\partial \mathbf{f}(\boldsymbol{\omega}; \mathbf{t}, \beta)}{\partial \mathbf{t}}\right). \tag{2.29}$$

Since

$$\frac{\partial \mathbf{f}(\boldsymbol{\omega}; \mathbf{t}, \beta)}{\partial \mathbf{t}} = \frac{\partial}{\partial \mathbf{t}}\left(\frac{\partial \bar{\mathcal{F}}(\boldsymbol{\omega}; \mathbf{t}, \beta)}{\partial \boldsymbol{\omega}}\right) = \frac{\partial}{\partial \boldsymbol{\omega}}\left(\frac{\partial \bar{\mathcal{F}}(\boldsymbol{\omega}; \mathbf{t}, \beta)}{\partial \mathbf{t}}\right) = -\frac{\partial \boldsymbol{\omega}}{\partial \boldsymbol{\omega}} = -\mathbf{I}, \tag{2.30}$$

where $\mathbf{I}$ is the identity matrix,

$$\boldsymbol{\chi}_{\omega} = \left(\frac{\partial \mathbf{f}(\boldsymbol{\omega}; \mathbf{t}, \beta)}{\partial \boldsymbol{\omega}}\right)^{-1} = \boldsymbol{\mathcal{H}}_{\omega}^{-1}\left[\bar{\mathcal{F}}\right](\boldsymbol{\omega}; \mathbf{t}, \beta), \tag{2.31}$$

where $\boldsymbol{\mathcal{H}}_{\omega}^{-1}\left[\bar{\mathcal{F}}\right](\boldsymbol{\omega}; \mathbf{t}, \beta)$ is the inverse of the Hessian of $\bar{\mathcal{F}}(\boldsymbol{\omega}; \mathbf{t}, \beta)$ in $\boldsymbol{\omega}$.

Note that if the susceptibility matrix $\boldsymbol{\chi}_{\omega}$ is positive definite, then the Hessian $\boldsymbol{\mathcal{H}}_{\omega}[\bar{\mathcal{F}}](\boldsymbol{\omega}; \mathbf{t}, \beta)$ is also positive definite; thus, the solution $\boldsymbol{\omega}$ is (meta)stable, which gives a useful stability criterion. The converse is not necessarily true, since $\boldsymbol{\omega}$ may be a degenerate (local) minimum, in which case the susceptibility $\boldsymbol{\chi}_{\omega}$ is undefined due to the violation of the implicit function theorem's conditions.

2.2 Approximation methods

2.2.1 Variational approach

When the exact computation of the free energy is unfeasible, which is usually the case, one can proceed using the *variational approach* in which the actual free energy of the system is replaced by its upper bound, which is optimised using the variational parameters.

The method can be explained as follows. Suppose $H(\mathbf{s}; \mathbf{t})$ is the Hamiltonian of the system in hand with parameters $\mathbf{t}$, and $H_0(\mathbf{s}; \boldsymbol{\zeta})$ is a *variational Hamiltonian* with variational parameters $\boldsymbol{\zeta}$.

The partition function of the actual system can be expressed as

$$Z_N(\mathbf{t}) = \sum_{\mathbf{s}} \mathrm{e}^{-\beta H(\mathbf{s};\mathbf{t})} = \frac{Z_N^0(\boldsymbol{\zeta})}{Z_N^0(\boldsymbol{\zeta})} \sum_{\mathbf{s}} \mathrm{e}^{-\beta(H(\mathbf{s};\mathbf{t})-H_0(\mathbf{s};\boldsymbol{\zeta}))} \mathrm{e}^{-\beta H_0(\mathbf{s};\boldsymbol{\zeta})}$$
$$= Z_N^0(\boldsymbol{\zeta}) \left\langle \mathrm{e}^{-\beta(H(\mathbf{s};\mathbf{t})-H_0(\mathbf{s};\boldsymbol{\zeta}))} \right\rangle_N^0, \quad (2.32)$$

where the notation $\langle \dots \rangle^0$ denotes expectations computed over the canonical ensemble defined by the Hamiltonian $H_0(\mathbf{s};\boldsymbol{\zeta})$ while $Z_N^0(\boldsymbol{\zeta})$ is the partition function of this ensemble. Due to the convexity of the exponential function and the Jensen's inequality [MacKay (2003)]

$$\left\langle \mathrm{e}^{-\beta(H(\mathbf{s};\mathbf{t})-H_0(\mathbf{s};\boldsymbol{\zeta}))} \right\rangle_N^0 \leq \mathrm{e}^{\langle -\beta(H(\mathbf{s};\mathbf{t})-H_0(\mathbf{s};\boldsymbol{\zeta}))\rangle_N^0},$$

which due to (2.32) means that

$$Z_N(\mathbf{t}) \geq Z_N^0(\boldsymbol{\zeta}) \mathrm{e}^{-\beta\langle H(\mathbf{s};\mathbf{t})-H_0(\mathbf{s};\boldsymbol{\zeta})\rangle_N^0} \text{ for all } \boldsymbol{\zeta}.$$

Finally, using the free energy definition (2.7) and the above expression, we obtain the upper bound on the free energy as

$$F_N(\mathbf{t}) \leq F_N^0(\boldsymbol{\zeta}) + \langle H(\mathbf{s};\mathbf{t}) - H_0(\mathbf{s};\boldsymbol{\zeta})\rangle_N^0, \quad (2.33)$$

where $F_N^0(\boldsymbol{\zeta})$ is the free energy of the canonical ensemble defined by the Hamiltonian H_0, and the inequality holds for all $\boldsymbol{\zeta}$.

If the Hamiltonian $H_0(\mathbf{s};\boldsymbol{\zeta})$ is simple enough, the right-hand side of (2.33) can be evaluated as a function of the parameters $\mathbf{t}$ and the variational parameters $\boldsymbol{\zeta}$, giving the variational upper bound on the free energy

$$\phi_N(\mathbf{t},\boldsymbol{\zeta}) \equiv F_N^0(\boldsymbol{\zeta}) + \langle H(\mathbf{s};\mathbf{t}) - H_0(\mathbf{s};\boldsymbol{\zeta})\rangle_N^0. \quad (2.34)$$

Minimisation of this upper bound with respect to $\boldsymbol{\zeta}$ brings it closer to the actual free energy $F_N(\mathbf{t})$, and using

$$\widetilde{F}_N(\mathbf{t}) = \min_{\boldsymbol{\zeta}} \phi_N(\mathbf{t},\boldsymbol{\zeta}) \quad (2.35)$$

as a substitute for $F_N(\mathbf{t})$ is the essence of the variational approach.

When all the variational parameters $\boldsymbol{\zeta}$ are continuous the minimisation of the variational free

energy usually requires stationarity

$$\frac{\partial \phi_N(\mathbf{t}, \boldsymbol{\zeta})}{\partial \boldsymbol{\zeta}} = 0, \tag{2.36}$$

which defines a map $\boldsymbol{\zeta}(\mathbf{t})$ useful for computing the approximate expressions for the expectations of the observables in the variational approach as

$$\begin{aligned}\langle \Omega_i(\mathbf{s}) \rangle_N(\mathbf{t}) \approx -\frac{\partial \widetilde{F}_N(\mathbf{t})}{\partial t_i} = -\frac{\partial \phi_N(\mathbf{t}, \boldsymbol{\zeta})}{\partial t_i} - \frac{\partial \phi_N(\mathbf{t}, \boldsymbol{\zeta})}{\partial \boldsymbol{\zeta}} \frac{\partial \boldsymbol{\zeta}(\mathbf{t})}{\partial t_i} = |(2.36)| = -\frac{\partial \phi_N(\mathbf{t}, \boldsymbol{\zeta})}{\partial t_i} \\ = |(2.34)| = -\frac{\partial}{\partial t_i} \langle H(\mathbf{s}; \mathbf{t}) - H_0(\mathbf{s}; \boldsymbol{\zeta}) \rangle_N^0 = -\left\langle \frac{\partial H(\mathbf{s}; \mathbf{t})}{\partial t_i} \right\rangle_N^0 \\ = |(2.2)| = \langle \Omega_i(\mathbf{s}) \rangle_N^0(\mathbf{t}, \boldsymbol{\zeta}(\mathbf{t})). \end{aligned} \tag{2.37}$$

At this stage $\langle \Omega_i(\mathbf{s}) \rangle_N^0(\mathbf{t}, \boldsymbol{\zeta})$ should already be computed since it is needed to compute $\langle H(\mathbf{s}; \mathbf{t}) - H_0(\mathbf{s}; \boldsymbol{\zeta}) \rangle_N^0$ in the expression (2.34) for the variational upper bound. Substituting $\boldsymbol{\zeta}(\mathbf{t})$ from (2.36) to (2.37) gives the desired approximate dependence of the expectations on the parameters of the model without the need of computing the optimal upper bound (2.35), which is usually impossible in elementary functions. Note that the stationarity conditions (2.36) may admit several solutions, in which case the map $\boldsymbol{\zeta}(\mathbf{t})$ is not unique, and to get the actual ensemble expectations one needs to make sure that the stationary point corresponds to the global minimum of $\phi_N(\mathbf{t}, \boldsymbol{\zeta})$ with respect to $\boldsymbol{\zeta}$.

2.2.2 Mean field theory

In statistical mechanics the mean field theory (aka MFT or self-consistent field theory) is a well-known method for approximate analysis of stochastic systems that works particularly well in high-dimensional cases. It originated in physics [Weiss (1907)], where it was first used to describe phase transitions, and can be applied in various settings, including all kinds of Ising-like models. The MFT is a special case of the variational approach[11] [MacKay (2003)] in which the variational

[11] Although, in the literature MFT is rarely presented as an instance of the variational approach due to the existence of other more intuitive and historic ways of introducing it for the models with quadratic interactions. The variational approach will be needed in Section 4.2 where the models with higher-order interactions are considered.

Hamiltonian is chosen to be linear in the dynamic variables

$$H_0 = -\sum_{i=1}^{N} h_i s_i, \tag{2.38}$$

where the variational parameters $\mathbf{h}$ are interpreted as mean local fields. Due to the linearity of the Hamiltonian (2.38) its corresponding GB distribution factorises as

$$P_0(\mathbf{s}) = \frac{1}{Z_N^0(\mathbf{h})} \mathrm{e}^{\beta \sum_{i=1}^{N} h_i s_i} = \frac{1}{Z_N^0(\mathbf{h})} \prod_{i=1}^{N} \mathrm{e}^{\beta h_i s_i},$$

where

$$Z_N^0(\mathbf{h}) = \sum_{\mathbf{s}} \mathrm{e}^{\beta \sum_{i=1}^{N} h_i s_i} = \sum_{\mathbf{s}} \prod_{i=1}^{N} \mathrm{e}^{\beta h_i s_i} = \prod_{i=1}^{N} \sum_{s_i} \mathrm{e}^{\beta h_i s_i},$$

and it is this factorisation that makes computing the variational upper bound (2.34) feasible for many systems of interest. When the variational upper bound is computed, it is minimised by requiring

$$\frac{\partial \phi_N(\mathbf{t}, \mathbf{h})}{\partial \mathbf{h}} = \mathbf{0}, \tag{2.39}$$

which gives the mean field *self-consistency equations*.

2.2.2.1 Precision of the mean field theory

Despite some theoretical ground coming from the variational approach, it is hard to quantify how precise the mean field approximation is in general. The precision of the MFT is known to improve with the dimensionality of the model. It is well known that for a 1D Ising model the MFT is completely wrong since it predicts phase transitions at a nonzero temperature which are absent in the exact solution. For a 2D Ising model, whose exact solution is known in zero field [Onsager (1944)], the MFT is only qualitatively correct, predicting the existence of a phase transition, but at a wrong temperature and with incorrect critical exponents. For the 4D and higher-dimensional Ising models the MFT is known to give the correct predictions for the critical exponents, while for the infinite-dimensional models (i.e. the models in which the number of interactions of a given node diverges in the thermodynamic limit) the MFT seems to be exact in the thermodynamic limit, as we will see in Chapter 4. The intuitive reasoning behind such high precision of the MFT for high-dimensional systems is that every node in such systems is involved in a large number of

interactions, which, due to the law of large numbers, means that each node receives an average (mean) field with negligible (compared to that field) fluctuations.

2.3 Mean field Ising-like models

There is a class of infinite-dimensional Ising-like models whose thermodynamic equations of state can be obtained exactly and coincide with the mean field self-consistency equations. The Hamiltonians of such models usually depend solely on the macroscopically large ($\mathcal{O}(N)$) sums of the individual spin variables, which allows solving such models by a variety of techniques. Such models are commonly known as the "mean field" models (systems) in the literature [Bianchi et al. (2003); Contucci and Gallo (2008); Fedele et al. (2013); Barra, Galluzzi, Guerra, Pizzoferrato and Tantari (2014); Barra, Di Lorenzo, Guerra and Moro (2014)].

The simplest nontrivial example of the mean field class is the Curie-Weiss model described in detail in the following section. The multicomponent Curie-Weiss model and the mean field random network model described later in the text are the more sophisticated examples of the class. As will be shown shortly, it turns out that the mean field models can be analysed using a PDE-based approach, which establishes a link between the statistical mechanics and certain integrable PDEs. Unfortunately, this approach does not seem to generalise to the models outside the mean field class, although a similar kind of analysis can be done for various (not necessarily discrete) systems at the level of thermodynamic relations [De Nittis and Moro (2012)].

2.4 Curie-Weiss model

Before considering more complicated systems it is instructive to demonstrate the methods on the simplest nontrivial[12] mean field model – the Curie-Weiss (CW) model defined by the Hamiltonian

$$H_{CW}(\boldsymbol{\sigma}) = -\frac{1}{2N}\sum_{i=1}^{N}\sum_{j=1}^{N} J\sigma_i\sigma_j - \sum_{i=1}^{N} h\sigma_i, \tag{2.40}$$

where $\sigma_i \in \{-1, 1\}$ are the binary dynamic variables (nodes or "spins"), $J \in \mathbb{R}$ is the coupling parameter, $h \in \mathbb{R}$ is the field, and $N \in \mathbb{Z}_N^+$ is the number of nodes. Fig. 2.1 gives a pictorial representation of this model as a complete graph in which every dynamic variable is associated

[12] Nontrivial means the one with interaction (mutual dependence) of dynamic variables.

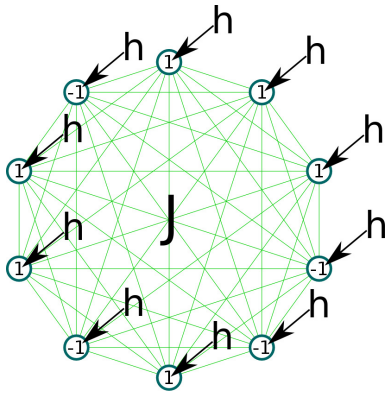

Fig. 2.1: CW model of 10 nodes with coupling J and field h. Dynamic variables are represented as circles (nodes), and pairwise interactions between them are shown as lines (edges). As can be seen, the CW model is an Ising model on a complete graph.

with a node, and pairwise interactions of the nodes are represented as edges. Note that self-interactions (not present in Fig. 2.1) are not excluded from the Hamiltonian (2.40), which is merely a matter of convenience and does not alter the model's behaviour due to the fact that in the case of $\{-s, s\}$-spins the only result of self-interactions is a constant shift of the Hamiltonian.

Introducing the magnetisation

$$m = \sum_{i=1}^{N} \sigma_i, \tag{2.41}$$

the Hamiltonian (2.40) can be written as

$$H_{CW}(m) = -\frac{Jm^2}{2N} - hm, \tag{2.42}$$

and the GB distribution (2.1) for the CW model reads as

$$P(\boldsymbol{\sigma}) = \frac{\mathrm{e}^{-\beta H_{CW}(\boldsymbol{\sigma})}}{Z_N} = \frac{\mathrm{e}^{\beta N(\frac{Jm^2}{2N^2} + h\frac{m}{N})}}{Z_N}; \tag{2.43}$$

$$Z_N = \sum_{\boldsymbol{\sigma}} \mathrm{e}^{-\beta H_{CW}(\boldsymbol{\sigma})} = \sum_{\boldsymbol{\sigma}} \mathrm{e}^{\beta N(\frac{Jm^2}{2N^2} + h\frac{m}{N})}. \tag{2.44}$$

2.4.1 Thermodynamic solution

Following the discussion from Section 2.1.6, the partition function of the MF model can be expressed as

$$Z_N(\mathbf{t},\beta) = \sum_{\boldsymbol{\sigma}} \mathrm{e}^{-\beta H_{CW}(\boldsymbol{\sigma})} = \sum_{m=-N}^{N} g_N(m)\mathrm{e}^{N\beta(\frac{Jm^2}{2N^2}+h\frac{m}{N})} = \sum_{m=-N}^{N} \mathrm{e}^{-\beta\mathcal{F}_N(m;\mathbf{t},\beta)}, \tag{2.45}$$

where

$$\mathcal{F}_N(m;\mathbf{t},\beta) = \frac{-1}{\beta N}\left(\ln g_N(m) + \frac{Jm^2}{2N^2} + h\frac{m}{N}\right) \tag{2.46}$$

is the microcanonical free energy.

To compute the degeneracy factor $g_N(m)$ we introduce k as the number of spins pointing up (i.e. $s = 1$), in terms of which $m = 2k - N$, since the rest of the spins are pointing down. From elementary combinatorics, the number of configurations with the fixed magnetisation m is given by

$$g_N(m) = \binom{N}{k(m)} = \binom{N}{\frac{(m+N)}{2}}. \tag{2.47}$$

Evaluating the factorials in the above binomial coefficient using the Stirling's formula gives the following expression for the microcanonical entropy

$$\begin{aligned}\mathcal{S}_N(m) \equiv \ln g_N(m) &= \ln\binom{N}{k} = \ln(N!) - \ln\big((N-k)!\big) - \ln(k!) \\ &\underset{N,k\to\infty}{=} N\ln N - N - (N-k)\ln(N-k) + N - k - k\ln k + k + \mathcal{O}(\log N + \log k) = \left|k = \frac{(m+N)}{2}\right| \\ &= -\frac{N}{2}\big((1-\bar{m})\ln(1-\bar{m}) + (1+\bar{m})\ln(1+\bar{m})\big) + N\ln 2 + \mathcal{O}(\log N + \log k), \end{aligned} \tag{2.48}$$

where

$$\bar{m} = \frac{m}{N} \tag{2.49}$$

is the specific magnetisation. It is not hard to see that $\bar{m} \in [-1, 1]$ is intensive, meaning that $k = \mathcal{O}(N)$, which justifies the use of the Stirling's approximation. Also, the fact that $\bar{m}$ is intensive means that the entropy (2.48) is extensive, and to prevent its divergence in the thermodynamic

limit, it needs to be rescaled as

$$\bar{\mathcal{S}}_N(\bar{m}) \equiv \frac{\mathcal{S}_N(\bar{m})}{N} = -\frac{(1-\bar{m})\ln(1-\bar{m}) + (1+\bar{m})\ln(1+\bar{m})}{2} + \ln 2 + \mathcal{O}(\frac{\log N}{N}), \quad (2.50)$$

where $\bar{\mathcal{S}}_N$ is the specific microcanonical entropy given by

$$\bar{\mathcal{S}}(\bar{m}) = -\frac{(1-\bar{m})\ln(1-\bar{m}) + (1+\bar{m})\ln(1+\bar{m})}{2} + \ln 2 \quad (2.51)$$

in the thermodynamic limit. A similar rescaling needs to be done with the microcanonical internal energy

$$\bar{\mathcal{E}}_N(\bar{m}; J, h) = \frac{\mathcal{E}_N(\bar{m}; J, h)}{N} = \frac{H_{CW}(\bar{m}; J, h)}{N} = -\frac{J\bar{m}^2}{2} - h\bar{m} \quad (2.52)$$

and the microcanonical free energy

$$\bar{\mathcal{F}}_N(\bar{m}; J, h, \beta) = \frac{\mathcal{F}_N(\bar{m}; J, h, \beta)}{N} = \bar{\mathcal{E}}_N(\bar{m}; J, h) - T\bar{\mathcal{S}}_N(\bar{m}). \quad (2.53)$$

As discussed in Section 2.1.6, when $\beta N \to \infty$ these properties coincide with expectations of their canonical counterparts on the actual thermodynamic solution given by $\bar{m}(J, h, \beta) = \operatorname{argmin}_{\bar{m}} \bar{\mathcal{F}}_N(\bar{m}; J, h, \beta)$.

Note that, unlike the general case discussed in Section 2.1.5, all of the above properties depend on just one observable $\bar{m}$ even though there are two independent parameters: J and h. This is a simple consequence of the mean field nature of the model, i.e. the fact that knowing $\bar{m}$, which is conjugated to h, fixes all other observables, particularly $\bar{m}^2$ conjugated to J.

From (2.49) it is clear that $\bar{m}$ is thermodynamically dense on $(-1, 1)$ in the sense of Definition 2, which allows minimising the specific microcanonical free energy using the following stationarity condition

$$\frac{\partial \bar{\mathcal{F}}(\bar{m}; J, h, \beta)}{\partial \bar{m}} = 0. \quad (2.54)$$

From the expressions (2.53), (2.50) and (2.52)

$$\frac{\partial \bar{\mathcal{F}}(\bar{m}; J, h, \beta)}{\partial \bar{m}} = -J\bar{m} - h + \frac{1}{2\beta}\ln\frac{1+\bar{m}}{1-\bar{m}}$$

which after basic manipulations gives the stationarity condition (2.54) as

$$\bar{m} = \tanh[\beta(J\bar{m} + h)]. \tag{2.55}$$

As discussed in Section 2.1.6, the stationarity condition (2.55) is the thermodynamic equation of state, which defines the specific magnetisation as a function of the model's parameters, and as will be shown shortly, it may admit multiple solutions, which can be (meta)stable, unstable or singular depending on the sign of the susceptibility $\chi_{\bar{m}}$. Note that the equation (2.55) is invariant under the addition of any constant to either S, E or F; thus the $\ln 2$ term in (2.51) can be omitted without affecting the predictions for the observables.

Finally, in terms of the specific microcanonical free energy, the expression (2.45) for the partition function reads as

$$Z_N(J, h, \beta) = N \sum_{k=-N}^{N} \Delta\bar{m} \mathrm{e}^{-\beta N \bar{\mathcal{F}}_N(k\Delta\bar{m}-1;J,h,\beta)}, \tag{2.56}$$

where $\Delta\bar{m} = 2/N \underset{N\to\infty}{\to} 0$ and $\bar{m} = k\Delta\bar{m} - 1$. Treating the above expression as a Riemann sum, for large models it can be recast as the following integral

$$Z_N(J, h, \beta) \underset{N\to\infty}{\sim} N \int_{-1}^{1} \mathrm{e}^{-\beta N \bar{\mathcal{F}}(\bar{m};J,h,\beta)} d\bar{m}, \tag{2.57}$$

which can be evaluated using the Laplace's approximation by expanding the specific microcanonical free energy around its global minimum $\bar{m}_0$ as

$$\bar{\mathcal{F}}(\bar{m}; J, h, \beta) = \bar{\mathcal{F}}(\bar{m}_0; J, h, \beta) + \bar{\mathcal{F}}''(\bar{m}_0; J, h, \beta)(\bar{m} - \bar{m}_0)^2 + \mathcal{O}\left((\bar{m} - \bar{m}_0)^3\right). \tag{2.58}$$

The first-order term in the above expansion is absent due to the fact that $\bar{m}_0$ is a stationary point of the specific microcanonical free energy. Furthermore, the second and higher-order terms in (2.58) can be neglected as long as the corresponding derivatives of the SMFE are finite, which gives

$$Z_N(J, h, \beta) \underset{N\to\infty}{\sim} N \int_{-1}^{1} \mathrm{e}^{-\beta N \bar{\mathcal{F}}(\bar{m}_0(J,h,\beta);J,h,\beta)} d\bar{m} \underset{N\to\infty}{\sim} 2N \mathrm{e}^{-\beta N \bar{\mathcal{F}}(\bar{m}_0(J,h,\beta);J,h,\beta)}. \tag{2.59}$$

As discussed in Section 2.1.3, the specific free energy in the thermodynamic limit is obtained from

(2.59) as

$$\bar{F}(J,h,\beta) = \lim_{N\to\infty} \frac{-1}{\beta N} \ln Z_N(J,h,\beta) = \bar{\mathcal{F}}(\bar{m}_0(J,h,\beta);J,h,\beta), \tag{2.60}$$

which is consistent with the results from Section 2.1.6.

Note that, as discussed in Section 2.1.9, $\bar{\mathcal{F}}''(\bar{m}_0(J,h,\beta);J,h,\beta) = -\chi_{\bar{m}_0}(J,h,\beta)$ and when this susceptibility diverges, which usually happens at phase transitions, the second-order term in the expansion (2.58) becomes important in the integral (4.49). However, in this work we deal directly with the observables' expectations for which at phase transitions we use the methods discussed in Section 2.4.4 and Section 2.4.5, thus computing the partition function using the Laplace's (saddle point) approximation in full generality is not needed.

2.4.2 Differential identities

As can be checked by direct substitution, the partition function (2.44) obeys the following linear PDE

$$\frac{\partial Z_N}{\partial J} = \frac{1}{2\beta N} \frac{\partial^2 Z_N}{\partial h^2}, \tag{2.61}$$

known as the *heat equation*, in which J plays the role of time and h plays the role of space coordinate. The initial condition for the above PDE is given by

$$Z_N(J=0,h,\beta) = \sum_{\boldsymbol{\sigma}} \exp\left(\beta h \sum_{i=1}^{N} \sigma_i\right) = \prod_{i=1}^{N} \sum_{\sigma_i\in\{-1,1\}} \mathrm{e}^{\beta h \sigma_i} = \left[2\cosh(\beta h)\right]^N, \tag{2.62}$$

which is easily computed due to the absence of nonlinear terms in the Hamiltonian and the consequent factorisation over sites. Note that since $\cosh(x) \geq 1$ for all $x \in \mathbb{R}$, the partition function (2.62) is a huge number even for moderate N, and, as discussed in Section 2.1.3, the specific free energy[13]

$$\bar{F}_N(J,h,\beta) \equiv \frac{-1}{\beta N} \ln Z_N(J,h,\beta) \tag{2.63}$$

needs to be introduced to study the system in the thermodynamic limit. In terms of the specific free energy, the equation (2.61) reads as

$$\frac{\partial \bar{F}}{\partial J} = -\frac{1}{2}\left(\frac{\partial \bar{F}}{\partial h}\right)^2 + \frac{1}{2\beta N}\frac{\partial^2 \bar{F}}{\partial h^2}, \tag{2.64}$$

[13]Note that (2.63) is, essentially, the inverse of the Cole-Hopf transformation [Hopf (1950), Cole (1951), Whitham (1974)], which is used to linearise the Burgers' equation.

and the initial condition (2.62) becomes

$$\bar{F}(J=0,h,\beta)=\frac{-1}{\beta}\ln\left[2\cosh\left(\beta h\right)\right]. \tag{2.65}$$

Differentiating (2.64) with respect to h and using the fact that

$$\langle\bar{m}\rangle_N=-\frac{\partial\bar{F}_N}{\partial h}, \tag{2.66}$$

we arrive to the *Burgers' equation* [Bateman (1915); Burgers (1948); Whitham (1974)] on $\langle\bar{m}\rangle_N$

$$\frac{\partial\langle\bar{m}\rangle_N}{\partial J}-\langle\bar{m}\rangle_N\frac{\partial\langle\bar{m}\rangle_N}{\partial h}=\nu\frac{\partial^2\langle\bar{m}\rangle_N}{\partial h^2}, \tag{2.67}$$

in which the factor $\nu\equiv(2\beta N)^{-1}$ plays the role of viscosity. The initial condition for the PDE (2.67) can be found from (2.65) using (2.66) and reads as

$$\langle\bar{m}\rangle_N(J=0,h)=\tanh(\beta h). \tag{2.68}$$

The initial value problem (2.67), (2.68) can be solved numerically (Fig. 2.9), but if one is interested in the thermodynamic limit ($N\to\infty$), then as long as

$$|\chi_{\bar{m}}(J,h,\beta)|=\left|\frac{\partial^2\bar{F}(J,h,\beta)}{\partial h^2}\right|<\infty, \tag{2.69}$$

the Burgers' equation (2.67) reduces to its inviscid limit

$$\frac{\partial\langle\bar{m}\rangle}{\partial J}-\langle\bar{m}\rangle\frac{\partial\langle\bar{m}\rangle}{\partial h}=0, \tag{2.70}$$

known as the *Hopf equation*, and the equation (2.64) reduces to

$$\frac{\partial\bar{F}}{\partial J}=-\frac{1}{2}\left(\frac{\partial\bar{F}}{\partial h}\right)^2, \tag{2.71}$$

which is a *Hamilton-Jacobi* equation for a free particle. The solution of the Hopf equation (2.70) can be found using the method of characteristics, in which the characteristic curves for the equation (2.70) are parametrically defined by the following system of ordinary differential equations

(ODEs)

$$\frac{dJ}{d\tau} = 1; \quad \frac{dh}{d\tau} = -\langle \bar{m} \rangle; \quad \frac{d\langle \bar{m} \rangle}{d\tau} = 0, \tag{2.72}$$

where τ is a parameter. Integration of the above ODEs gives

$$J = \tau; \quad \langle \bar{m} \rangle = \mu; \quad h = -\mu\tau + h_0, \tag{2.73}$$

where in the first equation we omitted the constant of integration due to the freedom in the offset of the parameter τ. Excluding τ and μ from the above equations gives

$$J\langle \bar{m} \rangle + h = h_0,$$

which is a family of lines parametrised by h_0, and since along the characteristics $\langle \bar{m} \rangle$ is constant it may only depend on h_0, i.e.

$$\langle \bar{m} \rangle(J, h) = f\big(h_0(J, h)\big) = f(J\langle \bar{m} \rangle + h),$$

where the arbitrary function f is fixed by the initial condition (2.68) as

$$f(h_0) = \tanh(\beta h_0),$$

which gives the solution to the initial value problem (2.70), (2.68) as

$$\langle \bar{m} \rangle = \tanh[\beta(J\langle \bar{m} \rangle + h)]. \tag{2.74}$$

Finally, the equation (2.71) can be written as

$$\frac{\partial \bar{F}}{\partial J} = -\frac{\langle \bar{m} \rangle^2}{2}; \quad \frac{\partial \bar{F}}{\partial h} = -\langle \bar{m} \rangle$$

and integrated along the characteristics (on which $\langle \bar{m} \rangle$ is constant) which gives

$$\bar{F}(J, h, \beta) = -\frac{J\langle \bar{m} \rangle^2}{2} - h\langle \bar{m} \rangle - T\bar{S}\left(\langle \bar{m} \rangle\right), \tag{2.75}$$

where $\langle \bar{m} \rangle$ should be substituted from (2.74), and $\bar{S}$ is an arbitrary function found from the initial

condition (2.65) to be

$$\bar{S}\left(\langle\bar{m}\rangle\right) = -\frac{1}{2}\ln\left[\left(1+\langle\bar{m}\rangle\right)^{(1+\langle\bar{m}\rangle)}\left(1-\langle\bar{m}\rangle\right)^{(1-\langle\bar{m}\rangle)}\right] + \ln 2. \tag{2.76}$$

Note that the results (2.75) and (2.74) were obtained under the assumption (2.69), which, as will be shown shortly, is violated on $\beta J = 1$ isotherm (see Fig. 2.2). Thus, the results (2.75) and (2.74) do not give the right answers for the specific free energy and the expected specific magnetisation of the canonical ensemble (2.43) if $J > T$, in which case, as will be shown shortly, (2.74) may have multiple solutions. For $J < T$ in the thermodynamic limit $\bar{m} = \langle\bar{m}\rangle$, and the results (2.75) and (2.74) are consistent with (2.53) and (2.55) from the previous section. Note that when $J > T$, the viscous term in the Burgers' equation (2.67) regularises the solution and makes it unique. Indeed, it is easy to show that the unique stationary solution of the Burgers' equation (2.67) satisfying the desired boundary conditions $\langle\bar{m}\rangle(J, h = -\infty, \beta) = -1$ and $\langle\bar{m}\rangle(J, h = +\infty, \beta) = 1$ is given by

$$\langle\bar{m}\rangle = \tanh(\beta N h), \tag{2.77}$$

which is a large J asymptotic of the actual solution for $\langle\bar{m}\rangle$. Note that in the thermodynamic limit the expression (2.77) becomes the sign function coinciding with the predictions of the thermodynamic theory discussed in the previous section, and in Section 2.4.4 we will see how the expression (2.77) can be obtained from simple statistical considerations.

2.4.3 Multivaluedness and spontaneous symmetry breaking

The specific microcanonical free energy (2.53) for various values of the parameters is shown in Fig. 2.3, from which it is clear that when $\beta J > 1$, the SMFE admits several (local) minima corresponding to (meta)stable macrostates, which results in a family of isotherms shown in Fig. 2.2 and the temperature dependencies shown in Fig. 2.4.

2.4.3.1 Gradient catastrophe and critical point

The equation of state (2.55) can be written in the equivalent explicit form

$$h(\bar{m}) = \frac{1}{2\beta}\ln\frac{1+\bar{m}}{1-\bar{m}} - J\bar{m}, \tag{2.78}$$

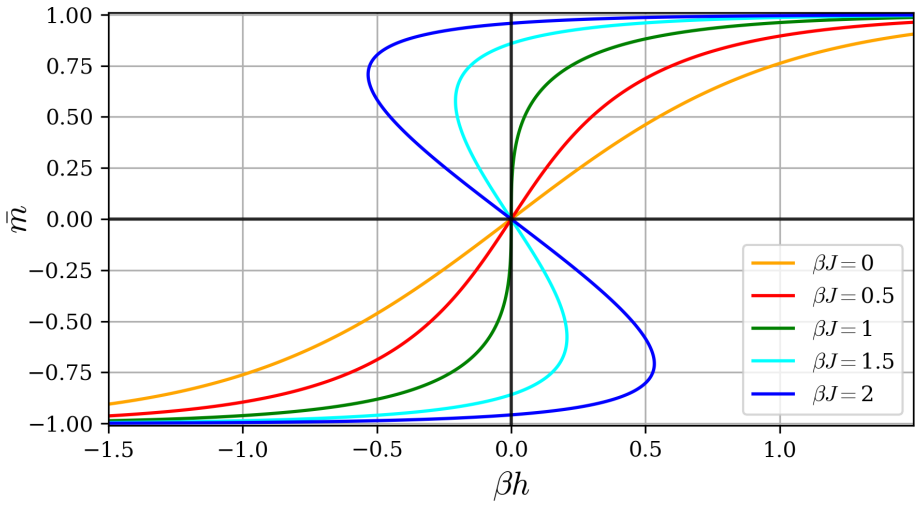

Fig. 2.2: The dependence of the specific magnetisation $\bar{m}$ on the field h obtained as a solution of the equation of state (2.55) for different values of βJ. When $\beta J = 1$, there is a critical point at $h = 0$ ($\bar{m} = 0$) associated with the gradient catastrophe in the solution of the Hopf equation (2.70) with the initial condition (2.68). When $\beta J > 1$, the equation of state (2.55) admits three solutions at certain ranges of the field h, one of which is unstable due to the negative susceptibility.

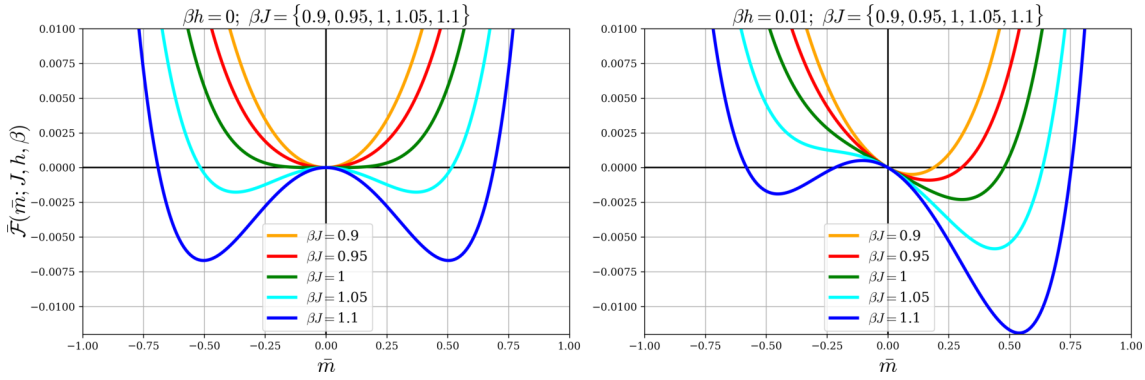

Fig. 2.3: The specific microcanonical free energy at zero (left) and non-zero (right) field as a function of $\bar{m}$ for various values of βJ. Note how in the left panel ($h = 0$) the SMFE for $\beta J = 1$ is very flat at $\bar{m} = 0$, which corresponds to a critical point.

which defines a smooth map $h(\bar{m})$ that maps the interval $(-1, 1)$ to $\mathbb{R}$.

The critical points of the CW model can be found by fulfilling the conditions

$$\frac{\partial h(\bar{m})}{\partial \bar{m}} = 0; \qquad \frac{\partial^2 h(\bar{m})}{\partial \bar{m}^2} = 0, \tag{2.79}$$

the first of which is the singularity condition, while the second ensures that the SMFE has a minimum instead of an inflection point. Indeed, it is easy to show that

$$\frac{d^3 h}{d\bar{m}^3} = \frac{2(1 + 3\bar{m}^2)}{\beta(1 - \bar{m}^2)^3} > 0 \text{ for all } \bar{m} \in (-1, 1), \tag{2.80}$$

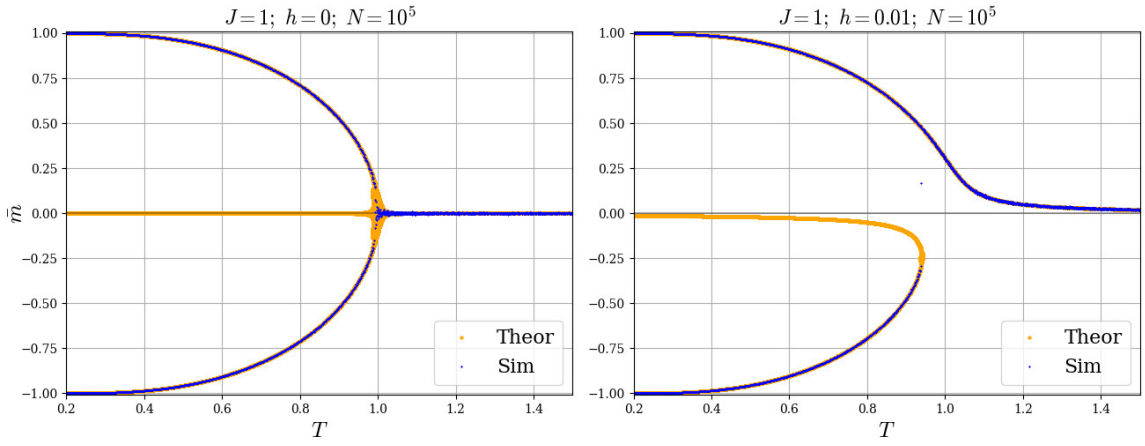

Fig. 2.4: Theoretical predictions and the results of the MC simulations for the temperature dependence of magnetisation of the CW model at zero (left) and nonzero (right) field. In the left panel, one can see the critical point at the Curie temperature $T_c = 1$, below which the model exhibits spontaneous magnetisation. In the presence of the field the critical point disappears, and there is a smooth branch consisting of stable macrostates (upper branch), while another two branches are either metastable or unstable.

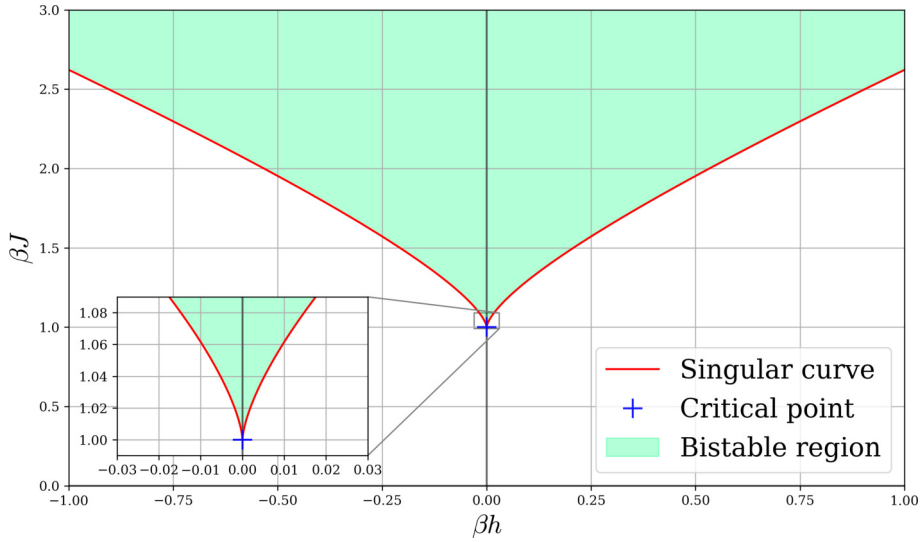

Fig. 2.5: Phase diagram of the CW model showing how the hysteresis grows in h as J increases. Note the cusp (indicated as the blue cross) corresponding to the critical point at $h = 0$, $\beta J = 1$.

meaning that as soon as the conditions (2.79) are satisfied, the corresponding stationary point of the SMFE is a degenerate minimum, i.e. corresponds to the critical macrostate in line with the discussion from Section 2.1.8. The conditions (2.79) together with the self-consistency equation

(2.78) give the following system of equations

$$\begin{cases} \dfrac{dh(\bar{m})}{d\bar{m}} = \dfrac{1}{\beta(1-\bar{m}^2)} - J = 0; \\ \dfrac{d^2h(\bar{m})}{d\bar{m}^2} = \dfrac{2\bar{m}}{\beta(1-\bar{m}^2)^2} = 0; \\ h(\bar{m}) = \dfrac{1}{2\beta}\ln\dfrac{1+\bar{m}}{1-\bar{m}} - J\bar{m}, \end{cases} \tag{2.81}$$

which implies that there is only one critical macrostate when $\beta J = 1$, $h = 0$ with expected specific magnetisation $\bar{m} = 0$. This critical macrostate corresponds to the gradient catastrophe in the solution of the initial value problem defined by (2.70) and (2.68), and marks the point at which the solution of the Hopf equation no longer corresponds to the actual expectation of $\bar{m}$ due to the influence of the viscous term in the Burgers' equation (2.67), which at the critical point cannot be neglected.

In physics such critical points are associated with the second-order phase transitions, which bring the system from an unordered (paramagnetic) to an ordered (ferromagnetic) phase. At such points (known as the *Curie points* for ferromagnets) the dependence of magnetisation on the parameters is continuous, but the susceptibility and the heat capacity diverge providing an easy way of finding such macrostates experimentally. In ferromagnets the temperature at which such phase transition occurs is known as *Curie temperature*, and in the CW model the critical point appears at $T_c = J$ and $h = 0$ ($\bar{m} = 0$). Note how at the critical point the SMFE becomes very flat (green line on the left panel of Fig. 2.3), and how sharply the specific magnetisation depends on h (green line in Fig. 2.2) and T (left panel of Fig. 2.4). When at zero field the temperature gets lower than T_c, the paramagnetic solution of the equation of state becomes unstable, and the two stable ferromagnetically ordered macrostates emerge, one of which realises spontaneously. If, in contrast, the field is nonzero, then the free energy is no longer symmetric (right panel of Fig. 2.3), and there is only one stable macrostate and no second-order phase transitions, as can be seen on the right panel of Fig. 2.4.

Of course, even in nonzero fields at low enough temperatures there are always two (local) minima of the free energy (Fig. 2.3), both of which correspond to the (meta)stable macrostates. However, when the field gets large enough, one of the (local) minima disappears, which results in the hystereses from Fig. 2.2 and the phase diagram shown in Fig. 2.5.

2.4.3.2 Graphical analysis

This section shows how the results discussed in Section 2.4.3 can be explained using simple graphical considerations. For this purpose the equation of state (2.55) can be expressed in the following form

$$\xi\left(\bar{m}\right) = \mathcal{A}(\bar{m}) - \mathcal{P}(\bar{m}; J, h, \beta) = 0, \tag{2.82}$$

where

$$\mathcal{A}(\bar{m}) \equiv \operatorname{artanh}(\bar{m}) = \frac{1}{2}\ln\frac{1+\bar{m}}{1-\bar{m}};$$
$$\mathcal{P}(\bar{m}; J, h, \beta) \equiv \beta J\bar{m} + \beta h,$$

whose plots are shown in the upper panels of Fig. 2.6 and Fig. 2.7.

Note that

$$\frac{\partial\xi}{\partial\bar{m}} = \frac{dh(\bar{m})}{d\bar{m}} = \frac{1}{\chi_{\bar{m}}} = \mathcal{A}'(\bar{m}) - \mathcal{P}'(\bar{m}; J, h, \beta), \tag{2.83}$$

which according to the definitions from Section 2.1.8 means that when $\mathcal{A}'(\bar{m}) > \mathcal{P}'(\bar{m}; J, h, \beta)$, the solution to (2.82) corresponds to a (meta)stable macrostate; when $\mathcal{A}'(\bar{m}) < \mathcal{P}'(\bar{m}; J, h, \beta)$, the solution to (2.82) corresponds to an unstable macrostate; and when $\mathcal{A}'(\bar{m}) = \mathcal{P}'(\bar{m}; J, h, \beta)$, the solution to (2.82) corresponds to a singular macrostate.

As can be seen on the upper left panel of Fig. 2.6, when $\beta J < 1$, there is always a unique intersection between $\mathcal{A}(\bar{m})$ and $\mathcal{P}(\bar{m}; J, h, \beta)$, which corresponds to a solution of the equations of state. This unique solution always corresponds to a (meta)stable macrostate, because in this high-temperature regime $\mathcal{A}'(\bar{m}) > \mathcal{P}'(\bar{m}; J, h, \beta)$ for all $\bar{m} \in (-1, 1)$. As can be seen on the upper right panel of Fig. 2.6, when $\beta J > 1$, there may be up to three solutions of the equation of state (2.55), in which case two of them are stable, while one is unstable. Fig. 2.7 shows the appearance of the two types of singular solutions, one of which is critical (left plot), while another is spinodal (right plot).

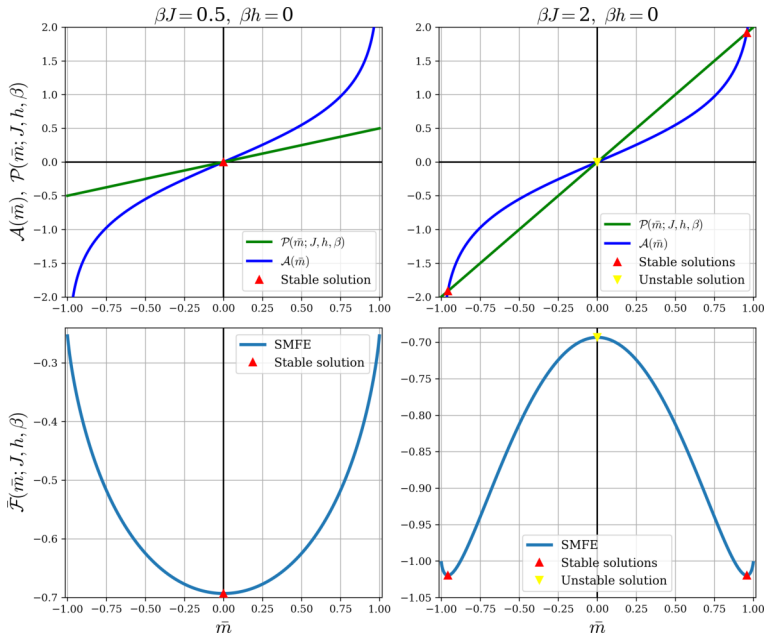

Fig. 2.6: The appearance of regular solutions in graphical analysis of the equation of state (2.55). Changing J adjusts the slope of $\mathcal{P}(\bar{m}; J, h, \beta)$ (green line), while changing h moves it vertically. When $J < 1$ (left plot), there can be only one intersection, when $J > 1$ (right plot), there can be up to three intersections, two of which correspond to (meta)stable macrostates, and one to unstable. Note how the (meta)stable solutions approach the boundaries of the domain $\bar{m} = -1$ and $\bar{m} = 1$ as βJ increases.

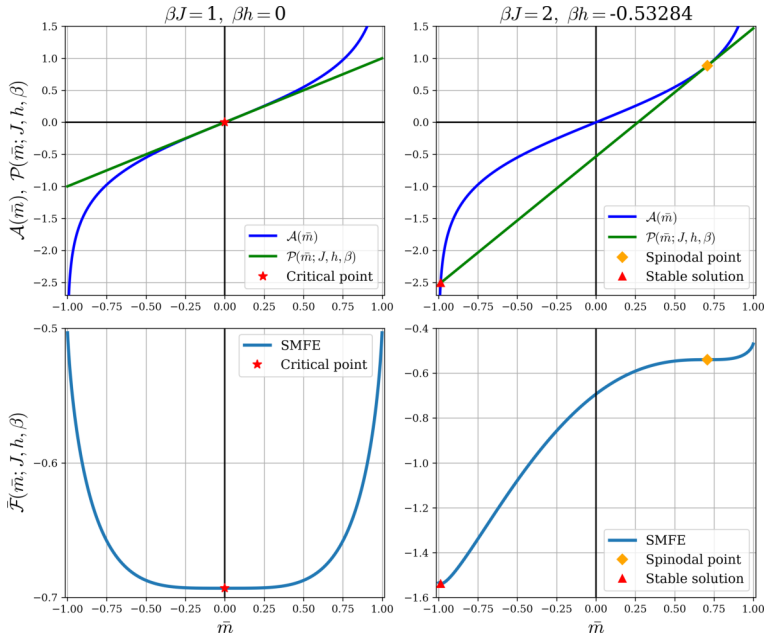

Fig. 2.7: The appearance of critical (left) and spinodal (right) solutions of the equation of state (2.55). When $\beta J = 1$ (left panels), there is a critical point at $h = 0$, $\bar{m} = 0$. When $\beta J > 1$ (right panels), spinodal macrostates are possible at nonzero fields, at which a metastable-unstable pair of macrostates is created or annihilated.

2.4.3.3 Susceptibility and narrow stability bands at low temperatures

From the definition of susceptibility (2.25) and the equation of state (2.55) it is easy to see that the susceptibility of the CW model is given by

$$\chi = \beta \left(\frac{1}{1 - \bar{m}^2} - \beta J \right)^{-1} \tag{2.84}$$

which, as discussed in Section 2.1.9, should be nonnegative on (meta)stable macrostates. From (2.84) it is clear that if $\beta J < 1$, then $\chi > 0$ for all $\bar{m} \in (0, 1)$, which agrees with the above discussion, according to which in such regimes there is only one solution of the equation of state (2.55), which corresponds to a stable macrostate. If, in contrast, $\beta J > 1$, there are two separated bands in $\bar{m}$, namely

$$\bar{m} \in \left(-1, -\sqrt{1 - \frac{1}{\beta J}} \right) \text{ and } \bar{m} \in \left(\sqrt{1 - \frac{1}{\beta J}}, 1 \right), \tag{2.85}$$

where $\chi > 0$ and the macrostates are (meta)stable. Note that the width of the stability bands (2.85) decreases to zero as $\beta J \to \infty$, which means that at low temperature it is extremely unlikely to find a CW model with moderate values of $\bar{m}$.

2.4.4 Phase transitions in (-1,1)-bistability

A simple approximate expression for the expected specific magnetisation $\langle \bar{m} \rangle$ in the regime with only two deep minima of the SMFE[14]: one very close to $\bar{m} = -1$ (corresponding to a single microstate $\boldsymbol{\sigma}_-$ in which all the spins are pointing down) and another very close to $\bar{m} = 1$ (corresponding to a single microstate $\boldsymbol{\sigma}_+$ in which all the spins are pointing up), can be easily obtained as follows. First, the partition function can be found from the normalisation condition

$$P(\boldsymbol{\sigma}_-) + P(\boldsymbol{\sigma}_+) = \frac{\mathrm{e}^{-\beta H_{CW}(\boldsymbol{\sigma}_-)}}{Z_N} + \frac{\mathrm{e}^{-\beta H_{CW}(\boldsymbol{\sigma}_+)}}{Z_N} = 1$$

to be

$$Z_N = \mathrm{e}^{-\beta H_{CW}(\boldsymbol{\sigma}_-)} + \mathrm{e}^{-\beta H_{CW}(\boldsymbol{\sigma}_+)}.$$

[14] In a CW model there can be at most two minima of the SMFE.

After that the expectations can be computed by definition as

$$\langle \Omega \rangle_N = \Omega(\boldsymbol{\sigma}_-) \frac{\mathrm{e}^{-\beta H_{CW}(\boldsymbol{\sigma}_-)}}{Z_N} + \Omega(\boldsymbol{\sigma}_+) \frac{\mathrm{e}^{-\beta H_{CW}(\boldsymbol{\sigma}_+)}}{Z_N},$$

which gives

$$\langle \bar{m} \rangle_N = -1 \cdot \frac{\mathrm{e}^{-\beta H_{CW}(\boldsymbol{\sigma}_-)}}{\mathrm{e}^{-\beta H_{CW}(\boldsymbol{\sigma}_-)} + \mathrm{e}^{-\beta H_{CW}(\boldsymbol{\sigma}_+)}} + 1 \cdot \frac{\mathrm{e}^{-\beta H_{CW}(\boldsymbol{\sigma}_+)}}{\mathrm{e}^{-\beta H_{CW}(\boldsymbol{\sigma}_-)} + \mathrm{e}^{-\beta H_{CW}(\boldsymbol{\sigma}_+)}} = \tanh(\beta N h) \quad (2.86)$$

and

$$\langle \bar{m}^2 \rangle_N = 1 \cdot \frac{\mathrm{e}^{-\beta H_{CW}(\boldsymbol{\sigma}_-)}}{\mathrm{e}^{-\beta H_{CW}(\boldsymbol{\sigma}_-)} + \mathrm{e}^{-\beta H_{CW}(\boldsymbol{\sigma}_+)}} + 1 \cdot \frac{\mathrm{e}^{-\beta H_{CW}(\boldsymbol{\sigma}_+)}}{\mathrm{e}^{-\beta H_{CW}(\boldsymbol{\sigma}_-)} + \mathrm{e}^{-\beta H_{CW}(\boldsymbol{\sigma}_+)}} = 1. \quad (2.87)$$

Note that the shape of the transition (2.86) does not depend on J and has a characteristic length of $1/(\beta N)$, while the result (2.87) is not surprising due to the $(-1, 1)$-bistability assumption and shows that $\langle \bar{m}^2 \rangle \neq \bar{m}^2$ even in the thermodynamic limit, which is a consequence of bimodality of the probability distribution.

2.4.5 Direct evaluation of expectations

Although in general the brute force evaluation of expectations by the definition (2.3) is unfeasible for all, but the smallest systems, the situation is not quite as bad for the mean field models, since the expectations can be expressed in the form

$$\langle \boldsymbol{\Omega}(\mathbf{s}) \rangle = \sum_{\boldsymbol{\omega}} \boldsymbol{\omega} g_{\boldsymbol{\omega}} \mathrm{e}^{-\beta H(\boldsymbol{\omega})} \left(\sum_{\boldsymbol{\omega}} g_{\boldsymbol{\omega}} \mathrm{e}^{-\beta H(\boldsymbol{\omega})} \right)^{-1},$$

in which for mean field models there are usually not too many macrostates to visit, and the degeneracy factors $g_{\boldsymbol{\omega}}$ are usually not too hard to compute. For example, in the case of a CW model there are only $N + 1$ macrostates to visit, and the degeneracy factors are given by (2.47).

This gives a fast and reliable way of computing the solution of the initial value problem defined by (2.67) and (2.68), which can (and should) be used instead of the iterative numerical methods

for PDEs[15]. Note that the opposite is also true, and certain initial value problems for PDEs can be solved using Monte Carlo simulations discussed in the section below.

2.4.6 Monte Carlo simulations using Metropolis dynamics

Monte Carlo (MC) simulations require large numbers of samples from the Gibbs-Boltzmann distribution (2.43), and since the direct and truly uncorrelated methods of sampling, such as, for instance, the rejection sampling, suffer from the curse of dimensionality [MacKay (2003)], the iterative methods known as *Markov chain Monte Carlo* (MCMC) are usually employed when the number of degrees of freedom is large. In general, MCMC methods work by defining the Markov chains that converge and equilibrate at the desired distributions, meaning that the ensemble of such Markov chains observed at a large iteration time should be distributed according to the desired distributions regardless of the initial configuration. Unfortunately, finding the number of iterations needed for convergence or detecting the convergence of a running computation is hard [Cowles and Carlin (1996)], and the samples obtained as a time series from the dynamics of a single Markov chain are correlated, although such correlations decay with the increasing number of iterations between the samples. In this section we look at how the MC simulations were done in this work using a simple MCMC, known as *Metropolis dynamics*, which is an archetypal example of the MCMC and a special case of the famous *Metropolis-Hastings algorithm* presented as Algorithm 1.

for $i \leftarrow 0$ **to** *(Number of iterations)* **do**
  In the current state $\mathbf{s}$ draw the proposed next state $\mathbf{s}'$ using the distribution $Q(\mathbf{s}'|\mathbf{s})$;
  $a \leftarrow \frac{P(\mathbf{s}')}{P(\mathbf{s})} \cdot \frac{Q(\mathbf{s}|\mathbf{s}')}{Q(\mathbf{s}'|\mathbf{s})}$;
  if $a \geq 1$ **then**
    Reconfigure the system to the state $\mathbf{s}'$ (i.e. $\mathbf{s} \leftarrow \mathbf{s}'$);
  else
    With the probability a reconfigure the system to the state $\mathbf{s}'$ (i.e. $\mathbf{s} \leftarrow \mathbf{s}'$);
  end
end

Algorithm 1: Sampling from a distribution $P(\mathbf{s})$ using Metropolis-Hastings algorithm.

When the *proposal distribution* $Q(\mathbf{s}|\mathbf{s}')$ is symmetric, the Metropolis-Hastings algorithm is known as *Metropolis dynamics*, which we use in this work with the desired distribution $P(\mathbf{s})$ being set to

[15] Although, in this work we sometimes use both methods as a proof of concept that statistical problems can be solved using numerical methods for PDEs.

the GB distribution (2.1). Finally, the algorithm used in this work is presented as Algorithm 2.

$N_{max} \leftarrow$(Maximal number of variables to flip at a single step of the dynamics);
$H \leftarrow H(\mathbf{s})$; // Compute Hamiltonian on the current state $\mathbf{s}$
for $i \leftarrow 0$ **to** *(Number of iterations)* **do**
  $n_f \leftarrow$(Random natural number from 1 to N_{max}); // Number of dynamic variables to flip
  $\mathbf{s}' \leftarrow$(Current state $\mathbf{s}$, where n_f randomly chosen distinct dynamic variables are flipped);
  $\Delta H \leftarrow H(\mathbf{s}') - H$;
  $r \leftarrow$(Random real number from 0 to 1);
  if $r < \exp(-\beta \Delta H)$ **then**
    /* Accept the proposal */
    $\mathbf{s} \leftarrow \mathbf{s}'$;
    $H \leftarrow H + \Delta H$;
  end
end

Algorithm 2: The particular reduction of Algorithm 1 to the case of Metropolis dynamics for the GB distribution and binary degrees of freedom. Note that computing ΔH does not usually require computing the Hamiltonian on every iteration, which gives an opportunity for a significant optimisation (see the code referenced in Appendix C).

2.4.6.1 Ergodicity issues

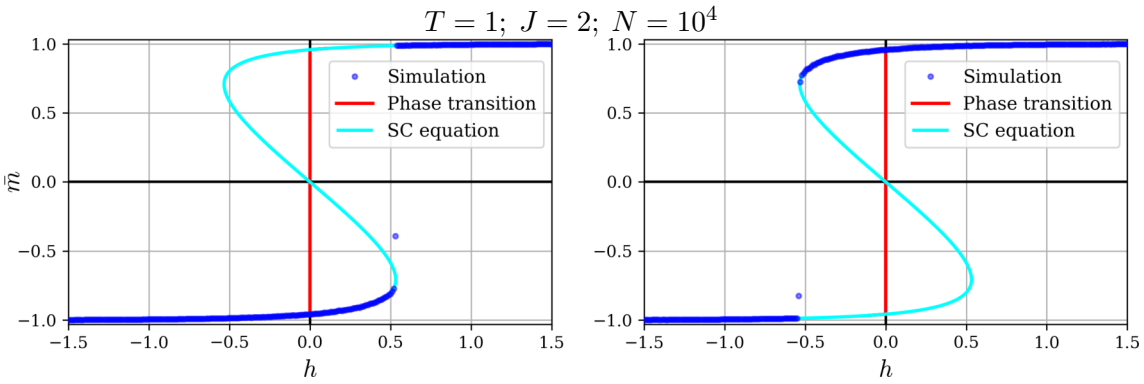

Fig. 2.8: The results of the MC simulations done using Metropolis dynamics (Algorithm 2) with $N_{max} = 1$ for the CW model of 10^4 nodes with $T = 1$, $J = 2$. At each point in h, 10^5 iterations are performed 10 times without the reinitialisation. The averages of the outcomes of 10 such samples are shown as the blue dots.

It is not hard to show that the Markov chains defined by Algorithm 2 satisfy the *detailed balance* with the desired GB distribution and converge to that equilibrium at large enough iteration time. Furthermore, since in such Markov chains there is a path of non-zero probability between any pair of states, the Markov chains are ergodic, meaning that the averaging over the ensemble of such Markov chains should be equivalent to the averaging over a time series of a single such Markov chain. However, as discussed in Section 2.1.8, when the SMFE admits several (local) minima the Markov chain may get stuck in one of the corresponding (meta)stable macrostates, and if the

time it spends in such (meta)stable macrostate[16] is comparable or larger than the time between the observations, then the time averages no longer coincide with the ensemble averages. This fact is not always undesirable, since it allows using such MCMC to recover all the (meta)stable macrostates (Fig. 2.4, Fig. 2.8), although it makes obtaining the true ensemble expectations problematic due to the slow convergence of the algorithm. For this reason, in Algorithm 2 there is a free parameter N_{max} which defines the maximum number of dynamic variables that can be flipped at a single step of the dynamics. Setting high N_{max} increases the fluctuations and largely decreases the iteration time needed for convergence. For example, the simulations from Fig. 2.9 were performed with $N_{max} = N$, while the simulations from Fig. 2.8 were done with $N_{max} = 1$ (in both cases a single point on the plots corresponds to the average over multiple samples), and it can be seen how in Fig. 2.8 the results of the simulations follow the branches of the hysteresis, whereas in Fig. 2.9 the results of the simulations follow the actual ensemble averages. For this reason, we refer to the simulations run to full convergence as *ensemble-averaging*, while the simulations deliberately left stuck in one of the macrostates are referred to as *time-averaging*. Since the lifetimes of (meta)stable macrostates[17] are usually much larger than the times needed to arrive at these macrostates from their attraction basins, there is a clear distinction between the time-averaging and the ensemble-averaging simulations in the parameter space of Algorithm 2. Namely, if βN is large, $N_{max} = 1$ and the number of iterations between the samples is small (compared to the lifetime of the desired macrostate), then the algorithm corresponds to the time-averaging simulations; while if βN is relatively small $N_{max} = N$ and the number of iterations between the samples is large (compared to the lifetime of the longest living macrostate), then the algorithm corresponds to the ensemble-averaging simulations. In practice, thermalisation of the Markov chains can be checked by comparing the results of simulations with and without the random initialisation after every sample, which should be the same if the number of iterations between the samples is enough for convergence and the decay of autocorrelation.

Finally, note that the dots in Fig. 2.8 that are significantly away from the predictions of the equation of state (2.55) correspond to spinodal transitions and do not carry any information other than the position of this first-order phase transition. Such dots can also be seen in Fig. 2.4 and other figures

[16] Which according to the Néel-Arrhenius relaxation theory [Brown (1963)], is expected to grow exponentially with the energy barrier between the macrostates, which, in turn, grows linearly with βN.

[17] Which can be easily measured in numerical experiments.

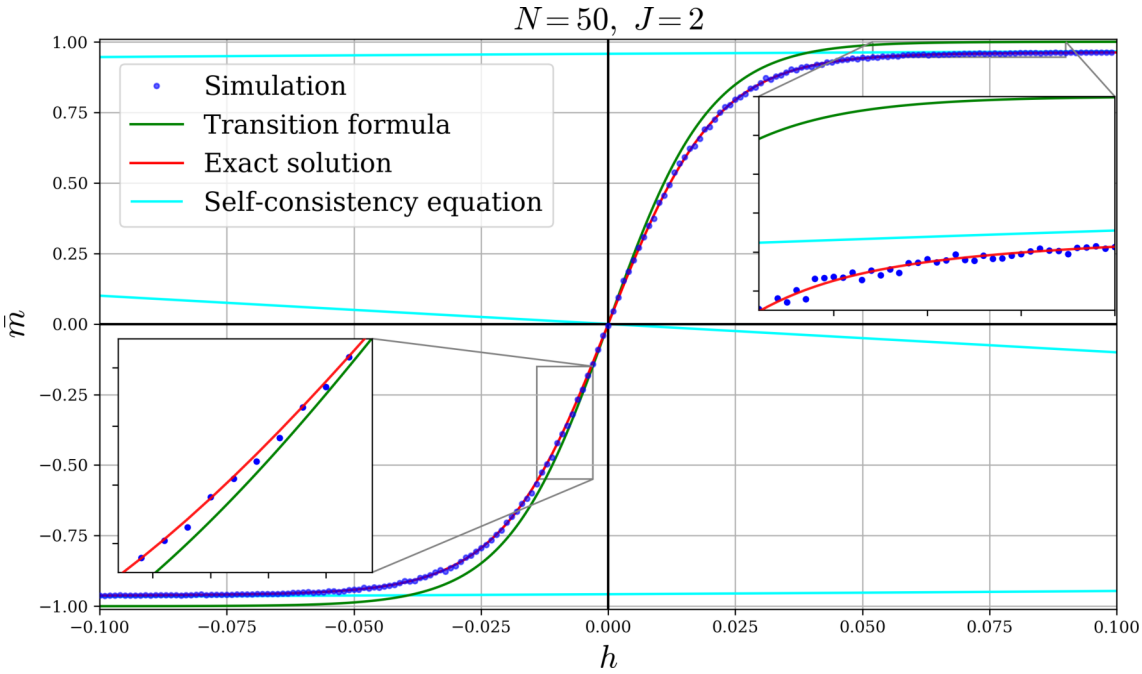

Fig. 2.9: Results of the ensemble-averaging MC simulations for a CW model of 50 nodes with $J = 2$ together with the numerical solution of the Burgers' equation (2.67), the solution of the equation of state (2.55) and the predictions of the (-1,1)-bistability transition formula (2.86). Note that the results of the MC simulations align well with the actual solution of the Burgers' equation while the (-1,1)-bistability transition formula goes to -1 and 1 quicker than the actual solution and the branches of the hysteresis defined by the self-consistency equation (2.55) due to the (-1,1)-bistability assumption which is not fully satisfied for $J = 2$.

later in the text, although on some plots with error bars such points were removed by hand for better visibility of more meaningful features[18].

2.4.7 Importance of scalability

Note that without the factor $1/N$ in front of the quadratic term in the Hamiltonian (2.40) the equation of state of the CW model (2.55) would be given by

$$\bar{m} = \tanh\left(\beta N J \bar{m} + \beta h\right),$$

where in the thermodynamic limit the first term under the hyperbolic tangent largely outweighs the second reflecting the fact that the number of node pairs is quadratic in N, while the number of nodes is linear. Furthermore, in the thermodynamic limit the magnetisation of such a model only depends on the sign of J while the field h does not play any role. We will further say

[18]The links to the code used for all MC simulations in this work can be found in Appendix C.

that such models do not possess a *meaningful thermodynamic limit* due to the trivial parameter dependence of the observables for large N. This shows the importance of scalability in the sense of Definition 1, and even if one is not interested in the thermodynamic limit, the non-scalable models of different finite sizes would have very different behaviour even if their parameters are the same, which creates significant inconveniences.

2.4.8 Notes on temperature

From the definition of the GB distribution (2.1), it is clear that setting $T = 1$ ($\beta = 1$) does not restrict the generality[19], and for convenience this is done in some of the following sections. Nevertheless, whenever the temperature dependence is explicitly discussed, the factor β should be reintroduced in front of all the couplings and fields.

Note that in physical applications the factor β is usually absent in front of the field h since it is normally considered as external to the system. For this reason, some results from this work may differ by a factor β from what would normally be anticipated by a physicist.

[19] Since β can always be absorbed into the parameters $\mathbf{t}$ of the Hamiltonian (2.2) and restored when needed.

Chapter 3

Multicomponent Curie-Weiss model

In this chapter we derive the equations of state for a multi-component analogue of the Curie-Weiss (CW) model discussed in Section 2.4 and analyse the two-component case in detail. The chapter is structured as follows. In the next section we define the multicomponent Curie-Weiss (MCW) model; then in Section 3.2 we obtain the thermodynamic equations of state for a generic MCW model using the elementary methods from statistical mechanics and the method of differential identities, and discuss the stability of their solutions; then in Section 3.3 we provide the detailed analysis of the two-component CW model; and in Section 3.4 we discuss some of its existing applications. Finally, in Section 3.5 we briefly summarise the results of the chapter and draw some conclusions regarding the MCW model.

3.1 Introduction

Multicomponent Curie-Weiss (MCW) model (Fig. 3.1) is defined by the Hamiltonian

$$H_{MCW}(\boldsymbol{\sigma}) = -\frac{1}{N}\sum_{i\leq j}\tilde{J}_{ij}\sum_{k,l=1}^{N_i,N_j}\sigma_k^{(i)}\sigma_l^{(j)} - \sum_{i=1}^{p}h_i\sum_{k=1}^{N_i}\sigma_k^{(i)}, \tag{3.1}$$

where N is the total number of spins in the system, N_i is the number of spins in the i-th CW-component, p is the number of the CW-components, $\tilde{J}_{ij}$ is the coupling[1] between the components i and j, h_i is the field acting on the i-th CW-component, $\sigma_k^{(i)}$ is the k-th spin of the i-th CW-

[1] At this stage we count the interactions inside the components twice which simplifies the expressions.

component.

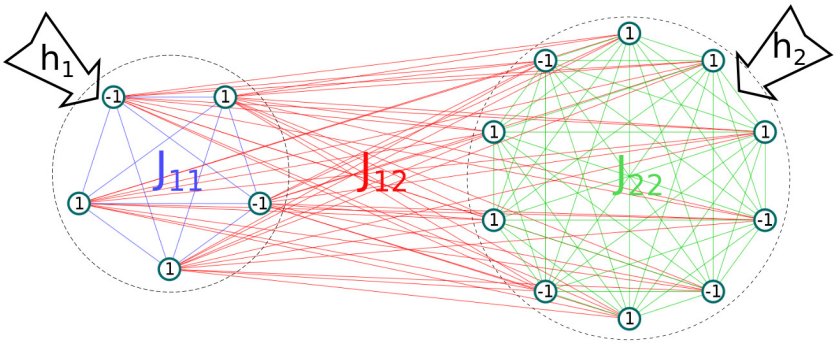

Fig. 3.1: The two-component Curie-Weiss model with 5 nodes in the first component (with the intracomponent coupling J_{11} and the field h_1) and 10 nodes in the second component (with the intracomponent coupling J_{22} and the field h_2). All the node pairs consisting of the nodes from different components are connected with the intercomponent coupling J_{12}.

As discussed in Section 2.4, the CW model is a special case of the Ising model for which the mean field approximation is exact, i.e. the equation of state coincides with the corresponding MF self-consistency equation. Similarly, the equations of state obtained for the MCW model can be viewed as the mean field self-consistency equations for the multispecies Ising models. This fact makes the MCW model applicable in many areas of science as a mean field theory for Ising models describing, e.g. magnetism [Weiss (1907); Smart (1955); Néel (1948); Bowers and Schofield (1981)], chemical reactions [Agliari et al. (2016)], social interactions [Contucci et al. (2008)] and numerous other complex phenomena. The MCW and similar models were studied before in a number of works [Néel (1948); Smart (1955); Contucci et al. (2008); Agliari et al. (2016); Berthet et al. (2019)] but, apparently, all the preceding works were focused on the particular special cases of the model instead of considering it in full generality.

3.2 General MCW model

3.2.1 Thermodynamic solution

Similarly to the Hamiltonian of a single-component CW model (2.40), the Hamiltonian of the MCW model (3.1) depends solely on the average magnetisations of the components, i.e.

$$H_{MCW}(\boldsymbol{\sigma}) = -N \sum_{i \le j} \gamma_i \gamma_j \tilde{J}_{ij} \bar{m}_i \bar{m}_j - N \sum_{i=1}^{p} h_i \gamma_i \bar{m}_i, \tag{3.2}$$

where $\gamma_i = N_i/N > 0$ are the splitting parameters, and

$$\bar{m}_i = \frac{1}{N_i}\sum_{l=1}^{N_i}\sigma_l^{(i)}, \;\; i \in \{1 \dots p\}$$

are the specific magnetisations of the components, which are thermodynamically dense in the sense of Definition 2. From the Hamiltonian (3.2) it is clear that the observables conjugated to the fields are given by $\mathfrak{m}_i = N_i\bar{m}_i$, in terms of which the specific microcanonical internal energy of the model is given by

$$\bar{\mathcal{E}}(\bar{\mathfrak{m}}; \mathbf{J}, \mathbf{h}) = \frac{H_{MCW}}{N} = -\sum_{i\leq j}\tilde{J}_{ij}\bar{\mathfrak{m}}_i\bar{\mathfrak{m}}_j - \sum_{i=1}^{p} h_i\bar{\mathfrak{m}}_i,$$

where

$$\bar{\mathfrak{m}}_i = \frac{\mathfrak{m}_i}{N}.$$

Note that, due to the fact that $\bar{m}_i \in [0,1]$ for all $i \in \{1,\dots,p\}$, it is usually more convenient to work with $\bar{\mathbf{m}}$ rather than $\bar{\mathfrak{m}}$.

From simple combinatorial considerations, it is clear that the degeneracy factor of a macrostate $\mathbf{m}$ is given by the product $g_{\mathbf{m}} = \prod_{i=1}^{p} g_{m_i}$. Thus the microcanonical entropy is given by the following sum

$$\mathcal{S}_{\mathbf{N}}(\mathbf{m}) = \sum_{i=1}^{p}\ln g_{m_i},$$

in which every term can be evaluated similarly to (2.48), resulting in the following expression for the specific microcanonical entropy in the thermodynamic limit

$$\bar{\mathcal{S}}(\bar{\mathbf{m}}; \boldsymbol{\gamma}) = \sum_{i=1}^{p}\gamma_i\left(-\frac{1}{2}[(1-\bar{m}_i)\ln(1-\bar{m}_i) + (1+\bar{m}_i)\ln(1+\bar{m}_i)] + \ln 2\right).$$

Finally, using (2.18) the specific microcanonical free energy in the thermodynamic limit is obtained as

$$\begin{aligned}\bar{\mathcal{F}}(\bar{\mathbf{m}}; \mathbf{J}, \mathbf{h}; \boldsymbol{\gamma}; T) = \bar{\mathcal{E}}(\bar{\mathbf{m}}; \mathbf{J}, \mathbf{h}; \boldsymbol{\gamma}) - T\bar{\mathcal{S}}(\bar{\mathbf{m}}; \boldsymbol{\gamma}) = -\sum_{i\leq j}\gamma_i\gamma_j\tilde{J}_{ij}\bar{m}_i\bar{m}_j - \sum_{i=1}^{p}\gamma_i h_i\bar{m}_i \\ + T\left(\sum_{i=1}^{p}\frac{\gamma_i}{2}[(1-\bar{m}_i)\ln(1-\bar{m}_i) + (1+\bar{m}_i)\ln(1+\bar{m}_i)] - \gamma_i\ln 2\right), \quad (3.3)\end{aligned}$$

whose stationarity conditions are given by

$$\frac{\partial \bar{\mathcal{F}}}{\partial \bar{\mathfrak{m}}_i} = \frac{1}{\gamma_i} \cdot \frac{\partial \bar{\mathcal{F}}(\bar{\mathbf{m}}; \mathbf{J}, \mathbf{h}; \boldsymbol{\gamma}; T)}{\partial \bar{m}_i} = -\gamma_i \tilde{J}_{ii} \bar{m}_i - \sum_{j=1}^{p} \gamma_j \tilde{J}_{ij} \bar{m}_j - h_i + \frac{T}{2} \ln \frac{1+\bar{m}_i}{1-\bar{m}_i} = 0. \quad (3.4)$$

The double-counting of the intracomponent interactions in the Hamiltonian (3.1) can be compensated with the following rescaling

$$\begin{cases} J_{ij} = 2\tilde{J}_{ij}, & i = j; \\ J_{ij} = \tilde{J}_{ij}, & i \neq j, \end{cases}$$

after which the stationarity condition (3.4) can be expressed in the following two equivalent useful forms

$$h_i = -\sum_{j=1}^{p} \gamma_j J_{ij} \bar{m}_j + \frac{T}{2} \ln \frac{1+\bar{m}_i}{1-\bar{m}_i}, \quad i \in \{1, 2, \ldots, p\} \quad (3.5)$$

and

$$\bar{m}_i = \tanh \left(\beta \sum_{j=1}^{p} \gamma_j J_{ij} \bar{m}_j + \beta h_i \right), \quad i \in \{1, 2, \ldots, p\}, \quad (3.6)$$

providing the equations of state for the MCW model.

The comparison of the expression (3.6) written as

$$\bar{m}_i = \tanh \left[\beta J_{ii} \bar{m}_i + \beta \left(\sum_{j(\neq i)} \gamma_j J_{ij} \bar{m}_j + h_i \right) \right] \quad (3.7)$$

with the expression (2.55) shows that every CW component can be regarded as a separate CW model exposed to the collective field created by all other components and the external field. Note that, although this kind of interpretation may be used to obtain the equation of state (3.6) directly from (2.55), it is often counterproductive due to the strong feedback occurring when the intercomponent couplings are relatively high.

3.2.2 Differential identities

In this section we give an alternative way of obtaining the equation of state for the MCW model based on the method of differential identities [Agliari et al. (2016); Barra, Di Lorenzo, Guerra and Moro (2014); De Matteis et al. (2018); Lorenzoni and Moro (2019)]. Following the discussion

from Section 2.4.2, the fact that the Hamiltonian (3.2) depends solely on $\bar{\mathbf{m}}$ allows deriving a set of partial differential equations (PDEs) on the partition function of the model

$$\frac{\partial Z_N}{\partial t_{ij}} = \frac{1}{N}\frac{\partial^2 Z_N}{\partial x_i \partial x_j}, \qquad i \leq j, \tag{3.8}$$

where t_{ij} and x_i are the couplings and the fields rescaled as follows

$$t_{ij} \equiv \beta\gamma_i\gamma_j\tilde{J}_{ij}; \qquad x_i \equiv \beta\gamma_i h_i. \tag{3.9}$$

The initial condition for the partition function is given by

$$Z_N(\mathbf{t}=\mathbf{0},\mathbf{x}) = \prod_{i=1}^{p}\left[2\cosh\left(\frac{N}{N_i}x_i\right)\right]^{N_i}, \tag{3.10}$$

and to study the system in the thermodynamic limit, the exponential growth of Z_N with N is compensated by the inverse of the Cole-Hopf transformation [Hopf (1950), Cole (1951)]

$$\Phi_N(\mathbf{x},\mathbf{t}) = \frac{1}{N}\log Z_N(\mathbf{x},\mathbf{t}), \tag{3.11}$$

which gives the specific free energy of the model up to a factor $-T$. For Φ the equation (3.8) reads as

$$\frac{\partial \Phi_N}{\partial t_{ij}} = \frac{\partial \Phi_N}{\partial x_i}\frac{\partial \Phi_N}{\partial x_j} + \frac{1}{N}\frac{\partial^2 \Phi_N}{\partial x_i \partial x_j}, \qquad i \leq j, \tag{3.12}$$

which in the thermodynamic limit ($N \to \infty$) and away from singularities can be approximated by

$$\frac{\partial \Phi}{\partial t_{ij}} = \frac{\partial \Phi}{\partial x_i}\frac{\partial \Phi}{\partial x_j}, \qquad i \leq j. \tag{3.13}$$

The equations (3.13) are of Hamilton-Jacobi type and can be solved using the method of characteristics, which gives

$$\Phi(\langle\bar{\mathbf{m}}\rangle;\mathbf{x},\mathbf{t}) = \sum_{i=1}^{p} x_i\langle\bar{m}_i\rangle + \sum_{i\geq j} t_{ij}\langle\bar{m}_i\rangle\langle\bar{m}_j\rangle - W(\langle\bar{\mathbf{m}}\rangle), \tag{3.14}$$

where $\langle \bar{m}_i \rangle = \partial\Phi/\partial x_i$ are the ensemble averages of partial magnetisations[2] and W is a function of the average partial magnetisations fixed by the initial conditions to be

$$W(\langle \bar{\mathbf{m}} \rangle) = \sum_{i=1}^{p} \gamma_i \left(\frac{1}{2} \left[(1 + \langle \bar{m}_i \rangle) \log (1 + \langle \bar{m}_i \rangle) + (1 - \langle \bar{m}_i \rangle) \log (1 - \langle \bar{m}_i \rangle) \right] - \ln 2 \right).$$

The equations of state can be obtained by finding the stationary points of Φ w.r.t. $\langle \mathbf{m} \rangle$ as

$$\frac{\partial \Phi}{\partial \langle \bar{m}_i \rangle} = x_i + \langle \bar{m}_i \rangle t_{ii} + \sum_{j=1}^{p} \langle \bar{m}_j \rangle t_{ij} - \frac{\partial W}{\partial \langle \bar{m}_i \rangle} = 0,$$

which in terms of the original couplings and fields can be written as

$$h_i + \gamma_i \tilde{J}_{ii} \langle \bar{m}_i \rangle + \sum_{j=1}^{p} \langle \bar{m}_j \rangle \gamma_j \tilde{J}_{ij} - T \operatorname{artanh}(\langle \bar{m}_i \rangle) = 0, \qquad i \in \{1, \dots, p\}. \tag{3.15}$$

The double-counting of the intracomponent interactions in the Hamiltonian (3.1) can be compensated by the following rescaling of the couplings

$$\begin{cases} J_{ij} = 2\tilde{J}_{ij}, & i = j; \\ J_{ij} = \tilde{J}_{ij}, & i \neq j, \end{cases}$$

after which the equations (3.15) simplify to

$$h_i + \sum_{j=1}^{p} \langle \bar{m}_j \rangle \gamma_j J_{ij} - \operatorname{artanh}(\langle \bar{m}_i \rangle) = 0, \qquad i \in \{1, \dots, p\}, \tag{3.16}$$

which is identical to (3.5) and (3.6) when $\bar{m}_i = \langle \bar{m}_i \rangle$.

3.2.3 Stability

In Section 3.2.1 the equations of state (3.5) were obtained by finding stationary points of the specific microcanonical free energy (3.4) with respect to $\bar{\mathbf{m}}$, and there is no guarantee that these stationary points are the (local) minima of $\bar{\mathcal{F}}(\bar{\mathbf{m}})$, which, as discussed in Section 2.1.8, is a necessary and sufficient condition for (meta)stability. Therefore, to ensure (meta)stability of a solution of the equation of state (3.5), one needs to check that the Hessian of the specific microcanonical

[2] Constant along the characteristics.

free energy

$$\mathcal{H}_{ij} \equiv \frac{\partial^2 \bar{\mathcal{F}}}{\partial \bar{\mathfrak{m}}_i \partial \bar{\mathfrak{m}}_j} = J_{ij} - \frac{1}{\gamma_i(1-\bar{m}_i^2)}\delta_{ij} \tag{3.17}$$

is positive definite, which requires the positivity of all of its eigenvalues. The condition

$$\det \boldsymbol{\mathcal{H}}(\bar{\mathbf{m}}; \mathbf{J}; \boldsymbol{\gamma}) = 0 \tag{3.18}$$

defines a hypersurface in the parameter space on which at least one of the eigenvalues of the Hessian (3.17) vanishes and (in most cases) changes its sign, meaning that, when this boundary is crossed, a (meta)stable solution may become unstable or vice versa[3].

3.3 Two-component Curie-Weiss model

We will now focus our attention on the two-component CW model[4] for which the equations of state (3.5) read as

$$\begin{cases} h_1 = -J_{11}\gamma_1\bar{m}_1 - \bar{m}_2\gamma_2 J_{12} + \operatorname{artanh}(\bar{m}_1) \\ h_2 = -J_{22}\gamma_2\bar{m}_2 - \bar{m}_1\gamma_1 J_{12} + \operatorname{artanh}(\bar{m}_2). \end{cases} \tag{3.19}$$

Similarly to the case of the CW model, discussed in Section 2.4, the dependence $\mathbf{h}(\bar{\mathbf{m}})$ defined by the equations of state (3.19) cannot be explicitly inverted, and some valuable insights about the model can be obtained through the following graphical analysis proposed in [Contucci and Gallo (2008)].

3.3.1 Graphical analysis

Solving the system (3.19) graphically can be done by expressing it in its equivalent form as

$$\begin{cases} \bar{m}_2 = \dfrac{1}{\gamma_2 J_{12}} \left(\operatorname{artanh}(\bar{m}_1) - J_{11}\gamma_1\bar{m}_1 - h_1\right) \\ \bar{m}_1 = \dfrac{1}{\gamma_1 J_{12}} \left(\operatorname{artanh}(\bar{m}_2) - J_{22}\gamma_2\bar{m}_2 - h_2\right) \end{cases} \tag{3.20}$$

and plotting each of the above equations on the $\mathbf{m}$-plane for a particular choice of the parameters $\mathbf{J}$, $\mathbf{h}$ and $\boldsymbol{\gamma}$. The plots of the equations (3.20), whose intersections correspond to the solutions

[3] However, most of the time an unstable solution remains unstable since (meta)stability requires nonnegativity of *all* eigenvalues of the Hessian (3.17).

[4] Which is a generalisation of the *Ising blockmodel* [Berthet et al. (2019)].

of the equations of state, are shown in Fig. 3.2, and from the left panel of Fig. 3.2 it is clear that the equations of state may admit nine solutions, which turns out to be the maximum number of solutions possible in the two-component model. To see this, note that when $J_{11}\gamma_1 > 1$, the derivative

$$\frac{d\bar{m}_2}{d\bar{m}_1} = \frac{1}{\gamma_2 J_{12}} \left[\frac{1}{1-\bar{m}_1^2} - J_{11}\gamma_1 \right] \tag{3.21}$$

changes its sign twice in the domain at

$$\bar{m}_1 = \pm\sqrt{1 - \frac{1}{J_{11}\gamma_1}}, \tag{3.22}$$

meaning that the corresponding orange curve in Fig. 3.2 becomes "folded". Due to symmetry, the analogous result holds for the second equation when $J_{22}\gamma_2 > 1$, and as clear from (3.21) and (3.22), the sign of the derivatives cannot change more than twice, meaning that both curves consist of at most 3 monotonic pieces. It is clear that the maximum number of intersections is achieved when every monotonic peace of one curve intersects all monotonic pieces of the other, which, when both curves are folded, gives $3 \cdot 3 = 9$ intersections in total, as shown in the left panel of Fig. 3.2.

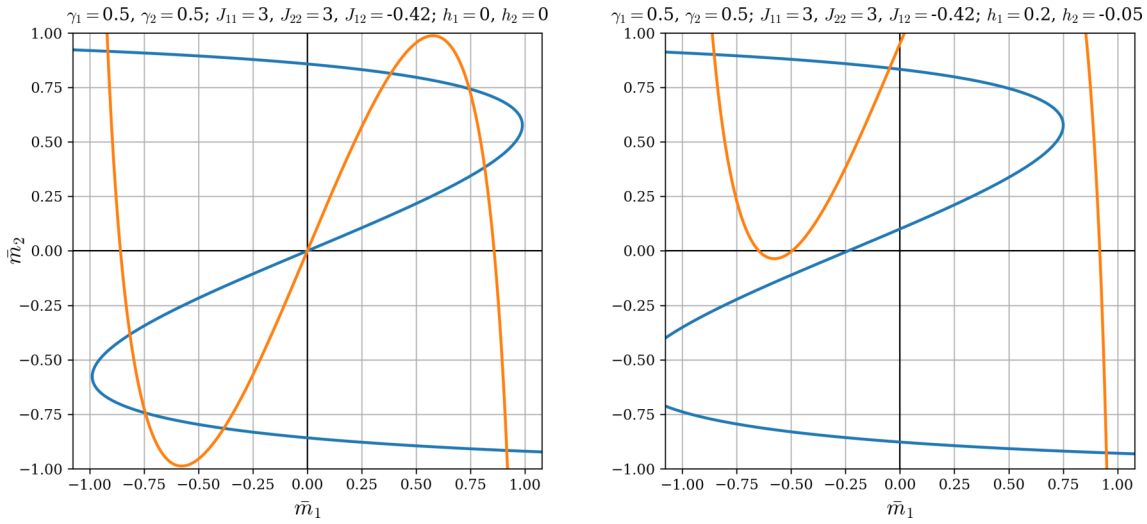

Fig. 3.2: The plots of the equations of state (3.20) for the particular choice of the parameters $\mathbf{J}$, $\mathbf{h}$ and $\boldsymbol{\gamma}$. The orange curve represents the first equation in (3.20), the blue curve represents the second, and the intersections of these curves correspond to the solutions of the system (3.20). The changes of h_1 result in the vertical shifts of the orange curve, the changes of h_2 result in the horizontal shifts of the blue curve, while the changes in $\mathbf{J}$ alter the shapes of the curves. It is clear that the maximum possible for this $\mathbf{J}$ number of intersections is nine, which is achieved in the left panel. It is also clear that with changing $\mathbf{h}$ the new solutions usually appear and disappear in pairs.

3.3.2 Stability

The solutions of the system (3.20) correspond to the stationary points of the free energy, and to identify their types, one needs to consider the Hessian (3.17), which for a two-component model reads as

$$\boldsymbol{\mathcal{H}}(\bar{\mathbf{m}};\mathbf{J};\boldsymbol{\gamma}) = -\begin{pmatrix} J_{11} - \frac{1}{\gamma_1(1-\bar{m}_1^2)} & J_{12} \\ J_{12} & J_{22} - \frac{1}{\gamma_2(1-\bar{m}_2^2)} \end{pmatrix} \equiv -\begin{pmatrix} \mathcal{J}_{11}(\bar{\mathbf{m}}) & J_{12} \\ J_{12} & \mathcal{J}_{22}(\bar{\mathbf{m}}) \end{pmatrix}, \quad (3.23)$$

where we introduced

$$\mathcal{J}_{ii}(\bar{\mathbf{m}};\gamma_i) \equiv J_{ii} - \frac{1}{\gamma_i(1-\bar{m}_i^2)}$$

to simplify the expressions. The eigenvalues of the above Hessian are given by

$$\lambda_{1,2}(\bar{\mathbf{m}};\mathbf{J};\boldsymbol{\gamma}) = -\frac{1}{2}\left(\mathcal{J}_{11} + \mathcal{J}_{22} \pm \sqrt{\left(\mathcal{J}_{11} - \mathcal{J}_{22}\right)^2 + 4J_{12}^2}\right), \quad (3.24)$$

and when both of them are positive, the specific microcanonical free energy has a (local) minimum; thus, in line with the discussion from Section 2.1.8, the corresponding macrostate is (meta)stable. When at least one of the eigenvalues (3.24) is negative, the stationary point does not correspond to a (local) minimum of the SMFE, which implies that the corresponding macrostate is unstable, and when at least one of the eigenvalues (3.24) is zero, the corresponding macrostate is singular.

Note that since, according to the Sylvester's criterion, a symmetric matrix is positive-definite iff all of its corner principal minors are positive, the Hessian of the specific microcanonical free energy (SMFE) cannot be positive definite if either $\partial^2\bar{\mathcal{F}}/\partial\bar{m}_1^2 \leq 0$ or $\partial^2\bar{\mathcal{F}}/\partial\bar{m}_2^2 \leq 0$. This fact has useful implications for the graphical analysis from Section 3.3.1, since it is easy to show[5] that the derivatives of the functions defined by (3.20) can be expressed as

$$\frac{d\bar{m}_2}{d\bar{m}_1} = \frac{\gamma_1}{\gamma_2 J_{12}}\frac{\partial^2\bar{\mathcal{F}}}{\partial\bar{m}_1^2}; \quad \frac{d\bar{m}_1}{d\bar{m}_2} = \frac{\gamma_2}{\gamma_1 J_{12}}\frac{\partial^2\bar{\mathcal{F}}}{\partial\bar{m}_2^2},$$

meaning that if $J_{12} < 0$, only the intersections at which both functions are decreasing correspond to (meta)stable macrostates, while if $J_{12} > 0$, only the intersections at which both functions are increasing correspond to (meta)stable macrostates. This, for example, means that at least five[6]

[5] Compare (3.21) with (3.23).

[6] In fact, exactly five, as will be shown later.

out of nine solutions from the left panel of Fig. 3.2 are unstable, and from the graphical analysis it is easy to see that this should be the case with any realisation of the maximum number of solutions.

3.3.2.1 Stability region of a regular macrostate

From the equations of state (3.19) it is obvious that at any couplings $\mathbf{J}$ and for any macrostate $\bar{\mathbf{m}}$ there exist such fields $\mathbf{h}(\bar{\mathbf{m}};\mathbf{J})$ that the equations of state are satisfied. However, the stability of a macrostate depends on $\mathbf{J}$, and in this section we find a region of the $\mathbf{J}$-space in which a given macrostate is (meta)stable.

As discussed above, the (meta)stability of a regular macrostate $\bar{\mathbf{m}}$ is equivalent to the positivity of both eigenvalues (3.24), and since the eigenvalues (3.24) are continuous functions of $\mathbf{J}$, they cannot change their signs without crossing zero. This means that the singularity condition

$$\det\left(\frac{\partial \mathbf{h}}{\partial \bar{\mathbf{m}}}\right) = \lambda_1\lambda_2 = 0 \tag{3.25}$$

defines where the stability status of a macrostate may change due to a sign change in one or both eigenvalues of the SMFE Hessian. As can be shown by a straightforward computation, the singularity condition (3.25) on $\bar{\mathbf{m}} \in (-1,1)^2$ is equivalent to

$$\left(J_{11}J_{22} - J_{12}^2\right)\gamma_1(1-\bar{m}_1^2)\gamma_2(1-\bar{m}_2^2) - J_{11}\gamma_1(1-\bar{m}_1^2) - J_{22}\gamma_2(1-\bar{m}_2^2) + 1 = 0, \tag{3.26}$$

which defines a cone[7] in $\mathbf{J}$-space with a normal form

$$\tilde{\tilde{J}}_{11}^2 = \tilde{\tilde{J}}_{22}^2 + 2\tilde{\tilde{J}}_{12}^2 \tag{3.27}$$

obtained in the coordinates transformed as

$$\mathbf{J} = \begin{pmatrix} \frac{1}{\sqrt{2}} & \frac{-1}{\sqrt{2}} & 0 \\ \frac{1}{\sqrt{2}} & \frac{1}{\sqrt{2}} & 0 \\ 0 & 0 & 1 \end{pmatrix} \tilde{\tilde{\mathbf{J}}} + \begin{pmatrix} \frac{1}{\gamma_1(1-\bar{m}_1^2)} \\ \frac{1}{\gamma_2(1-\bar{m}_2^2)} \\ 0 \end{pmatrix}, \tag{3.28}$$

[7] In this work a cone should be understood as a surface (sometimes called a double cone) consisting of two nappes (half cones) sharing a common apex.

which corresponds to a shift in $J_{11}J_{22}$-plane together with a $\frac{\pi}{4}$ rotation along the J_{12} axis. Note that the shape and the orientation of the cone are independent of $\bar{\mathbf{m}}$ and $\boldsymbol{\gamma}$, and only the apex located at

$$\mathcal{J} = \begin{pmatrix} \frac{1}{\gamma_1(1-\bar{m}_1^2)} \\ \frac{1}{\gamma_2(1-\bar{m}_2^2)} \\ 0 \end{pmatrix} \tag{3.29}$$

travels in the $J_{12} = 0$ plane as magnetisations and/or splitting parameters change. From (3.29) it is clear that $\mathcal{J}_{11} \geq 1/\gamma_1;\ \mathcal{J}_{22} \geq 1/\gamma_2$ for all $\bar{\mathbf{m}} \in (-1,1)^2$, and the closest to $\mathbf{J} = \mathbf{0}$ position of the apex is achieved when $\bar{\mathbf{m}} = \mathbf{0}$, therefore we introduce

Definition 10. *Principal cone is the cone in* $\mathbf{J}$*-space defined by the singularity condition (3.26) for* $\bar{\mathbf{m}} = \mathbf{0}$.

Note that the nappe of the principal cone enclosing $\mathbf{J} = \mathbf{0}$ is the closest to zero locus on which there are singular macrostates, meaning that in the models, whose couplings are enclosed by this nappe, all the macrostates are regular, and the first singular macrostate ($\bar{\mathbf{m}} = \mathbf{0}$) appears when this boundary is being crossed. Furthermore, due to the absence of singular macrostates, the conditions of the implicit function theorem[8] are never violated; thus the map $\mathbf{h}(\bar{\mathbf{m}})$ defined by the equations of state (3.19) is globally invertible, meaning that the equations of state admit a unique solution for all $\mathbf{h}$ as long as $\mathbf{J}$ belongs to this nappe, which makes it useful to introduce

Definition 11. *Uniqueness nappe is the nappe of the principal cone enclosing* $\mathbf{J} = \mathbf{0}$.

As can be checked by substitution, both eigenvalues (3.24) are positive at $\mathbf{J} = \mathbf{0}$ for all $\bar{\mathbf{m}} \in (-1,1)^2$, which means that the nappe of the cone (3.26) that encloses zero (Fig. 3.3) is the boundary separating the (meta)stable solutions from the unstable, therefore we introduce

Definition 12. *Stability nappe of a given macrostate* $\bar{\mathbf{m}}$ *is the nappe of the cone defined by the singularity condition (3.26) enclosing* $\mathbf{J} = 0$.

Note that the uniqueness nappe is always enclosed inside the stability nappe (Fig. 3.3), meaning that, as expected, in the models whose couplings are inside the uniqueness nappe, the unique solution of the equations of state corresponds to a stable macrostate. This means that, in line with the discussion from Section 2.1.7, in the models whose couplings are within the uniqueness

[8] Used as discussed in Section 2.1.9.

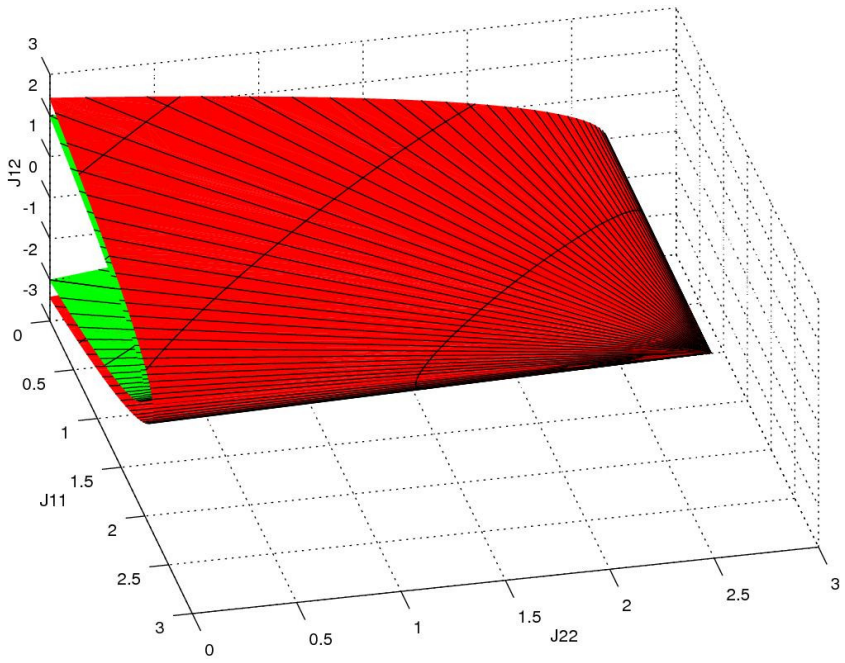

Fig. 3.3: The uniqueness nappe (green) inside the stability nappe (red) for $\bar{m}_1 = 0.3$; $\bar{m}_2 = 0.5$ in the 2-component CW model with $\gamma_1 = \gamma_2 = 0.5$. Both nappes have the same shape, but the apex of the stability nappe is shifted further away from zero in accordance with (3.29).

nappe, the distributions of macrostates never become multimodal, meaning that the values of the observables found in the individual samples are close to their expectations.

Note that in a model in which some (or all) of the parameters $\mathbf{J}$ are large, the partial magnetisations of some (or all) of the components in (meta)stable macrostates should be close to -1 or 1 in order to accommodate these high couplings inside the stability nappe.

3.3.3 Singularities and critical macrostates

Since the equations of state for a two-component CW model

$$\mathcal{G}_i(\bar{\mathbf{m}}, \mathbf{h}; \mathbf{J}, \boldsymbol{\gamma}) \equiv \frac{\partial \bar{\mathcal{F}}(\bar{\mathbf{m}}; \mathbf{J}, \mathbf{h}; \boldsymbol{\gamma})}{\partial \bar{m}_i} = 0, \quad i \in \{1, 2\} \tag{3.30}$$

at fixed $\boldsymbol{\gamma}$ and $\mathbf{J}$ implicitly define a map $\mathbf{h}(\bar{\mathbf{m}})$ of a plane to a plane, they can be analysed using the ideas from the Whitney's catastrophe theory [Whitney (1955)], according to which such maps may have two types of singularities that do not disappear after no matter how small perturbations of the map[9], namely *folds* and *cusps*. In line with Definition 6, all singularities satisfy the condition

[9] In catastrophe theory such singularities are known as *stable*, although we do not use this term to avoid its confusion with the notion of stability defined in Section 2.1.8.

$$\det\left(\frac{\partial \boldsymbol{\mathcal{G}}(\bar{\mathbf{m}},\mathbf{h};\mathbf{J},\boldsymbol{\gamma})}{\partial \bar{\mathbf{m}}}\right)=0 \tag{3.31}$$

known as a *general fold*, which in our case is given by (3.26) and shown in red in Fig. 3.4, where it is plotted in the $\bar{\mathbf{m}}$-space and then mapped into the $\mathbf{h}$-space using the equations of state in their explicit form (3.19). The cusps satisfy the following additional constraints

$$\underset{\mathbf{v}}{\nabla}\,\boldsymbol{\mathcal{G}}=0; \tag{3.32}$$

$$\underset{\mathbf{v}}{\nabla}\underset{\mathbf{v}}{\nabla}\,\boldsymbol{\mathcal{G}}\neq 0, \tag{3.33}$$

where $\mathbf{v}$ is the vector in $\bar{\mathbf{m}}$-space tangential to the general fold, and $\underset{\mathbf{v}}{\nabla}$ denotes the directional derivative along $\mathbf{v}$. Assuming the absence of the higher-order singularities which, as discussed above, can always be removed by no matter how small of a change in $\mathbf{J}$ and/or $\boldsymbol{\gamma}$, the points on the general fold that are not cusps are called folds. The folds usually form a disconnected curve in $\bar{\mathbf{m}}$ and $\mathbf{h}$ spaces[10], while the cusps are isolated points attached to this curve, and together they form the whole general fold. In Fig. 3.4 one of the two cusp points of the model with $J_{11}=1,\ J_{22}=-0.487664,\ J_{12}=-1.615554;\gamma_1=\gamma_2=0.5$ is shown as the violet cross, while the rest of the general fold (red line) consists entirely of folds.

We will now show that all critical macrostates that cannot be removed by arbitrarily small perturbations in $\mathbf{J}$ and/or $\boldsymbol{\gamma}$ correspond to the cusp points of the $\mathbf{h}(\bar{\mathbf{m}})$ map. It is clear that, since every critical macrostate is singular, it should be located on the general fold where, as discussed in Section 3.3.2.1, at least one of the eigenvalues of the SMFE Hessian vanishes. Furthermore, from the explicit expressions for the eigenvalues (3.24), it is clear that both eigenvalues can vanish simultaneously only when

$$J_{11}=\frac{1}{\gamma_1(1-\bar{m}_1^2)};\quad J_{22}=\frac{1}{\gamma_2(1-\bar{m}_2^2)};\quad J_{12}=0, \tag{3.34}$$

which corresponds to the uninteresting cases of the two disconnected singular CW components, and every singularity of this type disappears under no matter how small of a change in J_{12}. For this reason, we further assume that on singularities of interest, only one eigenvalue of the Hessian

[10] Apart from the cases when the curve shrinks to a point having zero measure in the parameter space.

is zero, and since we are interested in critical points, the other eigenvalue should be positive since otherwise the macrostate would, clearly, be unstable. In such a case, one of the two principal curvatures of the SMFE surface shown in Fig. 3.5 is positive, while the other vanishes and changes its sign when the general fold is being crossed. Suppose that the principal direction corresponding to the zero eigenvalue is transversal to the general fold in $\bar{\mathbf{m}}$-space, in which case moving along this direction means changing the sign of that eigenvalue, which implies an inflection point of the SMFE along this direction leading to an unstable macrostate. Conversely, if the principal direction corresponding to the zero eigenvalue is parallel to the general fold, then moving along this direction does not change the sign of the eigenvalue, and if before the singularity the eigenvalue was positive, it will remain positive after the singularity is crossed along this direction[11]. Of course, if the singularity is crossed along any other direction, this eigenvalue will change its sign, but since the other eigenvalue is positive, its contribution to the SMFE difference is dominant in some vicinity of the singularity, meaning that the SMFE can only increase. This means that the SMFE has a local minimum and the macrostate is (meta)stable and, therefore, critical according to Definition 8. Thus, we have shown that, as long as the general fold is a smooth curve[12] in $\bar{\mathbf{m}}$-space, on every critical macrostate the singularity condition (3.31) should be satisfied together with (3.32). The condition (3.33) is unnecessary but, according to the catastrophe theory, singularities on which it is violated can be removed by arbitrarily small perturbations of the parameters.

It is important to understand that, as will become clear in the following two sections, not all cusps correspond to critical points and not all critical points correspond to cusps, but due to the famous result from the catastrophe theory [Whitney (1955)] discussed above, the critical points that do not disappear under no matter how small perturbations of $\mathbf{J}$ and/or $\boldsymbol{\gamma}$ always correspond to cusps of the $\mathbf{h}(\bar{\mathbf{m}})$ map (3.19).

Note that at a critical point fluctuations are high along the direction parallel to the general fold in $\bar{\mathbf{m}}$-space due to the flatness of the free energy along this direction (Fig. 3.5).

[11] Note how the cyan curve in the right panel of Fig. 3.4 always stays in the region where both eigenvalues are positive (yellow), apart from the point marked by the violet cross, where it touches the general fold and one of the eigenvalues vanishes.

[12] As opposed to a point, as will be discussed later.

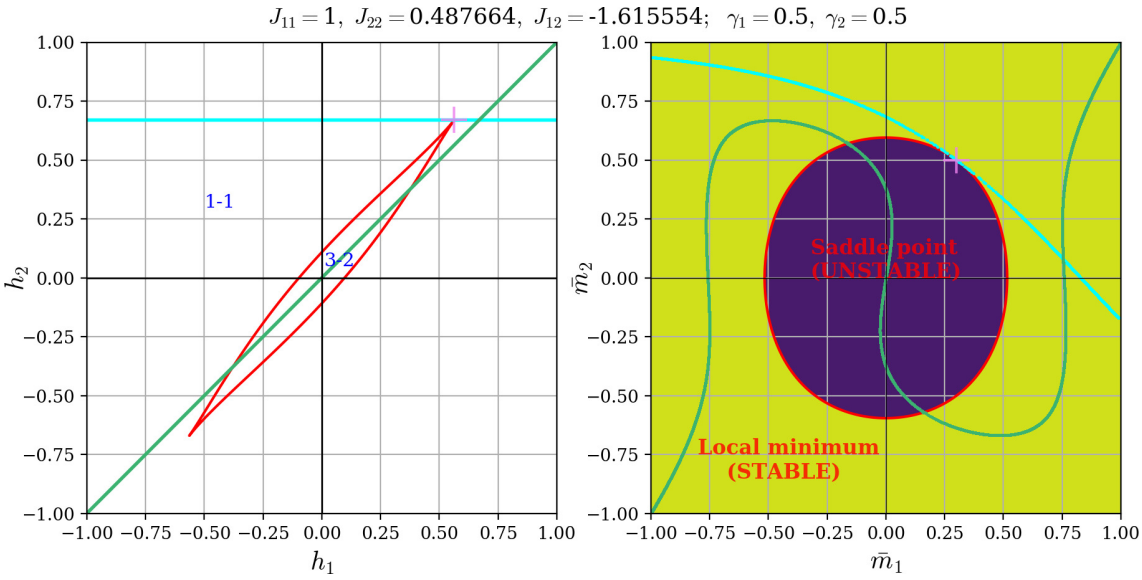

Fig. 3.4: Graphical representation of the $\mathbf{h}$-plane (left) and the $\bar{\mathbf{m}}$-plane (right) related by the map (3.19). The general fold (shown in red) separates the $\bar{\mathbf{m}}$-plane into regions where the eigenvalues (3.24) have different signs corresponding to the different types of non-degenerate stationary points of the SMFE (3.3), and only the solutions from the yellow region, corresponding to the (local) minima, are (meta)stable (indicated as "stable" in the image). Furthermore, the $\mathbf{h}$-plane is separated by the general fold into regions with different stability indices, i.e. (*total number of solutions*)-(*number of stable solutions*) shown as the blue numbers in the left panel. The cyan line shows the trajectory of the solutions of the equations of state (3.19) when $h_2 = 0.669723$ and h_1 is being changed, while the green line shows the trajectory of the solutions when the fields are constrained by $h_1 = h_2 = h$ and h is being changed. The animation showing the emergence of these trajectories is available at https://youtu.be/2gJrtE2QUaY and the stop-frames from it can be found in Appendix B in Fig. 2.2, from which one may conclude that crossing the general fold results in a creation (or annihilation) of a pair of solutions of the equation of state (3.19). Note that both cusp points from this image (one of which is marked by the violet cross) correspond to the critical macrostates that appear in non-zero fields, which, as discussed in Section 2.4.3.1, is impossible in a single-component CW model.

3.3.3.1 Critical ray of a given macrostate

The explicit form of the condition (3.32) is given by

$$\sum_{j=1}^{2} \frac{\partial \mathcal{G}_i}{\partial \bar{m}_j} v_j = \sum_{j=1}^{2} \frac{\partial^2 \bar{\mathcal{F}}(\bar{\mathbf{m}}; \mathbf{J}, \mathbf{h}; \boldsymbol{\gamma})}{\partial \bar{m}_i \partial \bar{m}_j} v_j = \sum_{j=1}^{2} \gamma_i \gamma_j \mathcal{H}_{ij}(\bar{\mathbf{m}}; \mathbf{J}; \boldsymbol{\gamma}) v_j = 0, \quad i \in \{1, 2\}, \tag{3.35}$$

where the tangential to the general fold vector $\mathbf{v}$ can be found as

$$\mathbf{v} \propto \begin{pmatrix} \frac{\partial \det \boldsymbol{\mathcal{H}}}{\partial \bar{m}_2} \\ -\frac{\partial \det \boldsymbol{\mathcal{H}}}{\partial \bar{m}_1} \end{pmatrix} \propto \begin{pmatrix} \gamma_1 \bar{m}_1 \left[J_{11} - \gamma_2 (1 - \bar{m}_2^2)(J_{11} J_{22} - J_{12}^2) \right] \\ -\gamma_2 \bar{m}_2 \left[J_{22} - \gamma_1 (1 - \bar{m}_1^2)(J_{11} J_{22} - J_{12}^2) \right] \end{pmatrix}, \tag{3.36}$$

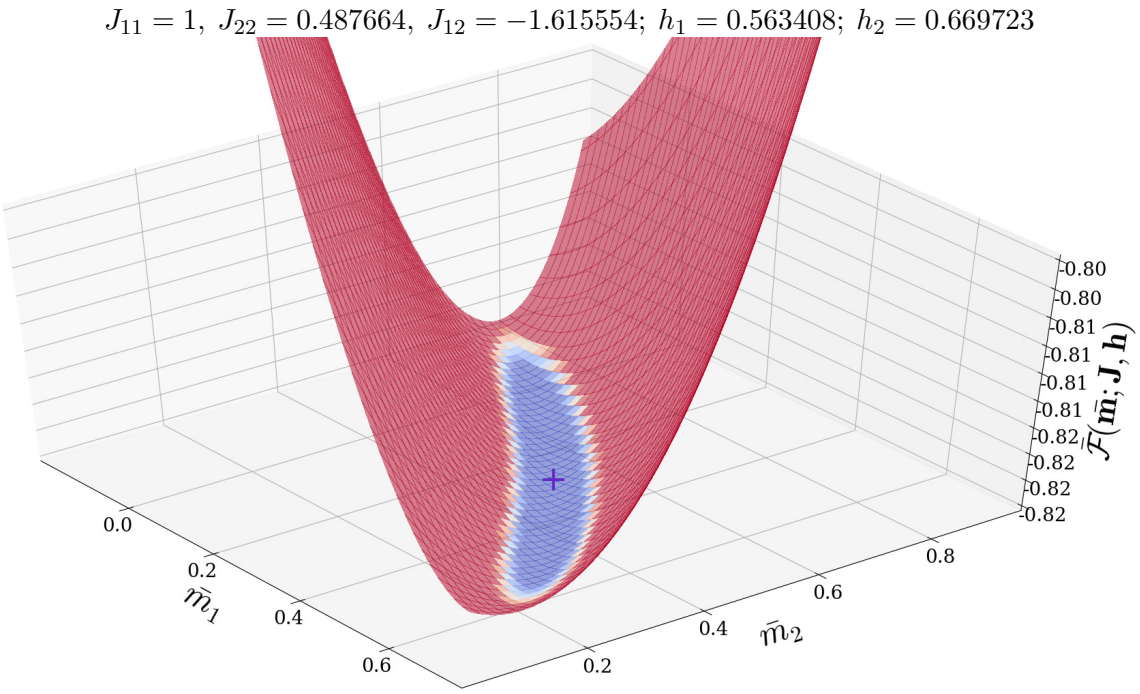

Fig. 3.5: The SMFE in the vicinity of the critical point (violet cross) found in Fig. 3.4 and the left panel of Fig. 3.8. Notice how flat the surface is in one direction compared to the other, which is the consequence of the fact that one of the eigenvalues of the Hessian is equal to zero, while the other is a positive number. This shape of the free energy allows large fluctuations along the principal direction corresponding to the zero eigenvalue (which is parallel to the general fold) at the critical point.

and its substitution to (3.35) gives the following equations

$$\bar{m}_2 \left[J_{11}\gamma_1(1-\bar{m}_1^2) - 1\right]^2 - J_{12}\bar{m}_1 \left[J_{22}\gamma_2(1-\bar{m}_2^2) - 1\right] \gamma_2(1-\bar{m}_2^2) = 0; \tag{3.37}$$

$$\bar{m}_1 \left[J_{22}\gamma_2(1-\bar{m}_2^2) - 1\right]^2 - J_{12}\bar{m}_2 \left[J_{11}\gamma_1(1-\bar{m}_1^2) - 1\right] \gamma_1(1-\bar{m}_1^2) = 0, \tag{3.38}$$

which define two quadrics in $\mathbf{J}$-space. It is straightforward to show that the transformation

$$\mathbf{J} = \begin{pmatrix} 1 & 0 & 0 \\ 0 & \frac{1}{\sqrt{2}} & \frac{-1}{\sqrt{2}} \\ 0 & \frac{1}{\sqrt{2}} & \frac{1}{\sqrt{2}} \end{pmatrix} \check{\mathbf{J}} + \begin{pmatrix} \frac{1}{\gamma_1(1-\bar{m}_1^2)} \\ \frac{1}{\gamma_2(1-\bar{m}_2^2)} \\ 0 \end{pmatrix} \tag{3.39}$$

brings (3.37) to its normal form

$$\frac{\bar{m}_2\gamma_1^2(1-\bar{m}_1^2)^2}{\bar{m}_1\gamma_2^2(1-\bar{m}_2^2)^2} \cdot 2\check{J}_{11}^2 + \check{J}_{12}^2 = \check{J}_{22}^2, \tag{3.40}$$

which is a normal form of a cone. Similarly, the transformation

$$\mathbf{J} = \begin{pmatrix} \frac{1}{\sqrt{2}} & 0 & \frac{1}{\sqrt{2}} \\ 0 & 1 & 0 \\ \frac{-1}{\sqrt{2}} & 0 & \frac{1}{\sqrt{2}} \end{pmatrix} \hat{\mathbf{J}} + \begin{pmatrix} \frac{1}{\gamma_1(1-\bar{m}_1^2)} \\ \frac{1}{\gamma_2(1-\bar{m}_2^2)} \\ 0 \end{pmatrix} \tag{3.41}$$

brings (3.38) to its normal form

$$\hat{J}_{11}^2 + \frac{\bar{m}_1\gamma_2^2(1-\bar{m}_2^2)^2}{\bar{m}_2\gamma_1^2(1-\bar{m}_1^2)^2} \cdot 2\hat{J}_{22}^2 = \hat{J}_{12}^2, \tag{3.42}$$

which is also a normal form of a cone. Note that, as clear from the transformations (3.39), (3.41) and (3.28), both of these cones share a common apex with the cone defined by the singularity condition (3.26), as demonstrated in Fig. 3.6, and in the coordinate system $\mathcal{J}$ defined by (3.28), which brings the later to its normal form (3.27), the equations (3.37) and (3.38) read as

$$\begin{aligned} &\gamma_1^2\bar{m}_2\left(1-\bar{m}_1^2\right)^2\left(\mathcal{J}_{11}-\mathcal{J}_{22}\right)^2 - \sqrt{2}\gamma_2^2\bar{m}_1\left(1-\bar{m}_2^2\right)^2\mathcal{J}_{12}\left(\mathcal{J}_{11}+\mathcal{J}_{22}\right) = 0; \\ &\gamma_2^2\bar{m}_1\left(1-\bar{m}_2^2\right)^2\left(\mathcal{J}_{11}+\mathcal{J}_{22}\right)^2 - \sqrt{2}\gamma_1^2\bar{m}_2\left(1-\bar{m}_1^2\right)^2\mathcal{J}_{12}\left(\mathcal{J}_{11}-\mathcal{J}_{22}\right) = 0. \end{aligned}$$

Introducing the new variables according to

$$\xi = \mathcal{J}_{11} + \mathcal{J}_{22}; \quad \eta = \mathcal{J}_{11} - \mathcal{J}_{22}; \quad \zeta = \sqrt{2}\mathcal{J}_{12}, \tag{3.43}$$

the equations (3.26), (3.37) and (3.37) can be written as

$$\begin{cases} \zeta^2 - \eta\xi = 0; \\ B(\bar{\mathbf{m}};\boldsymbol{\gamma})\eta^2 - \zeta\xi = 0; \\ \xi^2 - B(\bar{\mathbf{m}};\boldsymbol{\gamma})\zeta\eta = 0, \end{cases} \tag{3.44}$$

where

$$B(\bar{\mathbf{m}};\boldsymbol{\gamma}) = \frac{\bar{m}_2}{\bar{m}_1} \cdot \left(\frac{\gamma_1(1-\bar{m}_1^2)}{\gamma_2(1-\bar{m}_2^2)}\right)^2. \tag{3.45}$$

Solving these equations yields to a line

$$\begin{cases} \mathcal{J}_{22} = \mathcal{J}_{11}\dfrac{B^{2/3}(\bar{\mathbf{m}};\boldsymbol{\gamma}) - 1}{B^{2/3}(\bar{\mathbf{m}};\boldsymbol{\gamma}) + 1}; \\ \mathcal{J}_{12} = \mathcal{J}_{11}\dfrac{\sqrt{2}B^{1/3}(\bar{\mathbf{m}};\boldsymbol{\gamma})}{B^{2/3}(\bar{\mathbf{m}};\boldsymbol{\gamma}) + 1}, \end{cases}$$

which in the untransformed coordinates reads as

$$\begin{cases} J_{22} = B^{2/3}(\bar{\mathbf{m}};\boldsymbol{\gamma})\left(J_{11} - \dfrac{1}{\gamma_1(1-\bar{m}_1^2)}\right) + \dfrac{1}{\gamma_2(1-\bar{m}_2^2)}; \\ J_{12} = B^{1/3}(\bar{\mathbf{m}};\boldsymbol{\gamma})\left(J_{11} - \dfrac{1}{\gamma_1(1-\bar{m}_1^2)}\right). \end{cases} \tag{3.46}$$

Fig. 3.6 shows how all three cones corresponding to the conditions (3.26), (3.37) and (3.37) intersect along the line defined by (3.46), and as discussed in Section 3.3.2.1, all couplings $\mathbf{J}$ that are outside the stability nappe correspond to the unstable macrostates, meaning that critical macrostates belong to the ray of the line defined by (3.46) which lies on the stability nappe. Therefore we introduce

Definition 13. *Critical ray is the intersection of the line defined by (3.46) and the stability nappe.*

Note that the initial point of the critical ray is the common apex of the cones whose location is given by (3.34) and corresponds to the case of the two disconnected critical CW components.

Fig. 3.4, Fig. 3.7, Fig. 2.5 and Fig. 2.6 and the corresponding animations show what happens to the solutions of the equations of state when the general fold is being crossed in various ways.

3.3.3.2 Role of the principal cone

As can be seen from (3.45), when $\bar{\mathbf{m}}$ approaches zero $B(\bar{\mathbf{m}};\boldsymbol{\gamma})$ becomes undefined together with the line (3.46). This can be explained by the fact that at $\bar{\mathbf{m}} = 0$ the cone defined by the singularity condition (3.26) coincides with the principal cone, and in the region of $\mathbf{J}$ enclosed by the uniqueness nappe the general fold does not exist[13] emerging from a single point when this boundary is being crossed. This reveals a role of the principal cone as a surface on which at $\bar{\mathbf{m}} = \mathbf{0}$

[13] Since, as discussed in Section 3.3.2.1, there are no singular macrostates in this region.

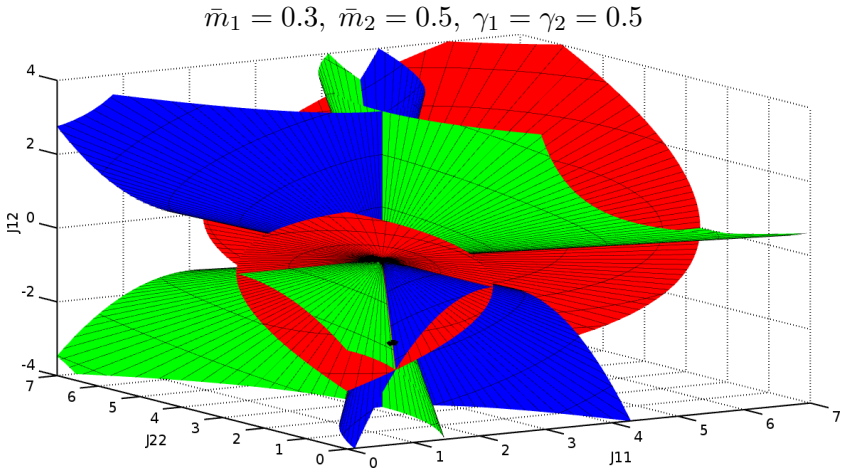

Fig. 3.6: The cones corresponding to the singularity condition (3.26) (red) and the conditions (3.37) and (3.38) intersect on a line whose half-line, starting from the apex and heading towards the negative values of the couplings, is the critical ray. The black dot at $J_{11} = 1,\ J_{22} = 0.487664,\ J_{12} = -1.615554$ shows the position of Fig. 3.4, Fig. 3.5 and the left panel of Fig. 3.8.

($\mathbf{h} = 0$) one of the components of the general fold shrinks to (or emerges from) a point. This can be seen in the animation available at[14] https://youtu.be/amoPQkPNDdI, which shows how the shape of the general fold changes with the temperature. The model from the animation is defined by $J_{11} = 3,\ J_{22} = 3,\ J_{12} = -0.42;\ \gamma_1 = \gamma_2 = 0.5$, and when the temperature decreases[15] from $T = 1.8$, the principal cone is being crossed twice, namely at $T = 1.71$ the model goes out of the uniqueness nappe, and at $T = 1.29$ it enters the second nappe of the principal cone. At both intersections of the principal cone the new disconnected components of the general fold emerge from a point $\bar{\mathbf{m}} = 0$ ($\mathbf{h} = 0$).

Note that although none of the singularities, appearing at $\bar{\mathbf{m}} = 0$ while the couplings belong to the principal cone, correspond to the cusp points of the map (3.19), all such singularities correspond to critical macrostates when the couplings lie on the uniqueness nappe, since a unique solution is always stable[16].

3.3.4 Comparison with simulations

Consider the two-component CW model with $\bar{m}_1 = 0.3,\ \bar{m}_2 = 0.5,\ N_1 = N_2 = 10^5$ for which the cones defined by (3.37), (3.38) and (3.26) are shown in Fig. 3.6. Let us pick a point on the

[14] Stop-frames can be found in Fig. 2.4 in Appendix B.
[15] Which can be thought of as couplings changing as $J_{11} = 3/T,\ J_{22} = 3/T,\ J_{12} = -0.42/T$.
[16] Since if a (local) minimum of the SMFE is unique, then it is a global minimum.

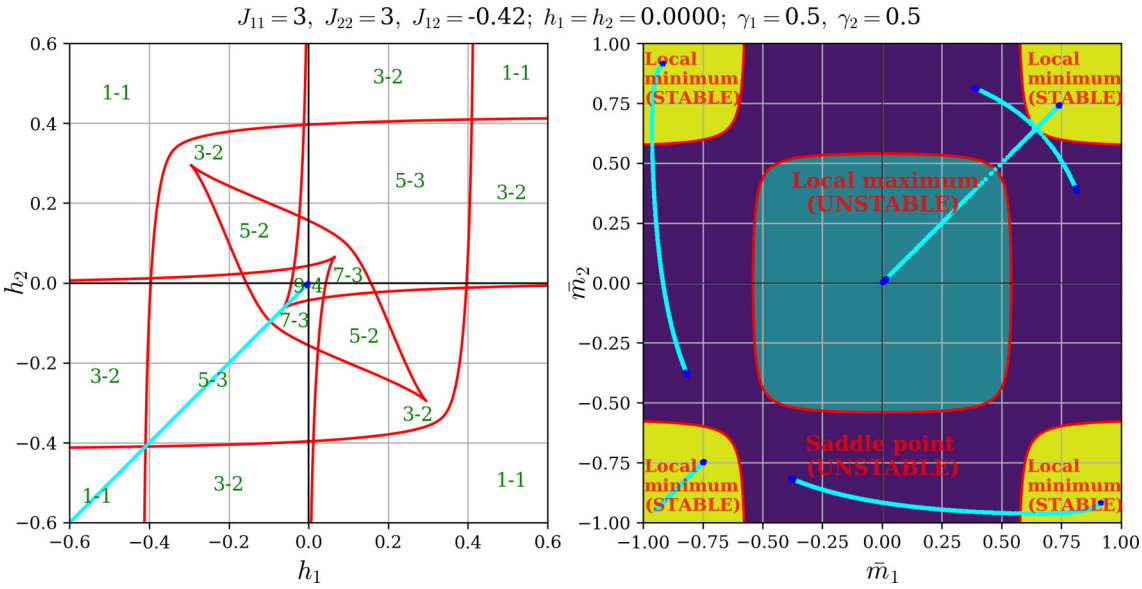

Fig. 3.7: Graphical representation of the $\mathbf{h}$-plane (left) and the $\bar{\mathbf{m}}$-plane (right) related by the equations of state (3.19). The cyan line shows the trajectory of the solutions of the equations of state (3.19) when the fields constrained as $h_1 = h_2 = h$ change from $h = -0.6$ to $h = 0$. The general fold (shown in red) separates the $\bar{\mathbf{m}}$-plane into regions in which the eigenvalues (3.24) have different signs corresponding to the different types of non-degenerate stationary points of the SMFE (3.3), and only the solutions from the yellow regions correspond to the (local) minima of the SMFE and, therefore, (meta)stable macrostates (marked as "stable" in the image). Furthermore, the $\mathbf{h}$-plane is separated by the general fold into the regions with different stability indices, i.e. (*total number of solutions*)-(*number of stable solutions*) shown as the green numbers in the left panel. This image is a stop-frame from the animation available at https://youtu.be/7w4y-KAysqA which demonstrates how the solutions change with h. More stop-frames from this animation are shown in Fig. 2.3 in Appendix B, from which one can conclude that when a cusp point is being crossed in the direction of the cusp (unlike the cyan line in Fig. 3.4), three solutions come together at a single point.

critical ray $J_{11} = 1,\ J_{22} = 0.487664,\ J_{12} = -1.615554$ (shown as the black dot in Fig. 3.6) and perform a Monte Carlo simulation of the system by scanning h_1 while keeping h_2 fixed[17] at $h_2 = 0.669723$, as predicted by the equations of state (3.19) for the above values of $\bar{\mathbf{m}}$ and $\mathbf{J}$. The results of this simulation are shown in the left panel of Fig. 3.8, where at each point in h_1 the observables are averaged over 10 samples obtained by running a single-spin Metropolis dynamics, discussed in Section 2.4.6, for $N \cdot 500$ iterations[18] without reinitialisation. As can be seen from Fig. 3.8, the simulations are in perfect agreement with the theory that predicts a criticality at $h_1 = 0.563408$.

The right panel of Fig. 3.8 corresponds to the case when the fields are constrained as $h_1 = h_2 = h$

[17] Cyan line from Fig. 3.4.

[18] 500 iterations per node is a relatively large iteration time needed to ensure thermalisation in the vicinity of the critical point where the simulation is slow to converge.

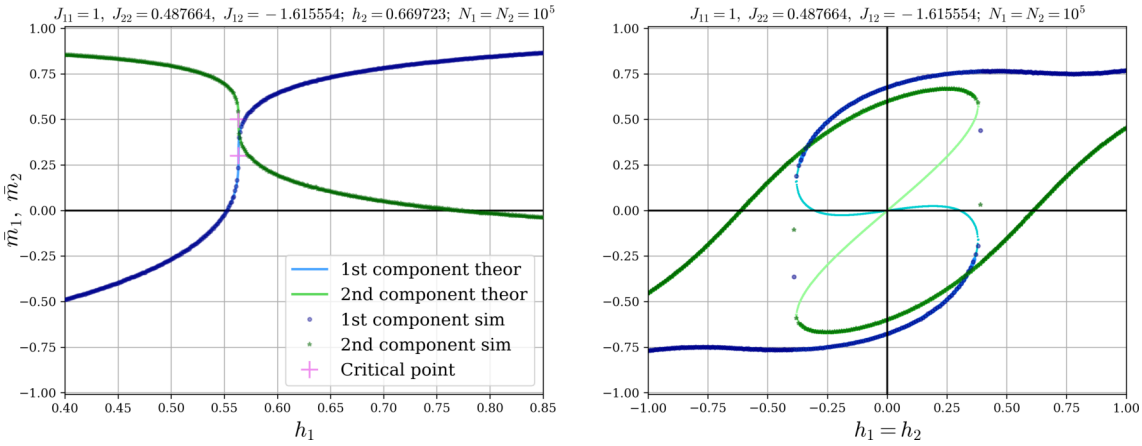

Fig. 3.8: The dependencies of the partial magnetisations on the fields corresponding to the cyan (left panel) and green (right panel) lines from Fig. 3.4. In the left panel the field acting on the second component is being fixed at $h_2 = 0.669723$ while the field h_1 is being varied, and the critical point is crossed at $h_1^{(crit)} = 0.563408$, which is confirmed by the MC simulations. In the right panel the fields are set to be equal $h_1 = h_2 = h$, and the dependencies of the partial magnetisations on h demonstrate bistability, which is confirmed by the time-averaging MC simulations run forwards and backwards in h.

and h changes[19], in which case the model enters a bistable regime. As before, the observables are averaged over 10 samples obtained by running a single-spin Metropolis dynamics for $N \cdot 10$ iterations[20] without reinitialisation. To recover both stable branches of the hysteresis the simulation is run both ways, and, as can be seen in Fig. 3.8, both stable branches are perfectly recovered.

3.3.5 Possible regimes

As can be seen in Fig. 3.7, a two-component CW model may be found in the regimes with any number of (meta)stable macrostates from one to four. The existence of at least one stable macrostate is a consequence of the fact that the specific microcanonical free energy (3.3) always has a minimum, while the fact that the number of (meta)stable macrostates cannot exceed four is clear from the discussion from Section 3.3.2.

The regimes in which there are one, two or four (meta)stable macrostates could have been anticipated from considering the models with $J_{12} = 0$, i.e. 1-stability arises when both components are 1-stable; 2-stability arises when exactly one of the two components is 2-stable; and 4-stability arises when both disconnected CW components are 2-stable, but the regime with exactly three

[19] Green line from Fig. 3.4.

[20] Which is enough to converge to a (meta)stable macrostate from relatively close initial configuration in the absence of criticalities.

(meta)stable macrostates can never be observed in such a disconnected model. For the model from Fig. 3.7 tristability can be heuristically explained by the disappearance of the ferromagnetically ordered metastable state, in which the spins are oriented in the opposite direction to the field. The appearance of tristability in the graphical analysis is shown in the right panel of Fig. 3.2.

3.4 Applications

Since, as discussed in Section 2.3, the equations of state (3.5) can be thought of as the mean field self-consistency equations for other multispecies Ising models, the above analysis applies to any such system at the level of the mean field approximation, which makes it widely applicable, albeit, often just qualitatively. The relations analogous to the equations of state (3.19) first appeared in physics [Néel (1948); Smart (1955)], where they emerged as the mean field self-consistency equations for ferrimagnets, and being restricted by the application were never considered in full generality. In the recent years such models were applied more widely [Contucci et al. (2008); Agliari et al. (2016)], and these new applications required considering the dependencies of magnetisations on the parameters other than the temperature and the external field[21], although, still, only the particular restrictions of the two-component CW model were considered in detail. In this section we discuss some of these applications.

3.4.0.1 Magnetism

As discussed in Section 2.4, the Curie-Weiss model can be used as a mean field model of a ferromagnet; however, it clearly cannot be used to describe ferrimagnets [Néel (1948); Néel (1952), Smart (1955)] which consist of several asymmetric sublattices with strong antiferromagnetic interactions between them. The asymmetry between the sublattices in such materials may come from the differences in the numbers of atoms (or ions) in the sublattices, in which case $\gamma_1 \neq \gamma_2$, and/or from the differences in the magnetic moments of the atoms (or ions) belonging to the different sublattices, which corresponds to the mean field models with different types of spins in different components considered in [Bowers and Schofield (1981)]. In some crystals[22], such as $FeCl_2$, along with the antiferromagnetic interaction between the sublattices, there are also strong

[21] Equal for both components in physical applications.
[22] Usually called metamagnets.

ferromagnetic interactions within the sublattices[23], and in the presence of a strong magnetic field all the spins in such materials may suddenly align, resulting in a dramatic increase of magnetisation. This phenomenon, known as *metamagnetism*, can be illustrated using the two-component CW model from Fig. 3.7 in which, as clear from the corresponding animation, when the field exceeds $h \approx 0.415$, there is only one stable macrostate, and in this macrostate the spins are ordered ferromagnetically. Moreover, when the ferromagnetic intracomponent couplings are large compared to the intermomponent antiferromagnetic coupling, then at sufficiently low temperatures the model allows ferromagnetically ordered metastable macrostates even when the field is completely removed, as can be seen in Fig. 3.7 and Fig. 3.9.

Note that in physical experiments it is natural to measure the temperature dependence of the full specific magnetisation $\gamma_1\bar{m}_1 + \gamma_2\bar{m}_2$ along with the heat capacity, which for the MCW model is given by[24]

$$\bar{c}_{\mathbf{h}} = T\left(\frac{\partial \bar{S}}{\partial T}\right)_{\mathbf{h}} = \mathbf{A}^{\top}\boldsymbol{\mathcal{H}}^{-1}(\bar{\mathbf{m}}; \mathbf{J}/T; \boldsymbol{\gamma})\mathbf{A}, \tag{3.47}$$

where $A_i = \operatorname{artanh}(\bar{m}_i)$ and $\boldsymbol{\mathcal{H}}(\bar{\mathbf{m}}; \mathbf{J}/T; \boldsymbol{\gamma})$ is the Hessian (3.17). Measuring the full specific magnetisation may result in a dependence qualitatively similar to what is observed on the left panel of Fig. 3.9, while measuring the heat capacity should reveal the obscured second-order phase transition at the Néel temperature[25] $T_N = 1.71$ since, as clear from (3.47), the heat capacity diverges at singular macrostates. Note that in the case of Fig. 3.9 the second-order phase transition at Néel temperature is obscured due to the symmetry of the components, but if the components are asymmetric, as can be seen in Fig. 3.10, the phase transition reveals itself by the emergence of the spontaneous magnetisation below the Néel temperature, which is the reason why ferrimagnets[26] were confused with ferromagnets before the seminal work of Louis Néel [Néel (1948)].

3.4.0.2 Other applications

It is clear that, essentially, every system consisting of several species, whose representatives can be in two different states while being subjects to an external influence can, with various degree of

[23] In such materials the asymmetry between the sublattices may, in principle, come from the different ferromagnetic couplings within different sublattices, although this is not the case with $FeCl_2$ in which sublattices can be assumed to be symmetric.

[24] Of course, in any real substance this is just a magnetic part of the full heat capacity.

[25] Néel temperature is the temperature of magnetic ordering similar to Curie temperature for ferromagnets, and, as discussed in Section 3.3.3.2, at this temperature the uniqueness nappe is being crossed from the inside.

[26] Which derive their name from ferrites.

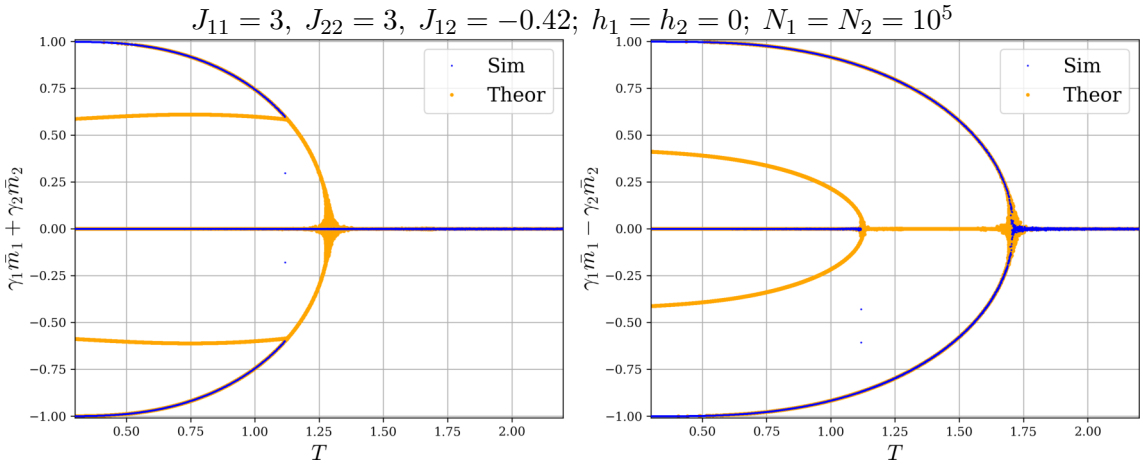

Fig. 3.9: Temperature dependencies of the total specific magnetisation $\gamma_1\bar{m}_1 + \gamma_2\bar{m}_2$ (left panel) and the difference $\gamma_1\bar{m}_1 - \gamma_2\bar{m}_2$ (right panel) obtained by solving the equations of state (3.19) numerically and by the MC simulations, which recover all the (meta)stable macrostates in great agreement with the theory. Note that due to the symmetry and negative intercomponent coupling J_{12} the magnetisations of the components in antiferromagnetically ordered stable macrostates perfectly compensate each other, thus the second-order phase transition at Néel temperature $T_N = 1.71$ (at which the uniqueness nappe is being crossed) does not reveal itself on the temperature dependence of the full specific magnetisation while being clearly visible on the temperature dependence of $\gamma_1\bar{m}_1 - \gamma_2\bar{m}_2$ (right panel). When the temperature is below $T = 1.29$ (at which the second nappe of the principal cone is being crossed) the model exhibits ferromagnetically ordered metastable macrostates along with the stable antiferromagnetic macrostates.

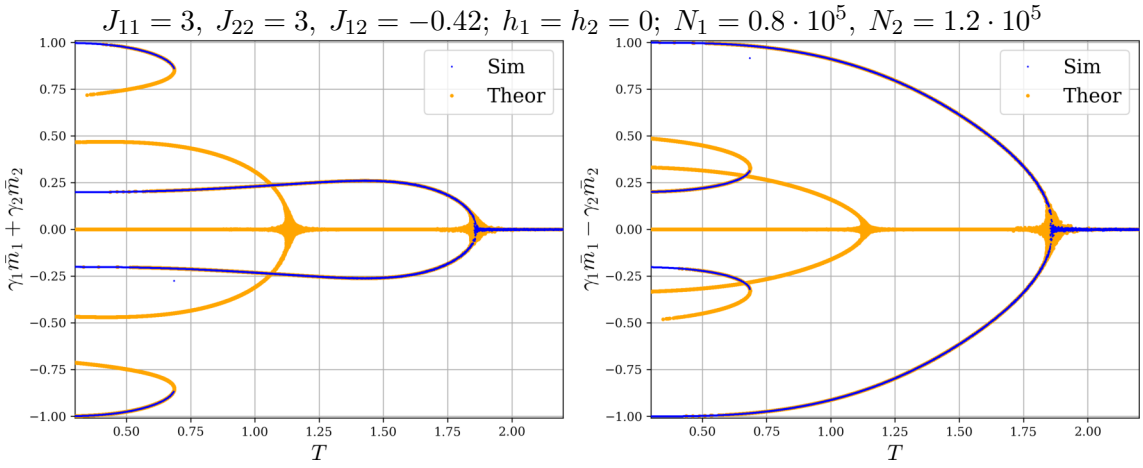

Fig. 3.10: Temperature dependencies of the total specific magnetisation $\gamma_1\bar{m}_1 + \gamma_2\bar{m}_2$ (left panel) and the difference $\gamma_1\bar{m}_1 - \gamma_2\bar{m}_2$ (right panel) obtained by solving the equations of state (3.19) numerically and by the MC simulations, which recover all the (meta)stable macrostates in great agreement with the theory. Note that below the Néel temperature $T_N \simeq 1.86378$ the model exhibits spontaneous magnetisation due to the asymmetry of the components, and below $T \simeq 1.13622$ there are ferromagnetically ordered metastable macrostates. This model can be thought of as a ferrimagnet exhibiting metamagnetism.

success, be described by the MCW model, whose spins may correspond to, e.g. ligands[27] of dif-

[27] Ions or molecules whose chemical potentials correspond to $\mathbf{h}$ in the MCW model.

ferent types which can be either free or bound to a macromolecule [Agliari et al. (2016)]; residents and immigrants possessing either resident or immigrant culture [Contucci et al. (2008)]; etc. Note that since the precision of the MFT increases with the dimensionality of the problem, applications of the MCW model in the fields like social statistics, where each individual usually interacts with a large number of other individuals, may, in principle, have some quantitative success if a sufficient data is available to fit the model. A discussion of fitting the MCW model to the synthetic data produced by another MCW model is given in [Fedele et al. (2013)], which shows how such inverse problem can be successfully solved, especially at high temperatures. From the discussion in Section 3.3.2.1 it is clear that, as long as the two-component model is inside its uniqueness nappe, the solution of the equations of state (3.19) is unique and smooth, meaning that, if the parameter estimates are found to be enclosed inside this nappe, then the estimated model may, indeed, have something to do with the data. However, if the parameters are found to be far outside the uniqueness nappe, a good fit is very unlikely due to the sharp dependencies of the expectations on the parameters and due to the multimodality of the distributions discussed in Section 2.1.7, which makes individual samples from the model be very different from the corresponding ensemble averages.

Finally, it should be pointed out that since the type of spins only enters the specific microcanonical free energy through the entropy (i.e. the initial conditions for the PDEs), deriving the equations of state for a model with the same Hamiltonian, but different spins requires only minor adaptations to the derivations discussed in Section 3.2.1 and Section 3.2.2. This fact further increases the applicability of such models, and in Section 4.8 one of such applications is discussed, although, of course, the specific results obtained for the two-component CW model are expected to be different for the models with different spins due to the differences in the entropies of such models.

3.5 Discussion

In this chapter we have derived the equations of state for the multi-component analogue of the Curie-Weiss model and provided the detailed analysis of the two-component case. From this analysis it is clear that, unlike the original CW model discussed in Section 2.4, the two-component model may have any number from one to four of (meta)stable macrostates and exhibits critical behaviour in nonzero fields, which is confirmed by the Monte Carlo simulations. The above analysis

gives a good orientation in the parameter space of the two-component model and identifies the region of the couplings in which the dependence of the observables on the parameters is smooth, which may facilitate fitting such models to empirical data. Finally, we have discussed some of the existing applications of the MCW model and how it can be used to qualitatively explain and predict interesting real-world phenomena.

Unfortunately, acquiring a good general understanding of the p-component cases for $p > 2$ is hard due to the high-dimensional parameter spaces of such models. Indeed, in general, a p-component model has $p(p+1)/2$ independent couplings, p fields (coupled to p observables) and $p-1$ independent splitting parameters, meaning that the dimension of the parameter space grows quadratically with p. It is easy to see that in a p-component model in which all the CW components are independent (i.e. $J_{ij} = 0$ for $i \neq j$), the maximum possible number of (meta)stable macrostates is 2^p, which grows exponentially with p.

Chapter 4

Exponential Random Graph Models

In this chapter we analyse various exponential random graph models (ERGMs) and show how well these models are described by the mean field theory (MFT). First we give a brief introduction to ERGMs and define the concepts needed for the later discussion. Then in Section 4.2, we derive the mean field theory for the entire class of homogeneous Markov random graphs. After that, in Section 4.4, we discuss the homogeneous mean field ERGM ("MF model") for which we derive and analyse the exact thermodynamic equation of state, which, as discussed in Section 2.3, coincides with the mean field self-consistency equation. This similarity is used in Section 4.5 to establish a correspondence between the MF model and homogeneous Markov random graphs, after which the results obtained for the MF model can be used for any ERGM at the level of the mean field approximation. In Section 4.6, this is followed by the detailed analysis of various special cases of Markov random graphs based on the theory developed in the preceding sections and the Monte Carlo simulations. Then in Section 4.7, we discuss the problems that prevent homogeneous ERGMs from mimicking the behaviour of real-world networks, and in Section 4.8, we consider a heterogeneous mean field ERGM based on the MCW model from Chapter 3, for which we derive the equations of state. Finally, in Section 4.9, we draw some conclusions summarising the results discussed in this chapter.

4.1 Background

In this work we deal with simple undirected graphs, and it is well known [Newman (2010)] that any such graph is fully determined by its symmetric adjacency matrix $\mathbf{A}$, whose entries $A_{ij} \in \{0, 1\}$ indicate the presence or absence of an edge (link) between the nodes i and j.

ERGMs are usually understood as log-linear models with the probability distribution of the form[1]

$$P(\mathbf{A}) = \frac{\exp\left[\sum_{i=1}^{q} t_i \Omega_i(\mathbf{A})\right]}{Z(\mathbf{t})} \equiv \frac{\mathrm{e}^{-H(\mathbf{A};\mathbf{t})}}{Z(\mathbf{t})}, \tag{4.1}$$

where the Hamiltonian $H(\mathbf{A}; \mathbf{t})$ is a linear function of the parameters $\mathbf{t}$ and the observables $\Omega_i(\mathbf{A})$, while

$$Z(\mathbf{t}) = \sum_{\{\mathbf{A}\}} \mathrm{e}^{-H(\mathbf{A};\mathbf{t})} \tag{4.2}$$

is the normalising constant (aka the partition function), which depends solely on the parameters of the model. Note that the family of distributions defined by (4.1) is exponential and, due to the entropy maximisation properties of such distributions discussed in Section 2.1.2, ERGMs provide a rigorous approach to constructing *null-models* [Park and Newman (2004*b*); Newman (2010)], which are defined as maximum-entropy ensembles of graphs constrained on certain features (e.g. a total number of edges and/or a total number of triangles). Such models are usually used to test the hypothesis that a given network exhibits nontrivial features beyond the ones that were constrained at the values found in data.

Two types of constraints are usually distinguished, namely the *hard constraints*, under which the constrained property is always equal to the desired value; and the *soft constraints*, under which only the expected value of the property is fixed, while fluctuations are allowed. In the case of hard constraints, the distribution that maximises the entropy is uniform, which results in a microcanonical ensemble discussed in Section 2.1.5; and when the constraints are soft, as discussed in Section 2.1.2, the entropy is maximised by the Gibbs-Boltzmann (GB) distribution. Note that since, as discussed in Section 2.1.6, the canonical and microcanonical ensembles become equivalent in the thermodynamic limit, the hard and soft constraints for large networks are almost identical[2].

[1] Following the discussion from Section 2.4.8, in this chapter we often suppress the factor β for convenience.

[2] Note that, according to [Squartini et al. (2015)], this ensemble equivalence may be violated in sparse networks with an extensive number of constraints, although sparsity is not enforced in the models considered here.

In line with the above discussion, ERGMs can be viewed as null-models with soft constraints on the observables, which are assumed to be interpretable (e.g. a total number of links or a total number of triangles) in order to get valuable insights from fitting such models to data. For example, if one of the observables is the number of triangles and its conjugated parameter estimate is positive, then the processes underlying the formation of the studied network may be thought of as having a propensity for triangulation. Furthermore, if it turns out that the graphs produced by the estimated model are similar to the studied network in every other way[3], one may conclude that this propensity for triangulation is the only significant characteristic of the processes involved in the formation of the network, i.e. apart from having a relatively high number of triangles the network looks completely random. On the other hand, if it turns out that the samples from the model significantly differ from the studied network, one may conclude that the network in hand carries more information than what was embedded into the null-model.

ERGMs in which all the nodes are equivalent are referred to as *homogeneous*, and *heterogeneous* otherwise.

4.1.1 Homogeneous Markov random graphs

The idea behind Markov random graphs is that of the nearest neighbour interactions in Ising models, i.e. Markov random graphs [Frank and Strauss (1986)] are ERGMs in which the linking sites (i.e. node pairs) that do not share a common node are conditionally independent. As proven in [Frank and Strauss (1986)] using the Hammersley-Clifford theorem [Besag (1974)], the Hamiltonian of a generic homogeneous Markov ERGM is given by

$$H(\mathbf{A}) = -\sum_{k=1}^{q} \frac{\tau_k}{n^{k-1}} \mathcal{S}_k(\mathbf{A}) - \frac{6}{n}\theta\mathcal{T}(\mathbf{A}), \tag{4.3}$$

where n is the number of nodes in the model,

$$\mathcal{S}_k(\mathbf{A}) \equiv \frac{1}{k!} \sum_{\substack{i,\mathbf{j} \\ (j_l \neq j_r \forall l,r)}} A_{ij_1} A_{ij_2} \dots A_{ij_k} \tag{4.4}$$

[3]Which, due to the reasons explained later in this chapter, almost never happens for empirical data.

is the number of k-stars (sets of k links attached to the same node), and

$$\mathcal{T}(\mathbf{A}) \equiv \frac{1}{6}\operatorname{tr}\left(\mathbf{A}^3\right) = \frac{1}{6}\sum_{i,j,k} A_{ij}A_{jk}A_{ki} \tag{4.5}$$

is the total number of triangles in the graph.

4.1.2 Erdős-Rényi model

The simplest homogeneous Markov ERGM useful for later discussion is the celebrated Erdős-Rényi (ER) model [Erdős and Rényi (1959)] defined by the Hamiltonian

$$H_{ER}(\mathbf{A}; h) = -h\sum_{i,j} A_{ij} = -2hL = -2hN\bar{L}, \tag{4.6}$$

where $N = n(n-1)/2$ is the number of node pairs in the graph, L is the number of links in the graph, and $\bar{L} = L/N$ is called the connectance [Park and Newman (2005)] which is thermodynamically dense on the interval $(0, 1)$ in the sense of Definition 2. Since the Hamiltonian (4.6) depends solely on the number of links, the ER model belongs to the mean field class discussed in Section 2.3. Furthermore, since the Hamiltonian (4.6) is linear in its dynamic variables, the partition function can be computed as

$$\begin{aligned} Z_{ER}(h) = \sum_{\mathbf{A}} \mathrm{e}^{2h\sum_{i<j} A_{ij}} = \sum_{\mathbf{A}}\prod_{i<j} \mathrm{e}^{2hA_{ij}} = \prod_{i<j}\sum_{A_{ij}=0}^{1} \mathrm{e}^{2hA_{ij}} = \prod_{i<j}\left(1+\mathrm{e}^{2h}\right) \\ = \left(1+\mathrm{e}^{2h}\right)^{N}. \end{aligned} \tag{4.7}$$

Therefore, the free energy of the ER model is given by

$$\bar{F}_{ER}(h) = \frac{-1}{N}\log\left(Z_{ER}\right) = -\log\left(1+\mathrm{e}^{2h}\right), \tag{4.8}$$

from which, using (2.8), the expected connectance is obtained as

$$\langle\bar{L}\rangle = -\frac{\partial\bar{F}_{ER}}{\partial(2h)} = \frac{\mathrm{e}^{2h}}{1+\mathrm{e}^{2h}}.$$

Note that using the above expression for the expected connectance and the expression (4.7) for the partition function, the probability distribution (4.1) for the ER model can be written as

$$P(\mathbf{A}|\mathbf{t}) = \frac{\mathrm{e}^{h\sum_{i,j}A_{ij}}}{(1+\mathrm{e}^{2h})^N} = \frac{\mathrm{e}^{2h\sum_{i<j}A_{ij}}}{(1+\mathrm{e}^{2h})^N} = \prod_{i<j}\frac{\mathrm{e}^{2hA_{ij}}}{1+\mathrm{e}^{2h}}$$
$$= \prod_{i<j}\left(\langle\bar{L}\rangle\delta_{A_{ij},1} + (1-\langle\bar{L}\rangle)\delta_{A_{ij},0}\right), \quad (4.9)$$

from which it is clear that all the linking sites in the ER model are statistically independent, and the probability of having a link between any two nodes is determined solely by the expected connectance $\langle\bar{L}\rangle$.

4.1.2.1 Expected degree distribution

The degree distribution in a graph with the adjacency matrix $\mathbf{A}$ is defined as

$$\mathrm{p}(k|\mathbf{A}) = \frac{1}{n}\sum_{i=1}^{n}\delta_{kk_i(\mathbf{A})}, \quad (4.10)$$

where k_i is the degree of a node i. The ensemble average of the degree distribution of the ER model can be computed as

$$\langle\mathrm{p}(k|\mathbf{A})\rangle = \frac{1}{n}\sum_{i=1}^{n}\langle\delta_{kk_i(\mathbf{A})}\rangle = \langle\delta_{kk_l(\mathbf{A})}\rangle,$$

where $k_l(\mathbf{A})$ is the degree of an arbitrary node in the graph, and the last equality comes from the homogeneity of the ER model. Note that due to (4.9) the expression $\langle\delta_{kk_l(\mathbf{A})}\rangle = 1\cdot P(k_l(\mathbf{A}) = k) = P(\sum_{i=1}^{n}A_{il} = k)$ is, essentially, the probability of k successes in $n-1$ Bernoulli trials given by the binomial distribution, so

$$\langle\mathrm{p}(k|\mathbf{A})\rangle = \binom{n-1}{k}\langle\bar{L}\rangle^k(1-\langle\bar{L}\rangle)^{n-1-k}. \quad (4.11)$$

4.1.2.2 Expected local clustering coefficient

The local clustering coefficient is defined as

$$c_i(\mathbf{A}) = \frac{\sum_{j,k} A_{ij}A_{jk}A_{ki}}{\sum_{j,l} A_{ij}A_{il}\,(1-\delta_{jl})} = \frac{\mathcal{T}_i(\mathbf{A})}{\mathcal{S}_2^{(i)}(\mathbf{A})}, \tag{4.12}$$

which for a given node i is the ratio between the number of triangles involving this node $\mathcal{T}_i(\mathbf{A})$ and the number of its 2-stars $\mathcal{S}_2^{(i)}(\mathbf{A})$. Since all the nodes in the ER model are equivalent, the expected LCC is independent of the index i and is given by [Coolen (2016)]

$$\langle c_i(\mathbf{A})\rangle = \langle \bar{L}\rangle \left[1 - \left(1-\langle \bar{L}\rangle\right)^{n-1} - \langle \bar{L}\rangle(n-1)\left(1-\langle \bar{L}\rangle\right)^{n-2}\right] \tag{4.13}$$

for any node.

To quantify clustering at the macroscopic level, the graph-average LCC

$$\bar{c}(\mathbf{A}) = \frac{1}{n}\sum_{i=1}^{n} c_i(\mathbf{A}) \tag{4.14}$$

is commonly used, and its expectation for homogeneous models can be obtained as

$$\langle \bar{c}(\mathbf{A})\rangle = \frac{1}{n}\sum_{i=1}^{n}\langle c_i(\mathbf{A})\rangle = \langle c_l(\mathbf{A})\rangle$$

where l is an arbitrary node, thus for the ER model $\langle \bar{c}\rangle$ is given by the expression (4.13).

Another commonly used measure of clustering is the global clustering coefficient defined as

$$C(\mathbf{A}) = \frac{\mathcal{T}(\mathbf{A})}{\mathcal{S}_2(\mathbf{A})}, \tag{4.15}$$

and it is not hard to see that in a graph with a narrow LCC distribution $\bar{c} \approx C$, whereas a significant mismatch of these two measures of clustering implies large variations of the LCCs in the graph.

4.2 Mean field theory of homogeneous Markov random graphs

In this section we exemplify the use of the mean field theory discussed in Section 2.2.2 on Markov random graphs. As discussed in Section 2.2.2, the mean field theory is a special case of the variational approach in which the variational Hamiltonian is taken to be linear in the dynamic variables $\{A_{ij}|i<j\}$, i.e.

$$H_0(\mathbf{A}) = -\sum_{i<j} h_{ij} A_{ij}.$$

Furthermore, due to the homogeneity, the local mean fields h_{ij} can be assumed to be equal for all sites[4] $h_{ij} \equiv 2h$, reducing the above Hamiltonian to

$$H_0(\mathbf{A}) = -h \sum_{i,j} A_{ij},$$

which is the Hamiltonian of the ER model from Section 4.1.2. Following the variational approach discussed in Section 2.2.1, the upper bound for the specific free energy is computed as

$$\bar{\phi}(\boldsymbol{\tau}, \theta, h) = \bar{F}_0(h) + \frac{1}{N}\langle H(\mathbf{A}) - H_0(\mathbf{A})\rangle_0(\boldsymbol{\tau}, \theta, h), \tag{4.16}$$

where $\bar{F}_0(h)$ and $\langle \dots \rangle_0$ stand for the specific free energy and the expectation computed for the canonical ensemble with the Hamiltonian H_0. Since the Hamiltonian H_0 is identical to that of the ER model (4.6), $\bar{F}_0(h)$ is given by (4.8), i.e.

$$\bar{F}_0(\mathbf{h}) = -\log\left(1 + \mathrm{e}^{2h}\right). \tag{4.17}$$

Computing $\langle H(\mathbf{A}) - H_0(\mathbf{A})\rangle_0 = \langle H(\mathbf{A})\rangle_0 - \langle H_0(\mathbf{A})\rangle_0$ is done as follows

$$\langle H_0(\mathbf{A})\rangle_0 = -h \sum_{i,j} \langle A_{ij}\rangle_0, \tag{4.18}$$

while

$$\langle A_{ij}\rangle_0 = -(1-\delta_{ij})\frac{\partial \bar{F}_0}{\partial(2h)} = (1-\delta_{ij})\langle \bar{L}\rangle_0, \tag{4.19}$$

[4] Which simplifies the intermediate expressions without affecting the final results.

where

$$\langle \bar{L} \rangle_0 = \frac{\mathrm{e}^{2h}}{1+\mathrm{e}^{2h}}, \tag{4.20}$$

and $(1-\delta_{ij})$ is inserted to account for the fact that $A_{ii}=0$. Substituting (4.19) into (4.18) gives

$$\langle H_0(\mathbf{A}) \rangle_0 = -hn(n-1)\langle \bar{L} \rangle_0 = -2Nh\langle \bar{L} \rangle_0. \tag{4.21}$$

Computing $\langle H(\mathbf{A}) \rangle_0$ is also simple due to the factorisation of the GB distribution over sites

$$\begin{aligned}
\langle H(\mathbf{A}) \rangle_0 &= -\sum_{s=1}^{q} \frac{\tau_s}{n^{s-1}s!} \sum_{\substack{i,\mathbf{j} \\ (j_l \neq j_r \forall l,r)}} \langle A_{ij_1} A_{ij_2} \dots A_{ij_s} \rangle_0 - \frac{\theta}{n} \sum_{i,j,k} \langle A_{ij} A_{jk} A_{ki} \rangle_0 \\
&= -\sum_{s=1}^{q} \frac{\tau_s}{n^{s-1}s!} \sum_{\substack{i,\mathbf{j} \\ (j_l \neq j_r \forall l,r)}} \langle A_{ij_1} \rangle_0 \langle A_{ij_2} \rangle_0 \dots \langle A_{ij_s} \rangle_0 - \frac{\theta}{n} \sum_{i,j,k} \langle A_{ij} \rangle_0 \langle A_{jk} \rangle_0 \langle A_{ki} \rangle_0 \\
&= -\sum_{s=1}^{q} \frac{\tau_s}{n^{s-1}s!} \langle \bar{L} \rangle_0^s \sum_{\substack{i,\mathbf{j} \\ (j_l \neq j_r \forall l,r)}} (1-\delta_{ij_1}) \dots (1-\delta_{ij_s}) - \frac{\theta}{n} \langle \bar{L} \rangle_0^3 \sum_{i,j,k} (1-\delta_{ij})(1-\delta_{jk})(1-\delta_{ki}).
\end{aligned}$$

The inner sum in the first term of the above expression can be evaluated as follows

$$\begin{aligned}
\sum_{\substack{i,\mathbf{j} \\ (j_l \neq j_r \forall l,r)}} (1-\delta_{ij_1}) \dots (1-\delta_{ij_s}) &= \sum_{\mathbf{j}(j_l \neq j_r \forall l,r)} \left(\sum_{i=1}^{n} (1-\delta_{ij_1}) \dots (1-\delta_{ij_s}) \right) \\
&= \sum_{\mathbf{j}(j_l \neq j_r \forall l,r)} (n-s) = s!(n-s)\binom{n}{s},
\end{aligned}$$

and the sum in the second term is given by

$$\sum_{i,j,k} (1-\delta_{ij})(1-\delta_{jk})(1-\delta_{ki}) = n^3 - 3n^2 + 2n,$$

which gives

$$\langle H(\mathbf{A}) \rangle_0 = -\sum_{s=1}^{q} \frac{\tau_s (n-s)}{n^{s-1}} \left(\frac{\mathrm{e}^{2h}}{1+\mathrm{e}^{2h}} \right)^s \binom{n}{s} - \theta(n^2-3n+2) \left(\frac{\mathrm{e}^{2h}}{1+\mathrm{e}^{2h}} \right)^3.$$

Combining the above results, we can write the expression for the variational upper bound on the specific free energy as

$$\bar{\phi}(\boldsymbol{\tau}, \theta, h) = -\log\left(1 + \mathrm{e}^{2h}\right) - \sum_{s=1}^{q} \frac{2\tau_s(n-s)}{n^s(n-1)} \binom{n}{s} \left(\frac{\mathrm{e}^{2h}}{1+\mathrm{e}^{2h}}\right)^s - \frac{2\theta(n^2-3n+2)}{n(n-1)} \left(\frac{\mathrm{e}^{2h}}{1+\mathrm{e}^{2h}}\right)^3 + 2h\frac{\mathrm{e}^{2h}}{1+\mathrm{e}^{2h}}, \quad (4.22)$$

and it is easy to show that the stationarity condition

$$\frac{\partial \bar{\phi}(\boldsymbol{\tau}, \theta, h)}{\partial h} = 0 \quad (4.23)$$

is equivalent to

$$h = \sum_{s=1}^{q} \frac{\tau_s s(n-s)}{n^s(n-1)} \binom{n}{s} \left(\frac{\mathrm{e}^{2h}}{1+\mathrm{e}^{2h}}\right)^{s-1} + 3\theta\frac{n-2}{n} \left(\frac{\mathrm{e}^{2h}}{1+\mathrm{e}^{2h}}\right)^2, \quad (4.24)$$

which is the mean field self-consistency equation.

It can be shown that for some values of $(\boldsymbol{\tau}, \theta)$ the equation (4.24) admits several solutions for h in which case, as discussed in Section 2.2.2, the best approximator for the free energy is obtained using the solution $h(\boldsymbol{\tau}, \theta)$ that minimises $\bar{\phi}(\boldsymbol{\tau}, \theta, h)$.

Finally, the MFT predictions for the expectations of the total numbers of triangles (4.5) and k-stars (4.4) can be found using (2.37), i.e.

$$\langle \mathcal{T}(\mathbf{A}) \rangle \approx \langle \mathcal{T}(\mathbf{A}) \rangle_0 = \frac{n^3 - 3n^2 + 2n}{6} \langle \bar{L} \rangle_0^3; \quad (4.25)$$

$$\langle \mathcal{S}_k(\mathbf{A}) \rangle \approx \langle \mathcal{S}_k(\mathbf{A}) \rangle_0 = n\binom{n-1}{k} \langle \bar{L} \rangle_0^k. \quad (4.26)$$

Note that using the fact that h and $\langle \bar{L} \rangle_0$ are in one-to-one correspondence given by (4.20), we can rewrite (4.22) and (4.24) fully in terms of $\langle \bar{L} \rangle_0$, which gives

$$\bar{\phi}(\boldsymbol{\tau}, \theta, \langle \bar{L} \rangle_0) = -\sum_{s=1}^{q} \frac{2\tau_s(n-s)}{n^s(n-1)} \binom{n}{s} \langle \bar{L} \rangle_0^s - 2\theta\frac{n-2}{n} \langle \bar{L} \rangle_0^3 + \langle \bar{L} \rangle_0 \log\langle \bar{L} \rangle_0 + \left(1 - \langle \bar{L} \rangle_0\right) \log\left(1 - \langle \bar{L} \rangle_0\right), \quad (4.27)$$

$$\langle \bar{L} \rangle_0 = \frac{1}{2}\left[1 + \tanh\left(\sum_{s=1}^{q} \frac{s(n-s)}{n^s(n-1)}\binom{n}{s}\tau_s \langle \bar{L}\rangle_0^{s-1} + 3\frac{n-2}{n}\theta\langle \bar{L}\rangle_0^2\right)\right]. \tag{4.28}$$

Since, as discussed in Section 2.2.2.1, the MFT of infinite-dimensional systems is exact in the thermodynamic limit, from (4.25), (4.26) and (4.28) it is clear that the homogeneous Markov ERGM defined by (4.3) is scalable in the sense of Definition 1.

4.3 Finite-size phase transitions in (0,1)-bistability

We will now derive a random network analogue of the result from Section 2.4.4, which gives an explicit expression for the ensemble averages of the observables of Markov ERGMs in the regime with only two deep minima of the microcanonical free energy: one close to $\bar{L} = 0$, and another close to $\bar{L} = 1$. In this regime the fully connected state $\mathbf{A}^C$ (the complete graph) and the fully disconnected state $\mathbf{A}^E$ (the empty graph) accumulate almost all the probability, i.e.

$$P(\mathbf{A}^C) + P(\mathbf{A}^E) \simeq 1, \tag{4.29}$$

where

$$P(\mathbf{A}^C) = \frac{1}{Z}\mathrm{e}^{-H(\mathbf{A}^C)}, \;\; P(\mathbf{A}^E) = \frac{1}{Z}\mathrm{e}^{-H(\mathbf{A}^E)}, \tag{4.30}$$

and

$$Z = \mathrm{e}^{-H(\mathbf{A}^C)} + \mathrm{e}^{-H(\mathbf{A}^E)}.$$

The numbers of stars and triangles in the empty graph are, of course, zero, and computing these observables for the complete graph can be done directly from the definitions (4.4) and (4.5), resulting in

$$\mathcal{S}_k(\mathbf{A}^C) = n\binom{n-1}{k}; \tag{4.31}$$

$$\mathcal{T}(\mathbf{A}^C) = \frac{n}{3}\binom{n-1}{2} = \frac{n^3 - 3n^2 + 2n}{6}. \tag{4.32}$$

Using the expressions (4.31) and (4.32), the expectations of the observables can be computed by definition as

$$\begin{aligned}\langle \mathcal{S}_k \rangle &\simeq \mathcal{S}_k(\mathbf{A}^C) \cdot P(\mathbf{A}^C) + \mathcal{S}_k(\mathbf{A}^E) \cdot P(\mathbf{A}^E) = n\binom{n-1}{k} \cdot P(\mathbf{A}^C) + 0 \cdot P(\mathbf{A}^E) \\ &= n\binom{n-1}{k} \frac{\mathrm{e}^{-H(\mathbf{A}^C)}}{\mathrm{e}^{-H(\mathbf{A}^C)} + \mathrm{e}^{-H(\mathbf{A}^E)}} = \frac{n}{2}\binom{n-1}{k} \left[1 + \tanh \frac{H(\mathbf{A}^E) - H(\mathbf{A}^C)}{2}\right] \\ &= \frac{n}{2}\binom{n-1}{k} \left[1 + \tanh\left(\sum_{s=1}^{q} \frac{\tau_s}{2n^{s-2}}\binom{n-1}{s} + \theta\binom{n-1}{2}\right)\right], \quad (4.33)\end{aligned}$$

and similarly

$$\begin{aligned}\langle \mathcal{T} \rangle &\simeq \mathcal{T}(\mathbf{A}^C) \cdot P(\mathbf{A}^C) + \mathcal{T}(\mathbf{A}^E) \cdot P(\mathbf{A}^E) = n\binom{n-1}{k} \cdot P(\mathbf{A}^C) + 0 \cdot P(\mathbf{A}^E) \\ &= \frac{n^3 - 3n^2 + 2n}{6} \frac{\mathrm{e}^{-H(\mathbf{A}^C)}}{\mathrm{e}^{-H(\mathbf{A}^C)} + \mathrm{e}^{-H(\mathbf{A}^E)}} = \frac{n^3 - 3n^2 + 2n}{12} \left[1 + \tanh \frac{H(\mathbf{A}^E) - H(\mathbf{A}^C)}{2}\right] \\ &= \frac{n^3 - 3n^2 + 2n}{12} \left[1 + \tanh\left(\sum_{s=1}^{q} \frac{\tau_s}{2n^{s-2}}\binom{n-1}{s} + \theta\binom{n-1}{2}\right)\right]. \quad (4.34)\end{aligned}$$

Note that the above derivation does not rely on the mean field approximation, which predicts discontinuity instead of a smooth transition.

4.4 Homogeneous mean field ERGM

Homogeneous mean field ERGM (or simply "MF model") is defined by the Hamiltonian

$$H_{MF}(\mathbf{A}) = -\sum_{k=1}^{q} \frac{t_k}{(2N)^{k-1}} \Big(\sum_{i,j} A_{ij}\Big)^k = -(2N)\sum_{k=1}^{q} t_k \left(\frac{L}{N}\right)^k, \quad (4.35)$$

where $N = n(n-1)/2$ is the maximum number of links in a simple undirected graph of n nodes, and $L = \sum_{i<j} A_{ij}$ is the number of links in the graph.

4.4.1 Thermodynamic solution

Following the discussion from Section 2.1.6, the partition function of the MF model can be expressed as

$$Z_n(\mathbf{t},\beta) = \sum_{\mathbf{A}} \mathrm{e}^{-\beta H_{MF}(\mathbf{A})} = \sum_{L=0}^{N} g_n(L)\mathrm{e}^{2N\beta\sum_{k=1}^{q} t_k\left(\frac{L}{N}\right)^k} = \sum_{L=0}^{N} \mathrm{e}^{-\beta\mathcal{F}_n(L;\mathbf{t},\beta)}, \tag{4.36}$$

where

$$\mathcal{F}_n(L;\mathbf{t},\beta) = \frac{-1}{\beta}\left[\ln g_n(L) + 2\beta N\sum_{k=1}^{q} t_k\left(\frac{L}{N}\right)^k\right] \tag{4.37}$$

is the microcanonical free energy of the model, in which

$$g_n(L) = \binom{N}{L} \tag{4.38}$$

is the number of simple undirected graphs of N node pairs and exactly L edges. Evaluating the factorials in the above binomial coefficient using the Stirling's formula gives the following expression for the microcanonical entropy

$$\begin{aligned}\mathcal{S}_n(L) \equiv \ln g_n(L) = \ln\binom{N}{L} &= \ln(N!) - \ln[(N-L)!] - \ln(L!)\\ &\underset{N,L\to\infty}{=} N\ln N - N - (N-L)\ln(N-L) + N - L - L\ln L + L + \mathcal{O}(\log N + \log L)\\ &= -N\left((1-\frac{L}{N})\ln(1-\frac{L}{N}) + \frac{L}{N}\ln\frac{L}{N}\right) + \mathcal{O}(\log N + \log L).\end{aligned} \tag{4.39}$$

To prevent the extensive properties from diverging in the thermodynamic limit, they need to be rescaled as discussed in Section 2.1.4, which gives the connectance

$$\bar{L} = \frac{L}{N}, \tag{4.40}$$

the specific microcanonical entropy

$$\bar{\mathcal{S}}_n(\bar{L}) \equiv \frac{\mathcal{S}_n(\bar{L})}{N} = -(1-\bar{L})\ln(1-\bar{L}) - \bar{L}\ln\bar{L} + \mathcal{O}\left(\frac{\log N + \log\bar{L}}{N}\right) \tag{4.41}$$

the specific microcanonical internal energy

$$\bar{\mathcal{E}}_n(\bar{L};\mathbf{t}) = \frac{\mathcal{E}_n(\bar{L};\mathbf{t})}{N} = \frac{H_{MF}(\bar{L};\mathbf{t})}{N} = -2\sum_{k=1}^{q} t_k \bar{L}^k, \tag{4.42}$$

and the specific microcanonical free energy

$$\bar{\mathcal{F}}_n(\bar{L};\mathbf{t},\beta) = \frac{\mathcal{F}_n(\bar{L};\mathbf{t},\beta)}{N} = \bar{\mathcal{E}}_n(\bar{L};\mathbf{t}) - T\bar{\mathcal{S}}_n(\bar{L}), \tag{4.43}$$

where $T = 1/\beta$ is the temperature. Thus, in the thermodynamic limit the SMFE is given by

$$\bar{\mathcal{F}}(\bar{L};\mathbf{t},\beta) = -2\sum_{k=1}^{q} t_k \bar{L}^k + T\left[(1-\bar{L})\ln(1-\bar{L}) + \bar{L}\ln\bar{L}\right]. \tag{4.44}$$

As discussed in Section 2.1.6, when $\beta N \to \infty$ the above microcanonical properties coincide with their canonical counterparts on the actual thermodynamic solution given by

$$\bar{L}(\mathbf{t}) = \operatorname*{argmin}_{\bar{L}} \bar{\mathcal{F}}_n(\bar{L};\mathbf{t},\beta).$$

It will be shown shortly that $\bar{L}(\mathbf{t})$ is indeed intensive, meaning that $L \underset{N\to\infty}{=} \mathcal{O}(N)$, which justifies the use of the Stirling's approximation for $L!$ in the expression (4.39) in the thermodynamic limit.

Note that, unlike the general case discussed in Section 2.1.5, all the above properties depend only on $\bar{L}$, even though there may be any number $q \geq 1$ of the observables conjugated to the parameters $\mathbf{t}$. This is a simple consequence of the fact that knowing $\bar{L}$ fixes the values of all observables due to the mean field nature of the model.

From the expression (4.40), it is clear that $\bar{L}$ is thermodynamically dense on the interval $(0,1)$ in the sense of Definition 2, which allows minimising the specific microcanonical free energy using the stationarity condition

$$\frac{d\bar{\mathcal{F}}(\bar{L};\mathbf{t},\beta)}{d\bar{L}} = 0. \tag{4.45}$$

From (4.43), (4.41) and (4.42)

$$\frac{d\bar{\mathcal{F}}(\bar{L};\mathbf{t},\beta)}{d\bar{L}} = -2\sum_{k=1}^{q} k t_k \bar{L}^{k-1} + T\ln\frac{\bar{L}}{1-\bar{L}}, \tag{4.46}$$

which after basic manipulations gives the stationarity condition (4.45) as

$$\bar{L} = \frac{1}{2}\left[1 + \tanh\left(\beta \sum_{k=1}^{q} k t_k \bar{L}^{k-1}\right)\right]. \tag{4.47}$$

As discussed in Section 2.1.6, the equation (4.47) is the thermodynamic equation of state which defines the dependence of the connectance on the model's parameters.

Finally, in terms of the specific microcanonical free energy, the expression (4.36) for the partition function reads as

$$Z_n(\mathbf{t}, \beta) = N \sum_{m=0}^{N} \Delta\bar{L} \mathrm{e}^{-\beta N \bar{\mathcal{F}}_n(m\Delta\bar{L}; \mathbf{t}, \beta)}, \tag{4.48}$$

where $\Delta\bar{L} = 1/N \underset{N\to\infty}{\to} 0$. Treating the above expression as a Riemann sum, for large networks it can be recast as the following integral

$$Z_n(\mathbf{t}, \beta) \underset{n\to\infty}{\sim} N \int_0^1 \mathrm{e}^{-\beta N \bar{\mathcal{F}}(\bar{L}; \mathbf{t}, \beta)} d\bar{L}, \tag{4.49}$$

which can be evaluated using the Laplace's approximation by expanding the SMFE around its global minimum $\bar{L}_0$ as

$$\bar{\mathcal{F}}(\bar{L}; \mathbf{t}, \beta) = \bar{\mathcal{F}}(\bar{L}_0; \mathbf{t}, \beta) + \bar{\mathcal{F}}''(\bar{L}_0; \mathbf{t}, \beta)(\bar{L} - \bar{L}_0)^2 + \mathcal{O}\left((\bar{L} - \bar{L}_0)^3\right). \tag{4.50}$$

The first-order term in the above expansion is absent due to the fact that $\bar{L}_0$ is a stationary point of the SMFE. Furthermore, the second and higher-order terms in (4.50) can be neglected as long as the corresponding derivatives are finite, which gives

$$Z_n(\mathbf{t}, \beta) \underset{N\to\infty}{\sim} N \int_0^1 \mathrm{e}^{-\beta N \bar{\mathcal{F}}(\bar{L}_0(\mathbf{t},\beta); \mathbf{t}, \beta)} d\bar{L} = N \mathrm{e}^{-\beta N \bar{\mathcal{F}}(\bar{L}_0(\mathbf{t},\beta); \mathbf{t}, \beta)}. \tag{4.51}$$

As discussed in Section 2.1.3, the specific free energy in the thermodynamic limit is obtained from (4.51) as

$$\bar{F}(\mathbf{t}, \beta) = \lim_{n\to\infty} \frac{-1}{\beta N} \ln Z_n(\mathbf{t}, \beta) = \bar{\mathcal{F}}\big(\bar{L}_0(\mathbf{t}, \beta); \mathbf{t}, \beta\big), \tag{4.52}$$

which is consistent with the results from Section 2.1.6.

Note that, as discussed in Section 2.1.9, $\bar{\mathcal{F}}''\big(\bar{L}_0(\mathbf{t}, \beta); \mathbf{t}, \beta\big) = -\chi_{\bar{L}_0}(\mathbf{t}, \beta)$ and when this susceptibility diverges, which usually happens at phase transitions, the second-order term in the expansion

(4.50) becomes important in the integral (4.49). However, in this work we deal directly with the observables' expectations for which at phase transitions we use the methods discussed in Section 2.4.4 and Section 2.4.5, thus computing the partition function using the Laplace's (saddle point) approximation in full generality is not needed.

4.4.2 Differential identities for the MF model

Another approach to the problem comes from the method of differential identities [Barra, Di Lorenzo, Guerra and Moro (2014); Agliari et al. (2016); De Matteis et al. (2018); Lorenzoni and Moro (2019)] based on the fact that the partition function[5]

$$Z_n(\mathbf{t}) = \sum_{\mathbf{A}} \mathrm{e}^{-H_{MF}(\mathbf{A})}, \tag{4.53}$$

satisfies a hierarchy of linear partial differential equations (PDEs) of the form

$$\frac{\partial Z_n}{\partial t_k} = \nu^{k-1} \frac{\partial^k Z_n}{\partial t_1^k}, \qquad k = 1, 2, \ldots, q. \tag{4.54}$$

where $\nu = (2N)^{-1}$. The above hierarchy is referred to as the *heat hierarchy*, since its first non-trivial equation is the heat equation

$$\frac{\partial Z_n}{\partial t_2} = \nu \frac{\partial^2 Z_n}{\partial t_1^2},$$

and it is immediate to check that it is compatible, meaning that

$$\frac{\partial}{\partial t_k}\left(\frac{\partial Z_n}{\partial t_l}\right) = \frac{\partial}{\partial t_l}\left(\frac{\partial Z_n}{\partial t_k}\right) \quad \forall l, k \in \{1, \ldots, q\}.$$

The partition function is given by the solution of the hierarchy (4.54) matching the initial condition

$$Z_{n,0}(t_1) \equiv Z_n|_{t_k=0 \; \forall k>1} = \sum_{\mathbf{A}} \mathrm{e}^{t_1 \sum_{i,j} A_{ij}}, \tag{4.55}$$

which corresponds to the ER model discussed in Section 4.1.2. However, since proceeding by finding the partition function is impractical due to its exponential growth with n, the thermodynamic asymptotics are obtained by performing the inverse Cole-Hopf transformation, which introduces

[5] As discussed in Section 2.4.8, we set $T = 1$.

a variable analogous to the specific free energy

$$\Phi_n = \nu \log Z_n. \tag{4.56}$$

Rewriting the heat hierarchy (4.54) in terms of Φ_n gives the following hierarchy of nonlinear viscous equations

$$\frac{\partial \Phi_n}{\partial t_k} = \nu^k \mathfrak{P}_k \left[\frac{1}{\nu} \frac{\partial \Phi_n}{\partial t_1} \right], \qquad k = 1, 2, \ldots, q \tag{4.57}$$

where $\mathfrak{P}_k[f]$ are defined recursively as follows

$$\mathfrak{P}_{k+1}[f] = \frac{\partial \mathfrak{P}_k[f]}{\partial t_1} + f \mathfrak{P}_k[f], \qquad \mathfrak{P}_0[f] = 1.$$

Assuming that $\Phi_n(\mathbf{t})$ is a solution of the hierarchy (4.57), its derivatives

$$\frac{\partial \Phi_n(\mathbf{t})}{\partial t_k} = \frac{\sum_{\mathbf{A}} \left[\bar{L}(\mathbf{A})\right]^k \mathrm{e}^{-H(\mathbf{A})}}{Z_n} = \langle \bar{L}^k \rangle_n, \quad k = 1, 2, \ldots, q \tag{4.58}$$

provide an effective way of calculating the connectance and its higher moments up to q.

The equations for $\langle \bar{L} \rangle_n$ follow from (4.57) by differentiating both sides w.r.t. t_1, which results in the so-called *Burgers' hierarchy*. For instance, the first three nontrivial equations of the hierarchy read as

$$\begin{aligned}
\frac{\partial \langle \bar{L} \rangle_n}{\partial t_2} &= \frac{\partial}{\partial t_1} \left(\langle \bar{L} \rangle_n^2 + \nu \frac{\partial \langle \bar{L} \rangle_n}{\partial t_1} \right); \\
\frac{\partial \langle \bar{L} \rangle_n}{\partial t_3} &= \frac{\partial}{\partial t_1} \left(\langle \bar{L} \rangle_n^3 + 3\nu \langle \bar{L} \rangle_n \frac{\partial \langle \bar{L} \rangle_n}{\partial t_1} + \nu^2 \frac{\partial^2 \langle \bar{L} \rangle_n}{\partial t_1^2} \right); \\
\frac{\partial \langle \bar{L} \rangle_n}{\partial t_4} &= \frac{\partial}{\partial t_1} \left(\langle \bar{L} \rangle_n^4 + 6\nu \langle \bar{L} \rangle_n^2 \frac{\partial \langle \bar{L} \rangle_n}{\partial t_1} + 3\nu^2 \left(\frac{\partial \langle \bar{L} \rangle_n}{\partial t_1} \right)^2 + 4\nu^2 \langle \bar{L} \rangle_n \frac{\partial^2 \langle \bar{L} \rangle_n}{\partial t_1^2} + \nu^3 \frac{\partial^3 \langle \bar{L} \rangle_n}{\partial t_1^3} \right).
\end{aligned} \tag{4.59}$$

To study the system in the thermodynamic limit, we assume that Φ_n is intensive, i.e.

$$\Phi_n = \Phi + \mathcal{O}(\nu), \tag{4.60}$$

and substitute it into (4.57), which at the leading order gives the following hierarchy of the

Hamilton-Jacobi equations

$$\frac{\partial \Phi}{\partial t_k} = \left(\frac{\partial \Phi}{\partial t_1}\right)^k, \qquad k = 1, 2, \ldots, q. \tag{4.61}$$

The expansion (4.60) implies that $\langle \bar{L} \rangle_n = \langle \bar{L} \rangle + \mathcal{O}(\nu)$, and in the thermodynamic limit $\langle \bar{L} \rangle$ fulfils the following hierarchy of hyperbolic PDEs known as the *Hopf hierarchy*

$$\frac{\partial \langle \bar{L} \rangle}{\partial t_k} = \frac{\partial \langle \bar{L} \rangle^k}{\partial t_1}, \qquad k = 1, \ldots, q \tag{4.62}$$

whenever t_1 derivatives of $\langle \bar{L} \rangle$ are bounded so that the viscous terms in (4.57) can be neglected. The general solution of the hierarchy (4.62) has the form

$$\sum_{k=1}^{q} k \langle \bar{L} \rangle^{k-1} t_k = f\left(\langle \bar{L} \rangle\right), \tag{4.63}$$

where the function f is specified by the initial condition.

The general solution of (4.61) obtained by integration along the characteristics (on which $\langle \bar{L} \rangle$ is constant) is given by

$$\Phi(\mathbf{t}) = \sum_{k=1}^{q} \langle \bar{L} \rangle^k t_k + g(\langle \bar{L} \rangle), \tag{4.64}$$

where the function g is specified by the initial condition.

As mentioned above, the initial condition (4.55) corresponds to the ER model for which the partition function is evaluated in (4.7), so

$$Z_{n,0} = \left(1 + \mathrm{e}^{2t_1}\right)^N.$$

Therefore, the initial condition for Φ_n is given by

$$\Phi_{n,0}(t_1) = \nu \log\left(Z_{n,0}\right) = \frac{1}{2} \log\left(1 + \mathrm{e}^{2t_1}\right), \tag{4.65}$$

from which the initial connectance is obtained as

$$\langle \bar{L} \rangle_{n,0} = \frac{\partial \Phi_{n,0}}{\partial t_1} = \frac{\mathrm{e}^{2t_1}}{1 + \mathrm{e}^{2t_1}}. \tag{4.66}$$

Note that $\Phi_{n,0}$ and $\langle \bar{L} \rangle_{n,0}$ do not depend on n, hence, the initial conditions for the hierarchies (4.61) and (4.62) are also given by (4.65) and (4.66) respectively, which determines the arbitrary functions from (4.63) and (4.64) as

$$f(z) = \frac{1}{2} \log \frac{z}{1-z}; \tag{4.67}$$

$$g(z) = -\frac{1}{2} \log \left[z^z \left(1-z\right)^{1-z} \right]. \tag{4.68}$$

Combining (4.63) and (4.67) gives the thermodynamic equation of state

$$\langle \bar{L} \rangle = \frac{1}{2} \left[1 + \tanh \left(\sum_{k=1}^{q} k t_k \langle \bar{L} \rangle^{k-1} \right) \right]. \tag{4.69}$$

Combining (4.64) and (4.68) gives the solution to (4.61) with the initial condition (4.65)

$$\Phi(\mathbf{t}) = \sum_{k=1}^{q} \langle \bar{L} \rangle^k t_k - \frac{1}{2} \log \left[\langle \bar{L} \rangle^{\langle \bar{L} \rangle} \left(1 - \langle \bar{L} \rangle\right)^{1-\langle \bar{L} \rangle} \right], \tag{4.70}$$

where $\langle \bar{L} \rangle$ is the function of $\mathbf{t}$ implicitly defined by (4.69).

The specific free energy of the MF model can be easily obtained from Φ as

$$\bar{F} = -2\Phi = -2 \sum_{k=1}^{q} t_k \langle \bar{L} \rangle^k + \log \left[\langle \bar{L} \rangle^{\langle \bar{L} \rangle} \left(1 - \langle \bar{L} \rangle\right)^{\left(1-\langle \bar{L} \rangle\right)} \right]. \tag{4.71}$$

4.4.2.1 Travelling wave solution

As discussed above, the large n solution of the hierarchy (4.57) is given by (4.70) if $\langle \bar{L} \rangle$ is p-smooth in t_1, which is not always the case due to the gradient catastrophe occurring in the Hopf hierarchy (4.62). It turns out that in certain regions of $\mathbf{t}$-space the equation (4.69) admits multiple solutions for $\langle \bar{L} \rangle$, while the solution of the actual hierarchy (4.57) is unique due to the presence of the viscous terms, which become significant when t_1-derivatives diverge. In this section we find the large $t_k,\ k \in \{2, ..., p\}$ asymptotics for the actual solution of (4.57), which replace the multivaluedness of (4.69) by a shock wave. For the sake of simplicity, we present the explicit calculations for the case of $p = 3$.

As may be expected, the equation (4.69) implies that

$$\lim_{t_1 \to -\infty} \langle \bar{L} \rangle = 0, \qquad \lim_{t_1 \to \infty} \langle \bar{L} \rangle = 1. \tag{4.72}$$

This is intuitive because the parameter t_1 acts as an external field enhancing or preventing the occurrence of links by being largely positive or negative respectively. Substituting into (4.59) the "travelling wave" solution of the form

$$\langle \bar{L} \rangle_n = \lambda(\theta), \qquad \theta = t_1 + c_2 t_2 + c_3 t_3, \tag{4.73}$$

and integrating once gives the following system of ordinary differential equations (ODEs)

$$c_2 \lambda = \lambda^2 + \nu \lambda' + k_0; \tag{4.74}$$

$$c_3 \lambda = \lambda^3 + 3\nu \lambda \lambda' + \nu^2 \lambda'' + l_0, \tag{4.75}$$

where $\lambda' = d\lambda / d\theta$. The boundary conditions (4.72) imply

$$c_2 = c_3 = 1, \qquad k_0 = l_0 = 0.$$

The equation (4.74) can be solved by separation, which gives

$$\lambda(\theta) = \frac{1}{2} \left[1 + \tanh \left(\frac{1}{2\nu} (\theta - c) \right) \right], \tag{4.76}$$

and this solution is compatible with the equation (4.75). As clear from (4.66), $\langle \bar{L} \rangle_n (\mathbf{t} = \mathbf{0}) = 1/2$, from which $c = 0$, and therefore

$$\langle \bar{L} \rangle (\mathbf{t}) = \frac{1}{2} \left[1 + \tanh \left(\frac{1}{2\nu} (t_1 + t_2 + t_3) \right) \right], \tag{4.77}$$

which smoothly connects the asymptotic macrostates specified by the boundary conditions (4.72).

4.4.3 Graphical analysis

An analysis similar to the one from Section 2.4.3.2 can be used to obtain valuable insights about the solutions of the equation of state (4.47). For this purpose, we rewrite the equation of state

(4.47) in the equivalent from

$$\frac{d\bar{\mathcal{F}}(\bar{L};\mathbf{t},\beta)}{d\bar{L}} \equiv \bar{\mathcal{F}}'(\bar{L};\mathbf{t},\beta) = \mathcal{A}(\bar{L};T) - \mathcal{P}(\bar{L};\mathbf{t}) = 0, \tag{4.78}$$

where

$$\mathcal{A}(\bar{L};T) \equiv 2T\,\mathrm{artanh}\left(2\bar{L}-1\right) = T\ln\frac{\bar{L}}{1-\bar{L}}; \tag{4.79}$$

$$\mathcal{P}(\bar{L};\mathbf{t}) \equiv 2\sum_{k=1}^{q} k t_k \bar{L}^{k-1}. \tag{4.80}$$

From the expression (4.78) it is clear that the intersections of the plots of $\mathcal{A}(\bar{L};T)$ and $\mathcal{P}(\bar{L};\mathbf{t})$ correspond to the solutions of the equation of state (4.47). Furthermore, the different types of intersections lead to the different types of the solutions, as clear from the following

Lemma 1. *A solution λ of the equation of state (4.78) corresponds to a (meta)stable macrostate iff there exists $\Delta > 0$ such that for all $\delta \in (0,\Delta)$, $\bar{\mathcal{F}}'(\lambda-\delta;\mathbf{t},\beta) < 0$ while $\bar{\mathcal{F}}'(\lambda+\delta;\mathbf{t},\beta) > 0$.*

Proof. From the explicit expression for the specific microcanonical free energy (SMFE) (4.44), it is clear that its $p+1$-th derivative is given by[6]

$$\frac{d^{p+1}\bar{\mathcal{F}}(\bar{L};\mathbf{t},\beta)}{d\bar{L}^{p+1}} = \frac{d^{p}t_1(\bar{L})}{d\bar{L}^{p}} = \begin{cases} \dfrac{T}{2}\left(\dfrac{(-1)^{p-1}}{\bar{L}^p} + \dfrac{1}{(1-\bar{L})^p}\right) - \displaystyle\sum_{k=p+1}^{q} \frac{k!}{(q-p-1)!} t_k \bar{L}^{k-p-1}, & 1 \le p \le q; \\ \dfrac{T}{2}\left(\dfrac{(-1)^{p-1}}{\bar{L}^p} + \dfrac{1}{(1-\bar{L})^p}\right), & p > q, \end{cases} \tag{4.81}$$

which means that $\bar{\mathcal{F}}(\bar{L};\mathbf{t},\beta)$ has a non-identically zero Taylor expansion around the macrostate $\lambda \in (0,1)$

$$\bar{\mathcal{F}}(\lambda+\delta;\mathbf{t},\beta) = \bar{\mathcal{F}}(\lambda;\mathbf{t},\beta) + \frac{\bar{\mathcal{F}}^{(k)}(\lambda;\mathbf{t},\beta)}{k!}\delta^k + \mathcal{O}(\delta^{k+1}), \tag{4.82}$$

where $k > 1$ since λ is assumed to be a solution of the equation of state (4.78).

Suppose that the solution λ is (meta)stable, which, according to Definition 3 (4), means that it corresponds to a (local) minimum of $\bar{\mathcal{F}}(\bar{L};\mathbf{t},\beta)$, which implies that k is even and $\bar{\mathcal{F}}^{(k)}(\lambda;\mathbf{t},\beta) >$

[6] In what follows $\bar{\mathcal{F}}^{(k)}(\bar{L};\mathbf{t},\beta)$ stands for the k-th derivative of $\bar{\mathcal{F}}$ with respect to $\bar{L}$.

0. This, in turn, means that the first nonzero term in the Taylor expansion of the derivative

$$\bar{\mathcal{F}}'(\lambda+\delta;\mathbf{t},\beta)=\frac{\bar{\mathcal{F}}^{(k)}(\lambda;\mathbf{t},\beta)}{(k-1)!}\delta^{k-1}+\mathcal{O}(\delta^k) \tag{4.83}$$

is of odd order $k-1$ with a positive coefficient, from which it is clear that the desired property ($\bar{\mathcal{F}}'(\lambda-\delta;\mathbf{t},\beta)<0$ while $\bar{\mathcal{F}}'(\lambda+\delta;\mathbf{t},\beta)>0$) is, indeed, valid as long as $\delta>0$ is sufficiently small.

Conversely, if there exists $\Delta>0$ such that for all $\delta\in(0,\Delta)$ $\bar{\mathcal{F}}'(\lambda-\delta;\mathbf{t},\beta)<0$ while $\bar{\mathcal{F}}'(\lambda+\delta;\mathbf{t},\beta)>0$, then it is clear that the Taylor expansion (4.83) should start from the term with an odd power and positive coefficient, thus k is even and $\bar{\mathcal{F}}^{(k)}(\lambda;\mathbf{t},\beta)>0$ which, as clear from (4.82), means that $\bar{\mathcal{F}}(\lambda;\mathbf{t},\beta)$ is a (local) minimum, so the macrostate λ is (meta)stable. □

From Lemma 1, it follows that when the plots of $\mathcal{A}$ and $\mathcal{P}$ intersect in a way that before the intersection $\mathcal{A}<\mathcal{P}$ and after the intersection $\mathcal{A}>\mathcal{P}$, then the macrostate corresponding to such solution is (meta)stable. If this is not the case, the corresponding macrostate is unstable (Fig. 4.1). For short, in what follows we will sometimes refer to the solutions corresponding to (meta)stable (unstable, regular, singular, critical, spinodal) macrostates as (meta)stable (unstable, regular, singular, critical, spinodal) solutions of the equation of state (4.47).

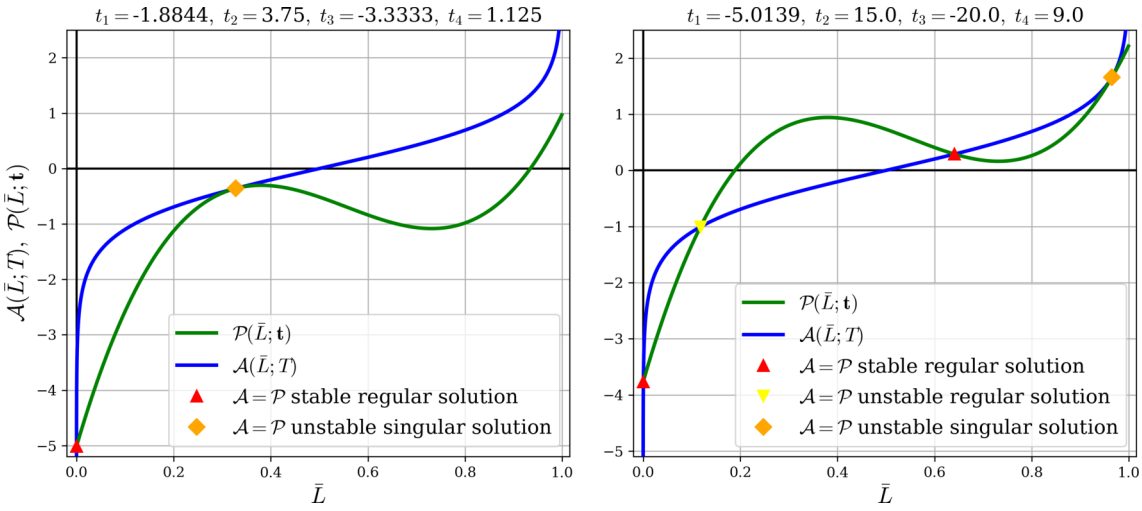

Fig. 4.1: Appearance of the regular and singular solutions of the equation of state (4.47) in the graphical analysis for the two MF4 models with different parameters. Intersections at which the curves are transversal to each other correspond to regular macrostates, while the intersections at which the curves are tangential correspond to singular macrostates, and only the intersections at which $\mathcal{A}(\bar{L};T)-\mathcal{P}(\bar{L};\mathbf{t})$ changes its sign from negative to positive as $\bar{L}$ increases correspond to (meta)stable macrostates.

4.4.4 Low-temperature behaviour

As discussed in Section 2.4.3.3, in a Curie-Weiss model with $\beta J \gg 1$, the specific magnetisation of all (meta)stable macrostates is very close to either -1 or 1. This is the consequence of the low-order interactions, and similar low-temperature behaviour can, of course, be exhibited by the MF model (Fig. 4.8), although using the graphical analysis, it is easy to show that, in general, the low-temperature behaviour of the MF model can be very rich. To see this, consider the expression (4.79) as $T \to 0$. Since

$$\lim_{T\to 0} \mathcal{A}(\bar{L}; T) = 0 \text{ for all } \bar{L} \in (0, 1);$$
$$\lim_{\bar{L}\to 0} \mathcal{A}(\bar{L}; T) = -\infty \text{ for all } T > 0;$$
$$\lim_{\bar{L}\to 1} \mathcal{A}(\bar{L}; T) = +\infty \text{ for all } T > 0,$$

$\mathcal{A}(\bar{L}; T \to 0)$ looks like an "inverted Heaviside function" (Fig. 4.2, Fig. 4.3); thus the solutions of the equation of state (4.78) are given by the roots of the polynomial $\mathcal{P}(\bar{L}; \mathbf{t})$ on the interval $(0, 1)$ and the intersections at the boundaries $\bar{L} = 0$ (if $\mathcal{P}(0; \mathbf{t}) < 0$) and $\bar{L} = 1$ (if $\mathcal{P}(1; \mathbf{t}) > 0$). Since, as clear from (4.80), $\mathcal{P}(\bar{L}; \mathbf{t})$ is a generic polynomial of a degree up to $q-1$, it may have a number of roots on the interval $(0, 1)$, and the roots, at which $\mathcal{P}(\bar{L}; \mathbf{t})$ changes its sign from negative to positive, correspond to the (meta)stable solutions of the equation of state (4.47) that exist even at extremely low temperatures[7].

4.4.5 Singularities

According to Definition 6, a macrostate λ is singular if

$$\bar{\mathcal{F}}''(\lambda; \mathbf{t}, \beta) = \mathcal{A}'(\lambda; T) - \mathcal{P}'(\lambda; \mathbf{t}) = 0, \tag{4.84}$$

which means that in the graphical analysis the singular solutions of the equation of state (4.47) correspond to the intersections of the plots of $\mathcal{A}(\bar{L}; T)$ and $\mathcal{P}(\bar{L}; \mathbf{t})$ at which the curves have the same slope as shown in Fig. 4.1.

[7] More on this in Section 4.6.1.3.

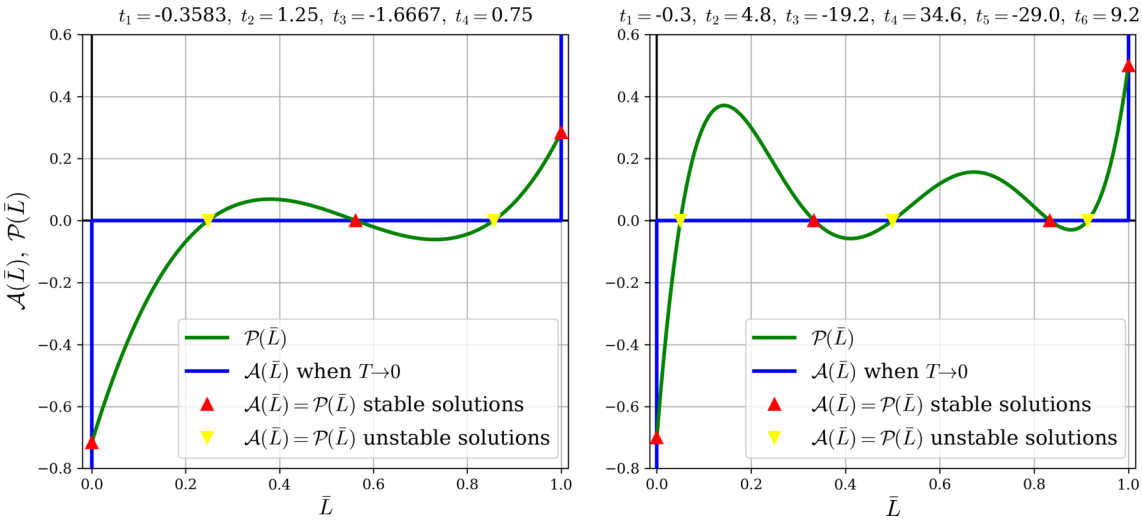

Fig. 4.2: Realisations of the maximal numbers of solutions in the MF models of order four (left) and order six (right). The polynomial $\mathcal{P}$ of the model of even order q has an odd degree $q-1$, and it is easy to see that the maximal number of solutions is always achieved when there are $q-1$ roots inside the $(0,1)$-domain and two solutions on the boundaries ($\bar{L}=0$ and $\bar{L}=1$). This, essentially, means that whenever a model of even order reaches its highest number of solutions, the (meta)stable connectance bands corresponding to the empty and complete graphs are always narrow, as can be seen in Fig. 4.4 and Fig. 4.5.

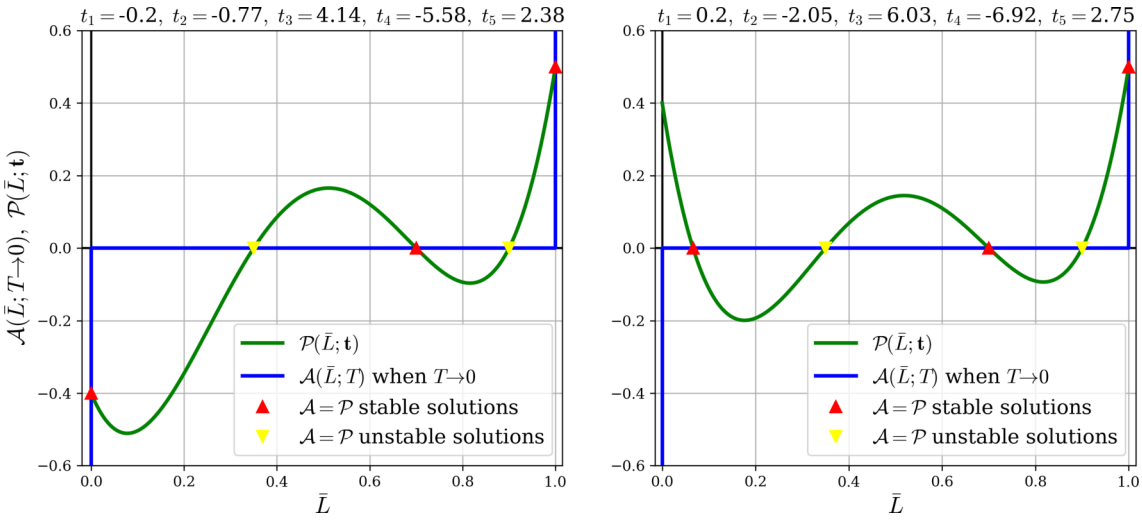

Fig. 4.3: Two distinct realisations of the maximal number of solutions in the 5-th order model for which $\mathcal{P}(\bar{L})$ is a polynomial of an even degree. The situation on the left plot is similar to what is observed in Fig. 4.2 for the models of even order, apart from the fact that not all the roots of $P(\bar{L})$ belong to $(0,1)$-interval. As can be seen on the right plot, the polynomial of even degree having its maximal number of roots on $\bar{L} \in (0,1)$ can only have one intersection with $\mathcal{A}(\bar{L})$ on the boundary of the domain.

Substituting the expressions (4.79) and (4.80) to (4.84) gives the singularity condition as

$$\bar{\mathcal{F}}''(\bar{L}; \mathbf{t}, \beta) = \frac{T}{\bar{L}(1-\bar{L})} - 2\sum_{k=2}^{q} t_k k(k-1)\bar{L}^{k-2} = 0. \tag{4.85}$$

Note that the equation of state (4.47) can be written in the equivalent form

$$t_1(\bar{L}) = \frac{T}{2}\log\frac{\bar{L}}{1-\bar{L}} - \sum_{k=2}^{q} k t_k \bar{L}^{k-1}, \tag{4.86}$$

in which t_1 is treated as a function of $\bar{L} \in (0,1)$ and it is easy to check that the singularity condition (2.31) is equivalent to

$$\frac{dt_1}{d\bar{L}}(\lambda) = \frac{1}{\chi_{\bar{L}}(\lambda)} = 0, \tag{4.87}$$

which is consistent with (2.31) and means that the susceptibility $\chi_{\bar{L}}$ diverges on singular solutions.

Definition 14. *A singular macrostate λ is said to be of order p if $\bar{\mathcal{F}}^{(m+1)}(\lambda;\mathbf{t},\beta) = 0$ for all $m \leq p$ while $\bar{\mathcal{F}}^{(p+2)}(\lambda;\mathbf{t},\beta) \neq 0$.*

Theorem 1. *Singular macrostates of odd orders are spinodal.*

Proof. As clear from (4.81), the microcanonical free energy $\bar{\mathcal{F}}(\bar{L};\mathbf{t},\beta)$ has a nonzero Taylor expansion around any macrostate $\lambda \in (0,1)$

$$\bar{\mathcal{F}}(\lambda+\delta;\mathbf{t},\beta) = \bar{\mathcal{F}}(\lambda;\mathbf{t},\beta) + \frac{\bar{\mathcal{F}}^{(k)}(\lambda;\mathbf{t},\beta)}{k!}\delta^k + \mathcal{O}(\delta^{k+1}), \tag{4.88}$$

where due to (4.78) and (4.84), $k > 2$ since λ is assumed to be a singular solution of the equation of state. Assume that the order of the singularity is an odd number p, so (from Definition 14) $k = p+2$ is also odd, thus from (4.88) it is clear that the macrostate λ is not a (local) minimum of the specific microcanonical free energy, thus, according to Definition 3, Definition 4 and Definition 5, it is unstable. Since the macrostate λ is singular and unstable, it is spinodal according to Definition 9. □

Theorem 2. *A singular macrostate of even order p is spinodal if $\bar{\mathcal{F}}^{(p+2)}(\bar{L};\mathbf{t},\beta) < 0$ and critical otherwise.*

Proof. As clear from (4.81), the microcanonical free energy $\bar{\mathcal{F}}(\bar{L};\mathbf{t},\beta)$ has a nonzero Taylor ex-

pansion around any macrostate $\lambda \in (0,1)$

$$\bar{\mathcal{F}}(\lambda+\delta;\mathbf{t},\beta) = \bar{\mathcal{F}}(\lambda;\mathbf{t},\beta) + \frac{\bar{\mathcal{F}}^{(k)}(\lambda;\mathbf{t},\beta)}{k!}\delta^k + \mathcal{O}(\delta^{k+1}), \tag{4.89}$$

where due to (4.78) and (4.84), $k > 2$ since λ is assumed to be a singular solution of the equation of state. Assume that the order of the singularity is an even number p, so (from Definition 14) $k = p + 2$ is also even, thus from (4.88) it is clear that the macrostate λ is an extremum of the specific microcanonical free energy.

If $\bar{\mathcal{F}}^{(k)}(\lambda;\mathbf{t},\beta) < 0$ then, as clear from (4.89), the macrostate λ corresponds to a (local) maximum of the specific microcanonical free energy, thus, according to Definition 3, Definition 4 and Definition 5, it is unstable. Since the macrostate λ is singular and unstable, it is spinodal according to Definition 9.

If $\bar{\mathcal{F}}^{(k)}(\lambda;\mathbf{t},\beta) < 0$ then, as clear from (4.89), the macrostate λ corresponds to a (local) minimum, thus, according to Definition 3 (4), it is (meta)stable. Since the macrostate λ is singular and (meta)stable, it is critical according to Definition 8. □

4.4.6 Multiple solutions of the equation of state

In this section we are interested in finding how many solutions can the equation of state (4.69) have and how many of these solutions are (meta)stable. For this purpose, we prove several simple lemmas that allow deriving general results for the numbers of solutions formulated as Theorem 7 and Theorem 9. Note that all the results obtained below can be easily verified by the graphical analysis.

Theorem 3. *The equation of state (4.69) always has at least one (meta)stable solution.*

Proof. Since

$$\lim_{\bar{L}\to 0} \bar{\mathcal{F}}'(\bar{L};\mathbf{t},T) = -\infty; \quad \lim_{\bar{L}\to 1} \bar{\mathcal{F}}'(\bar{L};\mathbf{t},T) = +\infty,$$

and $\bar{\mathcal{F}}'(\bar{L};\mathbf{t},T)$ is a continuous function on $\bar{L} \in (0,1)$, there exists such $\lambda \in (0,1)$ that $\bar{\mathcal{F}}'(\lambda;\mathbf{t},T) = 0$ and the function changes its sign, which, according to Lemma 1, corresponds to the (meta)stable solution of the equation of state (4.78). □

Lemma 2. *For any 1-smooth on $\mathcal{D} \subset \mathbb{R}$ function $f : \mathcal{D} \to \mathbb{R}$, if $n \in \mathbb{N}$ is the number of zeros of $f'(x) \equiv df(x)/dx$, then the number of solutions of the equation $f(x) = 0$ cannot be greater than $n + 1$.*

Proof. By contradiction, assume that $f(x)$ does have $m > n + 1$ distinct zeros in $\mathcal{D}$, which can be ordered in ascending order $\{x_1, x_2, \ldots, x_m\}$ resulting in $m - 1$ closed intervals $[x_i, x_{i+1}]$, $i \in \{1, \ldots, m\}$. As follows from the *Rolle's theorem*, there should be at least one zero of $f'(x)$ per every open interval (x_i, x_{i+1}), which means that $n \geq m - 1$. Combining the last expression with the assumption that $m > n + 1$ leads to a contradiction $n > n$. □

Lemma 3. *For any $a, b \in \mathbb{R}$ such that $a < b$, a polynomial $f(x)$ of an odd degree d such that $f(a) > 0$ and $f(b) > 0$ cannot have more than $d - 1$ roots on the interval (a, b).*

Proof. Let n be the number of roots of $f(x)$ on the interval (a, b), and m be the number of its roots outside this interval. Due to the *fundamental theorem of algebra*

$$n + m \leq d. \tag{4.90}$$

Assume that the leading coefficient is positive, then since d is odd, $\lim_{x\to-\infty} f(x) = -\infty$ but $f(a) > 0$ and, as any polynomial, $f(x)$ is continuous; thus, due to the *intermediate value theorem*, there is at least one root $x_0 < a$, which is outside the interval (a, b), and so $m \geq 1$. Combining it with (4.90) gives $n \leq d - 1$, which completes the proof for the case of the positive leading coefficient.

Similarly, assume that the leading coefficient is negative, then, since d is odd, $\lim_{x\to+\infty} f(x) = -\infty$, but $f(x)$ is continuous and $f(b) > 0$ which, due to the *intermediate value theorem*, implies that there is at least one root $x_0 > b$ that is outside the interval (a, b), and so $m \geq 1$. Combining it with (4.90) gives $n \leq d - 1$, which completes the proof for the case of the negative leading coefficient. □

Theorem 4. *The number of solutions of the equation of state (4.78) cannot be greater than $q + 1 - (q \mod 2)$.*

Proof. Consider the condition (4.85), which on $\bar{L} \in (0,1)$ is equivalent to

$$f(\bar{L}) = 1 - 2\sum_{k=2}^{q} k(k-1)\beta t_k \bar{L}^{k-1}(1-\bar{L}) = 0. \tag{4.91}$$

Since $f(\bar{L})$ defined above is a polynomial of degree q, due to the *fundamental theorem of algebra* it may have at most q roots on the interval $(0,1)$, which due to the one-to-one correspondence of these roots with zeros of $\bar{\mathcal{F}}''(\bar{L};\mathbf{t},T)$ means that according to Lemma 2, there can be at most $q+1$ zeros of $\bar{\mathcal{F}}'(\bar{L};\mathbf{t},T)$ on the interval $(0,1)$; thus the theorem is proven for even q. Furthermore, since $f(0) = 1$ and $f(1) = 1$, due to Lemma 3, if q is odd, then $f(\bar{L})$ may have at most $q-1$ roots on the interval $(0,1)$, which due to Lemma 2 implies that $\bar{\mathcal{F}}'(\bar{L};\mathbf{t},T)$ may have at most q zeros on the interval $(0,1)$, which completes the proof for odd q. □

Lemma 4. *For any natural number $0 \leq p \leq d$ and any interval $\mathcal{D} \subset \mathbb{R}$ there exists a real polynomial of the degree up to d that has exactly p roots in $\mathcal{D}$, all of which are simple.*

Proof. The fact that the number of solutions cannot be greater than d is a direct consequence of the *fundamental theorem of algebra*. The rest of the proof is done by the following construction. Define a sequence $\{x_1,\ldots,x_m\}$, $p \leq m \leq d$ in which $\{x_1,\ldots,x_p\}$ are distinct real numbers belonging to D, while $\{x_{p+1},\ldots,x_m\}$ are either real numbers not belonging to D or complex numbers entering in pairs of complex conjugates. The expression $(x-x_1)(x-x_2)\ldots(x-x_m)$ is a real polynomial of the degree $m \leq d$ having the desired number $p \leq d$ of simple roots on the desired interval $\mathcal{D} \subset \mathbb{R}$. □

Since all the singular macrostates satisfy the singularity condition (4.85), the set of the parameters corresponding to singular macrostates is of zero measure in the parameter space, which makes it interesting to find how many regular solutions of the equation of state (4.47) can there be.

Theorem 5. *If the equation of state (4.47) does not admit singular solutions and r_s is the number of its (meta)stable solutions while r_u is the number of its unstable solutions, then $r_s - r_u = 1$.*

Proof. As follows from Definition 7, the function $\bar{\mathcal{F}}'(\bar{L};\mathbf{t},T)$ has a nonzero derivative on any regular solution; hence the regular solutions correspond to the points at which $\bar{\mathcal{F}}'(\bar{L};\mathbf{t},T)$ changes its sign. From Lemma 1, it is clear that on the (meta)stable solutions the sign of $\bar{\mathcal{F}}'(\bar{L};\mathbf{t},T)$

changes from negative to positive; thus, r_s is the number of such sign changes. Furthermore, from Definition 5 and Lemma 1, it is clear that at the unstable solutions the sign of $\bar{\mathcal{F}}'(\bar{L};\mathbf{t},T)$ either changes from positive to negative or does not change, which is not the case for regular solutions. Therefore, r_u is the number of the positive-to-negative sign changes of $\bar{\mathcal{F}}'(\bar{L};\mathbf{t},T)$. Since the function $\bar{\mathcal{F}}'(\bar{L};\mathbf{t},T)$ is continuous and, as easy to check from (4.46),

$$\lim_{\bar{L}\to 0}\bar{\mathcal{F}}'(\bar{L};\mathbf{t},T)=-\infty;\quad \lim_{\bar{L}\to 1}\bar{\mathcal{F}}'(\bar{L};\mathbf{t},T)=+\infty,$$

the number of its negative-to-positive sign changes is $r_s = r_u + 1$. □

Theorem 6. *If the equation of state (4.47) does not admit singular solutions, then the number of its solutions is odd.*

Proof. Due to Theorem 5, the number of stable regular solutions r_s and the number of unstable regular solutions are related by $r_s - r_u = 1$, which means that the total number of solutions $r = r_s + r_u = 2r_u + 1$, which is odd for all $r_u \in \mathbb{N}_0$. □

Theorem 7. *For any natural number $q > 0$ and any odd number p from 1 to $q + 1 - (q \mod 2)$, there exists a mean field model of order q, whose equation of state (4.47) does not have singular solutions and has exactly p regular solutions.*

Proof. According to Theorem 3, one solution always exists and, since all solutions are assumed to be regular, the number of regular solutions cannot be less than one.

Consider the $T \to 0$ limit. Since

$$\lim_{T\to 0}\mathcal{A}(\bar{L};T)=0 \text{ for all } \bar{L}\in(0,1), \tag{4.92}$$

$\lim_{T\to 0}\bar{\mathcal{F}}'(\bar{L};\mathbf{t},T) = \mathcal{P}(\bar{L};\mathbf{t})$, thus at low temperatures the roots of $\mathcal{P}(\bar{L};\mathbf{t})$ belonging to the $(0,1)$ interval correspond to the solutions of the equation of state (4.78), and the solutions corresponding to the simple roots of $\mathcal{P}(\bar{L};\mathbf{t})$ are regular. Furthermore, due to (4.92) and the fact that

$$\lim_{\bar{L}\to 0}\mathcal{A}(\bar{L};T)=-\infty \text{ for all } T>0,$$

as long as $\mathcal{P}(0;\mathbf{t}) < 0$, there is a solution $\lambda_0 \underset{T\to 0}{\to} 0$. Similarly, since for all $T > 0$

$$\lim_{\bar{L}\to 1} \mathcal{A}(\bar{L};T) = +\infty \text{ for all } T > 0,$$

as long as $\mathcal{P}(1;\mathbf{t}) > 0$, there is a solution $\lambda_1 \underset{T\to 0}{\to} 1$. The particular examples are shown in Fig. 4.2 and Fig. 4.3.

Due to Lemma 4, it is always possible to find such parameters $\mathbf{t} = \mathbf{t}_n$ that the polynomial $\mathcal{P}(\bar{L};\mathbf{t}_n)$ has exactly $n \leq (q-1)$ roots on the interval $(0,1)$, all of which are simple.

Suppose n is even. If $\mathcal{P}(0;\mathbf{t}_n) < 0$, then due to the fact that the sign of $\mathcal{P}(\bar{L};\mathbf{t}_n)$ alternates on every simple root of which there is an even number, $\mathcal{P}(1;\mathbf{t}_n) < 0$. This means that in addition to n solutions coming from the roots of $\mathcal{P}(\bar{L};\mathbf{t}_n)$, there is another solution coming from the boundary $\bar{L} = 0$, and no solution at $\bar{L} = 1$. Similarly, if $\mathcal{P}(0;\mathbf{t}_n) > 0$, then $\mathcal{P}(1;\mathbf{t}_n) > 0$, which means that in addition to n solutions coming from the roots of $\mathcal{P}(\bar{L};\mathbf{t}_n)$, there is another solution coming from the boundary $\bar{L} = 1$, and no solution at $\bar{L} = 0$. So, for even n, there are always $n+1$ solutions. The cases when $\mathcal{P}(0;\mathbf{t}_n) = 0$ or $\mathcal{P}(1;\mathbf{t}_n) = 0$ are not considered since for any finite temperature these solutions disappear.

Suppose n is odd. If $\mathcal{P}(0;\mathbf{t}_n) < 0$, then due to the fact that the sign of $\mathcal{P}(\bar{L};\mathbf{t}_n)$ alternates on every simple root of which there is an odd number, $\mathcal{P}(1;\mathbf{t}_n) > 0$. This means that in addition to n solutions coming from the roots of $\mathcal{P}(\bar{L};\mathbf{t}_n)$, there is another pair of solutions coming from the boundaries $\bar{L} = 0$ and $\bar{L} = 1$, meaning that the total number of solutions is $n+2$. On the other hand, if $\mathcal{P}(0;\mathbf{t}_n) > 0$, then due to the fact that the sign of $\mathcal{P}(\bar{L};\mathbf{t}_n)$ alternates on every simple root of which there is an odd number, $\mathcal{P}(1;\mathbf{t}_n) < 0$, which means that there are no boundary solutions, but only n solutions corresponding to the roots of $\mathcal{P}(\bar{L};\mathbf{t}_n)$. Therefore, for odd n there may be either n or $n+2$ solutions.

Combining the above results gives $p = n + 1 \pm (n \mod 2)$ for the number of solutions of the equation of state (4.69) in $T \to 0$ limit for a given number of roots n of $\mathcal{P}(\bar{L};\mathbf{t})$ on the interval $(0,1)$. Since, due to Lemma 4, n can be any number from 0 to $q-1$, p can be any odd number from 1 to $q + 1 - (q \mod 2)$.

At this stage the statement of the theorem is proven in the $T \to 0$ limit, which due to continuity

means that it holds in some vicinity of $T = 0$. Furthermore, since, due to Theorem 4, the number of solutions cannot exceed $q + 1 - (q \mod 2)$ at any T, it is always between 1 and $q + 1 - (q \mod 2)$, and as shown above, there are values of the parameters at which the number of regular solutions can be equal to any given odd number from this range. □

Lemma 5. *Let $\mathcal{L} = \{\bar{L}_1, \bar{L}_2, \ldots, \bar{L}_s\}$ be an exhaustive set of solutions of the equation of state (4.47) ordered in ascending order. For $1 \leq i < s$, if $\bar{L}_i$ and $\bar{L}_{i+1}$ are regular, then one of these solutions is (meta)stable while another is unstable.*

Proof. As discussed in Section 4.4.1, the self-consistency equation (4.47) is a stationarity condition for $\bar{\mathcal{F}}(\bar{L}; \mathbf{t}, T)$, so

$$\bar{\mathcal{F}}'(\bar{L}_j; \mathbf{t}, T) = 0 \text{ for all } j \in \{1, \ldots, n\}. \tag{4.93}$$

Assume the solution $\bar{L}_i$ to be regular and (meta)stable, which, as clear from Lemma 1, implies that $F''(\bar{L}_i; \mathbf{t}, T) > 0$, therefore since $\mathcal{L}$ is exhaustive (i.e. there are no solutions between $\bar{L}_i$ and $\bar{L}_{i+1}$)

$$\bar{\mathcal{F}}'(\bar{L}; \mathbf{t}, T) > 0 \text{ everywhere on } (\bar{L}_i, \bar{L}_{i+1}). \tag{4.94}$$

Due to (4.93) $\bar{\mathcal{F}}'(\bar{L}_{i+1}; \mathbf{t}, T) = 0$, which together with (4.94) implies that $F''(\bar{L}_{i+1}; \mathbf{t}, T) \leq 0$, but if the solution $\bar{L}_{i+1}$ is regular, then from Definition 7 $F''(\bar{L}_{i+1}; \mathbf{t}, T) \neq 0$, which means that $F''(\bar{L}_i; \mathbf{t}, T) < 0$, i.e. the solution $\bar{L}_{i+1}$ is unstable due to Lemma 1 and Definition 5.

Similarly, assume the solution $\bar{L}_i$ is regular and unstable, which, as clear from Lemma 1, implies that $F''(\bar{L}_i; \mathbf{t}, T) < 0$, therefore since $\mathcal{L}$ is exhaustive (i.e. there are no solutions between $\bar{L}_i$ and $\bar{L}_{i+1}$)

$$\bar{\mathcal{F}}'(\bar{L}; \mathbf{t}, T) < 0 \text{ everywhere on } (\bar{L}_i, \bar{L}_{i+1}). \tag{4.95}$$

Due to (4.93) $\bar{\mathcal{F}}'(\bar{L}_{i+1}; \mathbf{t}, T) = 0$, which together with (4.95) implies that $F''(\bar{L}_{i+1}; \mathbf{t}, T) \geq 0$, but if the solution $\bar{L}_{i+1}$ is regular, then from Definition 7 $F''(\bar{L}_{i+1}; \mathbf{t}, T) \neq 0$, which means that $F''(\bar{L}_i; \mathbf{t}, T) > 0$, i.e. the solution $\bar{L}_{i+1}$ is (meta)stable due to Lemma 1. □

Lemma 6. *Let L_1 be the smallest solution of the equation of state (4.47) and L_s be the largest, then if $\bar{L}_1$ is regular, then $\bar{L}_1$ is (meta)stable, and if $\bar{L}_s$ is regular, $\bar{L}_s$ is (meta)stable.*

Proof. From (4.46) it is clear that

$$\lim_{\bar{L}\to 0} \bar{\mathcal{F}}'(\bar{L};\mathbf{t},T) = -\infty; \tag{4.96}$$

$$\lim_{\bar{L}\to 1} \bar{\mathcal{F}}'(\bar{L};\mathbf{t},T) = +\infty. \tag{4.97}$$

Since $\bar{L}_1$ is the solution of the equation of state (4.47), $\bar{\mathcal{F}}'(\bar{L}_1;\mathbf{t},T) = 0$, and since it is regular, $\bar{\mathcal{F}}''(\bar{L}_1;\mathbf{t},T) \neq 0$, which means that the continuous function $\bar{\mathcal{F}}'(\bar{L};\mathbf{t},T)$ changes its sign at L_1. Furthermore, due to continuity, (4.96) and the fact that $\bar{L}_1$ is the closest to zero solution of the equation of state, the sign of $\bar{\mathcal{F}}'(\bar{L};\mathbf{t},T)$ should be changing from negative to positive at $\bar{L}_1$ which, due to Lemma 1, means that the solution $\bar{L}_1$ is (meta)stable.

Similarly, if $\bar{L}_s$ is the closest to $\bar{L} = 1$ regular solution of the self-consistency equation (4.47), it is the closest to $\bar{L} = 1$ point such that $\bar{\mathcal{F}}' = 0$ and $\bar{\mathcal{F}}'' \neq 0$, therefore (4.97) means that $\bar{\mathcal{F}}'(\bar{L};\mathbf{t},T)$ changes its sign from negative to positive at $\bar{L} = L_s$, thus due to Lemma 1 the solution is (meta)stable. □

Theorem 8. *If the equation of state (4.47) admits p solutions and all of them are regular, then $1 + (p-1)/2$ of these solutions are (meta)stable.*

Proof. Let $\mathcal{L} = \{\bar{L}_1, \bar{L}_2, \ldots, \bar{L}_p\}$ be the exhaustive set of the solutions of the equation of state (4.47) on the interval $(0,1)$ ordered in ascending order. Assuming all the solutions to be regular, consider the set $\mathcal{L}' = \mathcal{L} \setminus \{L_1\} = \{\bar{L}_2, \ldots, \bar{L}_p\}$ consisting of $p-1$ elements. According to Theorem 7, $p-1$ is even, and due to Lemma 5, $\mathcal{L}'$ contains $(p-1)/2$ (meta)stable solutions. Since, due to Lemma 6, the solution $\bar{L}_1$ is (meta)stable, the total number of (meta)stable solutions is $1 + (p-1)/2$. □

Theorem 9. *The equation of state (4.47) of a generic model of degree q may have any number from 1 to $1 + \big(q - (q \mod 2)\big)/2$ of (meta)stable regular solutions.*

Proof. Assume all the solutions of the equation of state (4.47) to be regular, and let p be the total number of solutions. According to Theorem 7, p can be any odd number from 1 to $1 + q - (q \mod 2)$, and due to Theorem 8, there are $1 + (p-1)/2$ (meta)stable solutions. Thus, since $p - 1$

can be any even number from 0 to $q-(q \mod 2)$, the number of (meta)stable solutions can indeed take any value from 1 to $1 + \big(q - (q \mod 2)\big)/2$. □

4.4.7 Complex phase transitions

As discussed in Section 4.4.6, the equation of state (4.47) for a model of order q may admit up to $q + 1 - (q \mod 2)$ solutions, of which more than a half are (meta)stable. This results in the complex hystereses shown in Fig. 4.4, Fig. 4.5 and Fig. 4.6. All (meta)stable branches of the hystereses (i.e. those on which $\bar{L}$ increases with t_1) correspond to the distinct "phases" and, as discussed in Section 2.1.7, stable solutions are selected by minimisation of the specific microcanonical free energy. For finite systems the distributions of macrostates are multimodal and, as can be seen in Fig. 4.4, Fig. 4.5 and Fig. 4.6, the width of the transitions between the phases decreases with the size of the connectance gap between them, which can be explained as follows.

Consider a transition from a macrostate with connectance $\bar{L}_1$ to a macrostate with connectance $\bar{L}_2$. For large βN one may assume that these two macrostates accumulate all the probability, i.e.

$$\langle \bar{L} \rangle = \frac{\bar{L}_1 \mathrm{e}^{-\beta \mathcal{F}_n(\bar{L}_1;\mathbf{t},\beta)} + \bar{L}_2 \mathrm{e}^{-\beta \mathcal{F}_n(\bar{L}_2;\mathbf{t},\beta)}}{\mathrm{e}^{-\beta \mathcal{F}_n(\bar{L}_1;\mathbf{t},\beta)} + \mathrm{e}^{-\beta \mathcal{F}_n(\bar{L}_2;\mathbf{t},\beta)}}. \tag{4.98}$$

Introducing the variables

$$\Lambda = \frac{\bar{L}_2 + \bar{L}_1}{2}; \quad \Delta = \frac{\bar{L}_2 - \bar{L}_1}{2},$$

which correspond to the center of the transition and the connectance gap between the macrostates' connectances and that center, the expectation (4.98) can be written as

$$\langle \bar{L} \rangle = \frac{(\Lambda - \Delta) \mathrm{e}^{-\beta \mathcal{F}_n(\bar{L}_1;\mathbf{t},\beta)} + (\Lambda + \Delta) \mathrm{e}^{-\beta \mathcal{F}_n(\bar{L}_2;\mathbf{t},\beta)}}{\mathrm{e}^{-\beta \mathcal{F}_n(\bar{L}_1;\mathbf{t},\beta)} + \mathrm{e}^{-\beta \mathcal{F}_n(\bar{L}_2;\mathbf{t},\beta)}},$$

which after basic manipulations reduces to

$$\langle \bar{L} \rangle = \Lambda + \Delta \tanh\left(-\frac{\beta}{2} \left[\mathcal{F}_n(\bar{L}_2;\mathbf{t},\beta) - \mathcal{F}_n(\bar{L}_1;\mathbf{t},\beta) \right] \right) \tag{4.99}$$

Using the expression (2.18) the expected connectance can be expressed as

$$\langle \bar{L} \rangle = \Lambda + \Delta \tanh \left(-\beta \frac{H_{MF}(\bar{L}_2; \mathbf{t}) - H_{MF}(\bar{L}_1; \mathbf{t})}{2} + \frac{\mathcal{S}_n(\bar{L}_2) - \mathcal{S}_n(\bar{L}_1)}{2} \right), \tag{4.100}$$

where only the first term under the hyperbolic tangent is relevant to the width of the transition in $\mathbf{t}$, since all the other terms do not depend on $\mathbf{t}$. Substituting the expression for the Hamiltonian of the MF model (4.35) gives

$$\langle \bar{L} \rangle = \Lambda + \Delta \tanh \left(-\beta N \sum_{k=1}^{q} t_k \left(\bar{L}_2^k - \bar{L}_1^k \right) + \frac{\mathcal{S}_n(\bar{L}_2) - \mathcal{S}_n(\bar{L}_1)}{2} \right), \tag{4.101}$$

from which it is clear that the characteristic length of the transition in t_1 decays as $(2\beta N \Delta)^{-1}$, i.e. inversely proportional to the connectance gap $\bar{L}_2 - \bar{L}_1$.

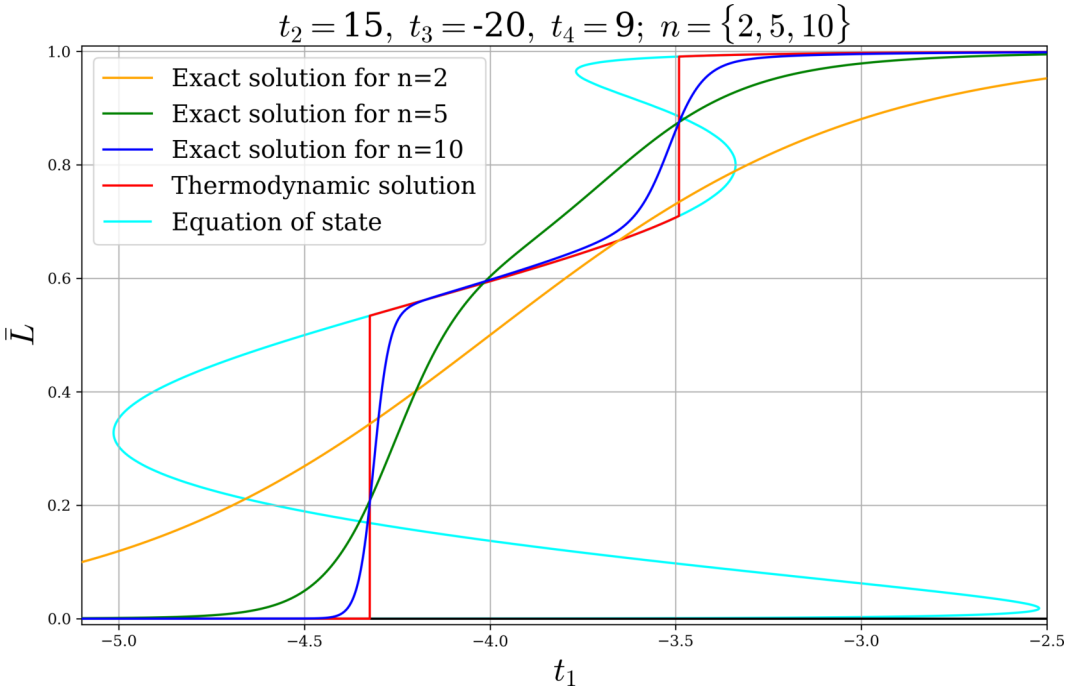

Fig. 4.4: Phase transitions in the MF4 model. Note that there is a region in t_1 with three (meta)stable solutions, which is the highest number of simultaneously (meta)stable states possible in the MF4 model. There are also two disjoint regions in t_1 with 2-stability and two disjoint infinite regions in t_1 with only one solution very close to either $\bar{L} = 0$ or $\bar{L} = 1$. The exact solutions for the models of 2, 5 and 10 nodes (shown in orange, green and blue respectively) demonstrate how quickly the exact finite-size solutions approach the thermodynamic solution (shown in red) as the number of nodes increases. From the shape of the exact solution for the model of 10 nodes (blue line), it is evident that the sharpness of the transition between two (meta)stable states increases with the gap in $\bar{L}$ between the states.

Note that the highly multistable solutions of the kind shown in Fig. 4.5 and Fig. 4.6 require

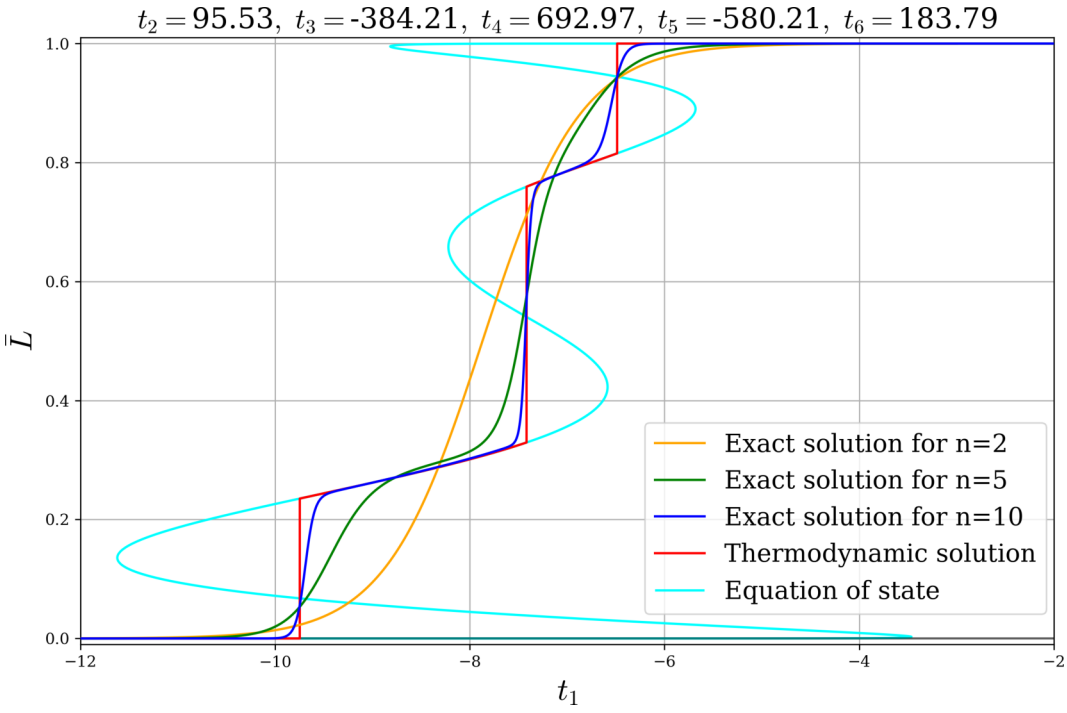

Fig. 4.5: Phase transitions in the MF6 model. Note that there is a region in t_1 with four (meta)stable solutions, which is the highest number of simultaneously (meta)stable states possible in the MF6 model. There are also two disjoint regions in t_1 with 3-stability, two disjoint regions in t_1 with 2-stability, and two disjoint infinite regions in t_1 with only one stable solution. Note that the couplings t_i are large in absolute value and have alternating signs, which is common for such oscillating solutions of the self-consistency equation (4.47). The exact solutions for the models of 2, 5 and 10 nodes (shown in orange, green and blue respectively) demonstrate how quickly the exact finite-size solutions approach the thermodynamic solution (shown in red) as the number of nodes increases. From the shape of the exact solution for the model of 10 nodes (blue line), it is evident that the sharpness of the transition between two (meta)stable states increases with the gap in $\bar{L}$ between the states. Finally, note that, even though the stability band $\bar{L} \in [0.6581, 0.8902]$ corresponds to the global minimum of the free energy for $t_1 \in [-7.417, -6.487]$, it cannot be retrieved in time-averaging MC simulations by scanning t_1 from $-\infty$ to $+\infty$ or from $+\infty$ to $-\infty$ without random initialisation. This fact shows the importance of the theory, which predicts the initial conditions for the MCMC needed to retrieve all the (meta)stable branches.

very high absolute values of $\beta\mathbf{t}$ and the alternation of the parameters' signs. For this reason, the complex structure of the hysteresis quickly dispels with the increasing temperature; moreover, in such regimes its dependence on the parameters $\mathbf{t}$ is very sharp. Indeed, there is less than a per cent difference in the parameters of the models shown in Fig. 4.5 and Fig. 4.4, yet their behaviours are qualitatively different - the model from Fig. 4.5 has a region of 4-stability, while the maximum stability index of the model from Fig. 4.4 is three. The situation is similar to what happens when a high-degree polynomial is fitted to multiple points on a small interval, in which case, in order to cross all of the desired points, the polynomial usually develops large oscillations, which requires

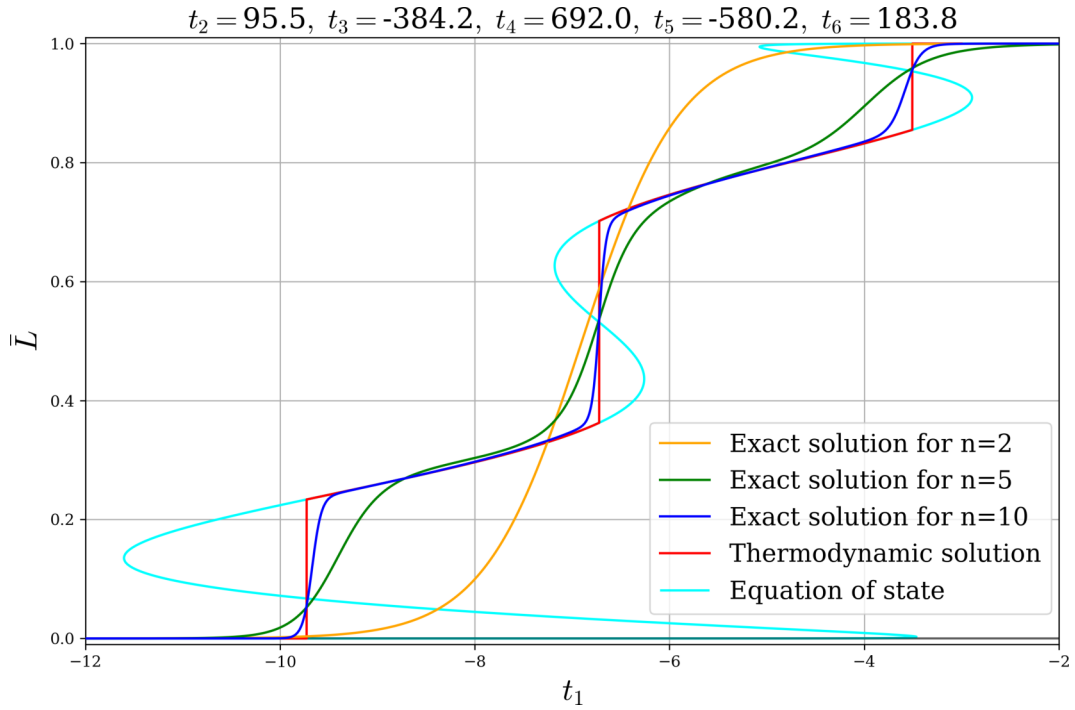

Fig. 4.6: Phase transitions in the MF6 model. Note how a tiny change in the parameters t_i, $1 < i \leq q$ compared to Fig. 4.5 results in a qualitatively different behaviour of the model, which no longer exhibits 4-stability.

large coefficients of alternating signs.

4.4.8 Uniqueness boundary

As discussed in Section 2.4.6, in the regimes with multiple (meta)stable macrostates, the Markov chains used in the algorithms designed to fit ERGMs to data are usually very slow at exploring the configuration space. Thus, if the parameter estimates obtained using MCMC[8]-based methods belong to the region of multistability, the model is unlikely to fit the data well. Furthermore, as discussed in Section 2.1.7, the distributions of macrostates in such regions are likely to be multimodal, which means that, even if the algorithm converges to the correct estimates, the networks sampled from the model may be very different from the data despite the fact that on average the desired observables match. Therefore, it is important to find the region in $\mathbf{t}$-space where there is only one stable macrostate to have a quick way of rejecting the parameter estimates belonging to the multistable regions.

In what follows we again set $T = 1$ and $\bar{\mathcal{F}}(\bar{L}; \mathbf{t}) \equiv \bar{\mathcal{F}}(\bar{L}; \mathbf{t}, T = 1)$, which does not restrict the

[8]Markov Chain Monte Carlo

generality, as discussed in Section 2.4.8.

Since in any open subset of $\mathbf{t}$-space containing a singular point there are values of $\mathbf{t}$ at which the equation of state (4.47) has multiple solutions, the singularity condition (4.85) together with the equation of state (4.47) define a hypersurface in $\mathbf{t}$-space, which marks the boundary of the uniqueness region.

It is interesting to establish whether the equation of state (4.47) defines the connectance $\bar{L}$ as a single-valued function of a parameter $t_i \in (-\infty, +\infty)$. Similarly to the case of the CW model discussed in Section 2.4.3.1, the first point at which the solution becomes multivalued is the point of gradient catastrophe corresponding to a critical point since at such point, the solution is unique and, therefore, stable. Since, due to Theorem 1, all the critical points are singularities of order higher than one, they are given by the equation of state (4.86) combined with the conditions (4.85) and

$$\frac{\partial^2 t_1}{\partial \bar{L}^2} = \frac{2\bar{L}-1}{\bar{L}^2(1-\bar{L}^2)} - \sum_{k=3}^{q} k(k-1)(k-2)t_k \bar{L}^{k-3} = 0, \tag{4.102}$$

which is obtained from (4.81) for $p = 2$. Together these three conditions define a $(q-2)$-manifold in $\mathbf{t}$-space, whose projection onto the $t_i = \text{const}$ hyperplane defines the uniqueness boundary on the hyperplane.

4.4.9 Distributions of local features and the degeneracy of the ground macrostate

Since the Hamiltonian of the MF model (4.35) depends solely on the connectance, the probability distribution (4.1) assigns the equal probability to all graphs having the same number of links[9]. Furthermore, as discussed in Section 4.4.4, the MF model may have states of moderate connectance at arbitrarily low temperatures, in which case, as can be seen from the expression (4.41), the specific entropy of the model is finite even as $T \to 0$. This, in turn, means that the ground macrostates[10] of the MF model not corresponding to the empty or complete graphs are highly degenerate, and the distributions of local features do not have to be very narrow even in $T \to 0$ limit, as can be seen in Fig. 4.7. Moreover, since, as discussed in Section 2.1.6, when $\beta N \to \infty$ the canonical and microcanonical ensembles become equivalent, in such regimes the MF model is equivalent

[9] As it is the case with Erdős-Rényi model from Section 4.1.2.

[10] Macrostates minimising the Hamiltonian.

to the ER model of matching connectance[11], which explains the great agreement of their degree distributions found in Fig. 4.14, Fig. 4.12 and Fig. 4.15.

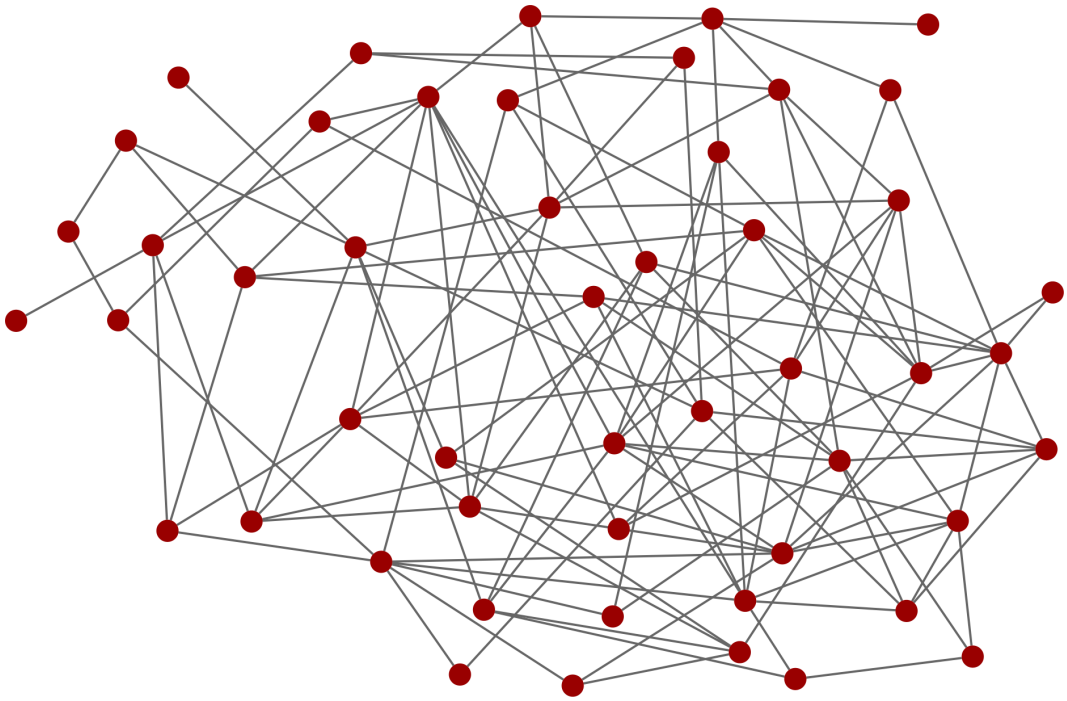

Fig. 4.7: A sample from the MF3 model of 50 nodes with the parameters $t_1 = 13.151388$, $t_2 = -75$, $t_3 = 25$. Note that despite the low temperature, the degree distribution of the sample spans from 1 to 9. The global clustering coefficient is 0.0270701, and the average local clustering coefficient is 0.0739683, which is close to their expectations in the ER model of the same connectance.

4.5 Relation of the MF model to homogeneous Markov ERGMs

Comparing (4.27) with (4.44) and (4.28) with (4.47), one can see that the exact thermodynamic solution for the MF model is identical to the mean field theory of homogeneous Markov ERGMs after the following rescaling of the parameters

$$t_s = \frac{n-s}{n^s(n-1)}\binom{n}{s}\tau_s + \delta_{s3}\frac{n-2}{n}\theta, \tag{4.103}$$

which establishes a correspondence between the MF model and homogeneous Markov ERGMs. Due to this equivalence, we further omit the use of $\langle ... \rangle_0$ notation keeping in mind that some expressions for ERGMs other than the MF model are obtained in the mean field approximation,

[11] Since the distributions of microstates in both models become uniform with a hard constraint $\bar{L}(\mathbf{A}) = \bar{L}$, and there are no other constraints since the Hamiltonians of both models depend solely on the connectance.

which, as discussed in Section 2.2.2.1, is believed to be exact in the thermodynamic limit.

Note that in general, the correspondence (4.103) is not a one-to-one relation since the 3-star parameter τ_3 and the triangle parameter θ both contribute to the single mean field parameter t_3. However, in the case studies below we restrict our attention to the models in which either τ_3 or θ are identically zero, in which case the correspondence (4.103) is, in fact, a one-to-one relation and it is convenient to present such models in a unified way by using $\mathbf{t}$ instead of $\boldsymbol{\tau}$ and θ. For example, the $(0,1)$-bistability transition formulas (4.33) and (4.34) can be expressed as

$$\langle \mathcal{S}_k(\mathbf{A}) \rangle = \frac{n}{2}\binom{n-1}{k}\left[1+\tanh\left(N\sum_{s=1}^{p} t_s\right)\right]; \tag{4.104}$$

$$\langle \mathcal{T}(\mathbf{A}) \rangle = \frac{n}{3}\binom{n-1}{2}\left[1+\tanh\left(N\sum_{s=1}^{p} t_s\right)\right]. \tag{4.105}$$

Note that for connectance $\bar{L} = S_1/\big(n(n-1)\big)$ the expression (4.104) coincides with (4.77).

4.6 Case studies

In this section we look at several special cases of homogeneous Markov ERGMs and compare the predictions of the theory with the results of the corresponding MC simulations. First we consider two models of order three, namely the *3-star model* and the *triad model*. After that we demonstrate how the theory works in higher-order cases such as the *4-star model* and the *alternating k-star (AKS) model*.

4.6.1 3-star model

The 3-star model is a homogeneous Markov ERGM (4.3) with $\theta = 0$ and $\tau_i = 0$ for all $i > 3$, i.e. the model defined by the following Hamiltonian

$$H_3(\mathbf{A}) = -\sum_{k=1}^{3} \frac{\tau_k}{n^{k-1}} \mathcal{S}_k(\mathbf{A}) = -2\tau_1 L(\mathbf{A}) - \frac{\tau_2}{n}\mathcal{S}_2(\mathbf{A}) - \frac{\tau_3}{n^2}\mathcal{S}_3(\mathbf{A}). \tag{4.106}$$

As follows from the discussion from Section 4.4.6, the MF self-consistency equation (4.47) for the model of order $q = 3$ admits up to three solutions, of which at most two can be simultaneously (meta)stable.

4.6.1.1 Observables of the 3-star model

Since the number of k-stars in the networks grows rapidly with n, it is easier to work with its rescaled version

$$\mathfrak{S}_k(\mathbf{A}) \equiv \frac{1}{n}\binom{n-1}{k}^{-1} \mathcal{S}_k(\mathbf{A}) \in [0,1], \tag{4.107}$$

for which the MFT predictions (4.26) read as

$$\langle \mathfrak{S}_k \rangle = \langle \bar{L} \rangle^k, \tag{4.108}$$

meaning that it is intensive. From the expression (4.108) it is clear that the 3-star model defined by the Hamiltonian (4.106) is scalable in the sense of Definition 1.

As can be seen in Fig. 4.8, the time-averaging MC simulations for large networks agree well with (4.108) for both corresponding models. This is not surprising because, as discussed in Section 2.2.2.1, the MFT is believed to be exact at predicting the observables of the infinite-dimensional systems in the thermodynamic limit. Furthermore, as can be seen in Fig. 4.9, even for small networks the mean field theory seems to work well away from the transition region where it predicts a discontinuous jump instead of a smooth transition for finite systems.

4.6.1.2 Critical points and uniqueness boundary

As discussed in Section 4.4.8, the self-consistency equation (4.47) defines the connectance as a single-valued function of any of the parameters $\mathbf{t}$ until the occurrence of the first critical point which, according to Theorem 1, requires singularity of order higher than one. Such singularities can be found by combining the self-consistency equation (4.86) together with the conditions (4.85) and (4.102), which for $q = 3$ gives

$$\begin{cases} t_1 = \dfrac{1}{2}\log\dfrac{\bar{L}}{1-\bar{L}} + \dfrac{4\bar{L}-3}{4(1-\bar{L})^2}; \\ t_2 = \dfrac{2-3\bar{L}}{4\bar{L}(1-\bar{L})^2}; \\ t_3 = \dfrac{2\bar{L}-1}{12\bar{L}^2(1-\bar{L})^2}. \end{cases} \tag{4.109}$$

The equations (4.109) define a curve in $\mathbf{t}$-space parameterised by $\bar{L} \in (0,1)$, and the projection

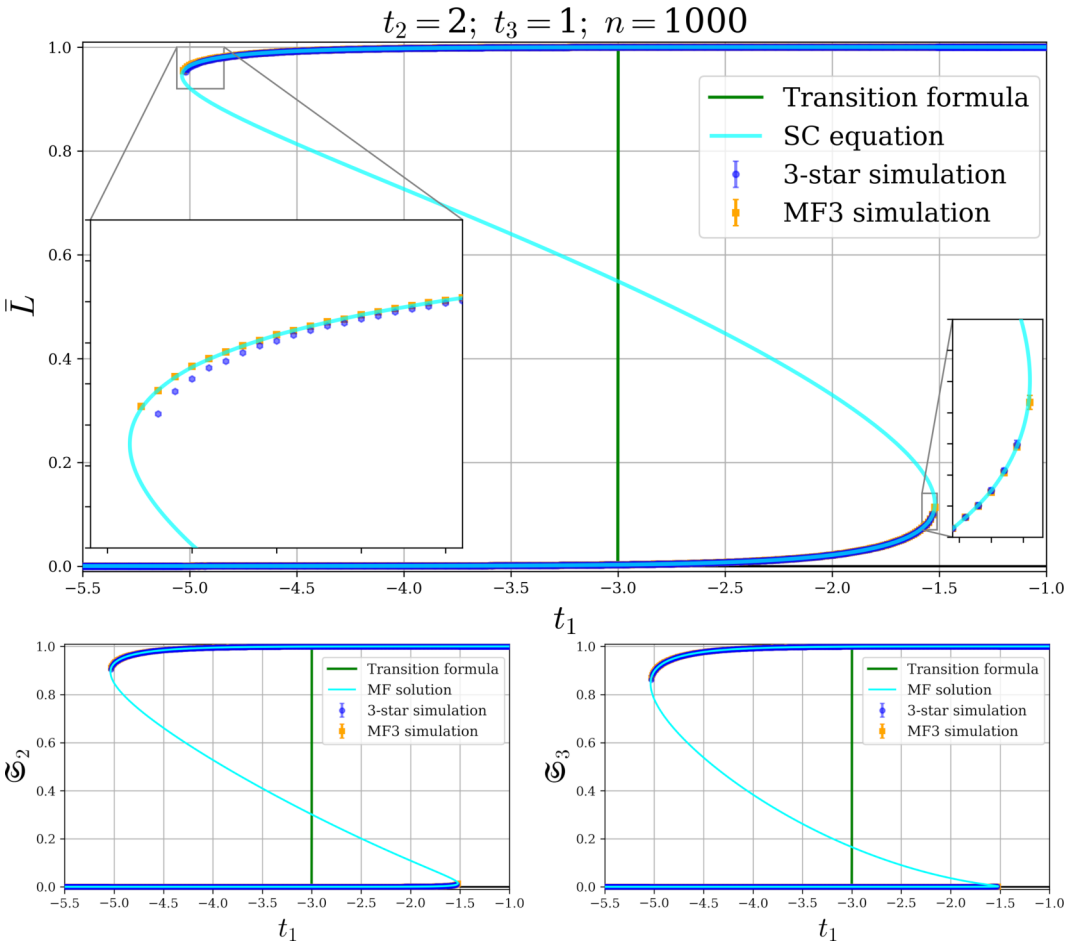

Fig. 4.8: Numerical solution of the self-consistency equation (4.47) and the results of the time-averaging MC simulations for the corresponding 3-star and MF3 models with 10^3 nodes. The theory seems to be precise for both models apart from the small deviations of the 3-star model near the spinodal points which decrease with the increase of the network size. The branch of the mean field solution on which $\bar{L}$ decreases with t_1 is unstable due to the negative susceptibility and corresponds to the (local) maximum of the free energy. The predictions of the transition formula (4.77) are shown in green.

of this curve on $t_i = \text{const}$ plane (Fig. 4.10) separates the plane into two regions: one where the system is 1-stable for all $t_i \in \mathbb{R}$, and another where the bistability occurs for some values of t_i. In this work we mainly focus on the t_1-dependence, treating t_2 and t_3 as fixed parameters.

4.6.1.3 Wide stability bands at low temperature

Well known is the fact that various ERGMs with sufficiently high couplings do not have (meta)stable macrostates of moderate connectance [Snijders et al. (2006); Robins, Snijders, Wang, Handcock and Pattison (2007); Newman (2010); Park and Newman (2005)], as can be seen in Fig. 4.8, where the connectance of (meta)stable macrostates can only belong to one of the two narrow

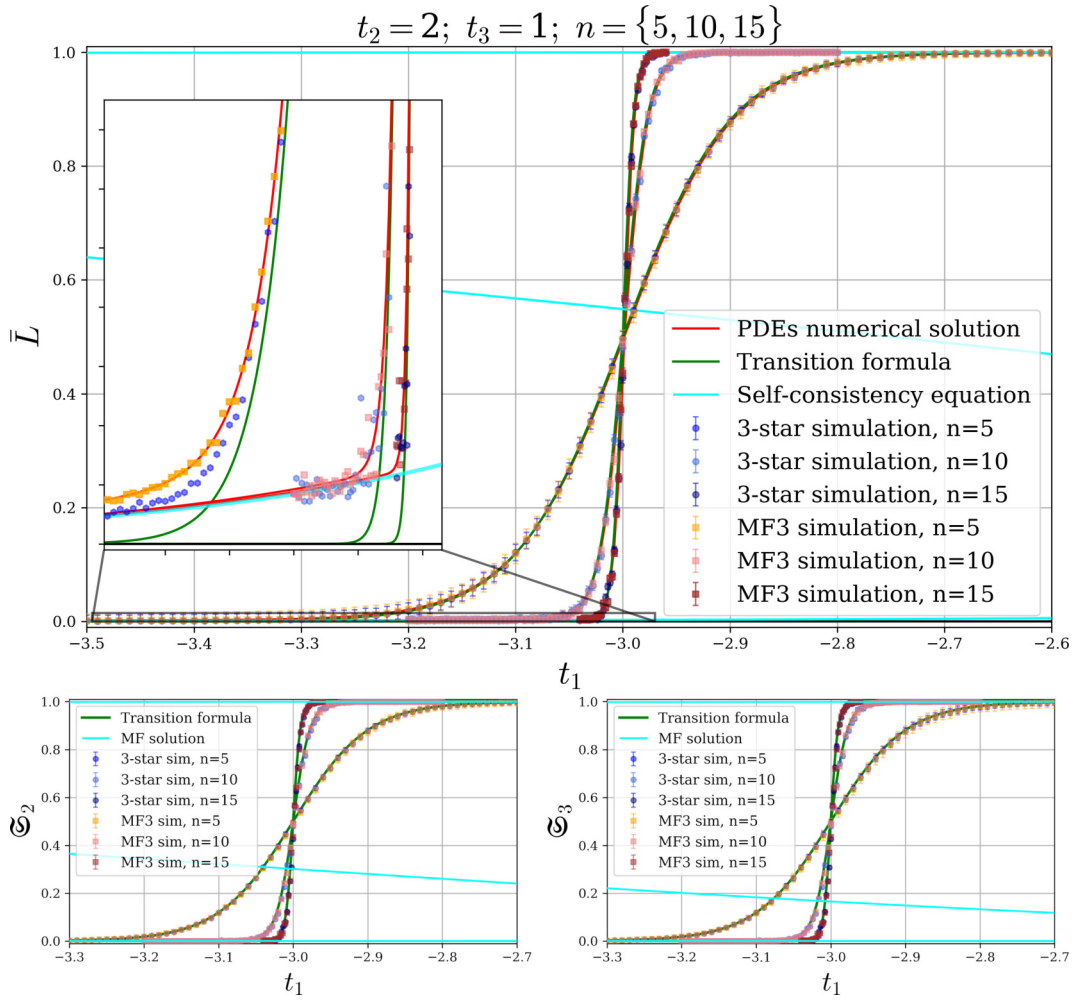

Fig. 4.9: Results of the ensemble-averaging MC simulations for the corresponding 3-star and MF3 models of 5, 10 and 15 nodes together with the MFT predictions (4.108) in which $\bar{L}$ is computed using (4.47) (cyan line), transition formula (4.33) (green line) and the numerical solution of the hierarchy (4.59) discretised using central differences in space with RK4 time stepping (red line). As can be seen on the upper plot, the numerical solutions of the hierarchy (4.59) agree with the simulations and follow the branches of the MFT hysteresis away from the transition region. The transition formula (4.33) also agrees with the simulations reasonably well but does not follow the actual branches of the hysteresis due to the (0,1)-bistability assumption used in its derivation. The statistical errors are estimated as weighted combinations of presumably Gaussian fluctuations around the (meta)stable macrostates with binomial fluctuations arising from the transitions between these two macrostates. The error bars on the insert plot for $\bar{L}$ are not shown to enhance visibility, and seem to be overestimated away from the transition region since the fluctuations near $\bar{L} = 0$ and $\bar{L} = 1$ are, clearly, not Gaussian due to the proximity to the border of the domain.

bands namely $0 < \bar{L} < 0.12037$ and $0.94531 < \bar{L} < 1$. We refer to a connectance band as narrow if its width decreases to zero together with temperature, and wide otherwise. This low-temperature behaviour can be explained by considering the shape of the specific microcanonical internal energy (4.42), which serves as a good proxy for the SMFE (4.43) as $T \to 0$. It is clear that when

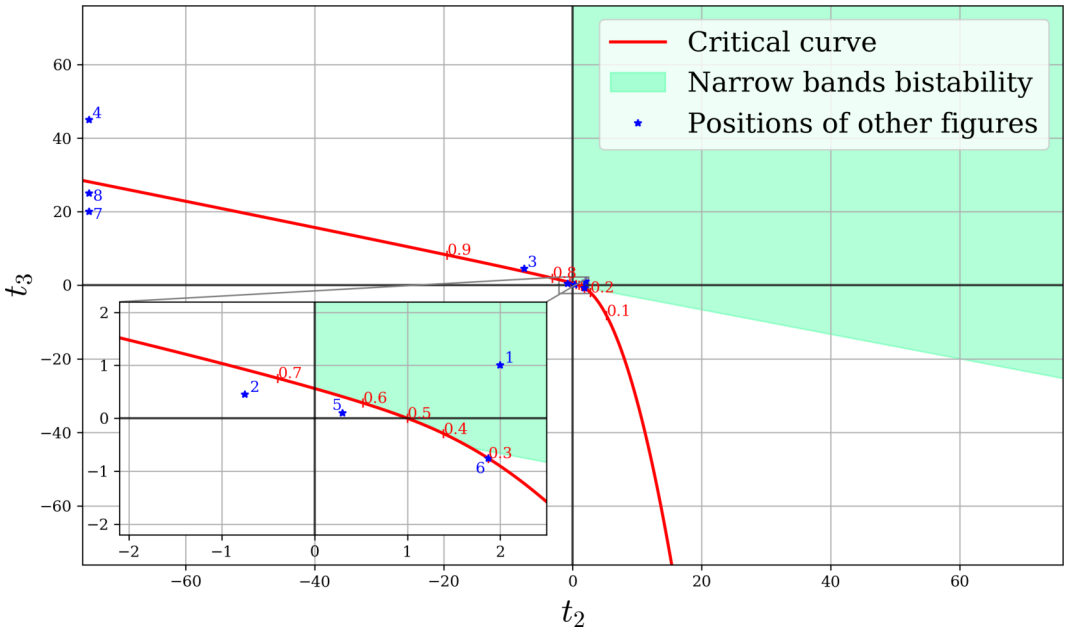

Fig. 4.10: Critical curve of the MF3 model (red line). Red numbers along the curve show the corresponding values of the connectance from (4.109). Below the curve there may only be one minimum of $\bar{\mathcal{F}}(\bar{L};\mathbf{t})$, i.e. one stable macrostate. Above the curve is a bistable region of t_1, in which there are two (local) minima of $\bar{\mathcal{F}}(\bar{L};\mathbf{t})$. The green region shows where the system is bistable, but $\bar{\mathcal{E}}(\bar{L};\mathbf{t})$ does not have stationary points, which results in the narrow connectance bands at low temperatures. Blue stars show the positions of the other figures on the t_2t_3-plane, namely the star with number 1 corresponds to Fig. 4.8, Fig. 4.9, Fig. 4.16 and Fig. 4.17; with numbers 2, 3 and 4 to Fig. 4.12; with number 5 to Fig. 4.14 and Fig. 4.18; with number 6 to Fig. 4.11; with number 7 to Fig. 4.21, Fig. 4.19 and the left panel of Fig. 4.22; and the star with number 8 corresponds to Fig. 4.7, Fig. 4.13, Fig. 4.20 and the right panel of Fig. 4.22.

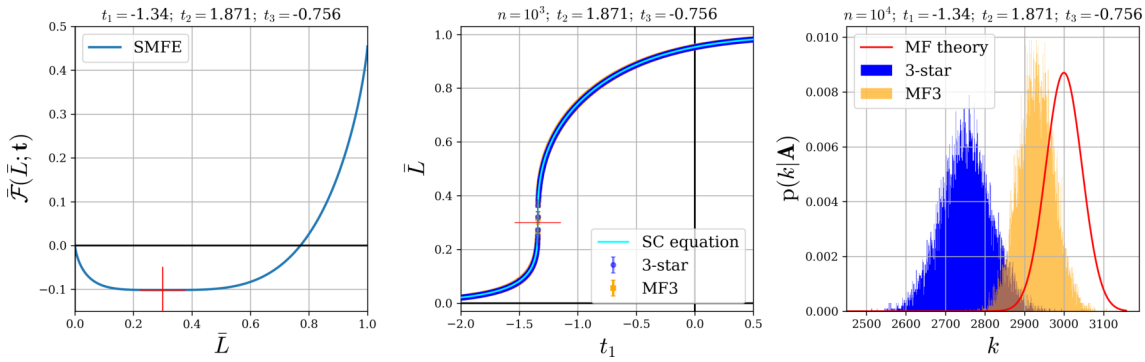

Fig. 4.11: From left to right: the SMFE; the connectance; and the degree distributions at the critical point occurring at $\bar{L} = 0.3$ (shown as red crosses in the left and middle panels) in the corresponding 3-star and MF3 models. Due to large fluctuations the degree distributions of single samples from the corresponding 3-star and MF3 models do not match well but still appear in a bell-like shape with exponential tails.

$t_k > 0$ for all $2 \leq k \leq q$

$$\frac{d^2\bar{\mathcal{E}}(\bar{L};\mathbf{t})}{d\bar{L}^2} < 0 \;\forall \bar{L} \in [0,1], \tag{4.110}$$

meaning that $\bar{\mathcal{E}}(\bar{L};\mathbf{t})$ may only have (local) minima on the boundaries of the domain, where the entropic term $TS(\bar{L})$ becomes significant even when $T \to 0$ causing the corresponding (local) minima of the free energy (4.71) to shift inside the domain from the boundaries[12]. However, the value of this shift decreases when the temperature gets lower, which explains why the connectance of ERGMs with strong positive couplings can only be close to either $\bar{L} = 0$ or $\bar{L} = 1$.

Consider, for instance, the MF model with $q = 2$ and $t_2 > 1$, whose susceptibility

$$\frac{\partial \bar{L}}{\partial t_1} = \left[\frac{1}{2\bar{L}(1-\bar{L})} - 2t_2\right]^{-1} \tag{4.111}$$

is negative whenever

$$\frac{1}{2} - \frac{1}{2}\sqrt{1-\frac{1}{t_2}} < \bar{L} < \frac{1}{2} + \frac{1}{2}\sqrt{1-\frac{1}{t_2}}, \tag{4.112}$$

meaning that the corresponding solution is unstable. From (4.112) it is clear that for large positive t_2 the connectance of (meta)stable macrostates can only be very close to either zero or one, i.e. the allowed connectance bands are narrow.

In applied studies [Robins, Snijders, Wang, Handcock and Pattison (2007)] it is often necessary to have relatively large positive values for some of the couplings; thus, ERGMs with only one coupling parameter are usually insufficient, since the desired connectance often belongs to the unstable region of the model. However, as pointed out in [Snijders et al. (2006); Robins, Snijders, Wang, Handcock and Pattison (2007)], the models with multiple higher-order terms in the Hamiltonian allow some parameters to be largely positive without bringing the system to the "near degenerate" state [Handcock (2003)] described above. This is possible due to the presence of potentially negative terms which can compensate the largely positive ones, and we will now look at how this works when $q = 3$ (while in Section 4.6.3 and Section 4.6.4 we will see how this works in the models of higher and infinite orders).

It is easy to see that the SMFE of the MF model (4.42) with $q = 3$ is at most cubic polynomial in $\bar{L}$, which may have either one or two minima on $\bar{L} \in [0,1]$ (unless $\mathbf{t} = \mathbf{0}$, which is trivial) and, unlike the case of $q = 2$, there can be a (local) minimum in the bulk of the domain for any value of t_2. This (local) minimum corresponds to a (meta)stable macrostate whose connectance at low temperatures does not have to be close to either 0 or 1. To find the range of the parameters for

[12] This can be easily seen using the graphical analysis from Section 4.4.3 since $d\bar{\mathcal{E}}(\bar{L};\mathbf{t})/d\bar{L} = -\mathcal{P}(\bar{L};\mathbf{t})$.

which it is the case, one needs to consider the stationarity condition for the specific microcanonical internal energy, i.e.

$$\frac{d\bar{\mathcal{E}}(\bar{L};\mathbf{t})}{d\bar{L}} = -2\left(3t_3\bar{L}^2 + 2t_2\bar{L} + t_1\right) = 0, \tag{4.113}$$

whose roots (assuming $t_3 \neq 0$) are given by

$$\bar{L}_{1,2} = \frac{-t_2}{3t_3} \pm \frac{\sqrt{t_2^2 - 3t_1t_3}}{3t_3}. \tag{4.114}$$

Since we are interested in finding the (local) minima, we need the root on which $\frac{d^2\bar{\mathcal{E}}(\bar{L};\mathbf{t})}{d\bar{L}^2} \geq 0$, which is

$$\bar{L}_{+} = \frac{-t_2}{3t_3} - \frac{\sqrt{t_2^2 - 3t_1t_3}}{3t_3}. \tag{4.115}$$

Note that if t_1 is arbitrary, then $\sqrt{t_2^2 - 3t_1t_3}$ is an arbitrary nonnegative number, which means that, if $t_3 > 0$, then $-t_2/(3t_3)$ should be greater than zero in order to make it possible for $\bar{L}_+$ to be inside the interval $(0,1)$ for some values of t_1. If $t_3 < 0$, then $-t_2/(3t_3)$ should be less than one in order to make it possible for $\bar{L}_+$ to be inside the interval $(0,1)$ for some values of t_1. Finally, if $t_3 = 0$, then $\bar{\mathcal{E}}(\bar{L};\mathbf{t})$ is quadratic in $\bar{L}$, hence the existence of a (local) minimum inside $(0,1)$ interval for some values of t_1 requires $t_2 < 0$. The above constraints combine into the following Boolean expression

$$(t_3 \geq 0 \wedge t_2 < 0) \vee (t_3 < 0 \wedge t_2 < -3t_3), \tag{4.116}$$

which can be reduced to

$$t_2 < 0 \vee t_2 < -3t_3 \tag{4.117}$$

and gives the conditions under which for certain values of t_1 there is a (local) minimum of the internal energy for $\bar{L} \in (0,1)$, meaning that even in the $T \to 0$ limit the model has stable macrostates of moderate connectance. The region of narrow stability bands, obtained as the complement of (4.117), is shown in green in Fig. 4.10, and at low temperatures in this region the phase transitions are always described well by the expressions (4.104) and (4.105) derived under the deep $(0,1)$-bistability assumption. Note that in order for the model to exhibit wide connectance bands, the parameters t_2 and t_3 should necessarily be of opposite signs.

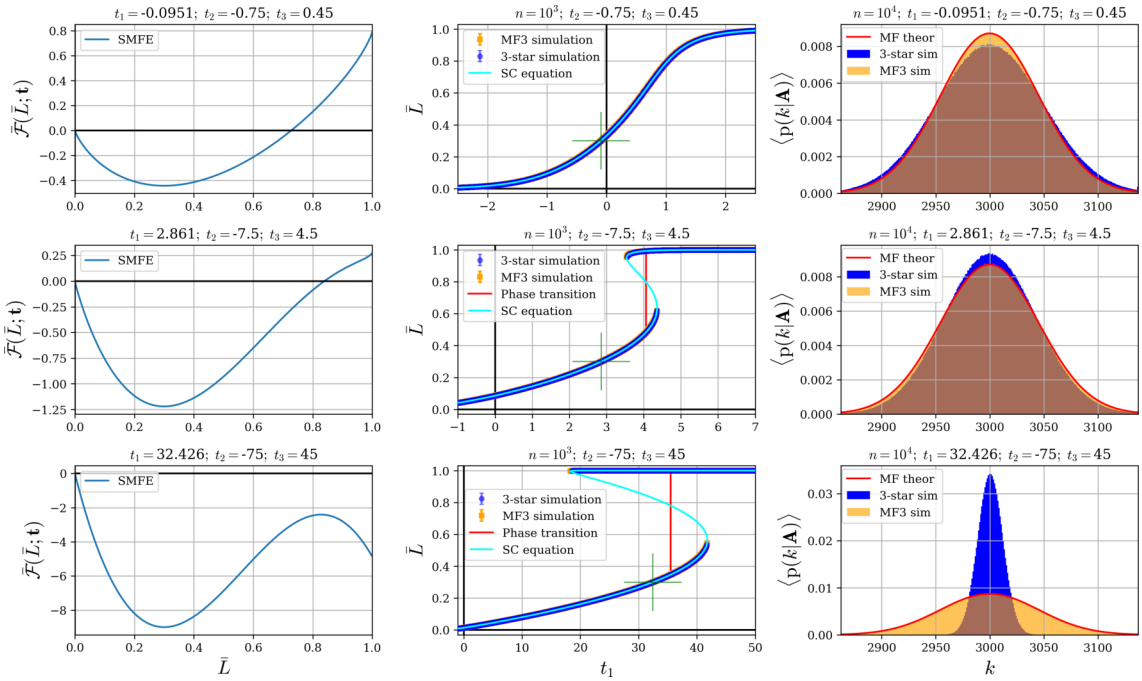

Fig. 4.12: From left to right: the SMFEs; the t_1-dependencies of the connectance; and the degree distributions of the 3-star and MF models. The parameters t_2 and t_3 scale by a factor of 10 from row to row while the parameter t_1 in the left and right panels changes in accordance with (4.47) to keep $\bar{L}$ fixed at 0.3 (the green crosses in the middle panels). It can be seen that the dependence of the connectance on t_1 for both 3-star and MF models matches the equation of state (4.47); however, the degree distribution of the 3-star model tends to be slightly wider than that of its corresponding MF3 model at high temperatures, but narrows down at low temperatures unlike the degree distribution of the MF model that remains the same.

4.6.1.4 Distributions of local features

An alternative way of looking at the q-star model comes from the fact that the number of q-stars of a given node i can be evaluated as

$$\mathcal{S}_q(k_i) = \begin{cases} \binom{k_i}{q}, & 0 \le q \le k; \\ 0, & \text{otherwise}, \end{cases} \tag{4.118}$$

which is a degree-q polynomial in the node's degree k_i. Thus, the Hamiltonian of the 3-star model can be written as

$$H_3(\mathbf{A}) = -\kappa_1 \sum_{i=1}^{n} k_i - \frac{\kappa_2}{2n} \sum_{i=1}^{n} k_i^2 - \frac{\kappa_3}{6n^2} \sum_{i=1}^{n} k_i^3, \tag{4.119}$$

where

$$\kappa_1 = \tau_1 - \frac{\tau_2}{2n} + \frac{\tau_3}{3n^2};\ \kappa_2 = \tau_2 - \frac{\tau_3}{n};\ \kappa_3 = \tau_3.$$

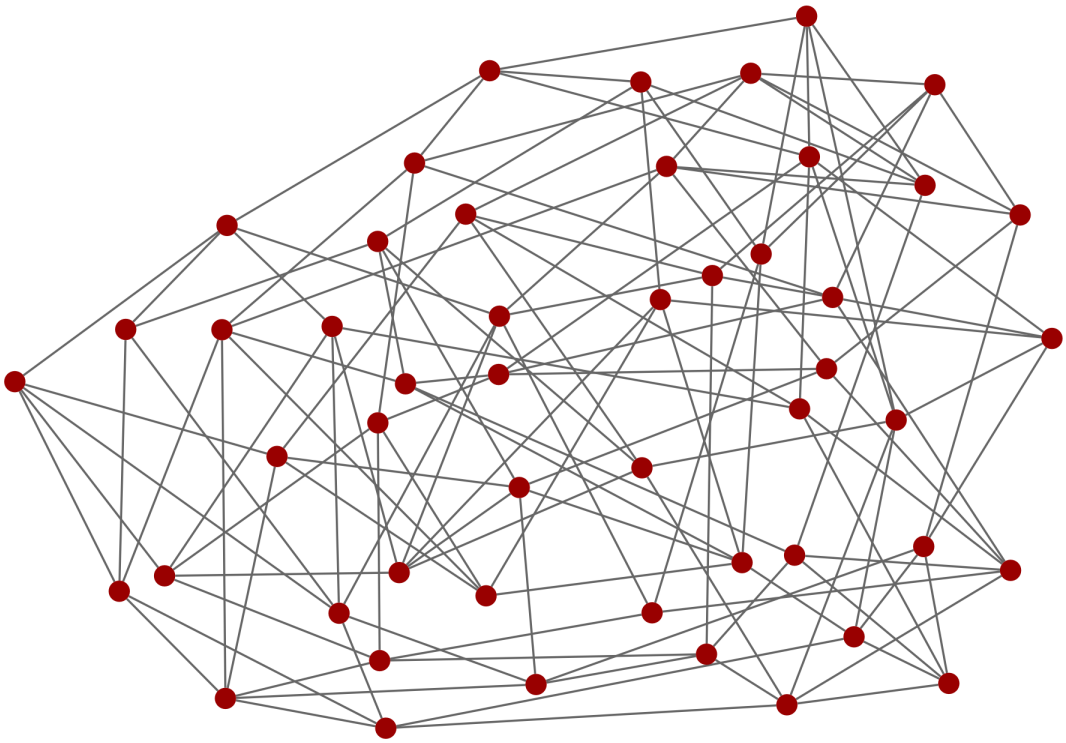

Fig. 4.13: A sample from the 3-star model of 50 nodes with the corresponding MF parameters $t_1 = 13.151388$, $t_2 = -75$, $t_3 = 25$, for which the unique solution of the self-consistency equation is $\bar{L} = 0.1$. The connectance of the sample $L = 131/1225 \approx 0.107$, which is close to the predictions of the self-consistency equation. Note that due to low temperature, the degree distribution is narrow (2 nodes with degree 4, 34 nodes with degree 5, 14 nodes with degree 6). The global clustering coefficient is 0.0266904, and the average local clustering coefficient is 0.0773333, which is close to the corresponding expectations in the ER model of the same connectance.

The expression (4.119) emphasises another nature of the q-star model, being the maximum-entropy ensemble with soft constraints on the sums of powers of nodes' degrees[13], which makes it interesting to consider the degree distributions of the graphs drawn from this ensemble.

Another microscopic property we consider is the local clustering coefficient (4.12), since in the following Section 4.6.2 we look at the triad model, whose Hamiltonian includes the contributions from 2-stars and the term proportional to the number of triangles in the graph, and it is interesting to see how the LCCs behave in the 3-star model where the triangle-counting term is replaced by the 3-star term[14].

As can be seen in Fig. 4.12 and Fig. 4.14, in general, the degree distributions of the corresponding 3-star and MF3 models do not match despite the agreement of the expected average degrees (pro-

[13] These sums of powers of nodes' degrees are, thus, an alternative set of sufficient statistics.
[14] As clear from (4.3), there can be no other third-order terms in Markov ERGMs.

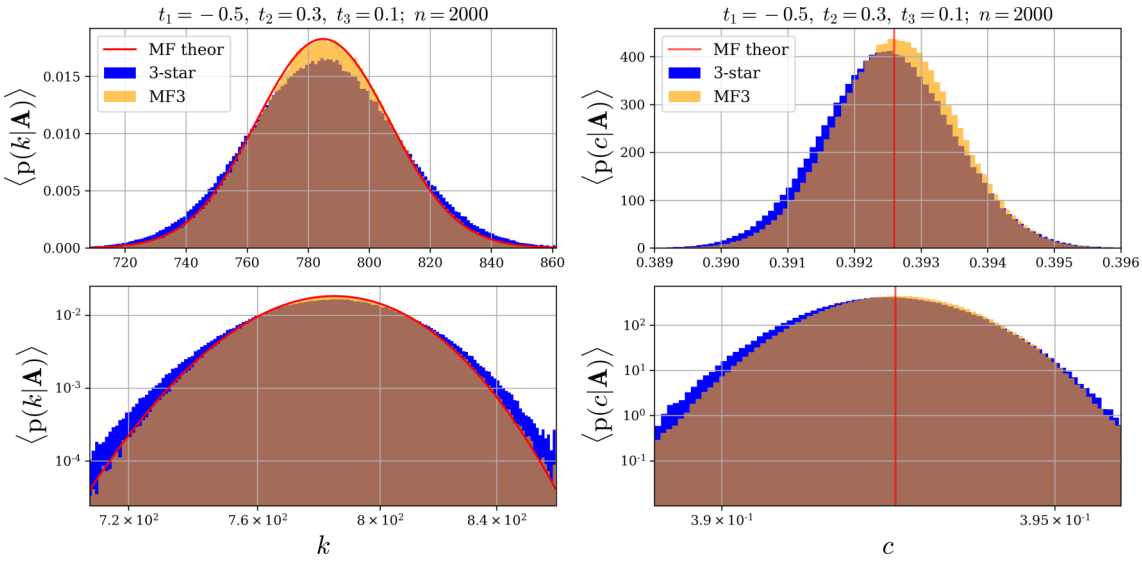

Fig. 4.14: Expected distributions of the degrees (left) and the local clustering coefficients (right) of the corresponding 3-star and MF3 models at $t_1 = -0.5,\ t_2 = 0.3,\ t_3 = 0.1$. The expected degree distribution of the MF3 model is described well by the expression (4.120) (red curve in the left panels). The vertical red lines in the right panels show the expected LCC obtained from the expression (4.13). The expected degree distribution of the 3-star model in this case is wider than that of the corresponding MF3 model, but the averages match well. The tails of the distributions seem to decay exponentially in both cases, as can be seen in the lower log-log plots.

portional to $\bar{L}$). As discussed in Section 4.4.9, the degree distribution of the MF3 model follows that of the ER model of matching connectance, i.e. the binomial distribution (4.11), which for large graphs of moderate connectance can be approximated by the following Gaussian

$$\langle \mathrm{p}(k|\mathbf{A}) \rangle = \sqrt{\frac{1}{2\pi n \langle \bar{L} \rangle (1 - \langle \bar{L} \rangle)}} \exp\left(-\frac{(k - \langle \bar{L} \rangle n)^2}{2n \langle \bar{L} \rangle (1 - \langle \bar{L} \rangle)} \right). \tag{4.120}$$

Conversely, the q-star model, in general, does not have this kind of degeneracy of the ground macrostate, and at low temperatures produces almost regular graphs (Fig. 4.12, Fig. 4.15, Fig. 4.13) with the average degree $\langle k \rangle = \bar{L}(n-1)$ that minimises its internal energy consistently with the MFT predictions for connectance. This is an example of a "frozen" behaviour, in which the specific entropy of the macrostate is very low.

The fact that degree distributions of the q-star model may also be wider than predicted by (4.11) (Fig. 4.14, Fig. 4.12) could be explained by the tendency of the q-star model with the positive couplings to create hubs [Annibale and Courtney (2015)], i.e. nodes with high degrees and, therefore, high star counts. The reason for this tendency comes from the nonlinear dependence of the Hamiltonian (4.119) on the degrees, which makes the high-degree nodes energetically favourable.

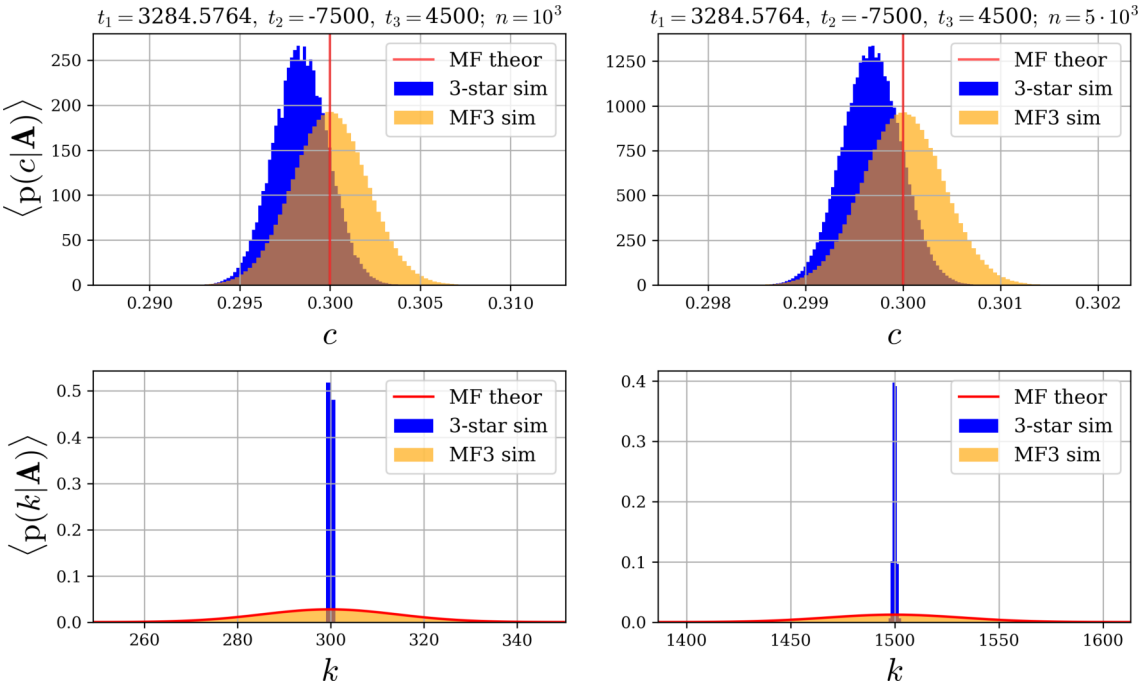

Fig. 4.15: Expectations of the degree (bottom) and LCC (top) distributions of the corresponding 3-star and MF3 models with 1000 and 5000 nodes at extremely low temperature ($t_1 = 3284.576351$, $t_2 = -7500$, $t_3 = 4500$). The degree distribution of the 3-star model is almost degenerate at the average value predicted by the MFT, while the degree distribution of the MF3 model obeys the predictions (4.120). The LCC distributions of both models keep a finite width at low temperatures and differ in shape, although, as expected, they become narrower with n approaching (4.13) in the thermodynamic limit.

However, this explanation is vague and the effect never results in the long-tailed degree distributions due to the fact that, when the parameters are too high (or too low), the model "freezes" in one of its low-entropy macrostates corresponding to almost regular graphs.

The degree distributions of the corresponding 3-star and MF3 models on the critical curve are shown in Fig. 4.11, and in this case their significant discrepancy is mainly due to large fluctuations.

The LCC distributions of the 3-star and MF3 models (Fig. 4.14, Fig. 4.15) are different in shape, but both get narrower with n approaching in the thermodynamic limit the average LCC of the ER model given by (4.13). Similarly to the degree distributions, depending on the parameters, LCC distributions of the 3-star model may be slightly wider (Fig. 4.14) or narrower (Fig. 4.15) than that of the corresponding MF3 model, but the tails of the distributions are exponential in both models. In contrast to the 3-star model's degree distribution, the LCC distributions of both models do not become degenerate even at very low temperatures (apart from the cases when $\bar{L} \simeq 0$ and $\bar{L} \simeq 1$).

This is due to the fact that the Hamiltonian $H_3(\mathbf{A})$ takes the same value on graphs with different triangle counts; thus the ground macrostate of the MF3 model is degenerate on the number of triangles as long as it does not correspond to an empty or complete graph.

4.6.2 Triad model

Triad model is another special case of homogeneous Markov ERGMs for which $\tau_i = 0$ for all $i > 2$. Hence, it is defined by the following Hamiltonian

$$H_t(\mathbf{A}) = -2\tau_1 L(\mathbf{A}) - \frac{\tau_2}{n}\mathcal{S}_2(\mathbf{A}) - \frac{6\theta}{n}\mathcal{T}(\mathbf{A}). \tag{4.121}$$

As follows from (4.28), the corresponding self-consistency equation reads as

$$\bar{L} = \frac{1}{2}\left[1 + \tanh\left(\tau_1 + \frac{n-2}{n}\tau_2\bar{L} + 3\frac{n-2}{n}\theta\bar{L}^2\right)\right], \tag{4.122}$$

and the correspondence with the MF model is given by

$$t_1 = \tau_1; \quad t_2 = \frac{n-1}{2n}\tau_2; \quad t_3 = \frac{n-2}{n}\theta. \tag{4.123}$$

4.6.2.1 Observables of the triad model

Since the triangle counts in the networks grow rapidly with n, it is easier to work with their rescaled version

$$\mathfrak{T}(\mathbf{A}) \equiv \frac{6}{n(n-1)(n-2)}\mathcal{T}(\mathbf{A}) \in [0,1], \tag{4.124}$$

in terms of which the MFT predictions (4.25) and (4.26) read as

$$\langle\mathfrak{S}_1\rangle = \langle\bar{L}\rangle; \quad \langle\mathfrak{S}_2\rangle = \langle\bar{L}\rangle^2; \quad \langle\mathfrak{T}\rangle = \langle\bar{L}\rangle^3, \tag{4.125}$$

meaning that these observables are intensive. From (4.125) it is clear that the triad model, defined by the Hamiltonian (4.121), is scalable in the sense of Definition 1; thus there exists a meaningful thermodynamic limit.

As can be seen in Fig. 4.16, the time-averaging MC simulations for large networks agree well

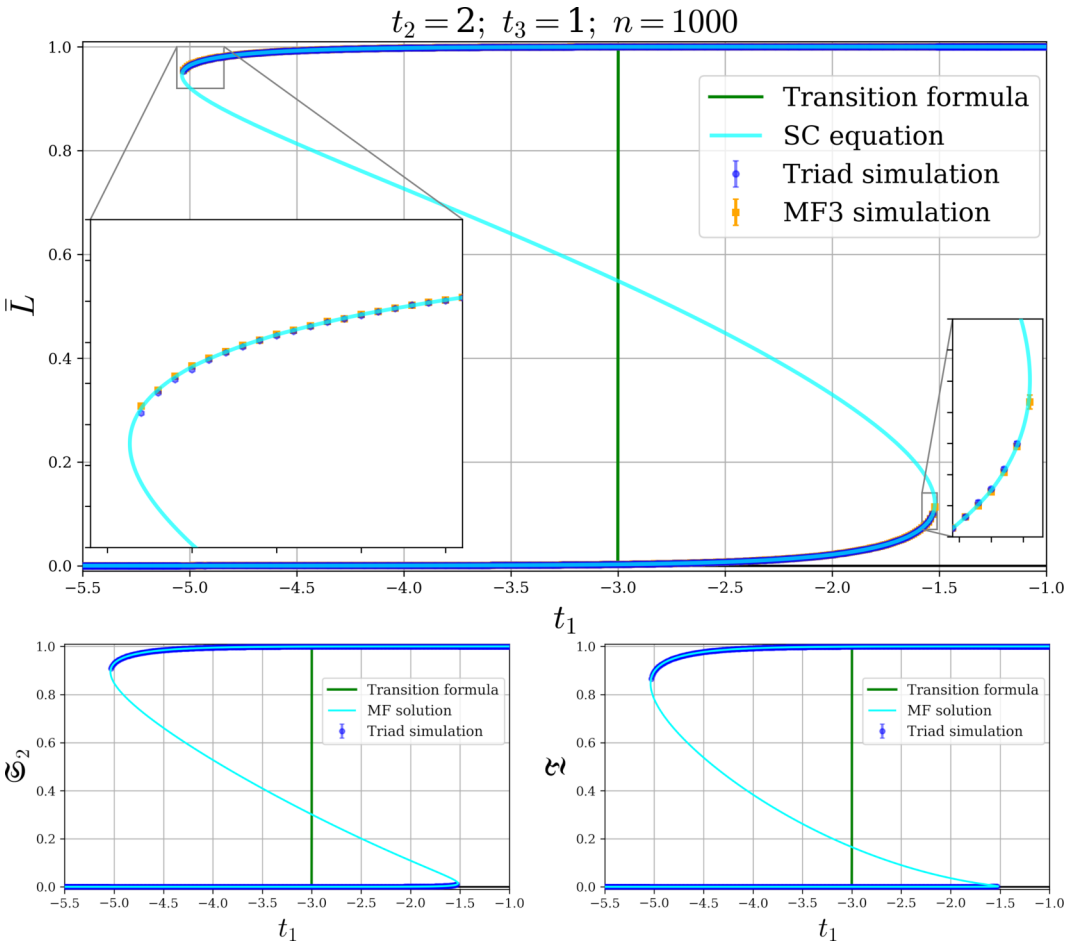

Fig. 4.16: Numerical solution of the self-consistency equation (4.47) and the results of the time-averaging MC simulations for the corresponding triad and MF models with 10^3 nodes. The theory seems to be precise apart from the small deviations of the triad model near the spinodal points, which decrease when the network size increases. The branch of the hysteresis on which $\bar{L}$ decreases with t_1 is unstable due to the negative susceptibility and corresponds to the (local) maximum of the SMFE. The predictions of the transition formulas (4.33) and (4.34) are shown in green.

with (4.125), which is not surprising because, as discussed in Section 2.2.2.1, the MFT is believed to be exact at predicting the observables of the infinite-dimensional systems in the thermodynamic limit. Furthermore, as can be seen in Fig. 4.17, even for small networks the mean field theory seems to work well away from the transition region where it predicts a discontinuous jump instead of a smooth transition for finite systems.

4.6.2.2 Distributions of local features

As can be seen in Fig. 4.18, the degree and LCC distributions of the high-temperature triad model are similar to those of the 3-star model from Fig. 4.14. The reason why the average LCC in Fig.

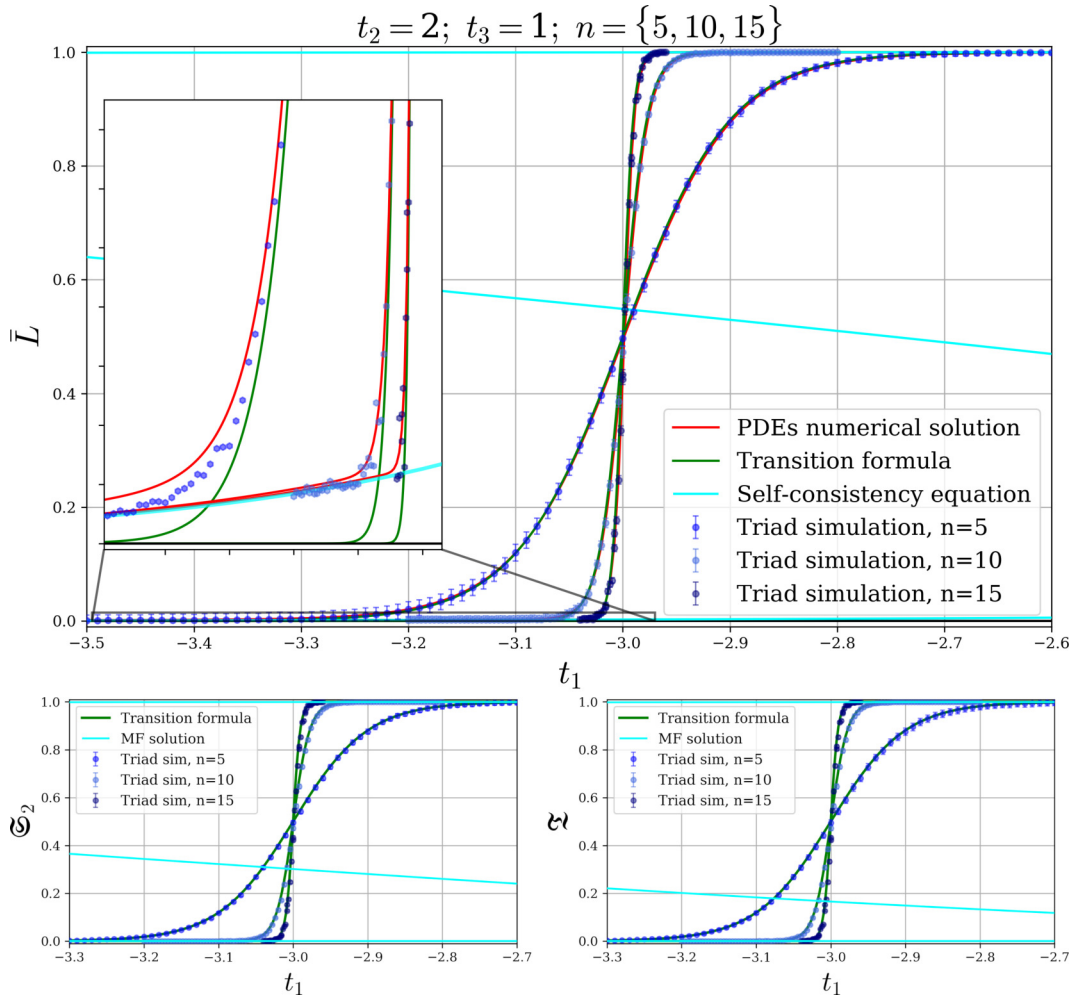

Fig. 4.17: Results of the ensemble-averaging MC simulations for triad models of 5, 10 and 15 nodes together with the MFT predictions (4.125) in which $\bar{L}$ is computed using (4.47) (cyan line), transition formulas (4.33) and (4.34) (green lines) and the numerical solution of the hierarchy (4.59) discretised by central differences in space with RK4 time stepping (red line). As can be seen on the upper plot, the numerical solution of (4.59) and the simulations agree with each other and follow the branches of the MFT hysteresis away from the transition region. The transition formula (4.33) also agrees with simulations reasonably well but does not follow the actual branches of the hysteresis due to the (0,1)-bistability assumption used in its derivation. The statistical errors are estimated as weighted combinations of presumably Gaussian fluctuations around the (meta)stable states with binomial fluctuations arising from the transitions between these two macrostates. Error bars on the insert plot for $\bar{L}$ are not shown to enhance visibility, and seem to be overestimated away from the transition region, since the fluctuations near $\bar{L} = 0$ and $\bar{L} = 1$ are, clearly, not Gaussian due to the proximity to the border of the domain.

4.18 is slightly higher than its MFT predictions can be explained by the positive parameter θ, which makes the formation of triangles energetically favourable. This difference increases further when the parameter τ_2 is negative while the parameter θ is positive, as can be seen in Fig. 4.19, which can be explained by the fact that in such model it is energetically favourable to have a large number of

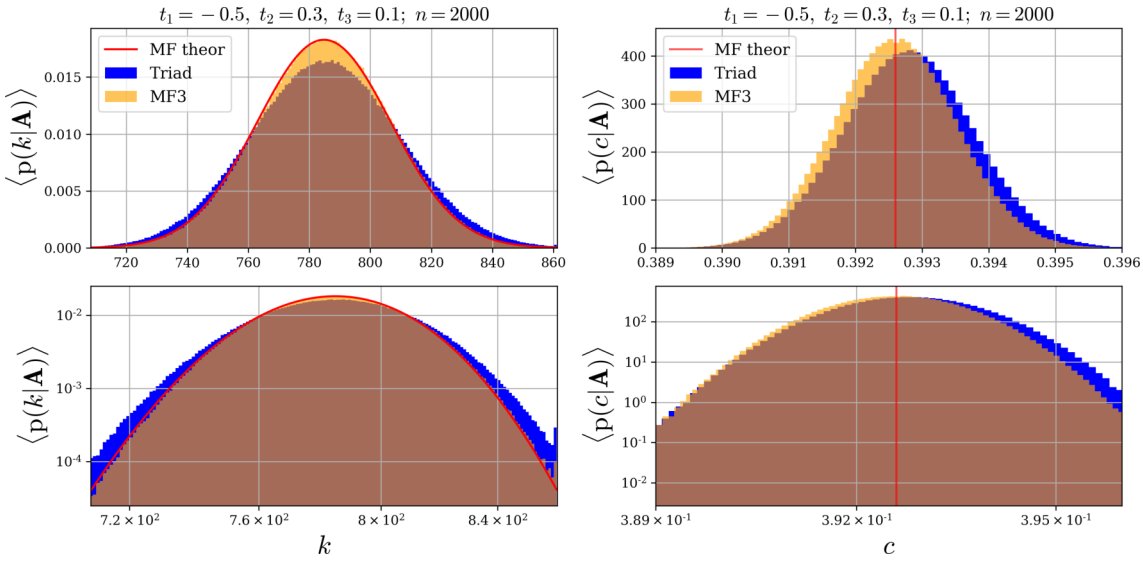

Fig. 4.18: Expected distributions of degrees (left) and local clustering coefficients (right) of the triad and MF3 models of $2 \cdot 10^3$ nodes at $t_1 = -0.5,\ t_2 = 0.3,\ t_3 = 0.1$ (compare with Fig. 4.14). The expected degree distribution of the MF3 model is described well by (4.120) (red curve in the left panels). The vertical red lines in the right panels show the expected LCC obtained from the expression (4.13). The expected degree distribution of the 3-star model in this case is wider than that of the corresponding MF3 model, but the expected average degrees of the models match well. The tails of the distributions seem to decay exponentially in both cases, as can be seen from the log-log plots in the lower panels.

triangles while having the lowest possible number of 2-stars, i.e. maximising the global clustering coefficient (4.15) which, as discussed in Section 4.1.2.2, should[15] be close to the average LCC, and thus, having positive θ at negative τ_2 pushes the LCC distributions to the right. Moreover, when in such triad model the temperature gets too low, the individual samples decompose into several highly connected components, as shown in Fig. 4.20, meaning that LCCs of all nodes in such samples become close or equal to one. This interesting phenomenon is discussed in the next section.

4.6.2.3 Finite-size effects

In simulation studies discussed in [Frank and Strauss (1986), Strauss (1986)] it was observed that when the parameter θ is large, the triad model enters the so-called degenerate state[16], in which it produces samples that consist of the highly connected components with little or no links between them (Fig. 4.20). An attempt to explain this behaviour was taken in [Park and Newman

[15] Because, as can be seen in Fig. 4.18, the LCC distributions are quite narrow.
[16] Detailed discussion of the degeneracy in ERGMs is given in [Handcock (2003)].

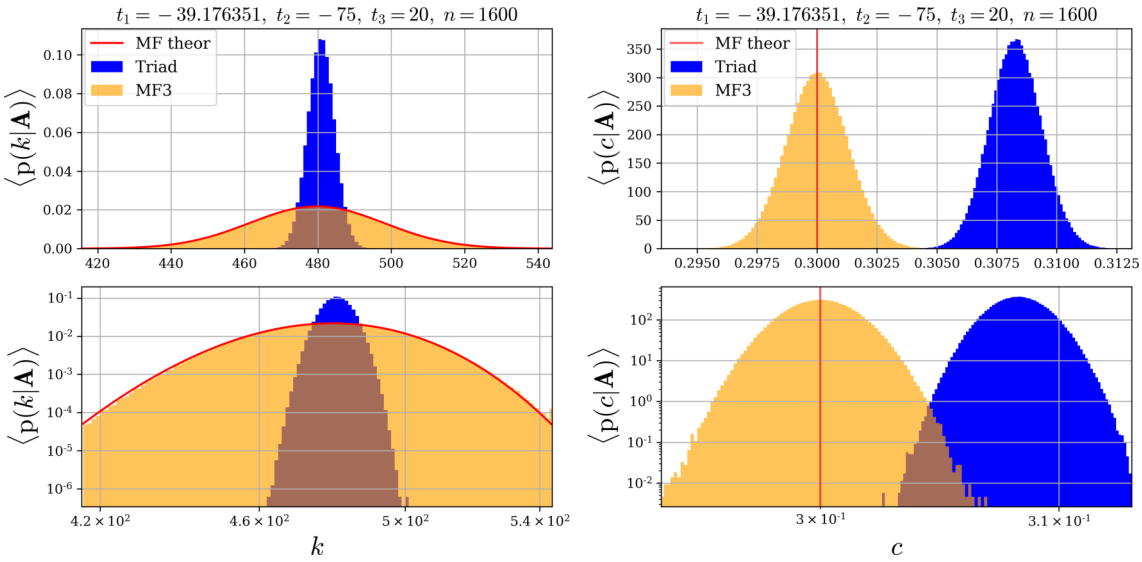

Fig. 4.19: Expected degree distribution (left) and LCC distribution (right) of the triad and MF3 models of 1600 nodes at $t_1 = -39.176$, $t_2 = -75$, $t_3 = 20$ (see Fig. 4.21 and Fig. 4.10). The degree distribution of the MF3 model is described well by (4.120) (red curve in the left panels), while the degree distribution of the triad model is much narrower, which can, probably, be explained by the existence of an optimal degree that minimises the internal energy (compare with Fig. 4.12). Vertical red lines in the right panels show the expected LCC given by (4.13), and the simulation results for the MF3 model agree well with this prediction, while the average LCC of the triad model is significantly higher, which is the desired effect coming from the tendency of a triad model with positive θ to form triangles, although, as can be seen in Fig. 4.21, this difference decreases when the network size increases. Note that the widths of the LCC distributions of the triad and MF3 modes are comparable, and all the distributions decay exponentially, as can be seen from the log-log plots from the lower panels.

(2005)], where the mean field theory was applied to the triad model with $\tau_2 \equiv 0$ for which[17], as clear from (4.103), the corresponding MF model has only two parameters: t_1 and t_3, that are not identically zero. As clear from the discussion in Section 4.6.1.2, the MF3 model with $t_2 = 0$ exhibits bistability at certain values of t_1 when[18] $t_3 > 9/16$, and in [Park and Newman (2005)] such bistability was interpreted as being responsible for the degenerate state reported by Strauss. However, while this, of course, is an example of degeneracy, from the condition (4.117) and Fig. 4.10 it is clear that when $t_2 = 0$, a model of order three may only have bistability with narrow connectance bands, meaning that for large t_3 such a model can only produce nearly empty or complete graphs, which by no means resembles the interesting behaviour reported in [Frank and Strauss (1986), Strauss (1986)], where the sample graphs have very high clustering at moderate connectance. Furthermore, as can be seen in Fig. 4.10, the parameters t_2 and t_3

[17] In [Park and Newman (2005)] this model is named "Strauss's models of clustering".
[18] This comes from the criticality condition (4.109) for $t_2 = 0$, i.e. $\bar{L} = 2/3$ (Fig. 4.10).

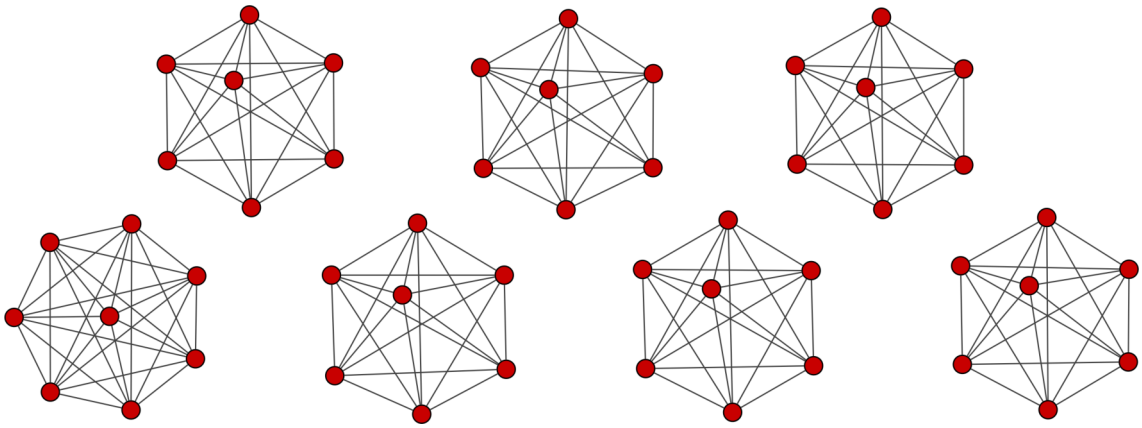

Fig. 4.20: A sample from the triad model of 50 nodes with the corresponding MF parameters $t_1 = 13.151388, t_2 = -75, t_3 = 25$ for which the unique solution of the self-consistency equation is $\bar{L} = 0.1$. The connectance of the sample $\bar{L} = 154/1225 \approx 0.126$, which is significantly higher than predicted by the self-consistency equation. Note that despite the fact that the parameters t_2 and t_3 are below the critical curve, the model is in "degenerate state" described in [Frank and Strauss (1986)], and the sample network consists of 6 fully connected components with 7 nodes, and one fully connected component with 8 nodes, hence the narrow degree distribution (42 nodes with degree 6 and 8 nodes with degree 7), and the average local clustering coefficient together with the global clustering coefficient are both equal to one.

used in obtaining the sample graph from Fig. 4.20 are below the critical curve, meaning that such behaviour can be observed even in the 1-stable regime of the triad model, in which it bluntly violates the MFT predictions (4.25). However, since, as discussed in Section 2.2.2.1, for infinite-dimensional systems the MFT is believed to be exact in the thermodynamic limit, this behaviour should merely be a finite-size effect as long as the model is scalable[19], and in this section we demonstrate how this degenerate state disappears with the increasing size of the model.

From the expression (4.13) for the expected local clustering coefficients of the ER model, it is clear that, if the model obeys the predictions of the linearised theory (such as the MFT), its average LCC should be approximately equal to its connectance when n is large. This makes it useful to plot the connectance alongside the average LCC in order to see if there are any significant deviations in clustering from what the ER model of matching connectance would have. This is shown in Fig. 4.21 and Fig. 4.22, from which it is clear that at low temperatures there are strong deviations from the MFT predictions, but these deviations tend to disappear as the size of the model increases.

The reason why at low temperatures the model enters the degenerate state is relatively clear since

[19] Which is needed for the existence of a meaningful thermodynamic limit.

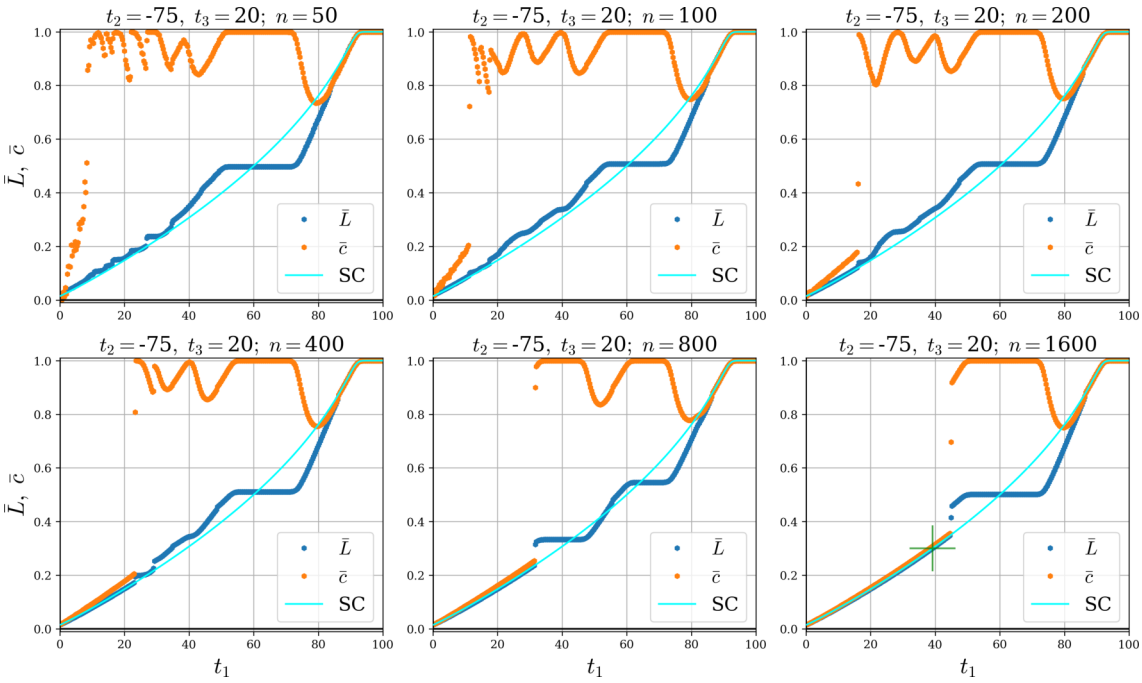

Fig. 4.21: The dependencies of the connectance and the average LCC on t_1 for low-temperature triad models of different sizes. Despite the fact that the parameters t_2 and t_3 are in the 1-stability region (below the critical curve from Fig. 4.10), the model enters the degenerate state described in [Strauss (1986)] and decomposes into several highly connected components with a few or no links between them (Fig. 4.20). Note how the onset of "degeneracy" shifts to the right with the increasing size of the model, which is consistent with Fig. 4.22. The green cross in the bottom right panel shows the position of Fig. 4.19.

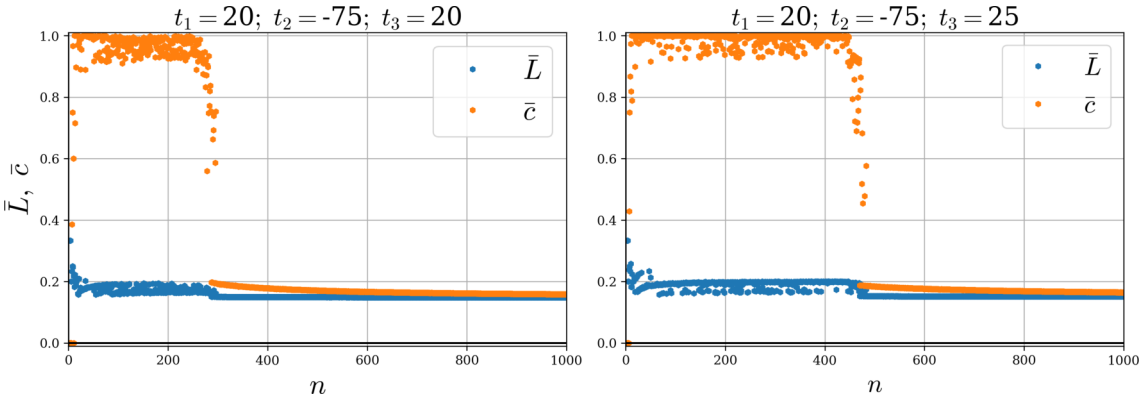

Fig. 4.22: The dependencies of the connectance and the average LCC on the number of nodes of the triad models with the corresponding MF parameters $t_1 = 20$, $t_2 = 75$, $t_3 = 20$ (left) and $t_1 = 20$, $t_2 = 75$, $t_3 = 20$ (right).

at sufficiently low temperatures the entropy is dominated by the internal energy and, as discussed in the previous section, when the parameter θ is positive while τ_2 is negative, it is energetically favourable to form the triangles while keeping the 2-star counts low and connectance close to its optimal value, which requires breaking the graphs into highly connected clusters. Such clustered

configurations turn out to be very robust since adding a link to the graph, similar to the one from Fig. 4.22, requires connecting two different clusters, which creates many 2-stars without increasing the number of triangles. This explains why in Fig. 4.21 the connectance increases in steps, each of which corresponds to such a robust clustered configuration.

4.6.3 Higher-order models

In this section we briefly look at how well the theory works for the higher-order models which, as discussed in Section 4.4.6 and Section 4.4.7, may exhibit highly complex phase transitions between multiple (meta)stable states. In Fig. 4.23 one can see an example of tristability in the model of order four and how all the (meta)stable branches of the hysteresis can be perfectly recovered by the time-averaging MC simulations of the large-size 4-star model.

As can be seen in the left panel of Fig. 4.24, there is a strong disagreement between the behaviours of the corresponding small-size 4-star and MF models, which demonstrates that the almost perfect match between the models appearing in Fig. 4.8 is a mere consequence of the (0,1)-bistability, under which both models are described well by the transition formula (4.33). Note that despite this disagreement for very small networks, the expected connectance of the corresponding 4-star and MF models quickly approaches the MFT predictions as the network size increases (Fig. 4.24).

Note that the MFT is particularly useful in highly multistable regimes (where the MCMC simulations are slow to converge) because it gives an idea of the inner structure of the hysteresis. For example, in the left panel of Fig. 4.23 the parameter t_1 is scanned from largely negative to largely positive values and the middle branch of the hysteresis is not recovered, which means that in a pure simulation study it could have been missed out[20]. Furthermore, the situation can be worse, as can be seen in Fig. 4.5, where the branch of the hysteresis corresponding to a stable solution for some values of $\mathbf{t}$ is hidden inside the main loop of the hysteresis emerging from the forward and backward time-averaging t_1-scans.

[20]Of course, when scanning the parameters it is possible to run several instances of simulation for every visited $\mathbf{t}$ starting from various initial microstates, but this adds computational cost, and could be unfeasible for models with a large number of independent observables like the MCW model discussed in Chapter 3.

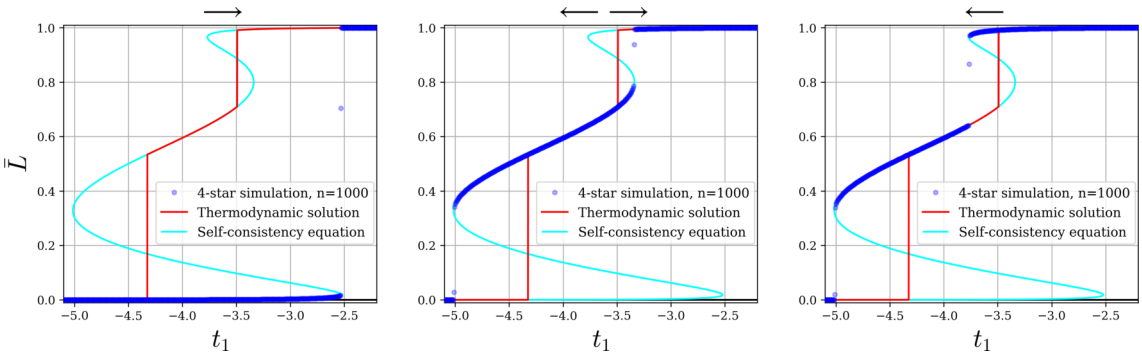

Fig. 4.23: Theoretical predictions along with the time-averaging MC simulations for the 4-star model of 10^3 nodes. All the positive-susceptibility branches of the hysteresis are (meta)stable, thus, recovered in simulations. Note how, when moving forwards in t_1 (left panel), the middle branch of the hysteresis is not visited, but, instead, visited when moving backwards in t_1 (right panel). Simulations from the central panel were done by initialising the system on the middle branch of the hysteresis and scanning t_1 in both directions.

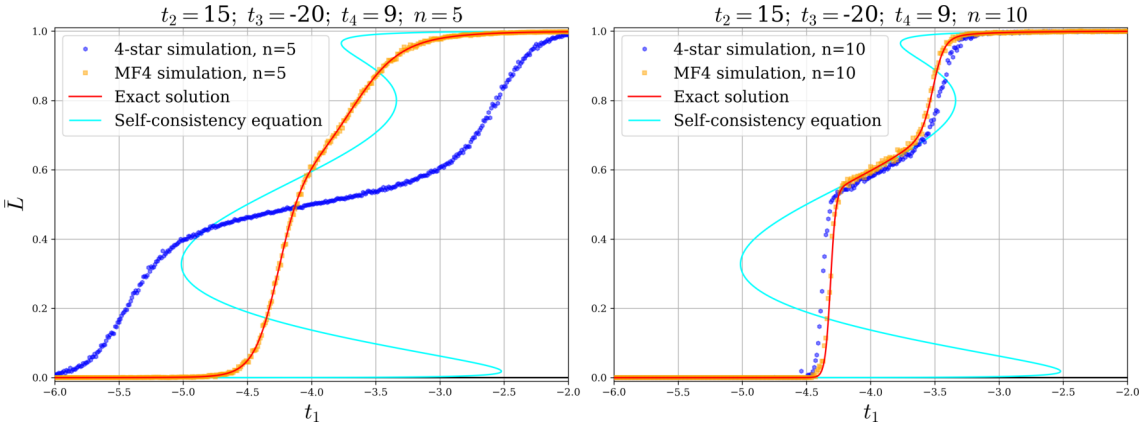

Fig. 4.24: Results of the ensemble-averaging MC simulations for the MF4 models of 5 (left panel) and 10 (right panel) nodes along with the exact theoretical predictions for the expected connectance of the MF4 model, and the thermodynamic equation of state (4.47). It can be seen how the connectances of the small MF4 and 4-star models deviate from each other and from the thermodynamic equation of state (4.47), and how quickly they approach the MFT predictions as the size of the models increases. The exact theoretical predictions are in great agreement with the results of the ensemble-averaging MC simulations.

4.6.4 AKS model

As follows from the previous discussion, when the signs of the parameters $\mathbf{t}$ alternate, the models tend to allow stable macrostates of moderate connectance, which is desirable in fitting them to empirical data. This observation inspired social statistics researchers [Snijders et al. (2006)] to

introduce the so-called "alternating k-stars" statistic[21]

$$\Omega_{AKS}(\mathbf{A};\lambda) = \sum_{k=2}^{n-1}(-1)^k \frac{\mathcal{S}_k}{\lambda^{k-2}}, \tag{4.126}$$

and to consider a model[22] of order $n-1$ defined by the Hamiltonian

$$H_{AKS}(\mathbf{A};\rho,\mu;\lambda) = -\rho\mathcal{S}_1(\mathbf{A}) - \mu\sum_{k=2}^{n-1}(-1)^k \frac{\mathcal{S}_k(\mathbf{A})}{\lambda^{k-2}}, \tag{4.127}$$

where $\lambda > 0$ is a parameter that allows controlling the weight of the higher-order stars. Since, as clear from the MFT predictions (4.26), $\mathcal{S}_k \underset{n\to\infty}{\sim} \mathcal{O}(n^{k+1})$, all the terms in the above Hamiltonian have a different scaling with n, i.e. the model is not scalable. This lack of scalability does not allow considering such models in the thermodynamic limit and makes the direct comparison of the parameters meaningless for the models of different sizes.

To avoid these complications we rescale the parameters of the model as

$$\mu = \frac{\tilde{\mu}}{n}; \quad \lambda = n\tilde{\lambda}, \tag{4.128}$$

in terms of which

$$H_{AKS}(\mathbf{A};\rho,\tilde{\mu};\tilde{\lambda}) = -\rho\mathcal{S}_1(\mathbf{A}) - \frac{\tilde{\mu}}{n}\sum_{k=2}^{n-1}(-1)^k \frac{\mathcal{S}_k(\mathbf{A})}{(n\tilde{\lambda})^{k-2}}. \tag{4.129}$$

As will be shown shortly, the rescaling (4.128) ensures the existence of a meaningful thermodynamic limit without restricting the generality (since the original parameters can always be recovered from the rescaled ones).

Note that if $\tilde{\lambda}$ is treated as a free parameter, then the model is no longer log-linear[23] since it is impossible to factor $\tilde{\lambda}$ out of $\Omega_{AKS}(\mathbf{A};\tilde{\lambda})$ (i.e. $\Omega_{AKS}(\mathbf{A};\tilde{\lambda}) \neq f(\tilde{\lambda})g(\mathbf{A})$). In practice, this simply means that the parameter $\tilde{\lambda}$ should not be treated as being conjugated to an observable, i.e. the expressions like (2.8) are invalid for $\tilde{\lambda}$.

[21] Along with the other statistics, which are not Markovian [Robins, Snijders, Wang, Handcock and Pattison (2007); Snijders et al. (2006)].

[22] Which we call the "AKS model" in this work.

[23] According to [Snijders et al. (2006)] this family of distributions belongs to the *curved exponential class*.

4.6.4.1 Mean field theory for the AKS model

It is clear that the Hamiltonian (4.129) defines a particular restriction of Markov ERGMs (4.3) with

$$\tau_1 = \rho; \quad \tau_k = (-1)^k \frac{\tilde{\mu}}{\tilde{\lambda}^{k-2}}, \quad k > 1; \quad \theta = 0,$$

and the mean field self-consistency equation (4.28) for this model can be written as

$$\langle \bar{L} \rangle_0 = \frac{1}{2} \left(1 + \tanh \left[\rho + \tilde{\mu} \sum_{s=2}^{n-1} \frac{s(n-s)}{n^2(n-1)} \binom{n}{s} \frac{(-1)^s}{(n\tilde{\lambda})^{s-2}} \langle \bar{L} \rangle_0^{s-1} \right] \right),$$

which after the evaluation of the sum in the hyperbolic tangent using the binomial identity becomes

$$\langle \bar{L} \rangle_0 = \frac{1}{2} \left(1 + \tanh \left[\rho + \tilde{\mu}\tilde{\lambda} - \tilde{\mu}\tilde{\lambda} \left(1 - \frac{\langle \bar{L} \rangle_0}{n\tilde{\lambda}} \right)^{n-2} \right] \right), \tag{4.130}$$

which in the thermodynamic limit reads as

$$\langle \bar{L} \rangle_0 \underset{n\to\infty}{\sim} \frac{1}{2} \left(1 + \tanh \left[\rho + \tilde{\mu}\tilde{\lambda} \left(1 - \mathrm{e}^{-\langle \bar{L} \rangle_0 / \tilde{\lambda}} \right) \right] \right).$$

Evaluation of the mean field prediction for the $\Omega_{AKS}(\mathbf{A}; \tilde{\lambda})$ is done using (4.26) i.e.

$$\langle \Omega_{AKS}(\mathbf{A}; \tilde{\lambda}) \rangle_0 = \sum_{k=2}^{n-1} (-1)^k \binom{n-1}{k} \frac{\langle \bar{L} \rangle_0^k}{(n\lambda)^{k-2}},$$

which, using the binomial identity, can be expressed as

$$\langle \Omega_{AKS}(\mathbf{A}; \tilde{\lambda}) \rangle_0 = (n\tilde{\lambda})^2 \left(1 - \frac{\langle \bar{L} \rangle_0}{n\tilde{\lambda}} \right)^{n-1} + n(n-1)\tilde{\lambda}\langle \bar{L} \rangle_0 - (n\tilde{\lambda})^2,$$

which in the thermodynamic limit scales as $\mathcal{O}(N)$, meaning that the model defined by the Hamiltonian (4.129) is, indeed, scalable. For the specific AKS observable $\bar{\Omega}_{AKS}(\mathbf{A}; \tilde{\lambda}) = \Omega_{AKS}(\mathbf{A}; \tilde{\lambda})/N$, in the thermodynamic limit we obtain

$$\langle \bar{\Omega}_{AKS}(\mathbf{A}; \tilde{\lambda}) \rangle_0 \underset{n\to\infty}{\sim} 2\tilde{\lambda}\langle \bar{L} \rangle_0 - 2\tilde{\lambda}^2 \left(1 - \mathrm{e}^{-\langle \bar{L} \rangle_0 / \tilde{\lambda}} \right). \tag{4.131}$$

The family of solutions of the thermodynamic self-consistency equation (4.131) is shown in Fig. 4.25. Note the large width of the high-$\tilde{\mu}$ stability bands for small $\tilde{\lambda}$, which may be a part of the

reason why infinite-order models showed superior results in fitting the empirical data compared to finite-order Markov ERGMs considered in [Robins, Snijders, Wang, Handcock and Pattison (2007); Snijders et al. (2006)]. The narrowness of the high-$\tilde{\mu}$ stability bands for relatively large $\tilde{\lambda}$ can be explained by the fact that with growing $\tilde{\lambda}$ the contributions of the higher-order stars in the AKS statistic decrease, and the model approaches the 2-star model for which the low-temperature stability bands are narrow as long as the parameter τ_2 is positive.

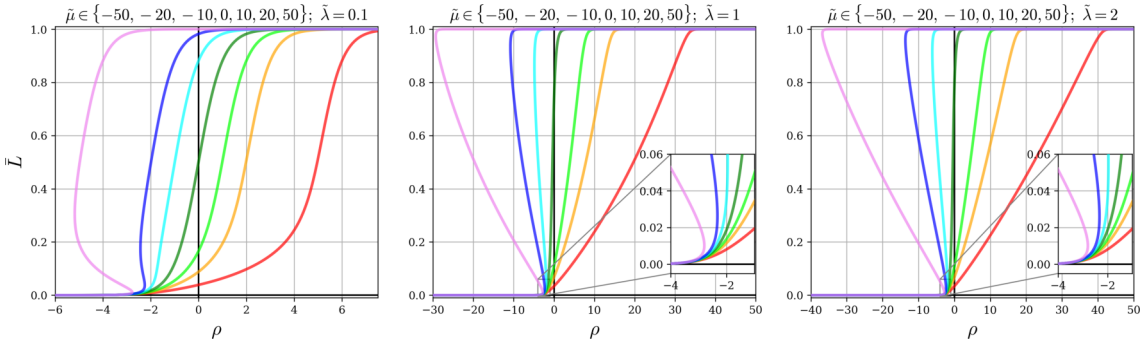

Fig. 4.25: The families of solutions of the thermodynamic self-consistency equation (4.131) for $\tilde{\lambda} = 0.1$ (left), $\tilde{\lambda} = 1$ (center) and $\tilde{\lambda} = 2$ (right) for $\tilde{\mu} = -50$ (red), $\tilde{\mu} = -20$ (orange), $\tilde{\mu} = -20$ (lime), $\tilde{\mu} = 0$ (green), $\tilde{\mu} = 10$ (cyan), $\tilde{\mu} = 20$ (blue), $\tilde{\mu} = 50$ (purple). Note that for small $\tilde{\lambda}$ the stability bands (the regions in $\bar{L}$ where $\chi_{\bar{L}} = d\bar{L}/d\rho > 0$) are wide even when $\tilde{\mu}$ is large, which is not the case for high $\tilde{\lambda}$.

For the AKS model, the the variational upper bound on the free energy (4.27) after the evaluation of the sum reads as

$$\phi(\rho, \tilde{\mu}, \langle \bar{L} \rangle_0; \tilde{\lambda}) = -2\rho \langle \bar{L} \rangle_0 - 2\tilde{\mu}\tilde{\lambda}^2 \left[\frac{n}{n-1} \left(1 - \frac{\langle \bar{L} \rangle_0}{n\tilde{\lambda}} \right)^{n-1} + \frac{\langle \bar{L} \rangle_0}{\tilde{\lambda}} - \frac{n}{n-1} \right] + \langle \bar{L} \rangle_0 \ln \langle \bar{L} \rangle_0 + (1 - \langle \bar{L} \rangle_0) \ln(1 - \langle \bar{L} \rangle_0),$$

from which the MF predictions for the specific internal energy is found to be

$$\langle \bar{E}(\rho, \tilde{\mu}; \tilde{\lambda}) \rangle_0 = -2\rho \langle \bar{L} \rangle_0(\rho, \tilde{\mu}; \tilde{\lambda}) - 2\tilde{\mu}\tilde{\lambda}^2 \left[\frac{n}{n-1} \left(1 - \frac{\langle \bar{L} \rangle_0(\rho, \tilde{\mu}; \tilde{\lambda})}{n\tilde{\lambda}} \right)^{n-1} + \frac{\langle \bar{L} \rangle_0(\rho, \tilde{\mu}; \tilde{\lambda})}{\tilde{\lambda}} - \frac{n}{n-1} \right] \underset{n\to\infty}{\sim} -2\rho \langle \bar{L} \rangle_0(\rho, \tilde{\mu}; \tilde{\lambda}) - 2\tilde{\mu}\tilde{\lambda}^2 \left[\mathrm{e}^{-\frac{\langle \bar{L} \rangle_0(\rho, \tilde{\mu}; \tilde{\lambda})}{\tilde{\lambda}}} + \frac{\langle \bar{L} \rangle_0(\rho, \tilde{\mu}; \tilde{\lambda})}{\tilde{\lambda}} - 1 \right],$$

where, as discussed in Section 2.2.1, $\langle \bar{L} \rangle_0(\rho, \tilde{\mu}; \tilde{\lambda})$ should be found as a minimiser of $\phi(\rho, \tilde{\mu}, \langle \bar{L} \rangle_0; \tilde{\lambda})$.

4.6.4.2 Critical points

In line with Definition 8 and the discussion from Section 2.4.3.1, the critical point of the AKS model in the thermodynamic limit can be found by imposing the conditions

$$\begin{cases} \rho = \dfrac{1}{2}\ln\dfrac{\bar{L}}{1-\bar{L}} - \tilde{\mu}\tilde{\lambda}\left(1-\mathrm{e}^{-\bar{L}/\tilde{\lambda}}\right); \\ \dfrac{d\rho(\bar{L})}{d\bar{L}} = \dfrac{1}{2\bar{L}(1-\bar{L})} - \tilde{\mu}\mathrm{e}^{-\frac{\bar{L}}{\tilde{\lambda}}} = 0; \\ \dfrac{d^2\rho(\bar{L})}{d\bar{L}^2} = \dfrac{2\bar{L}-1}{2\bar{L}^2(1-\bar{L})^2} + \dfrac{\tilde{\mu}}{\tilde{\lambda}}\mathrm{e}^{-\bar{L}/\tilde{\lambda}} = 0, \end{cases} \tag{4.132}$$

which is a system of equations for a second-order singularity in which, as before, we replaced $\langle\bar{L}\rangle_0$ by $\bar{L}$ for short (since in the thermodynamic limit the MFT is believed to be exact). Multiplying the third equation in (4.132) by $\tilde{\lambda}$ and adding it to the second gives

$$\frac{1}{2\bar{L}(1-\bar{L})} + \tilde{\lambda}\frac{2\bar{L}-1}{2\bar{L}^2(1-\bar{L})^2} = 0,$$

which is equivalent to

$$\bar{L}^2 - (1+2\tilde{\lambda})\bar{L} + \tilde{\lambda} = 0.$$

The roots of this quadratic equation are given by

$$\bar{L}_\pm = \frac{1+2\tilde{\lambda} \pm \sqrt{1+4\tilde{\lambda}^2}}{2},$$

out of which only

$$\bar{L}_c \equiv \bar{L}_- = \frac{1+2\tilde{\lambda} - \sqrt{1+4\tilde{\lambda}^2}}{2} \tag{4.133}$$

should be kept since $\bar{L} \in (0,1)$. Note that, unlike the critical connectance of the MF3 model (which can take any value between zero and one), the critical connectance of the AKS model is between zero and $1/2$ for all $\tilde{\lambda} > 0$, which is clear from (4.133). This can be intuitively explained by the fact that the 2-star term is always present in the AKS statistic, and if $\tilde{\lambda} \to \infty$, then Ω_{AKS} reduces to $\mathcal{S}_2$, which results in the critical point at $\bar{L}_c = 1/2$, as can be seen from (4.109) and Fig. 4.10. Furthermore, as can be seen from Fig. 4.10, for the positive 2-star parameter, adding the 3-star statistic with the opposite sign reduces the critical connectance, which heuristically explains why decreasing $\tilde{\lambda}$ (i.e. increasing the contribution of the higher-order stars) results in a smaller

critical connectance.

4.6.4.3 Finite-size phase transitions in (0,1)-bistability

Although, as clear from (4.26), for a fixed q the total number of q-stars in the graph scales as $\mathcal{S}_q \underset{n\to\infty}{\sim} \mathcal{O}(n^{q+1})$, the AKS statistic always includes the high-order ($q \sim n$) stars for which this scaling is invalid due to the fact that the number of q-stars of a node, given by (4.118), quickly decreases as q approaches the degree of the node. For this reason, in the Hamiltonian (4.129) the contribution from the high-order stars is greatly suppressed for $\lambda \gtrsim 1$, meaning that the behaviour of the AKS model should be similar to that of the lower-order models. This is indeed the case, as can be seen on the center and right panels of Fig. 4.25 and in Fig. 4.26, from which it is clear that, like a 2-star model[24], the AKS model develops (0,1)-bistability for large $\tilde{\mu}$. This makes it interesting to consider the (0,1)-bistability transition formula (4.33), which, using the relation (4.128), can be expressed as

$$\mathcal{S}_k = \frac{n}{2}\binom{n-1}{k}\left(1+\tanh\left[\frac{\rho n(n-1)}{2}+(n\tilde{\lambda})^2\frac{\tilde{\mu}}{2}\left(\left(1-\frac{1}{n\tilde{\lambda}}\right)^{n-1}+\frac{n-1}{n\tilde{\lambda}}-1\right)\right]\right), \tag{4.134}$$

and, as can be seen in Fig. 4.26, works very well.

Note that from (4.134) it is clear that in the thermodynamic limit the phase transition (shock wave) propagates in the parameter space according to

$$\rho+\tilde{\lambda}^2\tilde{\mu}\left(\mathrm{e}^{-1/\tilde{\lambda}}+\frac{1}{\tilde{\lambda}}-1\right)=0 \tag{4.135}$$

as long as the parameters $\tilde{\mu}$ and $\tilde{\lambda}$ are high enough to ensure (0,1)-bistability.

4.6.4.4 Distributions of local features

The average degree and LCC distributions of the AKS model are shown in Fig. 4.27 and Fig. 4.28 together with the MFT predictions (4.11) and (4.13). As discussed in Section 4.6.4.3, when $\tilde{\lambda}$ is relatively large, the behaviour of the AKS model is similar to that of the lower-order models, which is reflected in Fig. 4.27. Note how at largely negative $\tilde{\mu}$ (left panel of Fig. 4.27) the degree distribution becomes very narrow, unlike the LCC distribution (compare with Fig. 4.15). This is the consequence of the fact that there is an optimal value of the degree that minimises the internal energy (which approaches the free energy at low temperatures). At the same time, there are many

[24] Which is approached by the AKS model when $\tilde{\lambda} \to \infty$.

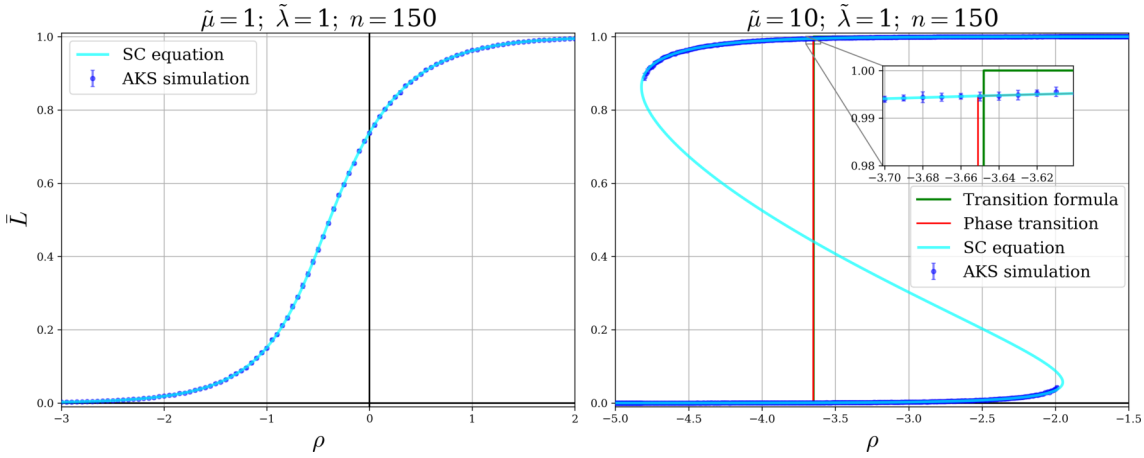

Fig. 4.26: Results of the time-averaging MC simulations together with the numerical solutions of the mean field self-consistency equation (4.130) for the two AKS models before (left) and after (right) the gradient catastrophe. The theory seems to be precise for both models apart from the small deviations of the AKS model near the spinodal points which decrease with the increase of the network size. The green line corresponds to the transition formula (4.134).

almost regular graphs, in which the degrees of all nodes are close to that optimal degree, while the LCCs have larger variations that do not change the Hamiltonian, which explains why the LCC distributions do not collapse to a single value (unless the graphs are either empty or complete). It is interesting to observe that at moderate positive values of $\tilde{\mu}$ the degree distributions can be slightly wider than that of the ER model of matching connectance, which seems to be of the similar origin to the analogous effect observed in the 3-star model (Fig. 4.14) discussed in Section 4.6.1.4. However, the degree distribution of the model from Fig. 4.27 does not get much wider than what is observed on the upper right panel of Fig. 4.27, and when the parameter $\tilde{\mu}$ increases slightly beyond $\tilde{\mu} = 3$, the model undergoes a first-order phase transition, after which it produces either almost empty or almost complete graphs.

So far, all of the effects discussed in this section were similar to those discussed in Section 4.6.1.4 for the 3-star model, but in Fig. 4.28 one can see that at certain low values of $\tilde{\lambda}$ the degree distributions of the AKS model follow that of the ER model of matching connectance regardless the very low temperatures. At first sight, this behaviour seems to be similar to that of the MF model in which, as discussed in Section 4.4.9, it is caused by the highly degenerate ground macrostate. However, despite the apparent similarities with the MF model, the degree distributions from Fig. 4.28 turn out to be "frozen", i.e. the fact that they are relatively wide does not come from a high entropy, but rather from the complexity of the Hamiltonian. This can be explained as follows.

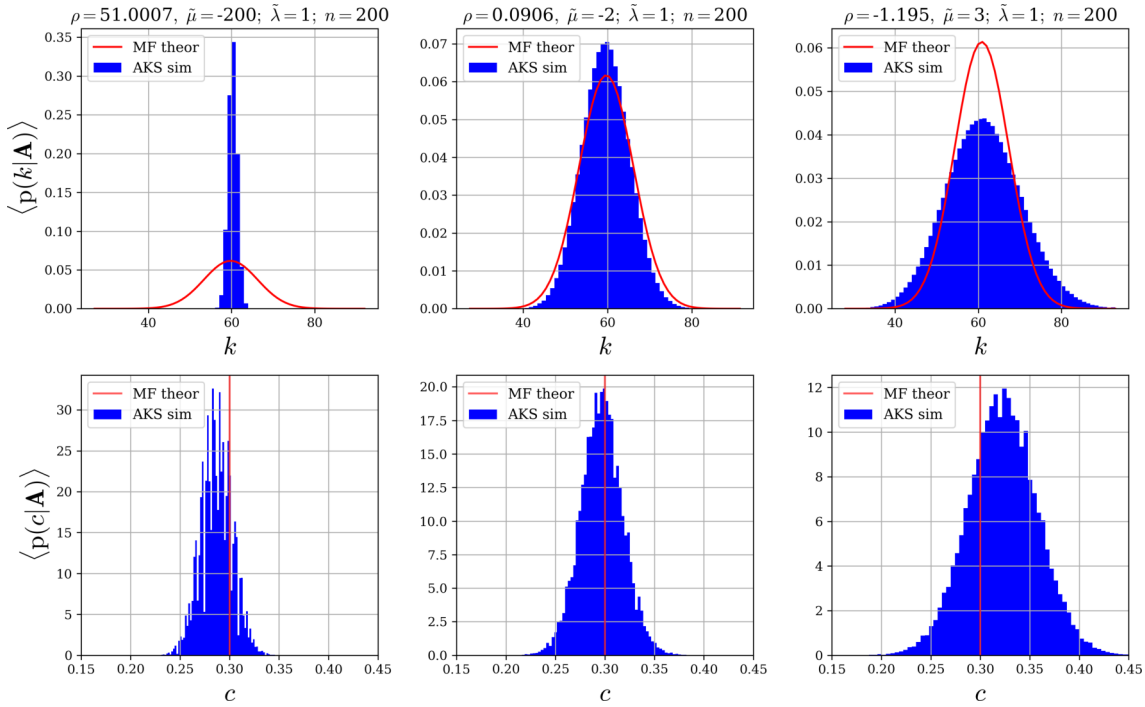

Fig. 4.27: Expected degree and LCC distributions of the three different AKS models. The parameters of the models are set in a way that their connectances are kept at $\bar{L} = 0.3$. Similarly to the case of the 3-star model (Fig. 4.14) the degree distributions of the AKS model can be slightly wider than that of the ER model of matching connectance (shown in red in the upper panels), but at sufficiently low temperatures the degree distributions of the AKS model are narrower than that of the matching-connectance ER model and become degenerate as $T \to 0$. The tails of the distributions appear to decay exponentially in all the cases.

When $\tilde{\lambda}$ is sufficiently low, the contributions from the higher-order stars in the AKS statistic are significant in comparison with the lower-order stars. This means that at low temperatures (when the entropy is dominated by the internal energy) all $\mathcal{S}_q$ should be fixed at their optimal values. Since the number of q-stars of a node, given by (4.118), depends solely on the degree of the node, the expression for the total number of q-stars in a graph can be written as

$$\mathcal{S}_q(\mathbf{A}) = \sum_{i=1}^{n} \mathcal{S}_q(k_i) = \sum_{i=1}^{n} \sum_{k=0}^{n-1} \mathcal{S}_q(k)\delta_{kk_i} = n \sum_{k=1}^{n-1} \mathcal{S}_q(k)\mathrm{p}(k), \tag{4.136}$$

where we used the definition of the degree distribution (4.10) and the fact that $\mathcal{S}_q(0) = 0$ for all k. From the equation (4.136) it is clear that fixing all $\mathcal{S}_q$ determines the degree distribution uniquely since the matrix $\mathbf{S}$, defined by $S_{qk} \equiv \mathcal{S}_q(k)$, is never degenerate[25], and $\mathrm{p}(0)$ is fixed by

[25] Which is easy to see from the fact that it is upper triangular with all the diagonal entries being equal to one, meaning that $\det \mathbf{S} = 1$.

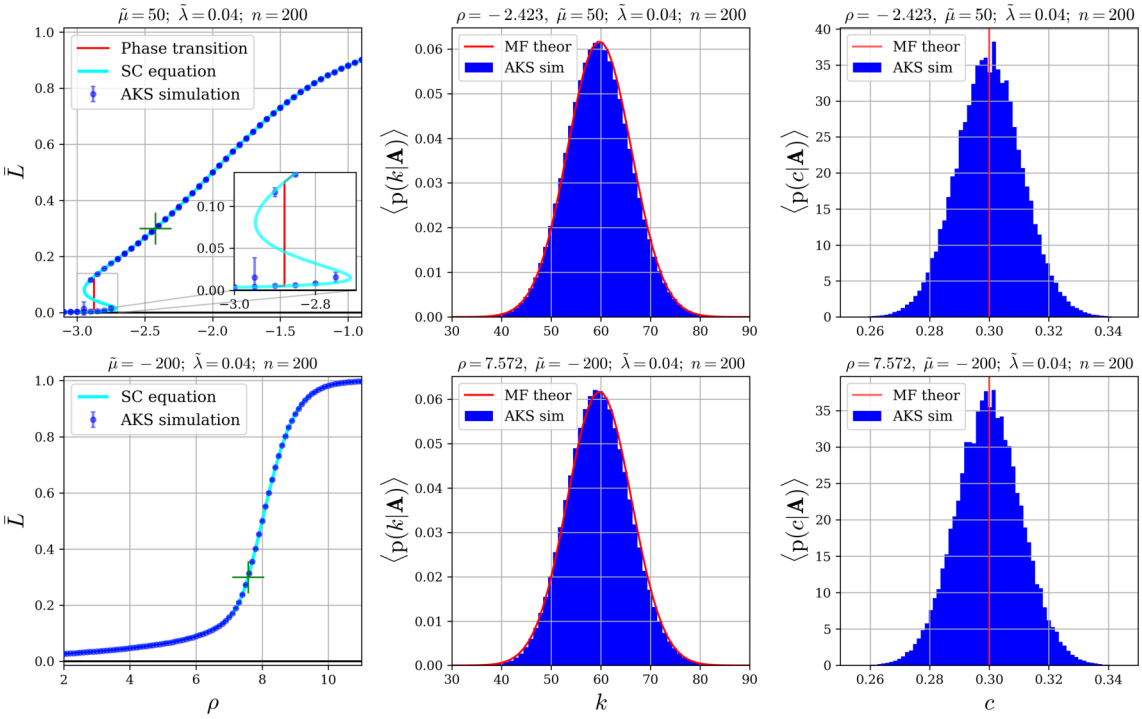

Fig. 4.28: Connectance as a function of $\tilde{\mu}$ (left) and the expected degree and LCC distributions (middle and right) of two different AKS models at low temperatures and low values of $\tilde{\lambda}$. The green crosses in the left panels show the positions where the distributions from the central and right panels were computed. Note that despite the low temperatures, the degree distributions seem to be identical to that of the ER model of matching connectance (shown in red in the central panels), which resembles the behaviour of the MF model (Fig. 4.15, Fig. 4.12), but has a completely different nature. It turns out that the degree distributions are, actually, "frozen" and their width comes from the complexity of the Hamiltonian instead of the high entropy of the ground macrostate (as in the case of the MF model).

the normalisation as

$$\mathrm{p}(0) = 1 - \sum_{k=0}^{n-1} \mathcal{S}_q(k). \tag{4.137}$$

Assuming that all $\mathcal{S}_q$ are fixed at their mean field values (4.26), from (4.136) we obtain

$$\sum_{k=1}^{n-1} \mathcal{S}_q(k)\mathrm{p}(k) = \binom{n-1}{q} \langle \bar{L} \rangle_0^q, \quad q \in \{1, \dots, n-1\}, \tag{4.138}$$

which together with (4.137) gives a nondegenerate system of n linear equations on n values of $\mathrm{p}(k),\ k \in \{0, \dots, n-1\}$. Comparison between the solution of this system of equations and the expected degree distribution of the ER model given by (4.11) is shown in Fig. 4.29, suggesting that these distributions are identical, which explains why the low-temperature degree distributions shown in Fig. 4.28 closely follow the predictions for the ER model of the matching connectance

(4.120).

Note that the low-temperature behaviour discussed above loosely resembles that of spin glasses, which also exhibit complex ground states, although the interactions in spin glasses are usually of low orders, and the complexity arises from the heterogeneity of the couplings between the dynamic variables, whereas the AKS model is homogeneous.

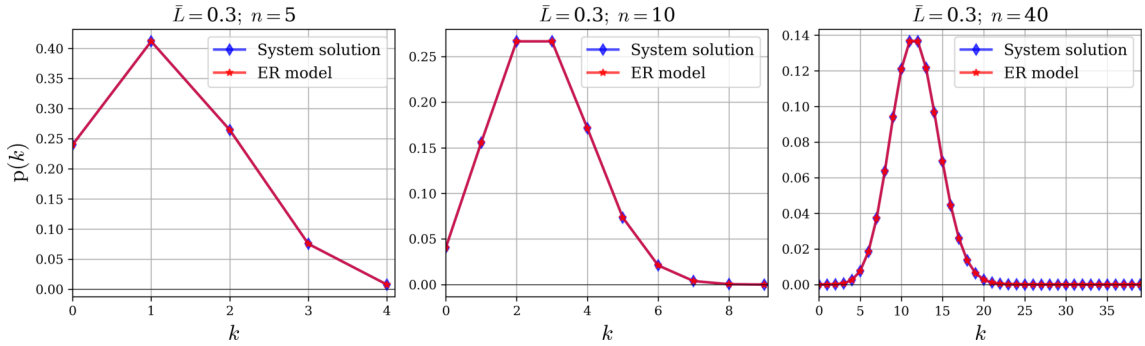

Fig. 4.29: Comparison of the expected degree distributions computed by solving the system of equations given by (4.138) and (4.137) with the expected degree distributions of the matching-connectance ER model (4.11). The agreement seems to be perfect for the networks of all sizes.

At first sight, it may appear that the narrow low-temperature degree distribution of the AKS model, shown in the upper left panel of Fig. 4.27, contradicts the idea used to explain the relatively wide degree distributions from the centre panels of Fig. 4.28, but as explained below, there is no contradiction. This difference in the low-temperature behaviour of the AKS models with different $\tilde{\lambda}$ comes from the suppression of the higher-order stars in the AKS statistic for relatively high $\tilde{\lambda}$, discussed in Section 4.6.4.3. Due to this suppression the contribution of the higher-order stars in the Hamiltonian goes to zero in the thermodynamic limit, which makes the model behave similarly to the models of finite orders, in which only the lower-order stars obey the MFT predictions. To see this, consider a k-regular graph $\mathcal{G}$ of connectance $\bar{L}$. From (4.118), the number of q-stars in such a graph is given by

$$\mathcal{S}_q(\mathcal{G}) = n\binom{k}{q},$$

and the ratio of $\mathcal{S}_q(\mathcal{G})$ to the MFT predictions (4.26) is given by

$$\frac{\mathcal{S}_q(\mathcal{G})}{\mathcal{S}_q(\bar{L})} = \frac{\binom{k}{q}}{\binom{n-1}{q}\bar{L}^q} = \frac{k(k-1)\dots(k-q+1)}{\bar{L}^q(n-1)\big((n-1)-1\big)\dots\big((n-1)-q+1\big)}$$
$$= \frac{1-\frac{1}{k}}{1-\frac{1}{n-1}} \cdot \frac{1-\frac{2}{k}}{1-\frac{2}{n-1}} \cdot \dots \cdot \frac{1-\frac{q-1}{k}}{1-\frac{q-1}{n-1}} \leq 1, \quad (4.139)$$

where we used the fact that in a k-regular graph the connectance is given by $\bar{L} = k/(n-1)$. From (4.139) it is clear that the MFT predictions for the star counts are inaccurate when q approaches k, but as long as $q \ll k$, the MFT predictions (4.26) are precise since all the factors in (4.139) are very close to one. This is the reason why very narrow degree distributions of the low-order models (Fig. 4.15) can arise without contradicting the fact that the MFT predictions for the observables are exact in the thermodynamic limit, and when the parameter $\tilde{\lambda}$ is relatively large, the AKS statistic of almost regular graphs can also be consistent with its MFT predictions (4.131) due to the suppression of the higher-order terms contradicting the MFT. However, when the contribution of the high-order[26] stars in the AKS statistic becomes important, the degree distribution is forced to follow the solution of the system of equations (4.138) in order for the AKS statistic to follow its MFT predictions (4.131).

4.6.4.5 Scaling and the validity of the MFT for infinite-order models

As discussed in Section 2.2.2.1, the MFT is believed to be exact in the thermodynamic limit, but in order for a meaningful thermodynamic limit to exist, the model should be scalable in the sense of Definition 1. For finite-order models like the 3-star or triad models discussed above, scalability can always be ensured by a proper rescaling of the parameters conjugated to the observables, but for the infinite-order models this is no longer the case[27]. Indeed, consider, for instance, an AKS model with $\tilde{\lambda} = 1/n^2$, in which case neither the mean field expressions such as (4.130) nor the (0,1)-bistability transition formula (4.134) are defined as $n \to \infty$, which happens due to the divergence of the sum in the AKS statistic. It is clear that this divergence cannot be removed by any rescaling of the parameter $\tilde{\mu}$, meaning that the MFT is likely to be inappropriate for such models[28].

4.7 Problems with homogeneous models

It is well known that in many real-world networks, the distributions of local features decay according to some power laws [Newman (2010)], as opposed to the exponential decay observed in all the ERGMs considered in this work. This exponential decay seems to be a consequence of the homo-

[26] Comparable to the average degree of the graph.

[27] As discussed in Section 4.6.4, $\tilde{\lambda}$ is not a parameter conjugated to an observable.

[28] For large models of this kind, the MFT predicts either complete or empty graphs (depending on the parity of n), which seems to be correct but not very useful, and there is no guarantee that the MFT will be accurate for small models.

geneity and can be considered as the main reason why such models fail to mimic the real-world networks, for most of which the equivalence of all the nodes is, clearly, an incorrect assumption. From the study of the triad model in Section 4.6.2, it is evident that some of the desired effects, such as the high clustering at a moderate connectance, can result from the spontaneous symmetry breaking; however, the resulting graphs (Fig. 4.20) are still unrealistically[29] simple and, as discussed in Section 4.6.2.3, such graphs only appear at relatively small sizes or at extremely low temperatures if scalability is assumed.

Another serious problem of infinite-dimensional homogeneous ERGMs is the fact that, as long as they possess a meaningful thermodynamic limit, at large sizes they are well-described by the linearised theory (MFT), which implies the lack of variability in the behaviour of such models. Indeed, as can be seen from the discussions from Section 4.6.1 and Section 4.6.2, for large networks the behaviours of the MF3, triad and 3-star models are very similar, since all of these models follow the MFT predictions at the macroscopic level. Moreover, the MFT is not restricted to Markov ERGMs, which means that all scalable homogeneous ERGMs of matching orders are expected to exhibit similar behaviour in the thermodynamic limit.

Furthermore, the results obtained for the AKS model in Section 4.6.4 suggest that even in the most general homogeneous Markov ERGM (4.3), in which all the parameters could be controlled separately, there is not much variability in the behaviour with the changes of the parameters. This is exemplified in Fig. 4.28, where the degree and LCC distributions are very similar for $\tilde{\mu}$ as large as 50 and as small as -200, which, as discussed in Section 4.6.4.4, is caused by the tendency of the model to follow the MFT predictions for stars of all orders, and as soon as the connectance is fixed the total star counts $\mathcal{S}_q,\ q \in \{1, 2, \ldots, n-1\}$ and, hence, the degree distributions follow that of the matching-connectance ER model, as predicted by the MFT. This observation dispels hopes that homogeneous infinite-order models may allow controlling the properties of large graphs significantly beyond that of the ER model, and, apparently, the only reason why in [Robins, Snijders, Wang, Handcock and Pattison (2007); Snijders et al. (2006)] the infinite-order ERGMs showed superior results in fitting the empirical data, is that the networks considered in these works were relatively small[30].

[29] Of course, there may be real-world networks consisting of several fully connected components, but there is, arguably, no need in their statistical analysis.

[30] Ranging in size from 10 to 39 nodes.

4.8 MCW random graph model

Homogeneity constraint can be relaxed by introducing a set of labels that correspond to the node attributes presumably relevant to the network's topology. Suppose there are $\mathcal{N}$ distinct node labels $y_i,\ i \in \{1,\dots,\mathcal{N}\}$, in which case the simplest of such models is the one in which the linking sites are independent given the labels, i.e.

$$P(\mathbf{A}|\mathbf{y}) = \prod_{i<j} \left[\mathcal{L}(y_i,y_j)\delta_{A_{ij},1} + \big(1-\mathcal{L}(y_i,y_j)\big)\delta_{A_{ij},0}\right], \tag{4.140}$$

where $\mathbf{y}$ is the full labelling of all the nodes in the graph. In this model[31] the links between the nodes with labels y_i and y_j appear with the probability $\mathcal{L}(y_i,y_j)$, and the model (4.140) can be regarded as a heterogeneous analogue of the ER model discussed in Section 4.1.2. It is easy to show that the probability distribution (4.140) can be expressed as

$$P(\mathbf{A}|\mathbf{y}) = \frac{\mathrm{e}^{\sum_p L_p h_p}}{Z(\mathbf{h})}, \tag{4.141}$$

where $p \in \{1,\dots,\mathcal{N}(\mathcal{N}+1)/2\}$ enumerates all the distinct unordered pairs of labels in the graph, L_p is the number of links that connect the nodes with labelling enumerated by p, and

$$h_p = \ln\frac{\mathcal{L}_p}{1-\mathcal{L}_p}; \quad Z(\mathbf{h}) = \prod_p (1+\mathrm{e}^{h_p})^{N_p}, \tag{4.142}$$

where N_p is the number of unordered pairs of nodes whose labels form the unordered pair of labels enumerated by p. Note that the expression (4.141) defines an exponential family of distributions parametrised by $\mathbf{h}$ and reveals the nature of the model, being the maximum-entropy ensemble with constraints on the expectations of $\mathbf{L}$ (which stands for the array of $L_p,\ p \in \{1,\dots,\mathcal{N}(\mathcal{N}+1)/2\}$). The Hamiltonian of the model defined by the distribution (4.141) is given by

$$H_0(\bar{\mathbf{L}}) = \sum_{i=1}^{p} h_i N_i \bar{L}_i, \tag{4.143}$$

where $\bar{L}_i \equiv L_i/N_i$.

Inspired by the fact that, as discussed in Section 2.3, the equations of state of the mean field

[31] Known as *stochastic block model* [Abbe (2018); Peixoto (2019)].

models are identical to the mean field self-consistency equations of the more complicated models, we introduce the quadratic interactions[32] to (4.143) in a way that keeps the model in the mean field class, namely

$$H(\bar{\mathbf{L}}) = -\frac{1}{N}\sum_{i\leq j} N_i N_j \tilde{J}_{ij}\bar{L}_i\bar{L}_j - \sum_{i=1}^{p} h_i N_i \bar{L}_i = -N\sum_{i\leq j}\gamma_i\gamma_j\tilde{J}_{ij}\bar{L}_i\bar{L}_j - N\sum_{i=1}^{p}\gamma_i h_i \bar{L}_i,$$

where $\gamma_i \equiv N_i/N$. The above Hamiltonian is, essentially, identical to that of the MCW model discussed in Chapter 3, which allows using the method of differential identities similarly to how it was applied in Section 3.2.2. Note that since the PDEs (3.8) are fully determined by the form of the Hamiltonian, in the variables rescaled identically to (3.9)

$$t_{ij} \equiv \beta\gamma_i\gamma_j\tilde{J}_{ij}; \qquad x_i \equiv \beta\gamma_i h_i$$

the PDEs for this model are identical to that of the MCW model (3.8), (3.12); hence, the general solution can be written straight away from (3.14) as

$$\Phi = \sum_{i=1}^{p} x_i\langle\bar{L}_i\rangle + \sum_{i\geq j} t_{ij}\langle\bar{L}_i\rangle\langle\bar{L}_j\rangle - W(\langle\bar{\mathbf{L}}\rangle), \tag{4.144}$$

where $\langle\bar{\mathbf{L}}\rangle = \partial_{\mathbf{x}}\Phi$ are the ensemble averages of partial connectances and $W(\langle\bar{\mathbf{L}}\rangle)$ is a function fixed by the initial conditions[33]

$$Z_0 = \prod_{i=1}^{p}(1+\mathrm{e}^{\beta h_i})^{N_i}; \quad \Phi_0 = \frac{1}{N}\log Z_0 \tag{4.145}$$

to be

$$W(\bar{\mathbf{L}}) = \sum_{i=1}^{p}\gamma_i\Big[\langle\bar{L}_i\rangle\log\langle\bar{L}_i\rangle + \Big(1-\langle\bar{L}_i\rangle\Big)\log\Big(1-\langle\bar{L}_i\rangle\Big)\Big]. \tag{4.146}$$

As discussed in Section 3.2.2, the specific microcanonical free energy can be found as

$$\bar{\mathcal{F}}(\bar{\mathbf{L}};\tilde{\mathbf{J}},\mathbf{h};\boldsymbol{\gamma}) = -T\Phi(\bar{\mathbf{L}};\mathbf{t},\mathbf{x};\boldsymbol{\gamma}) = \bar{\mathcal{E}}(\bar{\mathbf{L}};\tilde{\mathbf{J}},\mathbf{h};\boldsymbol{\gamma}) - T\bar{\mathcal{S}}(\bar{\mathbf{L}};\boldsymbol{\gamma}), \tag{4.147}$$

[32] Pairwise statistical dependencies between the links.

[33] The initial conditions depend on the structure of the configuration space which is the only thing that distinguishes this model from the MCW model discussed in Chapter 3.

where

$$\bar{\mathcal{E}}(\bar{\mathbf{L}};\tilde{\mathbf{J}},\mathbf{h};\boldsymbol{\gamma}) = -\sum_{i=1}^{p}\gamma_i h_i \bar{L}_i - \sum_{i\geq j}\gamma_i\gamma_j \tilde{J}_{ij}\bar{L}_i\bar{L}_j; \tag{4.148}$$

$$\bar{\mathcal{S}}(\bar{\mathbf{L}};\boldsymbol{\gamma}) = -\sum_{i=1}^{p}\gamma_i\Big[\bar{L}_i\log\bar{L}_i + \Big(1-\bar{L}_i\Big)\log\Big(1-\bar{L}_i\Big)\Big], \tag{4.149}$$

are the specific microcanonical internal energy and the specific microcanonical entropy of the model.

As clear from (4.148), the specific observable of the model conjugated to the field h_i is given by $\bar{\mathfrak{L}}_i = \gamma_i\bar{L}_i$ and the equations of state can be obtained by minimising $\bar{\mathcal{F}}$ with respect to $\bar{\mathfrak{L}}$, thus, requiring stationarity as

$$\frac{\partial\bar{\mathcal{F}}}{\partial\bar{\mathfrak{L}}_i} = -\tilde{J}_{ii}\bar{L}_i - \sum_{j=1}^{p}\tilde{J}_{ij}\gamma_j\bar{L}_j - h_i + \frac{T}{2}\ln\frac{\bar{L}_i}{1-\bar{L}_i} = 0, \quad i\in\{1,2,\ldots,p\},$$

which after compensating for the double-counting of the intracomponent interactions by the following rescaling

$$\begin{cases} J_{ij} = 2\tilde{J}_{ij}, & i = j \\ J_{ij} = \tilde{J}_{ij}, & i \neq j \end{cases}$$

becomes

$$h_k = -\sum_{j=1}^{p}\gamma_j J_{kj}\bar{L}_j + T\log\frac{\bar{L}_k}{1-\bar{L}_k}, \tag{4.150}$$

or, equivalently, when $T = 1$

$$\bar{L}_k = \frac{1}{2}\left(1+\tanh\left[h_k + \sum_{j=1}^{p}\gamma_j J_{kj}\bar{L}_j\right]\right), \qquad k\in\{1,2,\ldots,p\}. \tag{4.151}$$

Using the equations of state (4.151), one may, in principle, do the analysis similar to the one from Chapter 3, although it is clear that the simplest model of this kind, in which there are only two distinct node labels, has tree components ($p = 3$) corresponding to the links connecting the node pairs with labellings (y_1, y_1), (y_2, y_2) and (y_1, y_2). This model, in full generality, has six couplings $\mathbf{J}$, three fields $\mathbf{h}$ and two independent[34] splitting parameters $\boldsymbol{\gamma}$, which adds up to a total of eleven

[34] All the three splitting parameters are fixed as soon as the numbers of nodes with labels y_1 and y_2 are defined.

free parameters.

4.9 Discussion

In this chapter we have considered a wide variety of infinite-dimensional ERGMs and found that, as expected, the mean field theory seems to be exact for all the considered models in the thermodynamic limit, suggesting its wide applicability in describing the large-scale ERGMs. This high precision of the linearised theory has positive and negative implications for the usability of such models in the analysis of complex networks.

On the positive side, a theory that works so well can potentially be used to accelerate the existing MCMC-based parameter estimation procedures used to fit such models to data [Robins, Snijders, Wang, Handcock and Pattison (2007)], in which, instead of running the MCMC on every iteration of the parameter adjustment, one could fit the model using the MFT predictions and then refine the estimates using the MCMC. Also, this kind of theory gives a simple way of finding and avoiding the parameter regions in which the desired properties can only be matched at the level of expectations, but individual samples from the model do not exhibit these properties due to the multimodality of the distributions discussed in Section 2.1.7.

On the negative side, as discussed in Section 4.7, the fact that the linearised theory works so well for all infinite-dimensional models in the thermodynamic limit, essentially, voids the ability of the homogeneous ERGMs to capture most of the characterising features of the large real-world networks whose properties go significantly beyond that of the ER model of matching connectance. It seems that homogeneous ERGMs may be of some use in fitting small real-world networks (in which case the MFT does not work so well) and, as discussed in [Robins, Pattison, Kalish and Lusher (2007); Robins, Snijders, Wang, Handcock and Pattison (2007); Snijders et al. (2006)], the infinite-order models show a decent performance on this path. However, since, as discussed in Section 4.1, the main virtue of ERGMs is their simple interpretation as maximum-entropy ensembles with some well-understood constraints, the usefulness of the infinite-order models as null-models for the data is questionable due to the lack of simple interpretations behind their infinite-order statistics.

The fact that homogeneous ERGMs are incapable of capturing many important features of real-

world networks means that the nodes in such networks cannot be assumed as equivalent. Thus, the heterogeneous models considered in Section 4.8 seem to be more appropriate for such data. Note that in order to keep the model interpretable and to prevent overfitting, the number of distinct node attributes should be much smaller than the number of nodes in the network. For example, in the case of maximum-likelihood estimation of the model defined by (4.140) in which the number of distinct node attributes is equal to the number of nodes, the estimated ensemble consists of a single graph identical to the modelled network. Such ensemble is, clearly, of no use, neither as a null-model, since it is not more interpretable than the modelled network itself, nor as a generative model, which is expected to produce graphs that are, in some way, similar to the modelled network, but not entirely the same.

Chapter 5

Conclusions

In this work we have considered two conceptually different discrete mean field models whose exact thermodynamic solutions coincide with the corresponding mean field self-consistency equations. It is shown that the partition functions of such models satisfy the systems of linear partial differential equations (PDEs) analogous to the heat equation, while their specific free energies satisfy the systems of viscous PDEs, whose viscosities vanish in the thermodynamic limit resulting in the Hamilton-Jacobi type PDEs. The universality of the mean field theory (MFT) across a wide range of statistical problems implies a connection between the above mentioned PDEs and various large-scale statistical models at the level of the mean field approximation.

The results obtained in Chapter 3 generalise the outcomes of the previous studies of the two-component Curie-Weiss model and give a good orientation in its parameter space. It turns out that, despite their conceptual simplicity, such models are capable of exhibiting complex behaviours and capturing various real-world phenomena, which makes them valuable in complex systems modelling. Therefore, it may be useful to extend this work by obtaining new results about the generic multicomponent Curie-Weiss model and by the analysis of its higher-component cases, which is hard due to the high dimensionality of the corresponding parameter spaces.

The results obtained in Chapter 4 generalise numerous preceding works on exponential random graph models (ERGMs) and partly explain the outcomes of the previous simulation studies. It turns out that due to the infinite-dimensional nature of the considered ERGMs, in the thermodynamic limit such models are precisely described by the MFT. While this fact may give certain compu-

tational advantages in fitting such models to data, it largely limits the variability of homogeneous ERGMs which, essentially, voids their value in the analysis of large empirical networks.

Finally, since MFT is a universal tool, the analytical framework from this work should be transferable to the analysis of other discrete probabilistic models.

Appendix A

Notation

In this section we discuss the terminology and notation used in this work. Unfortunately, it was not practical to completely avoid the terminology clashes, and the term *degenerate* is particularly overloaded in the text. In various contexts it may correspond to a degenerate probability distribution; a degenerate ground macrostate (i.e. a macrostate realising on several microstates); a degenerate matrix (whose determinant is zero); a degenerate stationary point of a function (at which its Hessian is a degenerate matrix).

A.1 Abbreviations

Abbreviation	**Meaning**
CW	Curie-Weiss
MCW	multicomponent Curie-Weiss
MCMC	Markov chain Monte Carlo
ERGM	exponential random graph model
MF	mean field
MFT	mean field theory
PDE	partial differential equation
ODE	ordinary differential equation
SMFE	specific microcanonical free energy
AKS	alternating k-star

A.2 Symbols

As usually done in physics, in this work the symbols correspond to the entities rather than functions, i.e. $H(\mathbf{s})$ is the Hamiltonian as a function of a microstate and $H(\mathbf{\Omega})$ is the same Hamiltonian but as a function of the observables, which is a different function corresponding to the same entity. Throughout this work, bold symbols represent arrays of numbers (variables), e.g. $\mathbf{s}$ is an array consisting of the values of all dynamic variables s_i, or $\mathbf{A}$ is the adjacency matrix of a graph. A bar over a symbol corresponding to some property means that property per degree of freedom, e.g. E is the internal energy, while $\bar{E} = E/N$ is the specific internal energy. The angular brackets $\langle \dots \rangle$ mean the expected value, e.g. if m stands for magnetisation, then $\langle m \rangle$ stands for the expected magnetisation. The subscript corresponding to the size of the model is attached to the symbols of entities which depend on the size, but do not depend on microstates, and in the thermodynamic limit the subscript is absent, e.g. $\bar{F}_N(T)$ is the specific free energy of a model with N degrees of freedom at the temperature T, while $\bar{F}(T) = \lim_{N\to\infty} \bar{F}_N(T)$ is that specific free energy at the same temperature T in the thermodynamic limit. The exclusion from this rule (introduced to avoid overloading the symbol with indices) is the susceptibility matrix $\boldsymbol{\chi}$ and its elements χ_{ij}. The semicolon separating the arguments of a function means that the arguments before the semicolon are those that usually change when the function is considered, while the arguments that come after are usually fixed, e.g. $H(\mathbf{s};\mathbf{t})$ is the Hamiltonian, which is a function of the microstate $\mathbf{s}$ with some parameters $\mathbf{t}$.

Some of the commonly used symbols are explained in the table below.

Symbol	Meaning
T	Temperature
β	Inverse temperature
$\mathbf{s}$	Configuration of all dynamic variables defining a microstate
$\boldsymbol{\omega}$	Configuration of all observables defining a macrostate
$\mathcal{C}$	Configuration space of a model (set of all possible microstates)
N	Number of dynamic variables (degrees of freedom)
H	Hamiltonian
$\mathbf{\Omega}$	Observables
P	Probability
p	Distribution of a local feature in a graph (e.g. degree distribution)
Z	Partition function of a canonical ensemble
S	Entropy of a canonical ensemble
F	Free energy of a canonical ensemble
E	Internal energy of a canonical ensemble
g	Degeneracy factor of a macrostate
$\mathcal{S}$	Entropy of a microcanonical ensemble
$\mathcal{Z}$	Partition function of a microcanonical ensemble
$\mathcal{F}$	Free energy of a microcanonical ensemble
$\mathcal{E}$	Internal energy of a microcanonical ensemble
χ	Susceptibility
ϕ	Variational upper bound on the free energy in the variational approach
$\widetilde{F}$	Optimal variational upper bound on the free energy in the variational approach
m	Magnetisation
$\mathbf{m}$	Magnetisations of the components of MCW model
L	Number of links (edges) in a graph
$\mathcal{S}_k$	Full number of k-stars in a graph
$\mathcal{S}_k$	Number of k-stars of a given node in a graph
$\mathcal{T}$	Full number of triangles in a graph
$\mathcal{T}_i$	Number of triangles of a given node i in a graph

Appendix B

MCW additional figures

B.1 Stop-frames

B.1.1 Crossing the critical point

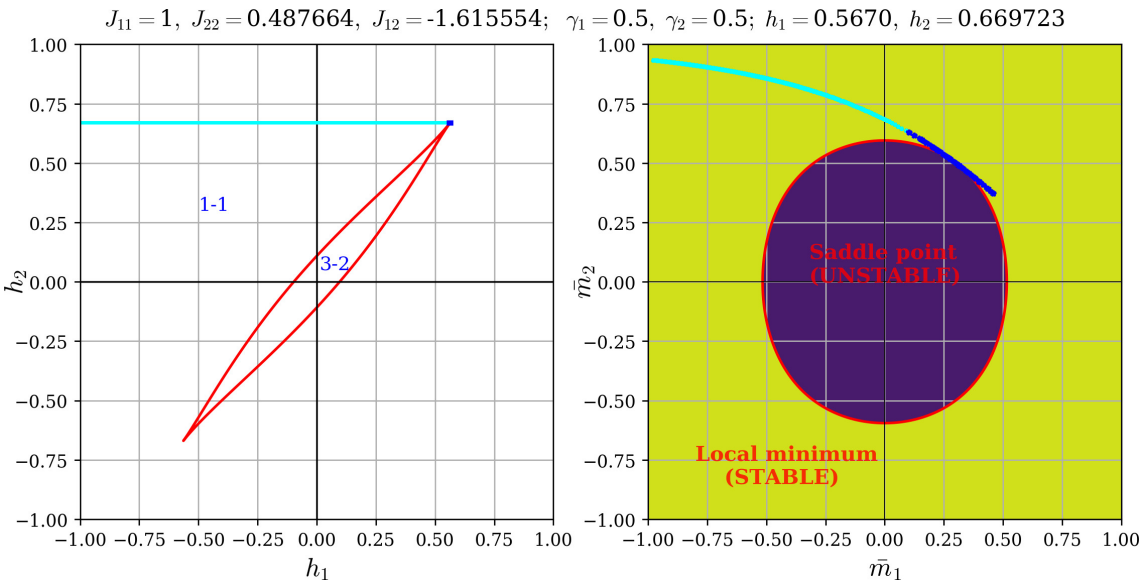

Fig. 2.1: A stop-frame from the animation available at https://youtu.be/2gJrtE2QUaY, showing how the partial magnetisations change with the field h_1 in the two-component CW model with $J_{11} = 1,\ J_{22} = 0.487664,\ J_{12} = -1.615554;\ h_2 = 0.669723;\ \gamma_1 = \gamma_2 = 0.5$ at $T = 1$. Note how sharp the dependence of partial magnetisations on the field is at the critical point (the small blue segment from the left panel is mapped to a much larger blue segment on the right panel).

B.1.2 Crossing the general fold away from the critical points

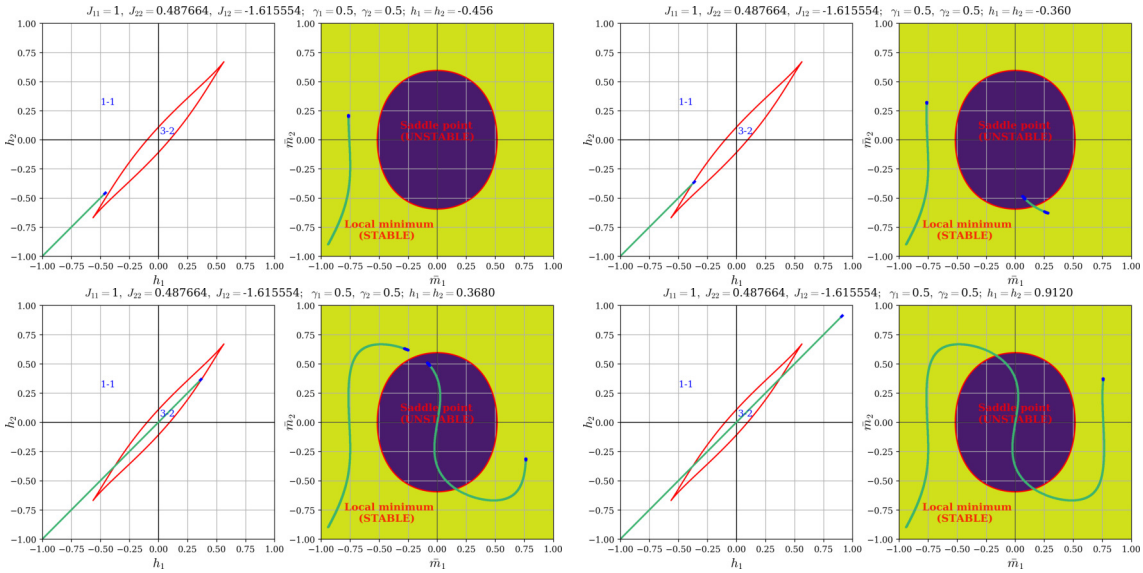

Fig. 2.2: Stop-frames from the animation available at https://youtu.be/2gJrtE2QUaY, showing how the partial magnetisations change with the field $h = h_1 = h_2$ in the two-component CW model with $J_{11} = 1,\ J_{22} = 0.487664,\ J_{12} = -1.615554;\ \gamma_1 = \gamma_2 = 0.5$ at $T = 1$.

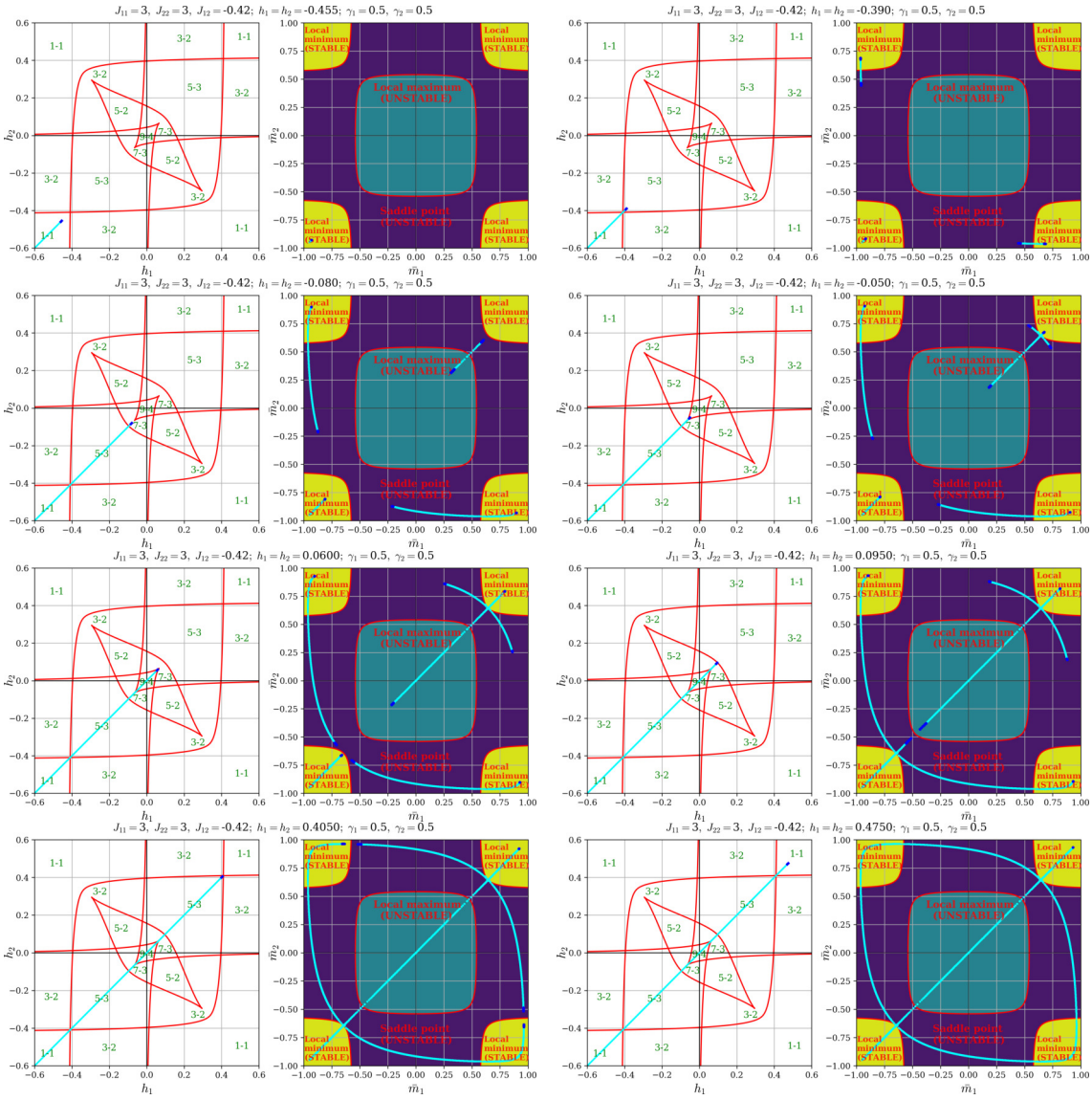

Fig. 2.3: Stop-frames from the animation available at https://youtu.be/7w4y-KAysqA, showing how the partial magnetisations change with the field $h = h_1 = h_2$ in the two-component CW model with $J_{11} = 3,\ J_{22} = 3,\ J_{12} = -0.42;\ \gamma_1 = \gamma_2 = 0.5$ at $T = 1$.

B.1.3 Evolution of the general fold with the decreasing temperature

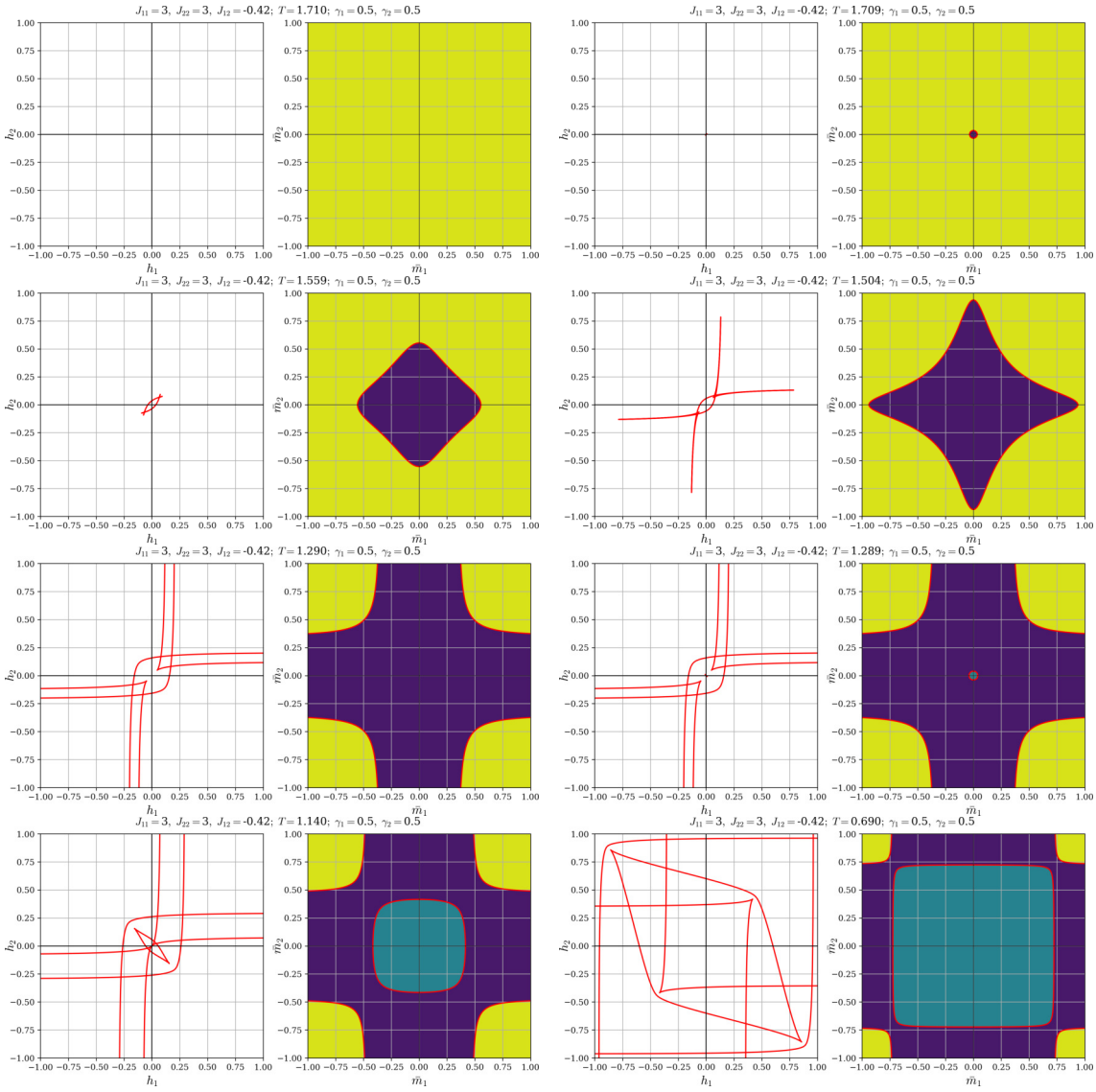

Fig. 2.4: Stop-frames from the animation available at https://youtu.be/amoPQkPNDdI, which shows how the general fold of the two-component CW model with $J_{11} = 3,\ J_{22} = 3,\ J_{12} = -0.42;\ \gamma_1 = \gamma_2 = 0.5$ evolves with the decreasing temperature. Note how the new disconnected components of the general fold appear when the nappes of the principal cone are being crossed at $T = 1.71$ and $T = 1.29$ (see Section 3.3.3.2).

B.2 Additional animations

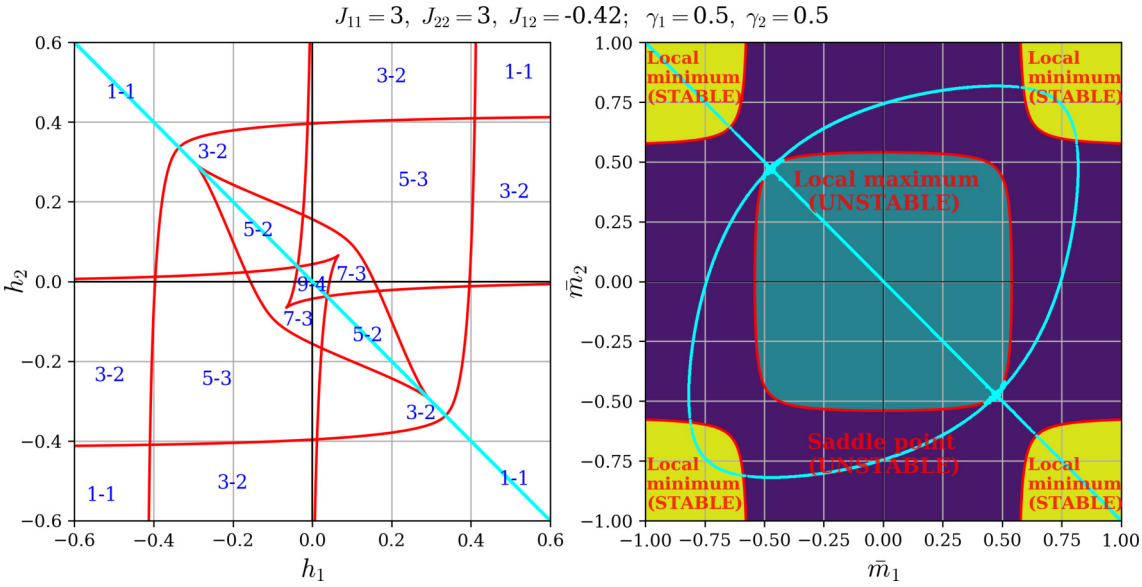

Fig. 2.5: Dependence of partial magnetisations on the field $h_1 = -h_2$ in the two-component CW model with $J_{11} = 3,\ J_{22} = 3,\ J_{12} = -0.42;\ \gamma_1 = \gamma_2 = 0.5$ at $T = 1$. The animation is available at https://youtu.be/8goNjSbzABs.

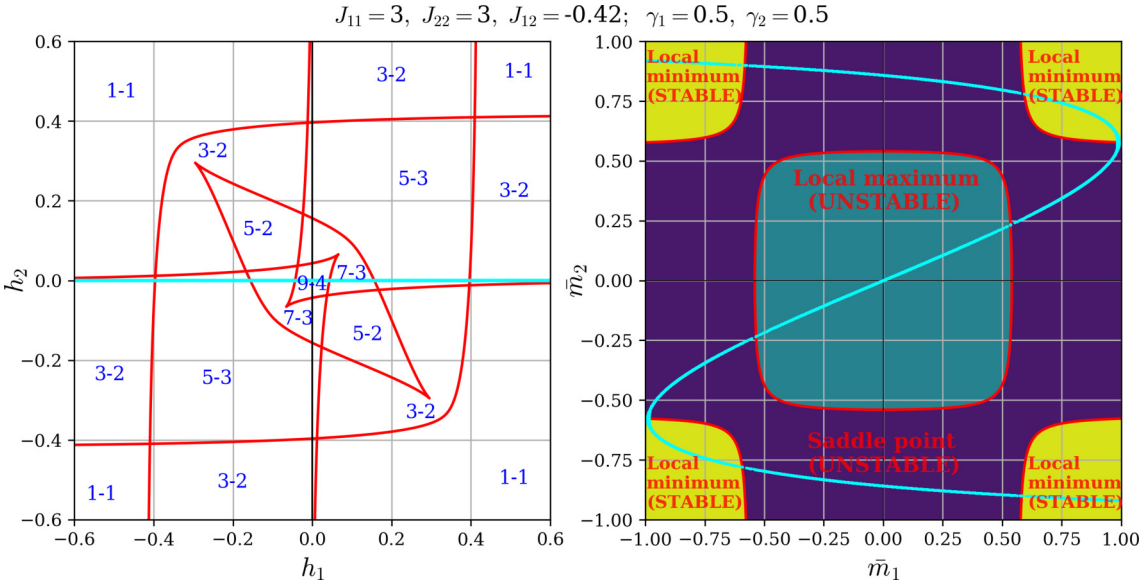

Fig. 2.6: Dependence of partial magnetisations on the field h_1 in the two-component CW model with $J_{11} = 3,\ J_{22} = 3,\ J_{12} = -0.42;\ h_2 = 0;\ \gamma_1 = \gamma_2 = 0.5$ at $T = 1$. The animation is available at https://youtu.be/nIIYAbZY5c0.

Appendix C

Code

The code used in this work can be found in the following Git repositories

- For Chapter 2 and Chapter 3: https://github.com/OlegRS/MCW_model;
- For Chapter 4: https://github.com/OlegRS/ERGMs.

The images Fig. 2.40, Fig. 3.1, Fig. 4.7, Fig. 4.13 and Fig. 4.20 were produced using Cytoscape [Shannon et al. (2003)] on the graphs generated using GraphOS (https://github.com/OlegRS/GraphOS).

References

Abbe, E. (2018), 'Community detection and stochastic block models: Recent developments', *Journal of Machine Learning Research* **18**(177), 1–86.

Agliari, E., Barra, A., Schiavo, L. D. and Moro, A. (2016), 'Complete integrability of information processing by biochemical reactions', *Nature, Scientific Reports — 6:36314 — DOI: 10.1038/srep36314* .

Annibale, A. and Courtney, O. T. (2015), 'The two-star model: exact solution in the sparse regime and condensation transition', *Journal of Physics A: Mathematical and Theoretical* **48**(36), 365001.

Barra, A., Di Lorenzo, A., Guerra, F. and Moro, A. (2014), 'On quantum and relativistic mechanical analogues in mean-field spin models', *Proc. R. Soc. A 2014 470, 20140589* .

Barra, A., Galluzzi, A., Guerra, F., Pizzoferrato, A. and Tantari, D. (2014), 'Mean field bipartite spin models treated with mechanical techniques', *The European Physical Journal B* **87**(74).

Bateman, H. (1915), 'SOME RECENT RESEARCHES ON THE MOTION OF FLUIDS', *Monthly Weather Review* **43**(4), 163 – 170.

Berthet, Q., Rigollet, P. and Srivastava, P. (2019), 'Exact recovery in the Ising blockmodel', *The Annals of Statistics* **47**(4), 1805 – 1834.

Besag, J. (1974), 'Spatial Interaction and the Statistical Analysis of Lattice Systems', *Journal of the Royal Statistical Society. Series B (Methodological)* **36**(2), 192–236.

Bianchi, A., Giardinà, C. and Contucci, P. (2003), 'Thermodynamic limit for mean-field spin models', *Mathematical Physics Electronic Journal* **9**(6), 1–15.

Binder, K. (1987), 'Theory of first-order phase transitions', *Reports on Progress in Physics* **50**(7), 783–859.

Bishop, C. M. (2006), *Pattern Recognition and Machine Learning (Information Science and Statistics)*, Springer-Verlag, Berlin, Heidelberg.

Bowers, R. G. and Schofield, S. L. (1981), 'The Curie–Weiss–Néel model of a ferrimagnet', *Canadian Journal of Physics, 1981, 59(7): 883-887, https://doi.org/10.1139/p81-114* .

Brown, W. F. (1963), 'Thermal Fluctuations of a Single-Domain Particle', *Phys. Rev.* **130**, 1677–1686.

Burgers, J. (1948), A Mathematical Model Illustrating the Theory of Turbulence, Vol. 1 of *Advances in Applied Mechanics*, Elsevier, pp. 171 – 199.

Bury, T. (2013), 'A statistical physics perspective on criticality in financial markets', *Journal of Statistical Mechanics: Theory and Experiment* **2013**(11), 11004.

Chandler, D. (1987), *Introduction to Modern Statistical Mechanics*, Oxford University Press, Inc.

Cole, J. D. (1951), 'ON A QUASI-LINEAR PARABOLIC EQUATION OCCURRING IN AERODYNAMICS', *Quarterly of Applied Mathematics* **9**(3), 225–236.

Contucci, P. and Gallo, I. (2008), 'Bipartite mean field spin systems. Existence and solution.', *Mathematical Physics Electronic Journal [electronic only]* **14**, Paper No. 1, 21 p.–Paper No. 1, 21 p.

Contucci, P., Gallo, I. and Menconi, G. (2008), 'PHASE TRANSITIONS IN SOCIAL SCIENCES: TWO-POPULATION MEAN FIELD THEORY', *International Journal of Modern Physics BVol. 22, No. 14, pp. 2199-2212 : https://doi.org/10.1142/S0217979208039423* .

Coolen, A. (2016), *Theory of Complex Networks*, Department of Mathematics, King's College London.

Cowles, M. K. and Carlin, B. P. (1996), 'Markov Chain Monte Carlo Convergence Diagnostics: A Comparative Review', *Journal of the American Statistical Association* **91**(434), 883–904.

De Matteis, G., Giglio, F. and Moro, A. (2018), 'Exact equations of state for nematics', *Annals of Physics* **396**, 386–396.

De Nittis, G. and Moro, A. (2012), 'Thermodynamic phase transitions and shock singularities', *Proc. R. Soc. A* **468**, 701–719.

Erdős, P. and Rényi, A. (1959), 'On Random Graphs I.', *Publicationes Mathematicae* **6**, 290–297.

Fedele, M., Vernia, C. and Contucci, P. (2013), 'Inverse problem robustness for multi-species mean-field spin models', *Journal of Physics A: Mathematical and Theoretical* **46**(6), 065001.

Frank, O. and Strauss, D. (1986), 'Markov Graphs', *Journal of the American Statistical Association* **81**(395), 832–842.

Handcock, M. (2003), 'Assessing degeneracy in statistical models of social networks', *Journal of the American Statistical Association* **76**, 33–50.

Holland, P. and Leinhardt, S. (1981), 'An Exponential Family of Probability Distributions for Directed Graphs', *Journal of The American Statistical Association - J AMER STATIST ASSN* **76**, 33–50.

Hopf, E. (1950), 'The partial differential equation $u_t + uu_x = \mu_{xx}$', *Communications on Pure and Applied Mathematics* **3**(3), 201–230.

Jaynes, E. T. (1957), 'Information theory and statistical mechanics', *Phys. Rev.* **106**, 620–630.

Lezon, T. R., Banavar, J. R., Cieplak, M., Maritan, A. and Fedoroff, N. V. (2006), 'Using the principle of entropy maximization to infer genetic interaction networks from gene expression patterns', *Proc Natl Acad Sci USA* **103**(50), 19033–19038.

Lorenzoni, P. and Moro, A. (2019), 'Exact analysis of phase transitions in mean-field Potts models', *Phys. Rev. E* **100**, 022103.

MacKay, D. J. C. (2003), *Information Theory, Inference, and Learning Algorithms*, Cambridge University Press.

Néel, L. (1952), 'Antiferromagnetism and Ferrimagnetism', *Proceedings of the Physical Society. Section A* **65**(11), 869–885.

Néel, M. L. (1948), 'Propriétés magnétiques des ferrites ; ferrimagnétisme et antiferromagnétisme', *Ann. Phys., Vol. 12, No. 3 (1948), pp. 137–198; https://doi.org/10.1051/anphys/194812030137* .

Newman, M. (2010), *Networks*, Oxford University Press.

Nguyen, H. C., Zecchina, R. and Berg, J. (2017), 'Inverse statistical problems: from the inverse Ising problem to data science', *Advances in Physics* **66**(3), 197–261.

Onsager, L. (1944), 'Crystal Statistics. I. A Two-Dimensional Model with an Order-Disorder Transition', *Phys. Rev.* **65**, 117–149.

Park, J. and Newman, M. E. J. (2004*a*), 'Solution of the two-star model of a network', *PHYSICAL REVIEW E* .

Park, J. and Newman, M. E. J. (2004*b*), 'Statistical mechanics of networks', *Phys. Rev. E* **70**, 066117.

Park, J. and Newman, M. E. J. (2005), 'Solution for the properties of a clustered network', *PHYSICAL REVIEW E* .

Peixoto, T. P. (2019), Bayesian stochastic blockmodeling, *in* 'Advances in Network Clustering and Blockmodeling', Wiley, chapter 11.

Robins, G., Pattison, P., Kalish, Y. and Lusher, D. (2007), 'An introduction to exponential random graph (p*) models for social networks', *Social Networks* **29**(2), 173 – 191. Special Section: Advances in Exponential Random Graph (p*) Models.

Robins, G., Snijders, T., Wang, P., Handcock, M. and Pattison, P. (2007), 'Recent developments in exponential random graph (p*) models for social networks', *Social Networks* **29**(2), 192 – 215. Special Section: Advances in Exponential Random Graph (p*) Models.

Schneidman, E., Berry, M. J., Segev, R. and Bialek, W. (2006), 'Weak pairwise correlations imply strongly correlated network states in a neural population', *Nature* **440**(7087), 1007–1012.

Shannon, P., Markiel, A., Ozier, O., Baliga, N. S., Wang, J. T., Ramage, D., Amin, N., Schwikowski, B. and Ideker, T. (2003), 'Cytoscape: a software environment for integrated models of biomolecular interaction networks', *Genome Res.* .

Smart, J. S. (1955), 'The Néel theory of ferrimagnetism', *American Journal of Physics 23, 356; https://doi.org/10.1119/1.1934006* .

Snijders, T. A. B., Pattison, P. E., Robins, G. L. and Handcock, M. S. (2006), 'New Specifications for Exponential Random Graph Models', *Sociological Methodology* **36**, 99–153.

Squartini, T., de Mol, J., den Hollander, F. and Garlaschelli, D. (2015), 'Breaking of Ensemble Equivalence in Networks', *Phys. Rev. Lett.* **115**, 268701.

Stein, R. R., Marks, D. S. and Sander, C. (2015), 'Inferring Pairwise Interactions from Biological Data Using Maximum-Entropy Probability Models', *PLOS Computational Bioligy* .

Strauss, D. (1986), 'ON A GENERAL CLASS OF MODELS FOR INTERACTION', *SIAM Rview, Vol. 28, No. 4, December* .

Wasserman, S. and Pattison, P. (1996), 'Logit models and logistic regressions for social networks: I. An introduction to Markov graphs and p*', *Psychometrika* **61**, 401–425.

Weiss, P. (1907), 'L'hypothèse du champ moléculaire et la propriété ferromagnétique', *J. Phys. Theor. Appl. 6, 661-690; DOI: 10.1051/jphystap:019070060066100* .

Whitham, G. B. (1974), *Linear and nonlinear waves*, Wiley.

Whitney, H. (1955), 'On singularities of mappings of Euclidean spaces. I. Mappings of the plane into the plane', *Annals of Mathematics, DOI: 10.2307/1970070* .